

Award Number: W81XWH-10-1-0201

TITLE: New image-based techniques for prostate biopsy and treatment

PRINCIPAL INVESTIGATOR: Mehdi Moradi, Ph.D.

CONTRACTING ORGANIZATION: University of British Columbia
Vancouver, CA V6T 1Z4

REPORT DATE: April 2012

TYPE OF REPORT: Annual Summary

PREPARED FOR: U.S. Army Medical Research and Materiel Command
Fort Detrick, Maryland 21702-5012

DISTRIBUTION STATEMENT: Approved for Public Release;
Distribution Unlimited

The views, opinions and/or findings contained in this report are those of the author(s) and should not be construed as an official Department of the Army position, policy or decision unless so designated by other documentation.

REPORT DOCUMENTATION PAGE				<i>Form Approved</i> OMB No. 0704-0188	
Public reporting burden for this collection of information is estimated to average 1 hour per response, including the time for reviewing instructions, searching existing data sources, gathering and maintaining the data needed, and completing and reviewing this collection of information. Send comments regarding this burden estimate or any other aspect of this collection of information, including suggestions for reducing this burden to Department of Defense, Washington Headquarters Services, Directorate for Information Operations and Reports (0704-0188), 1215 Jefferson Davis Highway, Suite 1204, Arlington, VA 22202-4302. Respondents should be aware that notwithstanding any other provision of law, no person shall be subject to any penalty for failing to comply with a collection of information if it does not display a currently valid OMB control number. PLEASE DO NOT RETURN YOUR FORM TO THE ABOVE ADDRESS.					
1. REPORT DATE April 2012		2. REPORT TYPE Annual Summary		3. DATES COVERED 1 April 2010 – 31 March 2012	
4. TITLE AND SUBTITLE New image-based techniques for prostate biopsy and treatment				5a. CONTRACT NUMBER	
				5b. GRANT NUMBER W81XWH-10-1-0201	
				5c. PROGRAM ELEMENT NUMBER	
6. AUTHOR(S) Mehdi Moradi, Ph.D. E-Mail: moradi@ece.ubc.ca				5d. PROJECT NUMBER	
				5e. TASK NUMBER	
				5f. WORK UNIT NUMBER	
7. PERFORMING ORGANIZATION NAME(S) AND ADDRESS(ES) University of British Columbia Vancouver, CA V6T 1Z4				8. PERFORMING ORGANIZATION REPORT NUMBER	
9. SPONSORING / MONITORING AGENCY NAME(S) AND ADDRESS(ES) U.S. Army Medical Research and Materiel Command Fort Detrick, Maryland 21702-5012				10. SPONSOR/MONITOR'S ACRONYM(S)	
				11. SPONSOR/MONITOR'S REPORT NUMBER(S)	
12. DISTRIBUTION / AVAILABILITY STATEMENT Approved for Public Release; Distribution Unlimited					
13. SUPPLEMENTARY NOTES					
14. ABSTRACT This report details the research and training outcomes of a prostate cancer postdoctoral training award. The work resulted in technologies for segmentation, cancer detection, and brachytherapy seed detection that take advantage of ultrasound vibroelastography and ultrasound RF signals. In segmentation, we report a fully automatic algorithm that combines B-mode and elastography data within an active shape model approach. For cancer detection, we report the sensitivity of 75.5% for elastography in cancer detection. In brachytherapy seed detection and dosimetry, we showed that the use of raw RF ultrasound signals can result in partial detection of the seed clouds, sufficient for registration to C-arm fluoroscopy for the purpose of dosimetry. The results were published in form of five journal publications and six conference presentations in international journals and conferences. The PI attended nine conferences and meetings during the course of the award.					
15. SUBJECT TERMS Prostate cancer, diagnosis, ultrasound					
16. SECURITY CLASSIFICATION OF:			17. LIMITATION OF ABSTRACT UU	18. NUMBER OF PAGES 94	19a. NAME OF RESPONSIBLE PERSON USAMRMC
a. REPORT U	b. ABSTRACT U	c. THIS PAGE U			19b. TELEPHONE NUMBER (include area code)

Table of Contents

	<u>Page</u>
Introduction.....	3
Body.....	3
Key Research Accomplishments.....	9
Reportable Outcomes.....	11
Conclusion.....	12
References.....	13
Appendices.....	14

Introduction

This documents reports the accomplishments of the PI, Dr Mehdi Moradi, supported by the postdoctoral training Award W81XWH-10-1-0201, from April 1, 2010 to March 31, 2012. The progress on the specific task listed in the award will be listed. Since this is a training award, other achievements of the trainee during the award will be enumerated as well. The technology developed for vibroelastography was described in the annual report. We will focus on progress towards specific clinical outcomes and achievements of the trainee.

The rationale of the proposal is that prostate tumors cannot be visualized in the ultrasound B-mode images used for interventional guidance. As a result, the current methodology of transrectal ultrasound (TRUS) guided biopsy is a systematic sampling approach, which can potentially miss or under sample cancerous tissue or may incorrectly stage the disease. Similarly, for therapeutic interventions such as brachytherapy and surgery, the lack of reliable radiologic characterization of the tissue forces the choice of radical treatment as opposed to focal therapy. The proposed research aims to produce highly demanded imaging technologies for ultrasound-based prostate biopsy and treatment procedures.

Body

Progress towards the research tasks defined in the statement of work:

Task 1: *Data collection and analysis to address specific aims (i) and (ii) in the research narrative:* Data collection for validation of *in-vivo* accuracy of cancer detection and extracapsular extension of prostate cancer based on RF time series and VE. This will be performed prior to prostatectomy. The gold standard will be histopathologic analysis of the extracted specimen. This serves specific aims 1 and 2 in the research narrative.

Progress toward task 1: data collection was performed under UBC IRB: "(H08-02696) Ultrasound studies for prostate imaging optimization". The protocol was designed to acquire ultrasound RF data and vibroelastography from the patients in the operating room, immediately before the radical prostatectomy surgery. We scheduled pre-operative multiparametric MRI from the same cases as well. After the surgery, we collected whole-mount pathology analysis of the extracted prostate tissue.

Due to operational issues, the acquisition of the pathology slides was slow and in some cases impossible. Table I lists the data acquired.

Table I: Number of cases and data types acquired during the study

Total number of cases	19
Cases with wholemount pathology	10
Cases with VE	19
Cases with RF ultrasound	12
Cases with pre-operative MRI	14

Task 2: *Analysis to address specific aims (iii) in the research narrative:* Data collection for validation of the visualization and segmentation of prostate with VE imaging. MR imaging is used for control.

Progress toward Task 2: The PI and the team in UBC have made significant progress towards improving the visualization and the segmentation of the gland. This has resulted in publications that we included as Appendices. The summary of the methodology and results are provided here:

VE as a tool to improve prostate visualization: Vibroelastography (VE), an ultrasound-based method that creates images of tissue viscoelasticity contrast, was evaluated as an imaging modality to visualize and segment the prostate. We performed a clinical study to characterize the visibility of the prostate in VE images and the ability to detect the boundary of the gland. Measures for contrast, edge strength characterized by gradient and statistical intensity change at the edge, and the continuity of the edges were proposed and computed for VE and B-mode ultrasound images. Furthermore, using MRI as the gold standard, we compared the error in the computation of the volume of the gland from VE and B-mode images. The results demonstrated that VE images are superior to B-mode images in terms of contrast, with an approximately six fold improvement in contrast-to-noise ratio, and in terms of edge strength, with an approximately two fold improvement in the gradient in the direction normal to the edge. The computed volumes showed that the VE

images provide an accurate 3D visualization of the prostate with volume errors that were slightly lower than errors computed based on B-mode images. The total gland volume error was $8.8 \pm 2.5\%$ for VE vs. MRI and $10.3 \pm 4.6\%$ for B-mode vs. MRI, and the total gland volume difference was $-4.6 \pm 11.1\%$ for VE vs. MRI and $-4.1 \pm 17.1\%$ for B-mode vs. MRI, averaged over nine patients and three observers. Our results showed that viscoelastic mapping of the prostate region using VE images can play an important role in improving the anatomic visualization of the prostate and has the potential of becoming an integral component of interventional procedures such as brachytherapy. Full description of the technology and the clinical study are published in Medical Image Analysis.

Task 3: Development of feature extraction and classification approaches for real-time tissue typing for cancer detection (based on RF time series).

On cancer detection, due to technical issues regarding motion compensation from passive RF time series, we focused mainly on cancer detection from ultrasound elastography (which is the active version of the time series). The most recent results acquired from data are outlined here.

Transrectal ultrasound with VE was performed intra-operatively, prior to the prostatectomy procedure, on patients diagnosed with prostate cancer. Transfer function images of the prostate, showing the relative stiffness of the tissue within and surrounding the prostate were created. For each case, 9-13 pathology slides extracted from the prostate at approximately 4mm intervals, with cancer marked, were available. Areas suspected for cancer were marked on the VE images and then compared to the pathology results.

Gleason scores for 51 tumors were available. Twenty of the 31 tumors with Gleason scores of 3+3 (64.5%), 13 of the 16 tumors with Gleason scores of 3+4 (81.25%), both tumors with Gleason scores of 4+3 with tertiary 5 (100%) and both tumors with Gleason scores of 4+5 (100%) were detected. **VE had an overall sensitivity of 75.5% for detecting prostate cancer, with a false negative and a false positive percentage of 24.4% and 37.3% respectively.** The sensitivity of VE for detecting cancer with a Gleason score of 7 and above was 85%. A region based analysis was also performed. **Some anterior lying tumors were detected in elastography.**

This study showed that the use of additional information from VE has the potential of improving the detection of prostate cancer. This alternative imaging method could aid prostate

biopsy by highlighting areas suspicious for cancer, reducing the need for repeated biopsy procedures. It could also potentially be used as augmented reality during robotic-assisted prostatectomy. An abstract featuring these results will be presented at the 67th Annual Meeting of the Canadian Urology Association in Banff, Alberta, Canada (June 24th, 2012).

A machine learning framework for cancer detection from image data: During the course of this award, the PI worked on a classification framework, based on support vector machine classification, to calculate cancer probability maps from image data. The details are reported in Appendix I on multiparametric MRI data. The use of the same approach for US data is the topic of a manuscript currently in preparation.

Task 4: Developing automatic segmentation methods for delineating VE images of prostate for real time gland visualization during prostatectomy.

Progress toward Task 4:

Prostate segmentation in B-mode images is a challenging task even when done manually by experts. We proposed a 3D automatic prostate segmentation algorithm which made use of information from both ultrasound B-mode and vibroelastography data. We exploited the high contrast to noise ratio of vibroelastography images of the prostate, in addition to the commonly used B-mode images, to implement a 2D Active Shape Model (ASM)-based segmentation algorithm on the midgland image. The prostate model was deformed by a combination of two measures, the gray level similarity and the continuity of the prostate edge on both image types. The automatically obtained midgland contour was then used to initialize a 3D segmentation algorithm which models the prostate as a tapered and warped ellipsoid. Vibroelastography images were used in addition to ultrasound images to improve boundary detection.

We reported a Dice similarity coefficient of 0.85 ± 0.10 and 0.84 ± 0.09 comparing the 2D automatic contours with manual contours of two observers on 61 images. For 11 cases, a whole gland volume error of $10.2 \pm 2.2\%$ and $13.5 \pm 4.1\%$ and whole gland volume difference of $-7.2 \pm 9.1\%$ and $-13.3 \pm 12.6\%$ between 3D automatic and manual surfaces of two observers was obtained. This was the first validated work showing the fusion of B-mode and vibroelastography data for automatic 3D segmentation of the prostate. Sample results are illustrated in Figure 1. The complete description of the methodology is currently under review in the IEEE Transactions on

Medical Imaging [1]. We have argued, in [1], that adding of vibroelastography images to the conventional B-mode, for improving prostate segmentation is very helpful and important.

Task 5: To investigate the sources of tissue typing information in RF time series.

Our clinical in vivo study showed that our RF time series analysis as reported in [2] and [3] on ex-vivo tissue, needs major modifications to be adopted for in-vivo work. This is due to the fact that the methods put forth in [2,3] rely on the assumption that continuously received samples of RF time series originate from the same physical location in the tissue. In the in-vivo case, breathing and patient motion violated this assumption. Therefore, we need to design motion compensation techniques to overcome this limitation. Since those methods are outstanding, we have sought funding from other sources to work on them. Since the goals of this award were clinical, our research group decided to separate Task 5 from the PI's responsibilities. Nevertheless, the study of the sources of tissue typing information in RF time series in ex-vivo studies were accomplished in our research group by studying the thermal effects of ultrasound. This is now published in [4].

Task 6: Training

The training goal of this award was to prepare the PI to assume the role of an independent researcher. We list the training activities of the PI here. It is worth mentioning that the PI has received a preliminary offer to start working as a grant-tenure track assistant professor in a joint position between the Electrical Engineering and Urological Sciences Department of the University of British Columbia.

As suggested in the statement of work, the PI attended regular research meetings with Professor Tim Salcudean (weekly), and contributed to the Medical Imaging course (ECE433) offered by Dr Robert Rohling in UBC's Department of Electrical and Computer Engineering in Fall term of 2010 and 2012. The PI also had a research visit to the Brigham and Women's Hospital in Boston where he started a collaboration with Professor Clare Tempany from Harvard Medical School on multimodality prostate imaging. This resulted in two conference abstracts that are listed in this report as Appendix VI and XI.

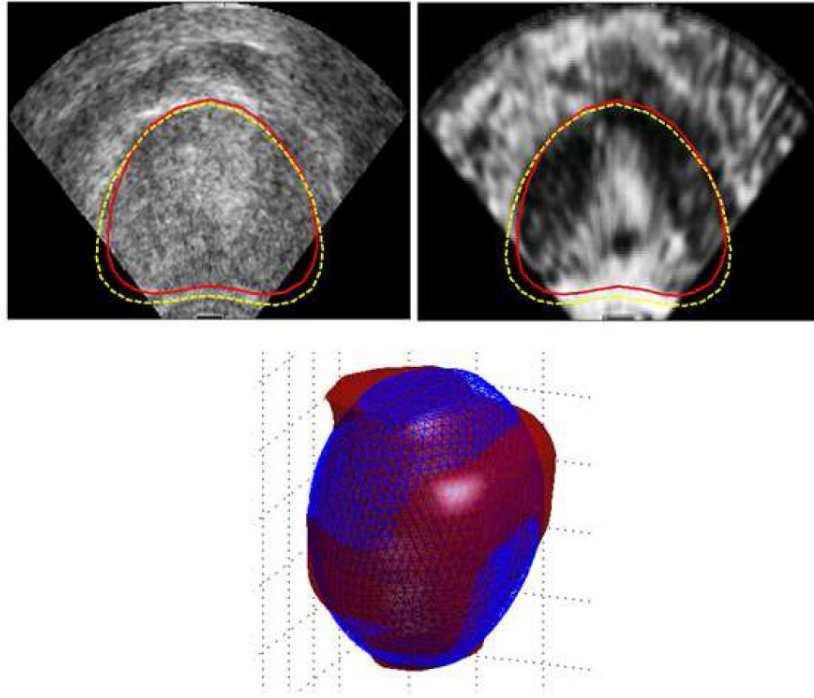


Figure 1 - 2D segmentation results shown on corresponding B-mode (left) and vibroelastography (right) mid-gland images. The initial contour is shown in dashed yellow and the final contour in solid red. The final 3D segmented surface (triangulated blue) is also compared to the manually created surface (red) in the lower image.

PI's conference presentations during the course of the award:

- 1) Poster Presentation: Towards joint MRI-US based tissue typing and guidance for prostate interventions in AMIGO, 4th NCIGT and NIH Image Guided Therapy Workshop, Washington DC, October 2011.
- 2) Workshop style presentation: Deformable prostate registration, 3D ultrasound to MRI, 2012 Winter Project Week of the National Alliance for Medical Image Computing, January 2012, Salt Lake City, Utah.
- 3) Poster Presentation: Towards intra-operative prostate brachytherapy dosimetry based on partial seed localization in ultrasound and registration to C-arm fluoroscopy, MICCAI 2011, Toronto, Canada, 2011.
- 4) Poster Presentation: Prostate Cancer Probability Estimation Based on DCE-DTI Features and Support Vector Machine Classification, ISMRM, Montreal, Canada, May 2011.

- 5) Poster Presentation: Ultrasound-based techniques for enhancing diagnostic and therapeutic prostate interventions, IMPaCT 2011, Orlando, FL, March 2011. [Travel funded by this award].
- 6) Poster Presentation: Brachytherapy strand visibility in reflected power ultrasound images: Comparison of EchoStrand vs. Regular Strands Using 3D Visibility Profiles, IEEE Ultrasonics Symposium, San Diego, CA, 2010.
- 7) Poster Presentation: Under-Determined Non-Cartesian MR Reconstruction with Non-convex Sparsity Promoting Analysis Prior, MICCAI, Beijing, China, 2010.
- 8) Poster Presentation: Automatic Prostate Segmentation Using Fused Ultrasound B-Mode and Elastography Images, MICCAI, Beijing, China, September 2010. [Travel partially funded by this award].
- 9) Podium Presentation: Ultrasound Image Segmentation Based on Statistical Unit-root Test of B-Scan Radial Intensity Profiles, The 33rd Conference of the Canadian Medical and Biological Engineering Society, Vancouver, Canada, 2010.

Invited Tutorials, talks

- 1) Invited Research Seminar: “Multiparametric ultrasound for tissue typing, results in prostate cancer characterization”, MIT Computer Science and Artificial Intelligence Laboratory, January 2012.
- 2) Research seminar: “Image based solutions for prostate interventions: from multiparametric to multimodality”, Department of Radiology, Brigham and Women’s Hospital, Harvard Medical School, October 2011.
- 3) Research seminar: “Image-based solutions for prostate interventions”, Vanderbilt University, Department of Biomedical Engineering, November 2010.
- 4) A three hour tutorial titled: “Imaging in Practice: Comparing the Applications of X-ray CT, US, and MRI Modalities”, The 5th Canadian Student Conference on Biomedical Computing and Engineering, Waterloo, ON, Canada, May 20, 2010.

Key Research Accomplishments

The main accomplishment of this postdoctoral fellowship is the success of the PI who will start an independent career as a researcher as of May 1st, 2012. The PI had an excellent opportunity to be trained in the general field of image-guided prostate interventions. The list of technical contributions can be summarized as follows:

- 1) We showed that ultrasound vibroelastography is a valuable technology in imaging the prostate gland. It improves the visualization of the prostate gland and enhances the segmentation.
- 2) We combined B-mode and vibroelastography and created a fully automatic method for prostate segmentation [1].
- 3) We studied ultrasound vibroelastography for cancer detection and showed that VE has a high sensitivity in cancer detection. However, the specificity of this imaging technology is not sufficient for cancer characterization.
- 4) An ultrasound-based methodology for visualization of radioactive brachytherapy seeds in prostate and dosimetry was designed and examined on a small clinical dataset **[Appendix VII]**.
- 5) We developed a machine learning framework for characterization of prostate tissue using features extracted from medical images. We used this methodology as reported in **[Appendix I]** with multiparametric MRI data. The use of this same technology with VE and B-mode ultrasound RF data is the subject of a manuscript currently in preparation.

Reportable outcomes

Journal Publications:

1. **M. Moradi**, S. E. Salcudean, S. D. Chang, E. C. Jones, Nicholas Buchan, Rowan G. Casey, S. L. Goldenberg and P. Kozlowski. Multiparametric MRI Maps for Detection and Grading of Dominant Prostate Tumors. *Magnetic Resonance Imaging*, In Press. DOI: 0.1002/jmri.23540, 2012. **[Appendix I]**.

2. J. Lobo, **M. Moradi**, N. Chng, E. Dehghan, W. J. Morris, G. Fichtinger, S. E. Salcudean. Use of Needle Track Detection to Quantify the Displacement of Stranded Seeds Following Prostate Brachytherapy. *IEEE Transactions on Medical Imaging*, vol. 31, no. 3, pp. 738-748, 2012. **[Appendix II]**.
3. E. Dehghan, **M. Moradi**, X. Wen, D. French, J. Lobo, W. J. Morris, S. E. Salcudean, G. Fichtinger. Prostate Implant Reconstruction from C-arm Images with Motion-Compensated Tomosynthesis. *Medical Physics*, vol 38, no. 10, pp. 5290-5302, 2011. **[Appendix III]**.
4. E. Dehghan, A. K. Jain, **M. Moradi**, X. Wen, W. J. Morris, S. E. Salcudean, and G. Fichtinger. Brachytherapy Seed Reconstruction with Joint-Encoded C-Arm Single-Axis Rotation and Motion Compensation. *Medical Image Analysis*, vol. 15, no. 5, pp. 760–771, 2011. **[Appendix IV]**
5. S. S. Mahdavi, **M. Moradi**, X. Wen, W. J. Morris, and S. E. Salcudean. Evaluation of Visualization of the Prostate Gland in Vibroelastography Images. *Medical Image Analysis*, vol. 15, no. 4, pp. 589–600, 2011. **[Appendix V]**.

Conference Publications:

- 6) **M. Moradi**, A. Fedorov, W. M Wells, K. Tuncali, S. N. Gupta, F. M. Fennessy, and C. M. Tempany, “Machine learning for target selection in MR-guided prostate biopsy: A preliminary study”, Accepted to appear in the Proceedings of the Annual Meeting of the International Society for Magnetic Resonance in Medicine (*ISMRM*), to appear in May 2012. **[Appendix VI]**
- 7) **M. Moradi**, S. Mahdavi, S. Deshmukh, J Lobo, E. Dehghan, G. Fichtinger, W. J. Morris, S. E. Salcudean. Towards intra-operative prostate brachytherapy dosimetry based on partial seed localization in ultrasound and registration to C-arm fluoroscopy. In: *MICCAI 2011*, Part I, LNCS 6891, pp. 291–298, 2011. **[Appendix VII]**.
- 8) **M. Moradi**, S. E. Salcudean, S. D. Chang, E. C. Jones, S. L. Goldenberg, and P. Kozlowski, “Prostate Cancer Probability Estimation Based on DCE-DTI Features and Support Vector Machine Classification,” Annual Meeting of the International Society for Magnetic Resonance in Medicine (*ISMRM*), pp 2638, 2011. **[Appendix VIII]**.

- 9) S. S. Mahdavi, **M. Moradi**, W. J. Morris and S. E. Salcudean. Automatic Prostate Segmentation Using Fused Ultrasound B-Mode and Elastography Images. In: *MICCAI2010*, LNCS 6362, pp. 76–83, 2010. **[Appendix IX]**.
- 10) [Abstract] Mehdi Moradi, et al., “Ultrasound-based techniques for enhancing diagnostic and therapeutic prostate interventions”, IMPaCT 2011, Orlando, FL, March 2011. **[Appendix X]**.
- 11) [Abstract] Mehdi Moradi, et al., Towards joint MRI-US based tissue typing and guidance for prostate interventions in AMIGO, 4th NCIGT and NIH Image Guided Therapy Workshop, Washington DC, October 2011. **[Appendix XI]**.

Conclusions

We have successfully completed four of the five tasks defined in the statement of work. One task (the study of the sources of tissue typing information in RF time series) was followed within our research group, with limited involvement from the PI due to the technical difficulty of acquiring high quality RF time series in vivo. The overall goal of the project which was the development of ultrasound-based technologies for image-guided prostate interventions was fully achieved. We have developed methodologies for segmentation of the gland, cancer visualization, and brachytherapy seed detection during this work. Eleven publications have been resulted from this work and two other submissions are currently in preparation. The PI has also met the training goals through the mentoring of world class scientists and clinicians including Professor Larry Goldenberg, Professor Tim Salcudean, and Professor Clare Tempany.

References:

1. S. S. Mahdavi, M. Moradi, and S. E. Salcudean. Automatic prostate segmentation using fused ultrasound B-mode and elastography images. Submitted to *IEEE Transactions on Medical Imaging*, April 2011.
2. M. Moradi, P. Mousavi, P. Abolmaesumi. Tissue Typing Using Ultrasound RF Time Series: Experiments with Animal Tissue Samples. *Medical Physics*, vol. 37, no. 8, pp 1401-1413, 2010.
3. M. Moradi, P. Abolmaesumi, R. Siemens, E. Sauerbrei, A. Boag, P. Mousavi, Augmenting Detection of Prostate Cancer in Transrectal Ultrasound Images Using SVM and RF Time Series. *IEEE Transactions on Biomedical Engineering*, vol. 56, no. 9, pp. 2214-2224, 2009 .
4. Mohammad I. Daoud, Parvin Mousavi, Farhad Imani, Robert Rohling, Computer-aided tissue characterization using ultrasound-induced thermal effects: analytical formulation and in-vitro animal study, Proceedings Vol. 7968, Medical Imaging 2011: Ultrasonic Imaging, Tomography, and Therapy, Jan D'hooge; Marvin M. Doyley, Editors, 79680G, , 2011.
5. Farhad Imani, Mohammad Daoud, M. Moradi, Purang Abolmaesumi, Parvin Mousavi. Tissue classification using depth-dependent ultrasound time series analysis: In vitro animal study, In: *SPIE Medical Imaging*, edited by Jan D'hooge, Marvin M. Doyley, Proc. of SPIE Vol. 7968, pp. 79680F1-79680F7, 2011.

Original Research

Multiparametric MRI Maps for Detection and Grading of Dominant Prostate Tumors

Mehdi Moradi, PhD,^{1*} Septimiu E. Salcudean, PhD,¹ Silvia D. Chang, MD,^{2,5,6} Edward C. Jones, MD,⁵ Nicholas Buchan, MD,⁶ Rowan G. Casey, MD,³ S. Larry Goldenberg, MD,^{3,4} and Piotr Kozlowski, PhD^{2–4,7}

Purpose: To develop an image-based technique capable of detection and grading of prostate cancer, which combines features extracted from multiparametric MRI into a single parameter map of cancer probability.

Materials and Methods: A combination of features extracted from diffusion tensor MRI and dynamic contrast enhanced MRI was used to characterize biopsy samples from 29 patients. Support vector machines were used to separate the cancerous samples from normal biopsy samples and to compute a measure of cancer probability, presented in the form of a cancer colormap. The classification results were compared with the biopsy results and the classifier was tuned to provide the largest area under the receiver operating characteristic (ROC) curve. Based solely on the tuning of the classifier on the biopsy data, cancer colormaps were also created for whole-mount histopathology slices from four radical prostatectomy patients.

Results: An area under ROC curve of 0.96 was obtained on the biopsy dataset and was validated by a “leave-one-patient-out” procedure. The proposed measure of cancer probability shows a positive correlation with Gleason score. The cancer colormaps created for the histopathology patients do display the dominant tumors. The colormap accuracy increases with measured tumor area and Gleason score.

Conclusion: Dynamic contrast enhanced imaging and dif-

fusion tensor imaging, when used within the framework of supervised classification, can play a role in characterizing prostate cancer.

Key Words: Multi-parametric MRI; support vector machines; prostate cancer; focal therapy
J. Magn. Reson. Imaging 2012;000:000–000.
 © 2012 Wiley Periodicals, Inc.

AS THE SECOND leading cancer-related cause of death among males (1), prostate cancer is the subject of research efforts worldwide. The improvements achieved in the screening techniques for prostate cancer have resulted in the diagnosis of a rising number of cases, among which lies a population with low risk and/or localized tumors. Nevertheless, radical prostatectomy remains the most common treatment for the disease. As a result, 30% of cases of radical prostatectomy are performed on patients with pathologically insignificant cancer (2), making them subject to complications such as sexual, urinary, and bowel morbidity after the surgery. These complications are associated with the techniques used during surgery. Even though these have improved significantly in the past decade (3,4), further improvements are difficult to envisage without knowledge of the cancer location, which can determine the need for and extent of the surgical positive margins applied. Furthermore, focal treatment of the disease with associated sparing of sensitive structures such as the neuro-vascular bundles, are viable options only if accurate patient-specific maps of cancer grade and stage can be provided preoperatively. In other words, the success of focal therapy relies on proper patient selection and adequate characterization of the tumor's location, extent and histology. The most commonly used method to assess prostate cancer is biopsy under transrectal ultrasound (TRUS). Because TRUS cannot accurately image prostate cancer, biopsy protocols suffer from significant sampling errors, resulting in false negatives or under-sampling of major tumors (5).

Magnetic resonance imaging has a proven ability to visualize the prostate anatomy (6). However, the conventional T2 weighted MRI has insufficient specificity and sensitivity for diagnosis, and specially grading, of prostate cancer even at 3T (7–9). Several MRI-based

¹Department of Electrical and Computer Engineering, University of British Columbia, Vancouver, Canada.

²Department of Radiology, University of British Columbia, Vancouver, Canada.

³Department of Urologic Sciences, University of British Columbia, Vancouver, Canada.

⁴Vancouver Prostate Centre, Vancouver, BC, Canada, Vancouver, Canada.

⁵Department of Pathology and Laboratory Medicine, University of British Columbia, Vancouver, Canada.

⁶St George's Medical Centre, Christchurch, New Zealand.

⁷MRI Research Center, University of British Columbia, Vancouver, Canada.

Contract grant sponsor: U.S. Army Medical Research and Materiel Command; Contract grant number: W81XWH-10-1-0201; Contract grant sponsor: the Canadian Institutes of Health Research (CIHR).

*Address reprint requests to: M.M., Department of Electrical and Computer Engineering, University of British Columbia, Vancouver, Canada. E-mail: moradi@ece.ubc.ca

Received March 25, 2011; Accepted November 22, 2011.

DOI 10.1002/jmri.23540

View this article online at wileyonlinelibrary.com.

techniques that provide physiological information about tissue have been studied to improve the grading of cancer. Earlier studies focused on Magnetic Resonance Spectroscopy (MRS), which allows the creation of metabolite maps in the prostate region (10). However, the diagnostic improvements due to MRS were limited and inconclusive (11). A more recent development is the use of diffusion, both diffusion weighted imaging (DWI) and diffusion tensor imaging (DTI), which characterize the de-phasing of the MR signal caused by molecular diffusion. Prostate cancer causes a pathological change in the tissue in which the regular pattern of distribution of prostatic glands is disrupted by masses of malignant epithelial cells and glands that are irregularly distributed (12). The increased cellular density can cause a decrease in apparent diffusion coefficients (ADC) in DWI, and average diffusivity $\langle D \rangle$ values in DTI, measured in prostate tumors. The structural changes are also likely to alter the molecular level diffusion and to cause differences in fractional anisotropy (FA) between regular and normal cells, intensified by the progress of the disease. Diffusion imaging is fast and convenient without the need for contrast agents. Radiologists have reported that ADC can help differentiate central gland tumors from stromal and glandular hyperplasia (13). Studies in case of DTI, however, are also inconclusive and report increased, decreased, or even unchanged values of FA (14–16). Dynamic Contrast Enhanced MRI (DCE MRI) has also been studied for grading of prostate cancer. When combined with a pharmacokinetic model, DCE characterizes the changes in tissue microvasculature which are linked to cancer growth (17). However, DCE prostate studies report moderate to weak correlations between cancer grade and Gleason score with individual DCE parameters (18,19). A review of the role of MRI in detection and staging of prostate cancer is recently published (20).

The inconclusive correlation of MRI-based physiologic parameters with the progression of the disease is partly due to the heterogeneous and complex nature of both the biological tissue and the physiologic process of cancer progression. It is difficult, if not impossible, to extract specific ranges for the values of the individual parameters matched to the cancer stage. In the absence of such statistics, the solution appears to be supervised classification of the multi-parametric MRI data to separate normal and cancer tissue (21–23). Therefore, in this work a machine learning approach based on support vector machine classification (SVM) is used.

The purpose of this work is to use machine learning to develop an image based technique capable of detection and grading of prostate cancer by combining features extracted from multiparametric MRI into a single parameter map of cancer probability. We also study the validity of this method by comparison of the probability maps with whole-mount pathology.

MATERIALS AND METHODS

Data Collection Protocols

The data used in this work were obtained in two studies, both reviewed and approved by the Clinical

Research Ethics Board of our institution. The data from a biopsy study were used for training the machine learning algorithm and leave-one-patient-out evaluation. A second dataset from patients scheduled for radical prostatectomy, with available whole-mount histopathology analysis after surgery, was used for further validation of the trained classifier.

Biopsy Data

These data were used to train classifiers and quantitatively assess the performance of the DTI-DCE parameters for cancer detection. During 2009, 29 patients with a high clinical suspicion for prostate adenocarcinoma due to an elevated prostate specific antigen (PSA) and/or palpable prostatic nodule, with no prior treatment, were consecutively recruited to this study. Average PSA was 8.5 ng/mL (range: 0.94–15 ng/mL). Written consent was obtained from each patient before entering the study. To ensure that the biopsy process or result did not affect the assessment of MRI as a diagnosis tool, the MRI scans in the original study were completed before biopsy for all patients; the biopsy was done the same day within a couple of hours following MRI. We use the same data here, with the goal of training a classifier to detect and grade prostate cancer.

The biopsies were performed under local anesthetic and the number of biopsies obtained from the peripheral zone (PZ) was determined by prostate gland size. In patients with a prostate gland of 30 cc or less, eight biopsies (base: right and left; midgland: right lateral, left lateral, right medial, left medial; apex: right and left) were taken. For prostate glands ranging from 31 to 60 cc, 10 biopsies (base: right lateral, left lateral, right medial, left medial; midgland; and apex biopsies as above) were obtained. For prostate glands greater than 60 cc, 12 biopsies were obtained (apex: right lateral, left lateral, right medial, left medial; base; and midgland biopsies the same as the 10 biopsy scheme).

The dataset included a total of 240 negative biopsy cores and 29 positive biopsy cores. The positive cores were from 10 patients. Detailed information about the positive cases is provided in Kozłowski et al (23) and Table 1. In seven cases, the patients went on to radical prostatectomy as their treatment. In these cases, the Gleason scores reported from postsurgical analysis were used as the Gleason score of the tumor. The histology was interpreted with assignment of the Gleason score by several different experienced anatomic pathologists who practice general and subspecialty uropathology.

Prostatectomy Data

In 2010, we started a new study in which patients scheduled for radical prostatectomy consent to an MRI imaging session before the surgery. This is a different population than the biopsy cases described above. The patients recruited for this study have not received any therapy before radical prostatectomy. At the time of writing, four datasets were obtained, providing 40 cross-sections.

To acquire the whole-mount pathology analysis, the radical prostatectomy specimens were dissected and

Table 1
Clinical Data for 10 Patients With Biopsy Confirmed Cancer

Patient	Age [years]	PSA [ng/mL]	No. of positive biopsies (size in mm)	Biopsy Gleason score	Prostatectomy Gleason score	Clinical stage
P003	62	5.3	5 (8, 6, 2, 2, 1)	3+4	4+3	cT2a
P004	67	7.1	4 (7, 5, 1, 1)	3+4	3+4	cT2b
P005	60	5.4	2 (1.5, 1)	3+3	n/a	n/a
P007	58	7.1	5 (2, 3, 1, 2, 2)	4+5	3+4	cT1c
P010	55	7.09	2 (0.5, 4)	3+3	n/a	cT1c
P015	72	12	3 (10, 1.5, <1)	4+4, 4+5	4+5	cT1c
P016	65	5.43	2 (<1, <1)	4+3, 3+3	3+4	cT1c
P020	64	6.8	2 (1, 7)	3+4	3+4	cT2a
P024	60	5.4	1 (3)	4+4	4+3	cT1c
P026	62	6.4	1 (not recorded)	3+3	n/a	cT2a

histopathologically examined in a uniform manner. The external surfaces of the specimens were inked and the seminal vesicles amputated. The specimens were dissected following a minimum of 24-h fixation in 10% buffered formalin. The apical and bladder neck tissue was removed, using 5-mm-thick layers. We developed a device (24) to cut the prostate gland in serial transverse cuts perpendicular to the posterior capsule, at 4-mm intervals, from inferior to superior. This procedure allowed us to obtain reasonably good correspondence between the pathology slices and the MR image slices. The processing and paraffin embedding were carried out in a routine manner, except using oversized baskets and blocks to accommodate the intact prostate gland. Whole-mount sections were cut using a Lieka RM2245 whole body rotary microtome, and were submitted as intact transverse sections mounted on oversize glass slides for hematoxylin and eosin staining.

MR Imaging Protocol

For both the biopsy and the prostatectomy studies, the MRI protocol was as follows. All MRI examinations were performed on a 3 Tesla (T) MRI scanner (Achieva, Philips Healthcare, Best, The Netherlands). MRI signals were acquired with a combination of an endorectal coil (Medrad, Pittsburgh, PA) and a cardiac phased-array coil (Philips Healthcare, Best, The Netherlands). Fast spin-echo T2-weighted images (repetition time [TR] = 1851 ms, effective echo time [TE] = 80 ms, field of view [FOV] = 14 cm, slice thickness = 4 mm with no gap, 284×225 matrix, 3 averages) were acquired in the axial and coronal planes to provide anatomical details of the prostate. From this sequence, 12 axial slices covering the entire gland were then selected and used for the DTI and DCE MRI scans. DTI data were acquired using a diffusion weighted single shot echo planar imaging (EPI) sequence (TR/TE = 2100/74 ms, FOV = 24 cm, slice thickness = 4 mm with no gap, 128×115 matrix, 6 noncollinear gradient directions, b-value = 0 and 600 s/mm², 18 averages, total acquisition time of 8 min; the relatively low b-value of 600 s/mm² was chosen to ensure sufficient SNR for quantitative measurements of DTI parameters).

DCE MRI was performed using a three-dimensional T1-weighted spoiled gradient echo sequence (TR/TE =

3.4/1.06 ms, flip angle = 15°, FOV = 24 cm, 256×163 matrix, 2 averages). Initially, proton density (PD) images (TR/TE = 50/0.95 ms, flip angle = 4°) were acquired to allow calculation of the contrast agent concentrations in the prostate. Next, a series of 75 T1-weighted dynamics were acquired before (3 images) and after (72 images) a bolus injection of Gd-DTPA (Magnevist, Berlex Canada, 0.1 mmol/kg injected with a motorized power injector within 10 s at the rate of 2 mL/s, followed by a 20-mL flush of saline. This resulted in a time resolution of 10.6 s per 12 slices. Currently, our scanner allows higher temporal resolution; however, we kept the same protocol over the duration of the study for consistency. T1 values were calculated based on PD-weighted and T1-weighted images according to the procedure described in Parker et al (25).

The total time of the MRI examination was approximately 45 min. The DTI data were processed off-line to calculate FA and average diffusivity ($\langle D \rangle$) values. Diffusion weighted images were registered to the nonweighted b = 0 image with a mutual information algorithm before calculating the eigenvalues of the diffusion tensor and generating maps of the average diffusivity $\langle D \rangle$ (i.e., trace of the diffusion tensor) and fractional anisotropy (FA) with the proprietary DTI processing toolbox PRIDE (Philips Healthcare, Best, The Netherlands).

DCE MRI data were processed off-line with software procedures developed in house using Matlab (Mathworks, Natick, MA) and Igor Pro (WaveMetrics, Portland, OR). Arterial Input Functions (AIFs) were extracted from voxels in the external iliac or femoral arteries in the central slice for each patient (26). Pharmacokinetic parameters: volume transfer constant, K^{trans} , fractional volume of the extra-vascular extra-cellular space, v_e , and fractional plasma volume, v_p , were calculated by fitting the contrast agent concentration versus time curves to the extended Kety model. Fitting was carried out in every pixel of every slice within a region of interest (ROI) encompassing the prostate gland to generate maps of the pharmacokinetic parameter as described by Tofts et al (27).

T2-weighted images were used to identify the prostate gland, the peripheral zone, and other anatomical details that helped with matching MRI with histology. DCE MRI and DTI images were acquired with the slice

thickness of 4 mm, location, and the same resolution; no interpolation was required. The vast majority of the glands were smaller than 48 mm and typically 8 – 10 slices were enough to cover the entire gland. We did not have any cases where the tumor was missed because of the insufficient MRI coverage.

Matching ROIs from MRI to Biopsy Cores

In the biopsy data, one ROI represented by one set of DCE and DTI parameters was defined for each biopsy core. To relate the DTI and DCE MRI parameters with biopsy results, we used the consensus in the literature on the values of $\langle D \rangle$ and K^{trans} in prostate tumors. It is widely reported that $\langle D \rangle$ is lower and K^{trans} is higher in the tumor than in normal PZ (19,28).

The following correspondences between MRI slice locations and gland anatomy was assumed: slices 5–8 corresponded to midgland area, slices 1–4 (2 or 3–4 for smaller glands) corresponded to the apex, and slices 9–12 (9–10 or 11 for smaller glands) corresponded to the base. The tumor identification in the MRI data was based on a threshold value determined separately for the DTI and DCE MRI data. To determine the threshold, first the areas with low intensity on the $\langle D \rangle$ maps were manually segmented, based on visual inspection, in the areas corresponding to the positive biopsy locations. For example, left lateral midgland positive biopsy corresponded to any low $\langle D \rangle$ value areas, not smaller than 3×3 contiguous pixels (approximately 3 mm \times 3 mm), in the left lateral peripheral zone within slices 5–8. The intensity threshold for the DTI data was defined as the average of all ROIs corresponding to positive biopsies plus one standard deviation. The addition of one standard deviation was applied to minimize the bias caused by manual segmentation. Similarly the intensity threshold for the DCE MRI data was determined as the average of the all high intensity areas on the K^{trans} maps corresponding to the positive biopsies, minus one standard deviation. Once the threshold values for the DTI and DCE MRI data were established across the dataset, the MRI data were analyzed again, and all the areas below the intensity threshold on the $\langle D \rangle$ maps and above the intensity threshold on the K^{trans} maps, corresponding to biopsy locations, were considered cancer. In the areas where no low $\langle D \rangle$ or high K^{trans} values were present, and also for negative cores, the average parameter values from the entire area corresponding to the biopsy location (e.g., average of the left lateral PZ in slices 5–8 corresponded to the left lateral midgland biopsy location) were calculated and used as the feature vector representing the biopsy core.

It should be noted that the ROIs from DCE and DTI were selected separately. This was to ensure that the selection criteria from one modality did not affect the selection in the other modality. Furthermore, the two datasets were not geometrically registered. Therefore, matching was neither possible nor helpful. Because we classify an area generally corresponding to a

biopsy, perfect geometric matching of the two image types is unnecessary.

Reference Standard in the Prostatectomy Data

The histology slides were examined and the regions of the prostatic carcinoma were outlined with assignment of the Gleason score by an anatomic pathologist with over 20 years of experience who practices general and subspecialty uropathology. The cancer probability maps acquired using the SVM-based measure of cancer probability (see the next section) were validated based on these histopathology results. Our cutting method and device ensured the matching of two-dimensional MRI slices with pathology slides. However, the MRI slices and pathology slides were not deformed to be registered to each other.

Classification

The MRI data processing resulted in three DCE parameter maps (K^{trans} , v_e , and v_p) and two DTI parameter maps ($\langle D \rangle$ and FA) per imaging plane. Each parameter map was of size 256×256 covering the field of view. In the biopsy data, each ROI constructed based on a biopsy core was represented by the five-dimensional feature vector $x = [K^{trans}, v_e, v_p, \langle D \rangle, FA]$ consisting of values of the DCE and DTI parameters averaged over the ROI. To generate the colormaps, every pixel of the DTI-DCE image was represented and classified as a feature vector.

Support Vector Machines

In its most common form, the SVM classification approach depends on using a kernel function to map the input data to a higher dimension space where a hyperplane can be used to separate the data into different classes. The process of training an SVM classifier is equivalent to finding the optimal hyperplane that minimizes a classification error measure on the training dataset and maximizes the perpendicular distance between the decision boundary and the closest data points in the classes, a quality that makes SVM a maximum margin classifier. These closest data points that define the decision boundary are called “support vectors”. In a two-class case, if the training dataset consists of N feature vectors $\{x_1, \dots, x_N\}$ with class labels $y_i \in \{1, -1\}$, then the SVM training problem is equivalent to finding w and b such that:

$$\frac{1}{2} w^T w + c \sum_{i=1}^{i=N} \varepsilon_i \quad [1]$$

is minimized subject to

$$y_i(w^T \phi(x_i) + b) \geq 1 - \varepsilon_i \quad [2]$$

where b and w (the normal vector) define the hyperplane, $\varepsilon_i \geq 0$ are the so-called slack variables that allow for misclassification of noisy and difficult data points, and $c > 0$ controls the trade-off between the slack variable penalty and the error margin, and $\phi(\cdot)$ is the mapping function to a higher dimension. As

shown in Cortes and Vapnik (29), w can be written as a linear combination of the transformed support vectors. In other words, $w = \sum \alpha_j \phi(x_j)$, where x_j 's are the support vectors. This observation means that the decision hyperplane and the optimization Eq. [2] only contain the mapping function in its dot product format. Therefore, one does not need an explicit expression for $\phi(\cdot)$ and the SVM optimization and decision hyperplane are defined fully given the kernel function of form $K(x_i, x_j) = \phi(x_i)^T \phi(x_j)$. The most common choice for the kernel function, also used in our work, is a Radial Basis Function (RBF) kernel defined as:

$$K(x_i, x_j) = e^{-\gamma \|x_i - x_j\|^2} \quad [3]$$

The use of this kernel is equivalent to mapping the data into an infinite dimensional Hilbert space (29). The RBF kernel has only one parameter ($\gamma > 0$) that can be adjusted. This means that the process of tuning the SVM classifier to a specific problem is limited to finding the appropriate values for just two parameters: c and γ . Once $\varepsilon_i \geq 0$ are given, for a given choice of c and γ , w , and b that solve Eqs. [1] and [2] are obtained by solving a quadratic program (QP). The details of the solution can be found in Fan et al (30) and in the publicly available C++ implementation of the SVM algorithms known as LIBSVM (<http://www.csie.ntu.edu.tw/~cjlin/libsvm>), which is the library that we have used.

SVM-based A Posteriori Class Probabilities

SVM is merely a decision machine:

If $f(x_n) = w^T \phi(x_n) + b > 0$, then the class label for x_n is $y_n = 1$. In other words, SVM does not provide a posteriori class probability. To generate the cancer distribution probability maps and also the receiver operating characteristic (ROC) curves, one needs a posteriori probability of cancer of the form:

$$P_c(x_n) = p(y_n = 1 | f(x_n) = w^T \phi(x_n) + b) \quad [4]$$

where $P_c(x_n)$ stands for probability of x_n being cancerous. To extend SVM for probability estimates, after the training step, we train the parameters of an additional sigmoid function of the form:

$$P_c(x_n) = p(y_n = 1 | f(x_n)) = \frac{1}{1 + \exp(Af(x_n) + B)} \quad [5]$$

to map the values of $f(x_n)$ to a posteriori probabilities. The values of parameters A and B are fitted using maximum likelihood estimation from the training set for which the actual labels are known (31,32). We used class probabilities generated with this method for creating the probabilistic cancer maps.

Cross Validation and Tuning the Classifier

To tune the classifier, with appropriate values of c and γ , we exhaustively searched the parameter space $1 \leq c \leq 100$, $1 \leq \gamma \leq 100$ with steps of 0.1. For each set of parameters, we trained the SVM using data from 28 biopsy patients and tested it on the data from

the 29th patient, and repeated the process for all 29 datasets. This exhaustive search could be completed in less than 10 min on a typical personal computer. Note that this process was only completed once to set the parameters of the classifier. The classifier parameter set resulting in the best classification performance, as measured by the average area under the ROC curve for the 29 tests, was chosen.

The biopsy dataset was unbalanced, with more normal biopsy cores than cancerous cores (240 versus 29). This could cause a bias toward the normal class during the optimization step of the SVM. To reduce the bias, we repeated the entire leave-one-patient-out training-testing cross validation 100 times, each time with a random subset consisting of half of the normal biopsies, and averaged the results to report the ROC curve. One-way analysis of variance (ANOVA) was used with the outcome of the 100 trials to compare the performance of DCE features alone, DTI features alone, and DCE-DTI combined.

ROCs and Colormaps

To generate the ROC curves, a posteriori cancer probability (P_c) was used to determine a decision boundary which we call t . A biopsy core was classified as cancerous if $P_c > t$. The value of t was incrementally increased from 0 to 1, with each t value yielding one point on the ROC curve (sensitivity versus 1-specificity). To create the colormaps used to validate the methods by comparison with the histopathologic analysis of whole-mount slides from prostatectomy cases, each pixel in the entire surface of the prostate gland in DCE-DTI images was classified using the SVM tuned and trained on the biopsy data. The P_c values were plotted in standard Jet colormap, with hot colors representing high cancer probabilities.

RESULTS

The results reported here are acquired using the SVM classifier with parameter values set at $c = 0.6$ and $\gamma = 4$, determined by the exhaustive search to improve the area under the ROC curve.

ROC Curves and Correlation With Gleason Score on Biopsy Data

To study the role of DCE and DTI separately, we report three sets of ROC curves acquired using only the DCE features, $[K^{trans}, v_e, v_p]$, only the DTI features $[\langle D \rangle, FA]$, and the combined feature vector, $[K^{trans}, v_e, v_p, \langle D \rangle, FA]$. The summary statistics for the five parameters in the biopsy dataset is presented in Table 2, separately for biopsy normal and cancerous regions of interest.

The area under ROC curve (AUC) was 0.867, 0.919, and 0.956 for DCE, DTI, and the combined DCE-DTI features (Fig. 1). The combined feature vector resulted in higher AUC than DCE ($P = 0.002$) and DTI ($P = 0.01$). With the combined feature vector, at the decision threshold of $P_c = 0.5$, three of the 29 tumors were misclassified while a specificity of 91% was obtained

Table 2
Summary Statistics in Format of Mean (Standard Deviation) for the Five Parameters Used in the Analysis*

	$\langle D \rangle$ ($1000^{-3}\text{mm}^2/\text{s}$)	FA	K_{trans} (min^{-1})	v_e	v_p
Normal	1.662 (0.317)	0.207 (0.067)	0.070 (0.047)	0.227 (0.115)	0.017 (0.011)
Cancer	1.120 (0.174)	0.198 (0.051)	0.148 (0.071)	0.202 (0.049)	0.007 (0.007)

*Values are reported for the normal and cancer biopsies.

(221 of 243 normal biopsy samples were correctly classified). When $P_c = 0.3$ was set as the threshold for cancer detection, only one tumor was misclassified, while the specificity of 87% was maintained (211 of 243 normal biopsy samples were correctly classified).

We also noted a positive correlation between the P_c value and the Gleason score of the tumors. The average P_c value was 0.555 for tumors of grade 3 + 3 (number of tumors=7), 0.778 for tumors of grade 3 + 4 and 4 + 3 ($n = 19$), and 0.963 for grade 4 + 5 ($n = 3$). The increase in P_c values was significant from Grade 6 to 7 ($P = 0.01$). The small number of tumors in grade 4 + 5 did not warrant an analysis of statistical significance. None of the 4 + 5 tumors were misclassified in any of the experiments.

The T2-weighted image and the cancer probability map obtained for the mid slice MRI data of a patient with positive biopsy cores in the mid-left-lateral and mid-left-medial regions of the prostate are illustrated in Figure 2. This was acquired by treating every pixel of the DCE-DTI image as a feature vector and computing P_c . The tumor was of grade 4 + 5. For this case, the $\langle D \rangle$ and K_{trans} maps are also strong indicators of the existence of cancer. These maps are presented in Figure 3.

Cancer Colormaps Revealing Significant Pathologic Conditions

The trained classifier was used on the second data set from patients who underwent radical prostatectomy followed by whole-mount pathology analysis. In three of these four patients we found a “dominant tumor.” This is in agreement with previous studies that point out the existence of a single dominant tumor with several much smaller foci also present in many prostatectomy specimens (33). In a study involving 100 prostatectomy patients, it was shown that the Gleason

score of the dominant tumor was identical to the primary Gleason score of the prostatectomy specimens in 97% of patients (34). Therefore, we believe a system designed to efficiently screen patients for possible focal therapy, can be assessed based on its ability to demonstrate the dominant tumor. Figure 4 shows the outcomes for case 1. For one of the prostate sections in this case, the parametric maps (K_{trans} and $\langle D \rangle$) are presented in Figure 5. For case 2 and 3, samples of the probabilistic maps, along with pathology finding and T2-weighted image are presented in Figures 6 and 7. As these Figures illustrate, in the cases with dominant tumors, the cancer colormaps created by pixel-wise computation of the P_c values demonstrate a visible tumor in the area validated by the histopathologic analysis. Note that the DTI and DCE data from these patients were not used in training the SVM classifier.

Table 3 reports the surface area and the Gleason score of the tumors determined by the pathologist and compares them with the surface area of the tumor and P_c determined from the colormaps. To calculate the surface area, pixels with $P_c > 0.5$ were considered part of the tumor. For each case, the data are presented for two consecutive cross-sections (pathology levels) that best depict the dominant tumor. In cases with Gleason score $> 3 + 3$, the area of the tumor is very close in the pathology slide to the area depicted by the SVM-based cancer colormap resulting in an average difference of 2.8%. In case of the 3 + 3 tumor, level 4 in case 2, the area of the tumor as depicted in the probability map is 40% smaller than the pathology finding. As expected, the colormaps more accurately depict the tumor in the cases of tumor grades 3 + 4 and 4 + 5 than in tumor grade 3 + 3. In one case (level 10, case 3), a 4 + 5 tumor was identified. The average P_c in this case was 0.86, providing a distinct appearance to the tumor. Note that if one considers the effect of shrinking due to specimen fixation, the depicted tumor area in the colormaps is smaller than the expected size of the tumor even in case of 3 + 4 and 4 + 5 tumors.

In one case, case 4, no dominant tumor could be identified. Cancer was bilateral involving all areas of the gland, occupying 25% of the overall volume of the prostate and up to 60% of the surface of certain cross-sections. The highest grade reported by the pathologist was 3 + 3. The colormap showed many hot spots. However, no dominant tumor was identified. In the middle plane of this 3 + 3 case, the cancer area depicted on the probability map, with threshold of $P_c > 0.5$, was 36% smaller than the area depicted by the pathologist.

DCE imaging is not always possible because contrast agents are contra-indicated in some cases. It

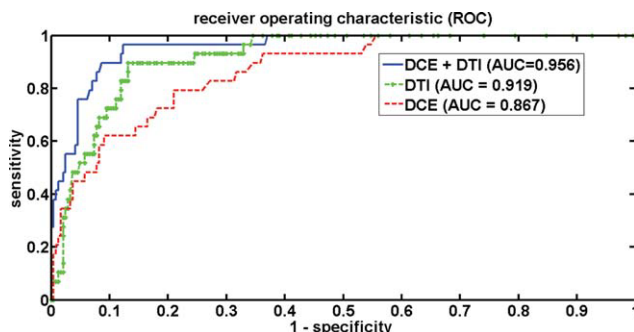


Figure 1. ROC curves for the biopsy data, for different groups of features acquired by changing the decision threshold, P_c , from 0 to 1. [Color figure can be viewed in the online issue, which is available at wileyonlinelibrary.com.]

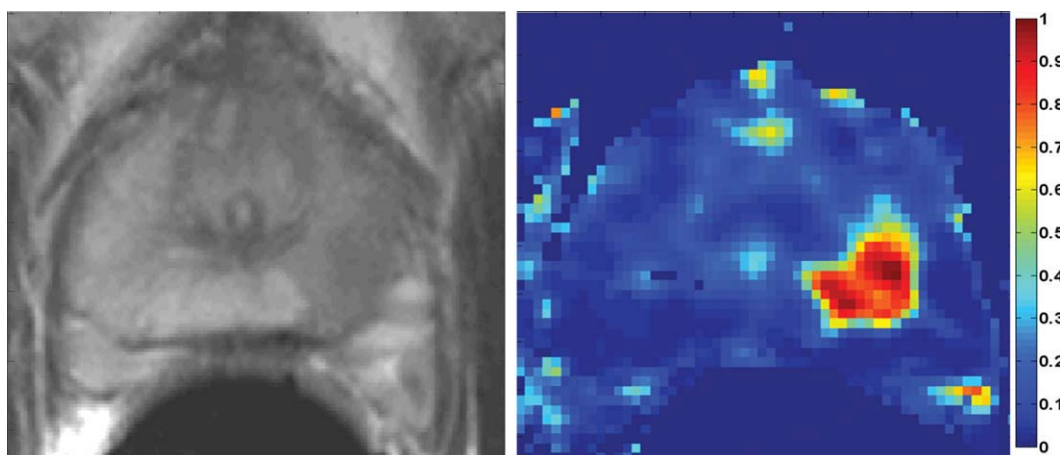


Figure 2. Left: T2-weighted MRI of the mid-gland of a patient with biopsy confirmed cancer in mid-left region. Right: The SVM-based cancer probability map, with hot colors showing higher P_c . The Gleason score: 4 + 5, the average P_c in the tumor area: 0.9. [Color figure can be viewed in the online issue, which is available at wileyonlinelibrary.com.]

was noted that DTI alone can also provide an efficient modality within our framework: for the three cases with a dominant tumor, using only DTI features we acquired maps showing an area difference with the combined DTI-DCE of approximately 6.1% in the dominant tumor.

DISCUSSION

We found that the combination of DTI and DCE provides an area under ROC curve of 0.96 and is more efficient in cancer detection than each method individually. DTI alone provides an area under ROC curve of 0.92 in the biopsy data. Using an extension of the standard SVM classification approach, we were able to compute a posteriori class probabilities that quantify the probability of cancer for each set of DCE-DTI parameters, based on the available training data. The average P_c value was 0.555 for tumors of grade 3 + 3, 0.778 for tumors of grade 3 + 4 and 4 + 3, and 0.963 for grade 4 + 5.

One distinction of our work compared with the previously published (21,23) work on multiparametric

MRI for cancer detection is our ability to combine DTI and DCE features and provide one reliable measure of cancer probability (P_c) that can be used for ROC curves and cancer probability maps. We also validate our cancer probability measure based on the reference standard of whole-mount pathology on a second group of patients.

In the past, we have reported the performance of the five parameters in detection of prostate cancer individually, and the use of a statistical approach, namely logistic regression, for combining the DTI and DCE parameters for cancer detection (23). The use of SVM in the current work provides two main advantages. The first one is the fact that SVM is a maximum margin classifier and provides the ability to generalize the trained classifier. The second one is the ability of the proposed framework to provide a value for the probability of cancer.

In analyzing the presented colormaps, one should note that the training of the SVMs used to compute these probability values was entirely based on the data from our biopsy datasets. This means that the outcomes are most reliable on the peripheral zone of the gland, which is usually the target of the

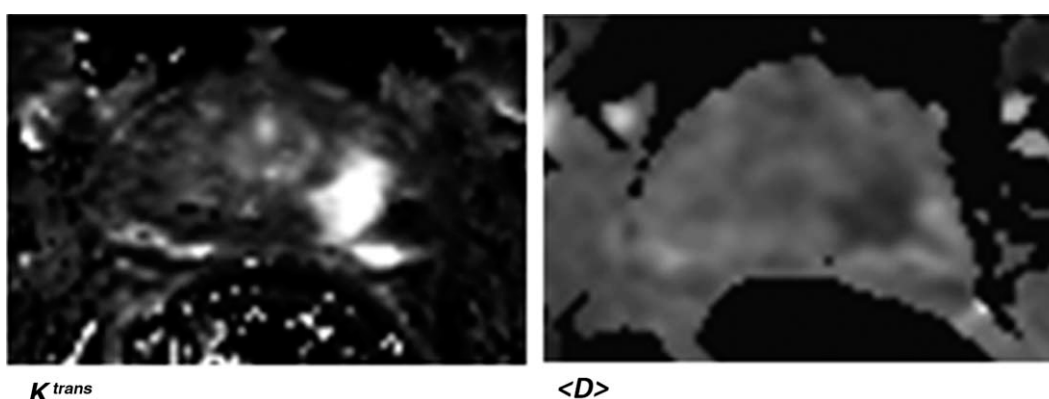


Figure 3. The $\langle D \rangle$ and K^{trans} maps for the patient presented in Figure 2.

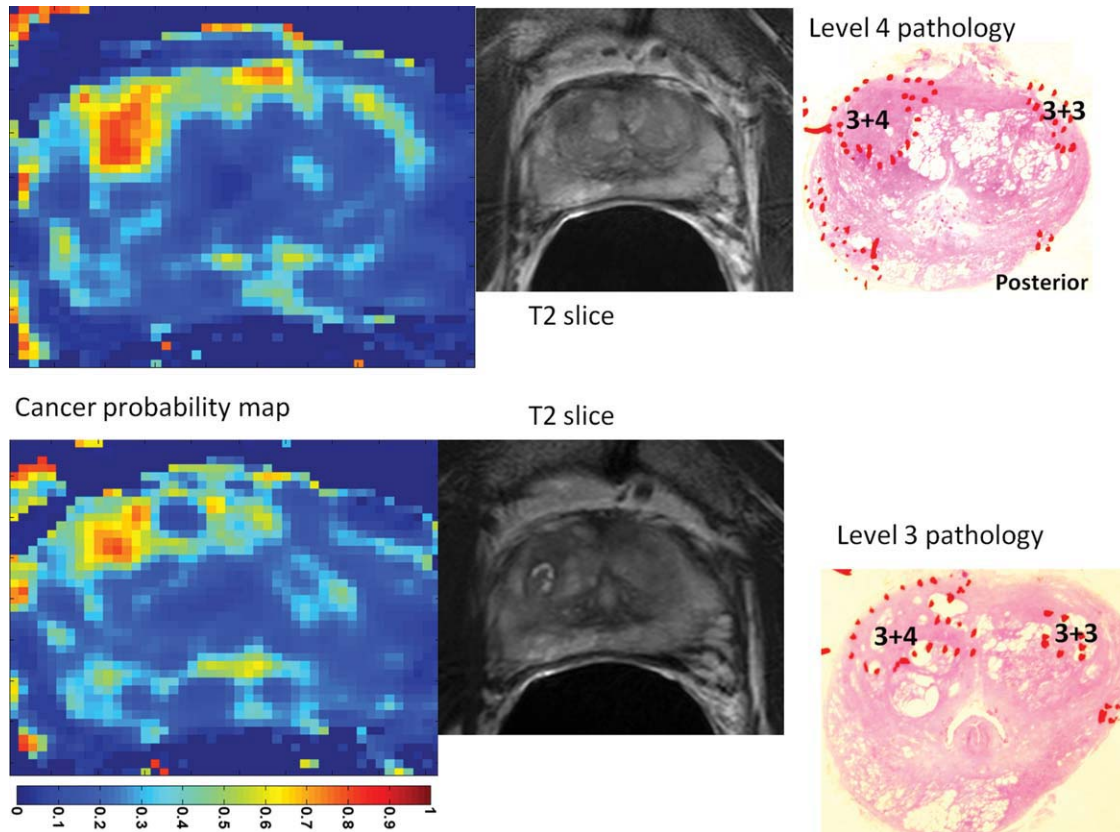


Figure 4. Cancer colormaps and MRI images with corresponding histopathology slide for case 1. The main pathologic finding is a 3+4 tumor in the transition zone, visible in two consecutive cross-sections. [Color figure can be viewed in the online issue, which is available at wileyonlinelibrary.com.]

biopsy studies. Nevertheless, as visible in Figure 4, we have also been successful in detection of the dominant tumor in the transition zone. Additional data from the transition zone are required as we have also encountered false positive findings in this zone (Fig. 6).

At this stage of our work, we decided not to use the data from prostatectomy patients for the training step of the SVM classification. This was due to several reasons, including the currently limited number of patients enrolled in the prostatectomy study, and the difficulty of accurately registering the pathology slides to MRI images to establish the reference standard for training. Also, our analysis does not target accurate

delineation of the individual tumor contours at this stage. This is partly due to the fact that specimen deformation during fixation limits our ability for establishing a reference standard for the exact geometry of the tumor.

As described earlier, we used a special cutting device that allowed us to slice the prostate in correspondence with the position of the MRI slices. Furthermore, we ensured the matching of the slices, visually, based on the anatomical details clearly visible in T2-weighted images and histology sections. We acknowledge that deformations caused by the fixation process and the potential slight shift of the slices in the axial direction exist and result in errors in the

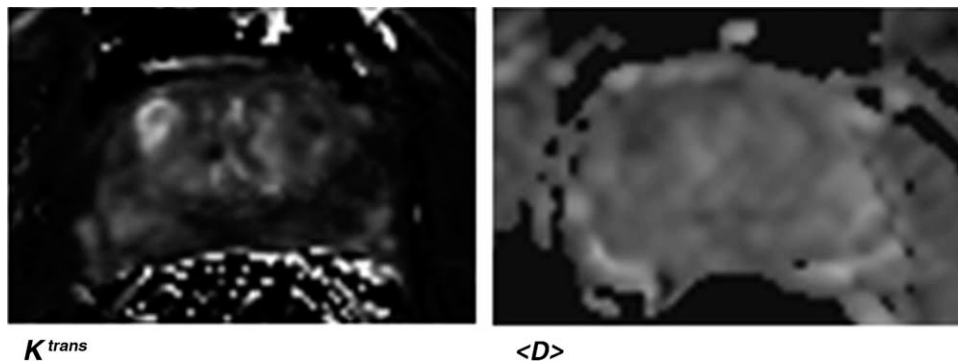


Figure 5. The $\langle D \rangle$ and K^{trans} maps corresponding to the case presented in Figure 4, row 1.

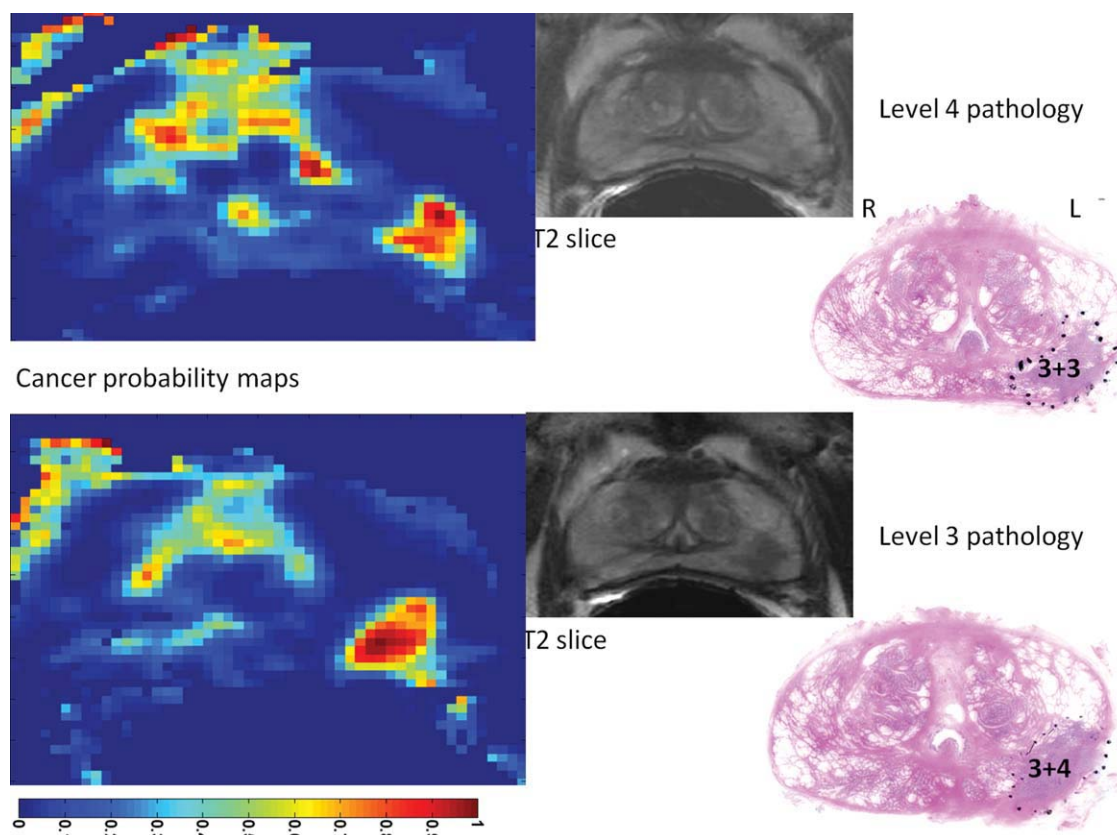


Figure 6. Cancer colormaps and MRI images with corresponding histopathology slide for case 2. The main pathologic finding is a tumor that is of Gleason score 3 + 4 in one cross-section and 3 + 3 in the neighbor cross-section. The hot-spot in the transition zone of the prostate is a false positive detection. This is most likely due to the fact that our SVM is trained only on data from peripheral zone. [Color figure can be viewed in the online issue, which is available at wileyonlinelibrary.com.]

process of matching the MRI and histology reference. Investigators have reported attempts directed toward developing deformable registration of the histology and MRI images (35–38). However, the validation of the registration process requires maintaining visible markers throughout the imaging, surgery and laboratory work. This has led to the lack of a clinically viable method for quantitative registration of MR slices with histology. Due to this limitation, we have not used the data from prostatectomy patients in the training stage. Instead, we used these data as a second validation dataset. We looked for the existence of dominant tumors in the areas of the slides corresponding to areas of the cancer maps with high probability of cancer. We report the surface area and the average probability of cancer from the maps and study their correlation with the surface area and Gleason score of the tumor determined by the pathologist. In the absence of a method for quantitatively validated deformable registration of slices from MRI and histopathology, we have used these measures for qualitative validation. In our current setup, when most areas of the gland are invaded by carcinoma (such as case 4 in our prostatectomy study), the interpretation and validation of the colormaps is difficult due to the lack of quantitative registration. These cases, however, are unlikely to be missed during conventional biopsy. Furthermore, they are not candidates for focal therapy.

Similar to any other machine learning method, our algorithm can be improved by presenting more data in the training stage. We require more data to represent all levels of cancer progression, including very high grade and very low grade cases, and also all areas of the gland including the central zone. As we continue our study, such data will be incorporated into the system. We will also consider the detection of benign pathologies such as benign prostatic hyperplasia when such cases are represented in our data for training purposes.

We found that tumor classification is increasingly more accurate for higher Gleason scores (with 2–3% area difference in 3 + 4 and 4 + 5 tumors versus 30–40% difference in 3 + 3 tumors). The sensitivity of our approach to the pathologically significant cases, accuracy in determining the dominant tumors with high Gleason score, and the correlation of the computed cancer probabilities with the Gleason score, are helpful features for treatment planning. This provides additional value to the routine radiological analysis of the images, even in cases where the tumor is visible on the T2-weighted image.

As it is evident from Figures 3 and 5, $\langle D \rangle$ and K^{trans} provide tumor contrast in many cases. Nevertheless, clinical challenges remain in dealing with false positive detections, and more importantly, separating indolent from aggressive tumors. This type of prognostic information is currently available only through

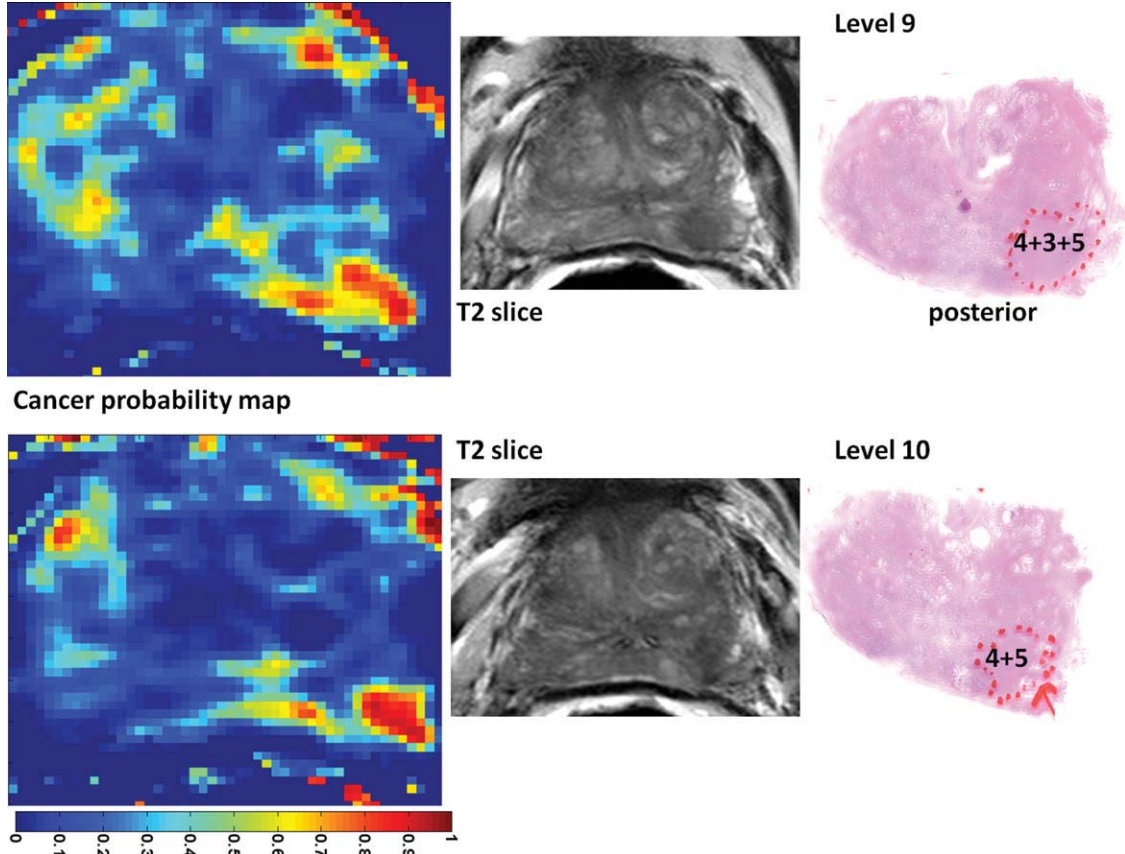


Figure 7. Cancer colormaps and MRI images with corresponding histopathology slide for case 3. The main pathologic finding is a tumor that is of Gleason score 4 + 3 (with considerable tertiary Gleason score of 5) in one cross-section and 4 + 5 in the neighboring cross-section.

pathology, which can be misleading due to under-sampling of the clinically significant diseased areas during biopsy. Our computational framework is a step toward developing the ability to quantitatively characterize prostate tumors noninvasively. The clinical impact of such system, if achieved, will be significant. We propose an objective, quantitative method to radiologically characterize prostate cancer and replace the standard practice of visual evaluation by a radiologist.

We recognize several limitations in the current stage of the study. One limitation is the current lack of a

quantitative registration mechanism between MRI and pathology. This has limited our quantitative analysis on the whole-mount data to cases with a dominant tumor. As described earlier, tackling this issue is among our immediate research goals. The potential geometric distortion of diffusion images is another shortcoming. This limits our ability to pinpoint the exact location of a tumor. At the current stage, we have not detected significant distortion away from the rectum in the DTI images from the prostatectomy cases for which we have whole-mount pathology. We will work toward a reliable technique to register DTI data to other MRI images as we progress. Finally, our current validation with whole-mount pathology is limited to a small dataset and we need to expand this study to a sufficiently large group of patients who represent different stages of the disease.

In conclusion, a combination of DCE and DTI MRI features, when used along with a SVM-based machine learning approach, can provide helpful cancer probability maps for detection and grading of prostate cancer. The performance of the method is reported on a biopsy dataset of 29 patients, and validated for three additional cases by comparison of the generated probability maps with whole-mount pathology in terms of the accuracy in depiction of the dominant prostate tumors.

Table 3
Area and Gleason Score of the Tumors in Six Cross-Sections From the Prostatectomy Cases Where a Dominant Tumor Was Present*

Patient	Tumor area (pathology)	Gleason Score	Tumor area (map)	P_c
Case 1, level 4	108 mm ²	3+4	106 mm ²	0.72
Case 1, level 3	94 mm ²	3+4	92 mm ²	0.70
Case 2, level 4	120 mm ²	3+3	70 mm ²	0.68
Case 2, level 3	93 mm ²	3+4	88 mm ²	0.75
Case 3, level 9	86 mm ²	4+3	83 mm ²	0.82
Case 3, level 10	72 mm ²	4+5	71 mm ²	0.86

*For each tumor, the area of tumor in the colormaps and also the average P_c are given.

REFERENCES

1. Jemal A, Bray F, Center MM, Ferlay J, Ward E, Forman D. Global cancer statistics. *CA Cancer J Clin* 2011;61:69–90.
2. Steyerberg EW, Roobol MJ, Kattan MW, van der Kwast TH, de Koning HJ, Schröder FH. Prediction of indolent prostate cancer: validation and updating of a prognostic nomogram. *J Urol* 2007;177:107–112.
3. Jayram G, Decastro GJ, Large MC, et al. Robotic radical prostatectomy in patients with high-risk disease: a review of short-term outcomes from a high-volume center. *J Endourol* 2011;25:455–457.
4. Shikanov SA, Zorn KC, Zagaja GP, Shalhav AL. Trifecta outcomes after robotic-assisted laparoscopic prostatectomy. *Urology* 2009;74:619–623.
5. Odowd GJ, Miller MC, Orozco R, Veltri RW. Analysis of repeat biopsy results within 1 year after a noncancer diagnosis. *Urology* 2000;55:533–559.
6. Bloch BN, Rofsky NM, Baroni RH, Marquis RP, Pedrosa I, Lenkinski RE. 3 Tesla magnetic resonance imaging of the prostate with combined pelvic phased-array and endorectal coils: initial experience. *Acad Radiol* 2004;11:863–867.
7. Augustin H, Fritz GA, Ehammer T, Auprich M, Pummer K. Accuracy of 3-Tesla magnetic resonance imaging for the staging of prostate cancer in comparison to the Partin tables. *Acta Radiol* 2009;50:562–569.
8. Fütterer JJ, Heijmink SW, Scheenen TW, et al. Prostate cancer: local staging at 3-T endorectal MR imaging—early experience. *Radiology* 2006;238:184–191.
9. Lv D, Guo X, Wang X, Zhang J, Fang J. Computerized characterization of prostate cancer by fractal analysis in MR images. *J Magn Reson Imaging* 2009;30:161–168.
10. Kurhanewicz J, Vigneron DB, Hricak H, Narayan P, Carroll P, Nelson SJ. Three-dimensional H-1 MR spectroscopic imaging of the in situ human prostate with high (0.24–0.7-cm³) spatial resolution. *Radiology* 1996;198:795–805.
11. Zakian KL, Sircar K, Hricak H, et al. Correlation of proton MR spectroscopic imaging with Gleason score based on step-section pathologic analysis after radical prostatectomy. *Radiology* 2005;234:804–814.
12. Issa B. In vivo measurement of the apparent diffusion coefficient in normal and malignant prostatic tissues using echo-planar imaging. *J Magn Reson Imaging* 2002;16:196–200.
13. Oto A, Kayhan A, Jiang Y, et al. Prostate cancer: differentiation of central gland cancer from benign prostatic hyperplasia by using diffusion-weighted and dynamic contrast-enhanced MR imaging. *Radiology* 2010;257:715–723.
14. Gibbs P, Pickles MD, Turnbull LW. Diffusion imaging of the prostate at 3.0 Tesla. *Invest Radiol* 2006;41:185–188.
15. Manenti G, Cariani M, Mancino S, et al. Diffusion tensor magnetic resonance imaging of prostate cancer. *Invest Radiol* 2007;42:412–419.
16. Xu J, Humphrey PA, Kibel AS, et al. Magnetic resonance diffusion characteristics of histologically defined prostate cancer in humans. *Magn Reson Med* 2009;61:842–850.
17. Buckley DL, Roberts C, Parker GJM, Logue JP, Hutchinson CE. Prostate cancer: evaluation of vascular characteristics with dynamic contrast-enhanced T1-weighted MR imaging—initial experience. *Radiology* 2004;233:709–715.
18. Engelbrecht MR, Huisman HJ, Laheij RJF, et al. Discrimination of prostate cancer from normal peripheral zone and central gland tissue by using dynamic contrast-enhanced MR imaging. *Radiology* 2003;229:248–254.
19. Padhani AR, Gapinski CJ, Macvicar DA, et al. Dynamic contrast enhanced MRI of prostate cancer: correlation with morphology and tumour stage, histological grade and PSA. *Clin Radiol* 2000;55:99–109.
20. Hoeks CM, Barentsz JO, Hambroek T, et al. Prostate cancer: multiparametric MR imaging for detection, localization, and staging. *Radiology* 2011;261:46–66.
21. Chan I, Wells W, Mulkern RV, et al. Detection of prostate cancer by integration of line-scan diffusion, T2-mapping and T2-weighted magnetic resonance imaging: a multichannel statistical classifier. *Med Phys* 2003;30:2390–2398.
22. Ozer S, Langer DL, Liu X, et al. Supervised and unsupervised methods for prostate cancer segmentation with multispectral MRI. *Med Phys* 2010;37:1873–1883.
23. Kozłowski P, Chang SD, Meng R, et al. Combined prostate diffusion tensor imaging and dynamic contrast enhanced MRI at 3T—quantitative correlation with biopsy. *Magn Reson Imaging* 2010;28:621–628.
24. Drew B, Jones EC, Reinsberg SA, Yung AC, Goldenberg SL, Kozłowski P. Device for sectioning prostatectomy specimens to facilitate comparison between histology and in vivo MRI. *J Magn Reson Imaging* 2010;32:992–996.
25. Parker GJ, Suckling J, Tanner SF, et al. Probing tumor microvasculature by measurement, analysis and display of contrast agent uptake kinetics. *J Magn Reson Imaging* 1997;7:564–574.
26. Parker GJ, Roberts C, Macdonald A, et al. Experimentally-derived functional form for a population-averaged high-temporal-resolution arterial input function for dynamic contrast-enhanced MRI. *Magn Reson Med* 2006;56:993–1000.
27. Tofts PS, Brix G, Buckley DL, et al. Estimating kinetic parameters from dynamic contrast-enhanced T1-weighted MRI of a diffusible tracer: standardized quantities and symbols. *J Magn Reson Imaging* 1999;10:223–232.
28. Hosseinzadeh K, Schwarz SD. Endorectal diffusion-weighted imaging in prostate cancer to differentiate malignant and benign peripheral zone tissue. *J Magn Reson Imaging* 2004;20:654–661.
29. Cortes C, Vapnik V. Support-vector networks. *Mach Learn* 1995;20:273–297.
30. Fan RE, Chen PH, Lin CJ. Working set selection using the second order information for training SVM. *Mach Learn Res* 2005;6:1889–1918.
31. Platt JC. Probabilistic outputs for support vector machines and comparison to regularized likelihood methods. In: Smola AJ, Bartlett PJ, editors. *Advances in large margin classifier*, 1st edition. Cambridge, MA: MIT Press; 2000. p 61–74.
32. Wu TF, Lin CJ, Weng RC. Probability estimates for multi-class classification by pairwise coupling. *J Mach Learn Res* 2004;5:975–1005.
33. Jayram G, Eggen SE. Patient selection for focal therapy of localized prostate cancer. *Curr Opin Urol* 2009;19:268–273.
34. Arora R, Koch MO, Eble JN, Ulbright TM, Li L, Cheng L. Heterogeneity of Gleason grade in multifocal adenocarcinoma of the prostate. *Cancer* 2004;100:2362–2366.
35. Ward AD, Cruckley C, McKenzie C, et al. Registration of prostate magnetic resonance images to digital histopathology images. *Proc Prostate Cancer Imaging*. 2010;66–76.
36. Mazaheri Y, Bokacheva L, Kroon DJ, et al. Semi-automatic deformable registration of prostate MR images to pathological slices. *J Magn Reson Imaging* 2010;32:1149–1157.
37. Zhan Y, Ou Y, Feldman M, Tomaszewski J, Davatzikos C, Shen D. Registering histologic and MR images of prostate for image based cancer detection. *Acad Radiol* 2007;14:1367–1381.
38. Jacobs MA, Windham JP, Soltanian-Zadeh H, Peck DJ, Knight RA. Registration and warping of magnetic resonance images to histological sections. *Med Phys* 1999;26:1568–1578.

Use of Needle Track Detection to Quantify the Displacement of Stranded Seeds Following Prostate Brachytherapy

Julio R. Lobo, Mehdi Moradi, Nick Chng, Ehsan Dehghan, William J. Morris, Gabor Fichtinger, and Septimiu E. Salcudean*

Abstract—We aim to compute the movement of permanent stranded implant brachytherapy radioactive sources (seeds) in the prostate from the planned seed distribution to the intraoperative fluoroscopic distribution, and then to the postimplant computed tomography (CT) distribution. We present a novel approach to matching the seeds in these distributions to the plan by grouping the seeds into needle tracks. First, we identify the implantation axis using a sample consensus algorithm. Then, we use a network flow algorithm to group seeds into their needle tracks. Finally, we match the needles from the three stages using both their transverse plane location and the number of seeds per needle. We validated our approach on eight clinical prostate brachytherapy cases, having a total of 871 brachytherapy seeds distributed in 193 needles. For the intraoperative and postimplant data, 99.31% and 99.41% of the seeds were correctly assigned, respectively. For both the preplan to fluoroscopic and fluoroscopic to CT registrations, 100% of the needles were correctly matched. We show that there is an average intraoperative seed displacement of 4.94 ± 2.42 mm and a further 2.97 ± 1.81 mm of postimplant movement. This information reveals several directional trends and can be used for quality control, treatment planning, and intraoperative dosimetry that fuses ultrasound and fluoroscopy.

Index Terms—Computed-tomography (CT), minimum cost network flow, prostate brachytherapy, X-ray fluoroscopy.

I. INTRODUCTION

PROSTATE brachytherapy is an effective, minimally invasive treatment technique for men with prostate cancer [1]. It involves transperineal insertion of permanent radioactive sources, or seeds, into the prostate using needles. A satisfactory

implant quality requires the target volume to be sufficiently irradiated while sparing noncancerous tissue. Poor implant quality can arise due to errors in the seed positions caused by needle deflection and prostate movement during insertion, as well as subsequent seed displacement due to inflammation of the prostate after operation. The American Brachytherapy Society identifies the need to assess the impact that seed displacement has on the effectiveness of the implant and recommends routine postimplant dosimetric analysis for all patients [2].

Measurement of the displacement of seeds after implantation has been performed by several research groups. Many of the published papers on measuring seed displacements and movement use manual seed detection [3]–[7]. The introduction of automatic methods for plan reconstruction [8], [9] is likely to facilitate postimplant dosimetry.

Pinkawa *et al.* investigated postimplant seed migration by looking at the dose levels over a 30 day period [10], [11]. Manual localization and contouring, without specific seed identification between datasets, was required in this study. The individual seed displacements, rather than the overall dose change, was quantified in Usmani *et al.*, in which the seed positions relative to fiducial markers were compared in repeated postimplant computed-tomography (CT) images [12]. In Chng *et al.*, seeds segmented from CT data were automatically grouped into their respective needles using a minimum cost network flow algorithm [13] following a coarse registration performed by iterating through all trajectory angles of every seed. The cost function consisted of complex correspondence functions used to compute the positional error, trajectory angle error, and the strand spacing error. Once the needle tracks were detected, a nonlinear optimization algorithm called Graduated Assignment was then used to match the entire “graphs” created by the needle track networks [9]. Accurate dose changes could be computed based on the seed positions.

The above investigations made use of postoperative data, and could only find the seed migration due to the *combined effect* of 1) seed misplacement at the time of the implant, and 2) postimplant inflammation.

We have combined several techniques, including the use of an iterative best line detection algorithm and network flow algorithms, to formulate a novel method to accurately identify corresponding brachytherapy seeds in different datasets to perform a seed displacement analysis. Our method extends the grouping of seeds into needles approach by simplifying the cost function components so that it is effective over multiple data types. We compare seed locations obtained from intraoperative fluoro-

Manuscript received October 21, 2011; accepted November 21, 2011. Date of publication December 06, 2011; date of current version March 02, 2012. The work was supported by Natural Sciences and Engineering Research Council of Canada and the Canadian Institutes of Health Research. The work of G. Fichtinger was supported as a Cancer Care Ontario Research Chair. The work of M. Moradi was supported by the Congressionally Directed Medical Research Program under W81XWH-10-1-0201. The work of E. Dehghan was supported by the Ontario Ministry of Research and Innovation Postdoctoral Fellowship. Asterisk indicates corresponding author.

J. R. Lobo and M. Moradi are with the Department of Electrical and Computer Engineering, University of British Columbia, Vancouver, BC V6T 1Z4, Canada (e-mail: juliol@ece.ubc.ca; moradi@ece.ubc.ca).

N. Chng and W. J. Morris are with the Vancouver Cancer Center, Vancouver, V5Z 4E6 BC Canada (e-mail: nchng@bccancer.bc.ca; jmorris@bccancer.bc.ca).

E. Dehghan and G. Fichtinger are with the School of Computing, Queen's University, Kingston, ON K7L 3N6, Canada (e-mail: ehsand@cs.queensu.ca; gabor@cs.queensu.ca).

*S. E. Salcudean is with the Department of Electrical and Computer Engineering, University of British Columbia, Vancouver, BC V6T 1Z4, Canada (e-mail: tims@ece.ubc.ca).

Color versions of one or more of the figures in this paper are available online at <http://ieeexplore.ieee.org>.

Digital Object Identifier 10.1109/TMI.2011.2178254

based images both to preplan data and to postimplant CT data. The two comparisons are done separately which allows us to investigate and distinguish between seed misplacement during surgery and postimplant movement. Our postimplant analysis uses CT images taken immediately after surgery so this study does not look at long term seed migration, although the same techniques described here can be used for CT data taken at later times to do so. The comparison with intraoperative seed positions, however, does allow an investigation of the effect of change in patient pose which changes from dorsal lithotomy during the implant procedure to horizontal recumbent during CT imaging. This has also not been analyzed using individual seed displacements before. Furthermore, we propose that given findings from Moradi *et al.* who show that given a complete reconstruction of the fluoroscopic data and identification of the seeds, registration can be performed with an incomplete reconstruction of the seed cloud in ultrasound data [13], we can use our methods to register the seed displacements within the prostate volume.

We have developed a new technique for registration, which is a required step for accurate computation of seed displacement. We stress that a full deformable registration by matching individual seeds is not desired as this can remove the trends in displacement that are to be measured. Therefore, instead of using individual seed positions, our method uses two global average parameters to register the different datasets. These parameters are the average implantation axis and the seed cluster centroid position. Aligning datasets to the same average parameters keeps local trend information, while bringing the datasets into the same coordinate system so that the measured values are actual distances. For the implantation axis detection we use an iterative sampling algorithm to obtain a ranked list of potential needle tracks in images. The average of the highest ranking few needle tracks is used to determine the implant axis direction. This can be done on each dataset independently removing the need for an exhaustive iterative closest point registration [14] comparing two datasets at a time.

A new method of matching detected needles between datasets is also presented. Another network flow algorithm is used where the needles are matched using only the location of the needle intersections with the transverse plane of implantation, and the number of seeds in each given needle. The same needle intersections can be used to register ultrasound data to fluoroscopic data leading to intraoperative dosimetry.

Our registration technique ignores any offset rotations about the insertion axis itself. However, we have developed a technique to automatically detect these offset rotations by finding the rotation that gives the minimum average seed displacement. The seed displacements must be recomputed for every new rotation until a minimum is found, but the insertion axis remains the same and the seeds are already matched between datasets and so the time complexity is increased only by a constant factor.

Since our institution only uses stranded implants for brachytherapy, this study focuses on measuring seed displacements during and after *stranded* seed implantation. Although it is possible to apply our methods to loose seeds, since they are usually inserted in needle tracks with regular spacers, studies have shown that stranded seeds provide better dose

coverage [15] and less seed loss [16] without compromising the biochemical no evidence of disease (bNED) [17]. As a consequence, stranded seeds are used in about 50% of cases in the United States and in over 80% of cases around the world. Therefore methods tuned to work on stranded implants alone do impact a large proportion of the brachytherapy field.

In this paper, we will refer to the difference between preplan seed locations to intraoperative seed location as “misplacement,” and the difference between intraoperative to postimplant seed locations as “movement.” The term “displacement” will be used to describe both differences. Although the term “misplacement” might imply that this method can distinguish between tissue deformation and physical implant misplacement this is not the case since we do not have any information about the tissue. The misplacement is purely the difference in locations of the seeds from the preplan data to the intraoperative data.

Preliminary results of this work are presented in Lobo *et al.* [18]. This paper contains a significantly expanded analysis and algorithmic details. Furthermore, the matching and registration details are updated and improved. The paper first describes the imaging used and the subsequent seed localization. The methods required to match seeds in different datasets and to compute the seed displacements are then described. Next, the results showing average displacements and trends are presented. Finally, an analysis of the results is given in the conclusion.

II. DATA COLLECTION AND DISCRETE TOMOGRAPHY APPROACH

Datasets from eight patients undergoing low-dose prostate brachytherapy were collected at the British Columbia Cancer Agency, Vancouver, Canada, after Institutional Research Ethics Board approval and patient consent were acquired. For each of the patients, the treatment plan was generated using the Variseed planning software (Varian Medical, Palo Alto, CA), and the planned seed positions, referred to as the preoperative plan or *preplan* were exported from it. The preplan data is obtained from the planned brachytherapy template needle position and depth, and was modified to account for changes made by the radiation oncologists during the procedure.

The postimplant CT was acquired approximately 1 h after the intervention. The coordinates of the postimplant CT, referred to as the *postimplant*, were also exported from the VariSeed planning software, as described in Chng *et al.* [9].

Intraoperative seed positions were reconstructed from fluoroscopic data acquired immediately after implanting all the required seeds. A series of five fluoroscopic images were taken, rotating the C-arm from approximately -10° to 10° , in the transverse plane. The joint angle was recorded for each image using a digital protractor secured to the C-arm. Fig. 1 illustrates the C-arm set up from the operating room. An example CT image showing real brachytherapy seeds is also shown in the inset for comparison.

A seed-projection matching approach with motion compensation was used to obtain seed reconstructions from the intraoperative data [19]. The method uses a network flow solution to minimize the distance between back-projected lines from seed projections [20], and motion compensation that recovers the

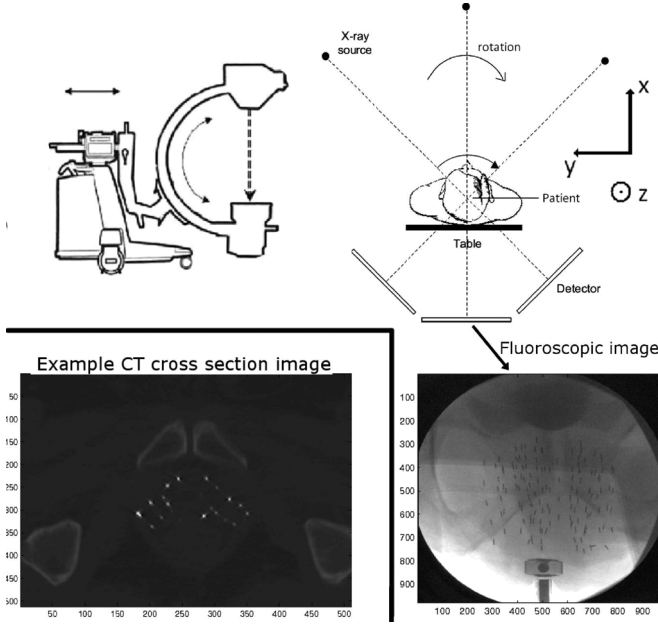


Fig. 1. Prostate Brachytherapy setup with C-arm used to take intraoperative fluoroscopic data. The coordinate system that is used is also shown. Inset: An example 2D CT cross section image for comparison.

C-arm pose without the need for fiducial markers or auxiliary trackers. Its results were carefully validated in simulations, implant phantoms and patient data [19].

III. METHODS

Seeds are matched between datasets by first finding the needle tracks they belong to. The minimum cost algorithm described by Chng *et al.* [9] is used to find these needles tracks in the different datasets. The intersections of the needles with the transverse insertion plane are computed next and a different minimum cost network flow algorithm is used to match these intersections between datasets. With the intersections and therefore needles matched, the seeds in each needle are then labeled and seed displacements are computed. The approach is summarized in Fig. 2. For all the descriptions and results presented in this paper we employ a conventional right-handed coordinate system in which the z axis is also the insertion axis and runs inferior to superior and the x axis runs posterior to anterior, as shown in Fig. 1. The terms yaw, pitch and roll refer to rotations about the x axis, y axis and z axis, respectively. Detailed descriptions of the methods are presented in the following five subsections.

A. Registration Using Insertion Axis Detection

Previous work has shown that to accurately compute the displacements, it is necessary to put the different datasets into correspondence [9]. Full point to point registration that can remove local trends is not desired. Instead, we carry out the registration using average components of the different clusters. Each dataset is globally translated and rotated so that the seed cluster centroid position is located at the origin and the average implantation axis is aligned with the z axis.

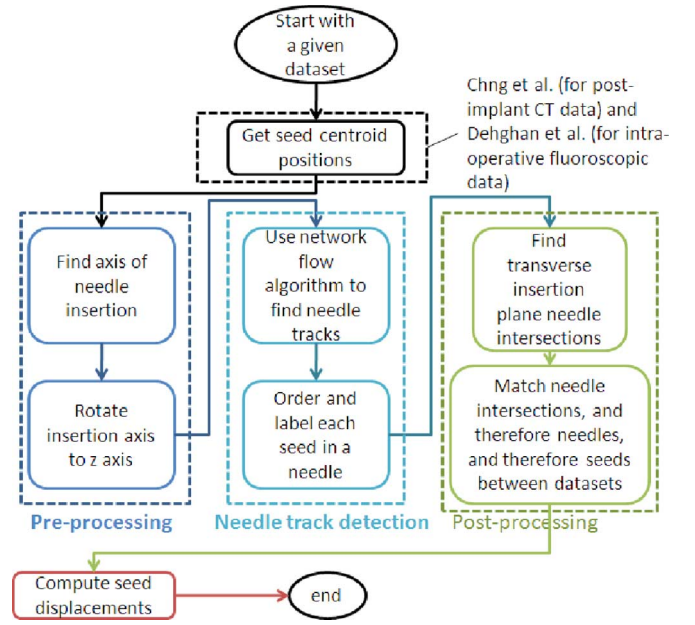


Fig. 2. Full seed displacement algorithm.

Usmani *et al.* show that the seed cluster centroid position can be used to register the datasets since it remains at the same position even with considerable postimplant migration [12]. Matching the implantation axes in the datasets removes global pitch and yaw differences. Local pitch and yaw trends are expected and can be measured since only the average insertion direction is used. No roll trends are expected so postprocessing is used to remove any slight roll differences. The axis detection is carried out on each dataset separately which reduces the computation that would be required to compute costs from looking at two datasets simultaneously, as would be carried out with an iterative closest point method.

The main component of our registration process involves finding and aligning the average implantation axes in different datasets. Our iterative best line algorithm to find the axis of insertion is similar to the RANSAC (RANDOM SAMPLE Consensus, [21]) algorithm which involves fitting lines to pairs of randomly chosen points and scoring each line. The highest scored lines are then kept as needles. However, our implementation has no random component. This is due to the fact that an exhaustive search on all possible pairs of points for this application is not computationally demanding. This gives an effective way of finding a *majority* of the needles but does not consistently detect all of them. However, as we will show, this allows us to find the implantation axis, which coincides with the ultrasound transducer axis.

Pairs of seeds are used to fit straight lines that define potential needle directions. Implausible pairs, calculated based on whether the lines are within a certain angle threshold from the z axis, are rejected immediately saving unnecessary calculations. Seeds belonging to the same needle may not necessarily lie on a straight line, as needle tracks can exhibit significant curvature which is not easily parameterizable, as illustrated in Fig. 3. Therefore, a tolerance region is required when matching seeds to a single line modeling the needle.

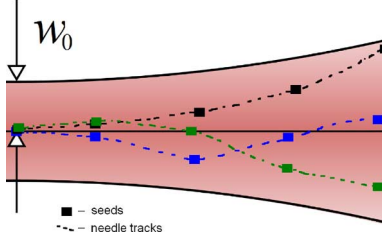


Fig. 3. Illustration of several possible curvatures that can be detected for a needle by using a Gaussian cone rather than a tube with fixed radius.

We chose a Gaussian cone as a tolerance region for each potential needle direction line since it applies tight constraints to potential tracks when they are close to the insertion plane and relaxes them farther away where there is more deviation. The depth of focus can be varied to give a sharper cut-off for higher angles than a simple cone tolerance region gives. A given seed, i , only contributes to the score if it is closer than a distance w_i to the potential line. w_i is the “waist” of the tolerance which increases with the distance from the insertion plane, a_i and is computed as

$$w_i = w_0 \sqrt{1 + \frac{a_i}{r}} \quad (1)$$

where w_0 is the minimum waist size and r is the distance at which $w_i = w_0 \sqrt{2}$. They control the waist at the insertion plane and the rate of expansion of the Gaussian tolerance cone. Finally, since the spacing in stranded seeds can only be a multiple of 10 mm we remove any seeds that do not satisfy this requirement with a tolerance of ± 2 mm. The spacing between seed i and an adjacent seed j is denoted sp_{ij} . This eliminates the cases when seeds from other needle tracks fall within the Gaussian cone when the waist size is large.

Letting d_i be the distance of seed i from the potential needle axis, the score becomes

$$\text{Score} = \sum_{\{i: d_i < w_i, |sp_{ij} - 10| < 2\forall j\}} e^{-d_i^2/w_i^2} \quad (2)$$

As shown in Section IV-A, the iterative best line detection algorithm finds a majority of the needles. However, in this work, we used this algorithm primarily to find the axis of insertion of needles which is an important piece of information to ensure the accuracy of the network flow algorithm. By relaxing the constraints and therefore allowing needles with a larger deviation from the z axis, we were able to find the implantation axis by averaging the direction vectors of the highest scoring eight needles. Eight needles were chosen instead of using a cutoff calculated for each patient for consistency. Each of the seed clusters were then rotated so that the implantation axis was parallel to the z axis. The preplan data has the transducer axis already parallel to the z axis, and obviously did not require any rotation.

B. Assigning Seeds to Needle Tracks

Once the dataset is rotated so that it is aligned with the implantation axis, it is possible to use a needle detection algorithm with tighter restrictions. The curvature problem, however, still

remains. Therefore, instead of looking at parameterizable lines the seeds are viewed as nodes within a network that allow a single unit of flow through them. Each arc between two nodes carries a cost for a unit flow. The Matlab Toolbox “matlog” developed by M. G. Kay at the North Carolina State University was used to determine the flow lines, which were tuned to be the needle tracks, that resulted in the lowest total cost¹ [22].

To summarize the process: first, two new nodes are created, one start node to supply all the flow and one end node to sink it. All the seeds are defined as transshipment nodes, located between the start and end node, where the inflow must equal the outflow. Each node is initially given the same negative cost so that they are all equally likely to be used, while a cost function is used to define the costs of flow going through every arc joining two nodes, from the source node to the sink node. This cost function allows for the correct needle track detection. Since each arc is independent of the previous one, there are no restrictions as to the direction of the flow based on the shape of the curve before the node which allows for the changes in direction that sometimes occur. A cost function with two components is used. These are the angle that a given flow line makes with the average insertion axis, and the length of the unit of flow—which should be a multiple of the 10 mm. Although each component function has a complex form derived in Chng *et al.* [9] we use much simpler functions that still give accurate results.

The angle cost component is defined as follows:

$$AC_{ij} = (e^{|\theta_{ij}|/\theta_0} - 1)^4 \quad (3)$$

and the spacing component of the cost is

$$SC_{ij} = -e^{-s_{ij}/s_d} \left(\left(\sum_n \delta(s_{ij} - ns_0) \right) \star e^{-(s_{ij}/s_v)^2} \right) \quad (4)$$

where s_{ij} is the spacing between node i and node j and $|\theta_{ij}|$ is the angle the line between the two nodes makes with the z axis. The symbol \star denotes convolution. The spacing cost is defined as a Gaussian with a variance of s_v convolved with a train of delta functions to give negative peaks at integer multiples of the smallest spacing ($s_0 = 10$ mm). The decaying exponential with a variance of $s_d = 10$ mm is aimed at penalizing larger seed spacing. It decreases the magnitude of the spacing cost by a factor $1/e$ for every successive integer multiple of the spacing s_0 . Note that the contribution of each successive Gaussian peak to the cost decreases exponentially as n increases. However, in practice, it is extremely unlikely that the seed spacing in a given needle is 40 mm or more so we only sum until $n = 3$. The fourth power for the angle cost ensures that the cost increases rapidly for increasing angles. θ_0 and s_v are tunable parameters that define how “strict” the function is with respect to the angle and seed spacing, respectively. For the fluoroscopic data, θ_0 was set to 43.0° and s_v to 1.2 mm. A large angle variance was needed since several needle tracks were visibly curved and rotated but tighter restrictions on the seed separation ensured that true tracks were identified. In contrast, for the postimplant CT data, θ_0 was set to 31.5° and s_v to 3 mm. Here, the seeds migrated a little so the seed separation requirement was relaxed.

¹<http://www.ise.ncsu.edu/kay/matlog/>

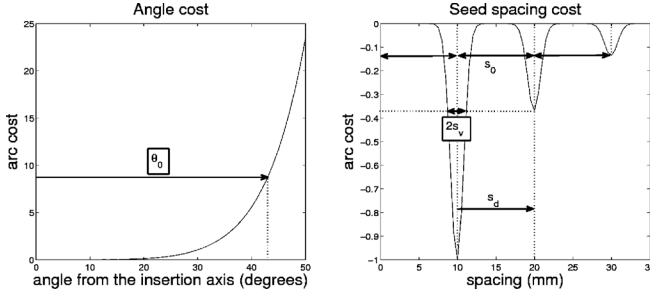


Fig. 4. Graphs of the angle (left) and spacing (right) cost functions showing high costs for higher angles and low costs for multiples of the smallest seed spacing (10 mm). The tunable parameters for the angle variance, θ_0 , and the spacing tolerance, s_v , are shown with a box around them. The spacing constants, s_0 and s_d are also shown.

Fig. 4 graphically shows the angle and seed spacing cost functions with the different parameters and constants.

The total cost is obtained by summing the two costs with a weighting parameter, γ , on the angle cost term. This parameter controls which component affects the cost most. We found that increasing the sensitivity of the function to the spacing of the seeds by decreasing the value of γ produced the best results. A lower sensitivity to the angle was needed to allow for the observed variation in the tracks. Therefore, for the intraoperative fluoroscopic and postimplant CT data, γ was set to 0.3. For the preplan data, however, γ is set to 1.2 so that the function is weighted more to the angle cost so that any angle deviation from the z axis has a much higher cost. The final objective function is

$$C_{ij} = \gamma AC_{ij} + SC_{ij}. \quad (5)$$

C. Needle Matching

The needle detection technique summarized above leverages intra-strand seed spacing, enforced physically by the stranded seed product routinely used in our implants, as the classification characteristic that is least sensitive to noise. This simplifies a matching of ~ 100 seeds to one of ~ 20 needles. This section explains how the needle matching across datasets is carried out.

After rotating the seed clusters and grouping the seeds into needles, the insertion plane intersection of each needle is computed. The insertion plane is the transverse plane passing through the most inferior seed (at the apex of the prostate). Matching is then performed using another minimum cost network flow algorithm. Each node of the network contains the x , y coordinates of an intersection as well as the number of seeds that were in the needle. In this case, instead of adding a source and sink node, all the nodes from one type of intersection data are defined as source nodes and all the nodes from the other type are defined as the sink nodes (there are no transshipment nodes). The cost of a unit flow from an intersection from one data type to that of another one is defined as

$$\text{MatchCost}_{ij} = d_{ij} + (N_i - N_j + 1)^4. \quad (6)$$

Here MatchCost_{ij} is the cost of matching a needle intersection, i , from one dataset to another needle intersection, j , in another dataset. d_{ij} is the distance between intersection i and intersection j , while N_i and N_j are the number of seeds in needle

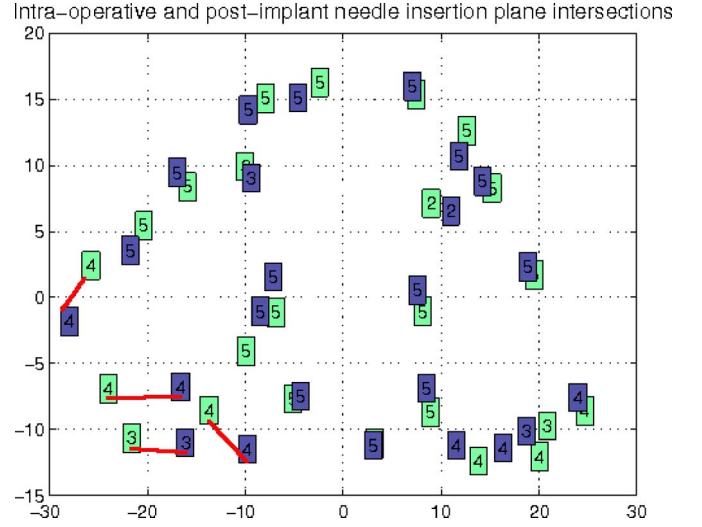


Fig. 5. Insertion plane intersections for one patient showing why the number of seeds per needle is also needed in the cost function.

i and needle j , respectively. We add 1 in the term $N_i - N_j + 1$ to emphasize the difference in seed numbers, even when that difference is only 1. A low cost is assigned if the corresponding needle intersection is close by and also has the same number of seeds in the needles. d_0 is the parameter used to control the effect of the spacing on the cost. Since the number of needles in the two datasets can now be set *a priori* the algorithm tries different pairings until all are matched at the lowest cost. Fig. 5 shows an example of insertion plane intersections. The red lines show some of the correct matches. Note that simply using a closest-to match would not work.

D. Seed Displacement Computation

Each seed position is compared to its corresponding seed from a different data type to obtain a displacement vector. An entire dataset of each seed displacement vector in each patient was computed to find trends. Sets of displacement vectors were generated both for intraoperative misplacement and for postimplant movement.

Scalar distances were used to quantify the motion. The total average distance was computed for each patient as well as for all the patients. The average distance was also computed for different regions of the prostate by dividing the entire volume into 27 subregions, where each axis was divided into three sections.

We also looked at the direction of seed motion. This was done by computing an average displacement vector in each of the subregions. These displacement vectors were used to analyze the trends the direction of motion in each region.

E. Postprocessing to Fine Tune Dataset Registration

Section III-A describes the registration used to correct differences in the global pitch and yaw which allows local trends to be measured. These trends are expected to be as a result of several mechanisms including needle deflection, prostate rotation, oncologist preferences, inflammation and change in patient pose. None of these, however, are expected to create any local roll trends. The global differences in roll, due to slight

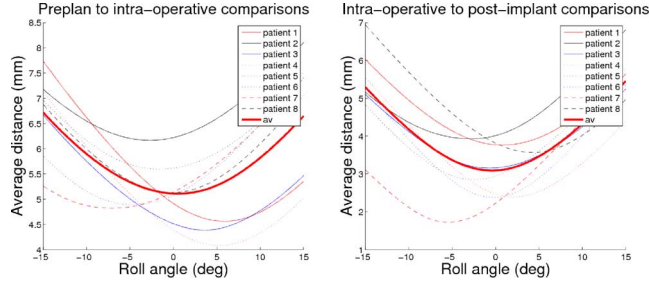


Fig. 6. Graphs showing how the average displacement distances varied with different roll values for the intraoperative data. The preplan to intraoperative comparisons are shown on the left and intraoperative to postimplant comparisons are shown on the right.

TABLE I
NEEDLE TRACK DETECTION USING THE ITERATIVE
BEST LINE DETECTION ALGORITHM

Patient	Number of incorrectly assigned seeds	Number of seeds inserted	Percent seeds correctly assigned
1	21	105	80%
2	14	105	86.67%
3	16	102	84.31%
4	25	122	79.51%
5	8	104	92.31%
6	13	115	88.70%
7	21	100	79%
8	8	118	93.22%

differences in imaging angles, were therefore automatically removed after the displacement calculations. This was done by computing the average displacement distance for each patient for different amounts of roll of the intraoperative data, which is used in both comparisons. Fig. 6 shows how the average displacement distance varied with roll angle for each patient. The roll angle which gives the minimum average displacement distance is taken as the value which aligns the roll between the datasets and the displacements with this roll are reported in this paper.

IV. RESULTS AND DISCUSSIONS

This section will first present the verification of the individual processes described in the methods followed by the actual seed displacement results. These results include quantitative values for the displacement for each patient and also for each region of the target volume (the prostate). A qualitative description of the direction of displacement is given following a numerical analysis to assess the presence of trends.

A. Finding the Transducer Axis

The iterative best line detection algorithm resulted in needle detection outcomes reported in Table I. The needle detection results vary from 79.0% to 93.22% of seeds that were correctly assigned. Based on the average vector directions of the eight highest scoring needles, we found the implantation axis and rotated the cluster of seeds so that it was aligned with the z axis. Fig. 7 shows that the alignment of the implantation axis with the z -axis was achieved for both intraoperative fluoroscopic data and postimplant CT data.

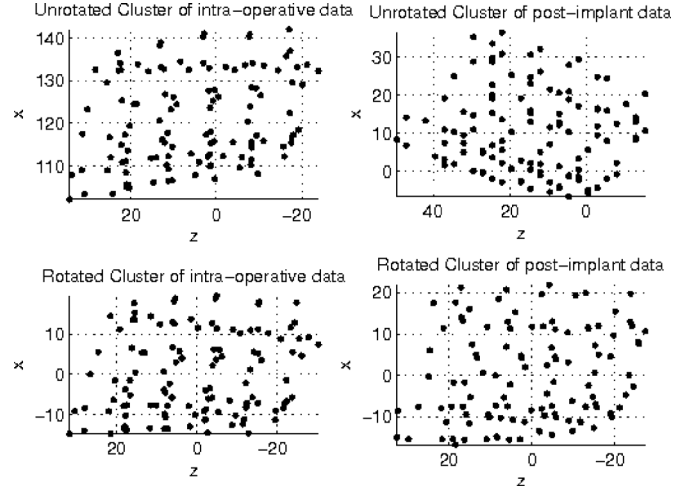


Fig. 7. Finding the implantation axis using an iterative best line detection for intraoperative fluoroscopic data.

The transducer axis is assumed to have the same pitch as the most posterior needles. Although Fig. 7 only shows the sagittal view, it is worth noting that the algorithm performed 3D rotations and not just a single rotation about the y axis.

B. Needle Track Detection

The full algorithm was tested on eight patient datasets. The number of needles and number of correctly assigned seeds were determined by comparing the result to the preplan (potentially modified by the oncologist during operation). Fig. 8 shows the results from a single patient for all three data types.

Intersections of detected needle lines at the insertion plane were used to compare to the plan, looking at the number of seeds per needle as well as the expected relative positions. This simplified the finding of potentially incorrectly assigned seeds. Fig. 9 shows an example of a plan comparison. The black ellipses show how the comparison can be used to identify which seeds were not assigned correctly.

The needle matching for the preplan data, not surprisingly, correctly assigned all the seeds in all patients. The results for the intraoperative and postimplant seed to needle assignment are summarized in Table II which shows the percentage of seeds that were correctly assigned.

It is worthwhile to note that patients 3 and 5 had two special load needles (needles with irregular seed spacing) each. As expected, this made it more difficult to find those needles and accounted for the incorrect seed assignments for both these patients. Summarizing the results, an average of 99.31% of the seeds were correctly assigned for the intraoperative data, while an average of 99.41% of the seeds were correctly assigned for the postimplant data. Once again, no preplan information is used in the needle detection and the algorithm takes between 1 to 2.5 s to rotate the cluster and find the needles.

C. Inter-Dataset Needle Matching

Before continuing, the few incorrectly assigned seeds in the various datasets were manually adjusted to be grouped with the correct needle. Insertion plane intersections, previously used to

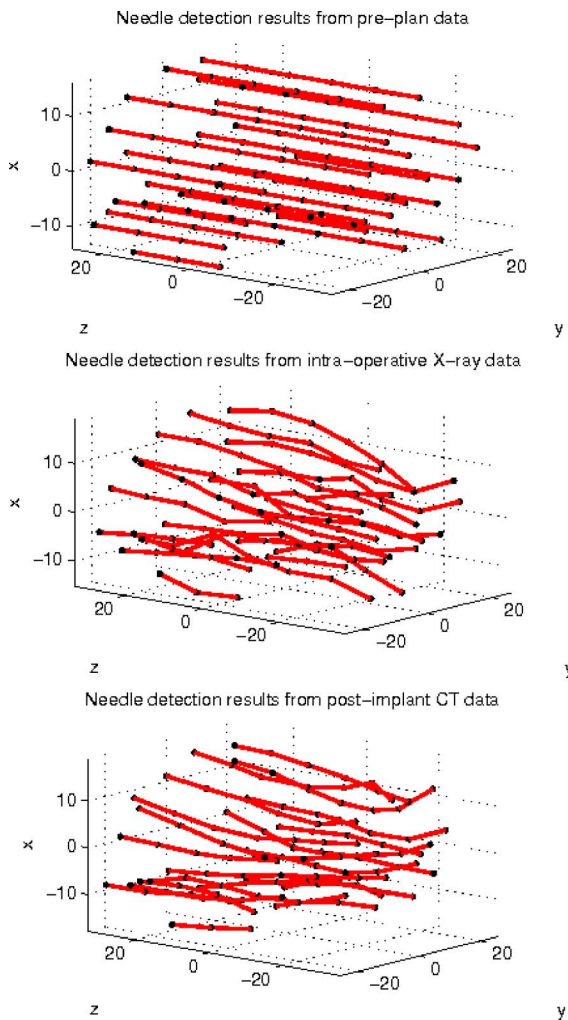


Fig. 8. Needle detection results for patient 4 for preplan, intraoperative and postimplant data.

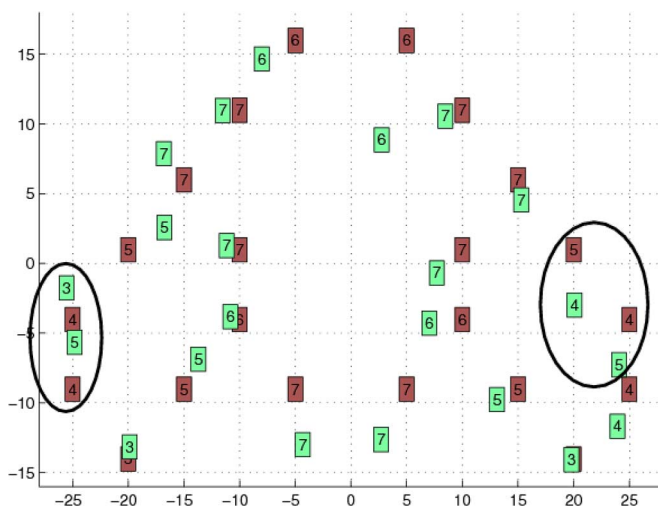


Fig. 9. Comparison of fluoroscopic intersection data with preplan data showing some incorrectly assigned seeds. The same images were used for CT to preplan comparison.

verify the needle detection, were then used to perform needle matching between the datasets. The matching of the preplan to

TABLE II
SUMMARY OF NEEDLE TRACK RESULTS FOR THE BOTH INTRAOPERATIVE AND POSTIMPLANT DATA, ON EIGHT PATIENTS

Patient	Number of seeds inserted	Percent intra-op seeds correctly assigned	Percent post-imp seeds correctly assigned
1	105	100%	100%
2	105	100%	98.10%
3*	102	98.04%	98.04%
4	122	98.36%	98.18%
5*	104	98.08%	100%
6	115	100%	100%
7	100	100%	100%
8	118	100%	100%

* patients with special load needles (needles with irregular seed spacing)

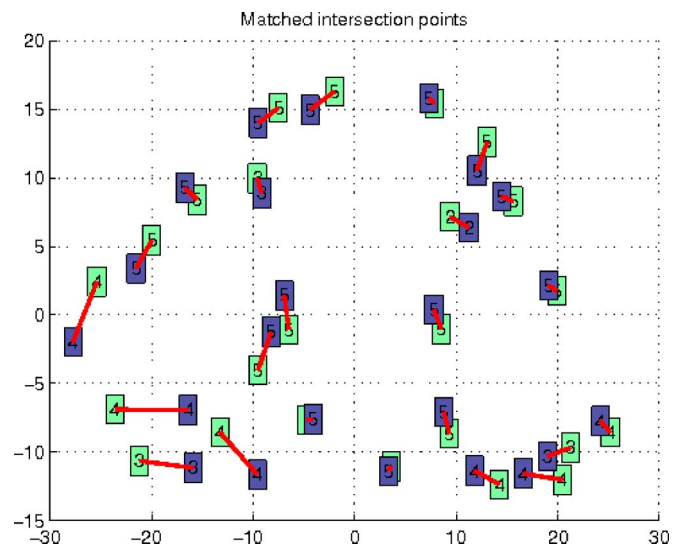


Fig. 10. Intraoperative to postimplant needle matching results for one patient. Matching needles are connected with the red lines.

the intraoperative data and the intraoperative data to the postimplant data still required verification since the expected displacement made the insertion plane intersections vary considerably between datasets. The method described earlier achieved a correct needle matching for all the datasets, for both comparisons. Fig. 10 shows how the intersection data displayed in Fig. 5 was correctly matched. The red lines connect needles that are matched by the algorithm.

D. Calculation of Seed Displacement

With the needles correctly identified and matched in corresponding data sets for a given patient, the seeds themselves could be directly compared which gave us a measure of the seed displacements. Figs. 11 and 12 show the movements of the seeds between the preplan and intraoperative data and between the intraoperative and postimplant data for one of the patients, respectively.

1) *Average Displacement Magnitude:* The 3-D Euclidean distance that every seed moved between datasets was computed. For each single patient the average distance was computed as the sum of all the distances moved divided by the total number of

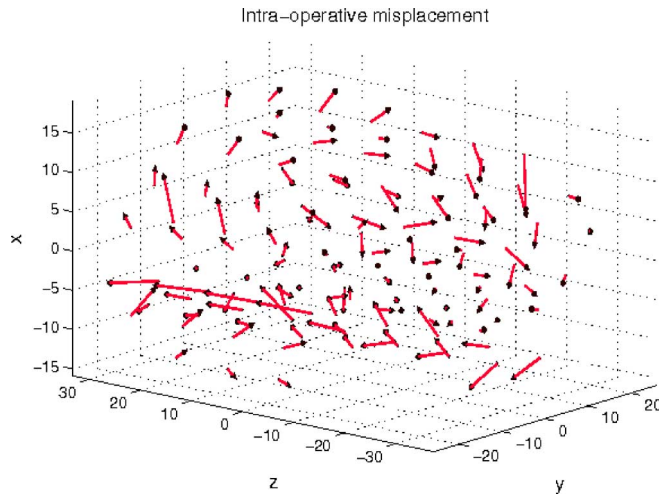


Fig. 11. Preplan to intraoperative seed misplacement results for patient 4.

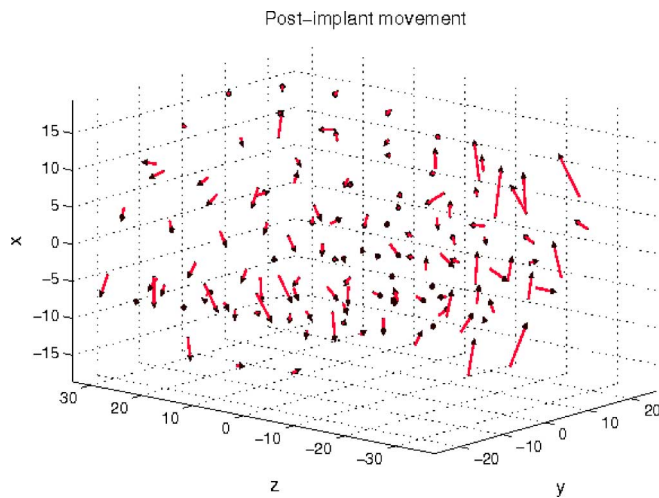


Fig. 12. Intraoperative to postimplant seed movement results for patient 4.

TABLE III
SEED DISPLACEMENT RESULTS FOR BOTH THE PREPLAN TO INTRAOPERATIVE DATA AS WELL AS THE INTRAOPERATIVE TO POSTIMPLANT DATA

Patient	Av. misplacement distance (pre to intra-op) /mm	Av. movement distance (intra-op to post-imp) /mm
1	4.56±2.10	3.76±1.89
2	6.17±2.44	3.93±2.45
3	4.39±1.78	3.16±1.78
4	4.08±2.25	2.39±1.41
5	5.59±2.25	2.85±1.73
6	4.89±2.18	2.38±1.09
7	4.82±2.46	1.72±0.75
8	5.12±3.02	3.57±1.72
Average	4.94±2.42	2.97±1.81

seeds inserted into the patient. The total average over all eight patients was also computed. Table III summarizes the results.

From Table III the average displacement was significantly larger for preplan to intraoperative case than intraoperative to postimplant data ($p < 0.01$, $n = 871$).

The error in our localization of the seeds in intraoperative fluoroscopy data, is reported to be less than 0.9 mm [19]. The

TABLE IV
INTRAOPERATIVE SEED MISPLACEMENT RESULTS FOR DIFFERENT REGIONS WITHIN THE PROSTATE VOLUME

		Average misplacement distance (mm)		
		left	mid y	right
inferior	anterior	5.42 ± 1.41	6.52 ± 2.63	4.81 ± 2.41
	mid x	4.11 ± 2.19	5.79 ± 2.41	4.01 ± 2.44
	posterior	4.25 ± 1.52	5.23 ± 1.76	4.16 ± 2.05
mid z	anterior	5.13 ± 1.51	6.58 ± 3.07	5.38 ± 2.92
	mid x	4.65 ± 2.14	6.15 ± 3.17	4.89 ± 2.36
	posterior	3.81 ± 1.68	5.07 ± 1.97	4.14 ± 2.88
superior	anterior	5.84 ± 1.25	6.70 ± 2.76	5.71 ± 2.09
	mid x	5.06 ± 2.20	5.55 ± 2.58	5.14 ± 2.51
	posterior	4.03 ± 1.93	5.24 ± 2.36	4.96 ± 3.01

TABLE V
POSTOPERATIVE SEED MOVEMENT RESULTS FOR DIFFERENT REGIONS WITHIN THE PROSTATE VOLUME

		Average distance moved (mm)		
		left	mid y	right
inferior	anterior	2.96 ± 1.71	3.67 ± 2.34	3.16 ± 1.81
	mid x	2.99 ± 1.76	2.82 ± 1.57	3.34 ± 1.85
	posterior	2.66 ± 1.55	2.58 ± 1.60	3.26 ± 1.76
mid z	anterior	2.68 ± 2.30	3.29 ± 2.45	3.13 ± 2.14
	mid x	3.03 ± 2.01	1.60 ± 0.86	2.59 ± 1.90
	posterior	3.15 ± 1.42	2.30 ± 1.30	2.98 ± 1.53
superior	anterior	3.28 ± 2.36	2.89 ± 1.67	3.85 ± 2.31
	mid x	3.04 ± 1.82	2.16 ± 0.98	2.56 ± 1.70
	posterior	3.10 ± 1.35	2.34 ± 1.18	3.04 ± 1.02

calculated displacement is therefore not due to errors in seed localization. The result suggests seed displacement due to oncologist preferences, needle deflection and prostate movement during needle insertion, seen from preplan to intraoperative misplacement as an average of 4.94 mm, is higher than displacement caused by a change in patient pose and immediate inflammation (measured as intraoperative to postimplant movement, an average of 2.97 mm).

2) *Regional Displacement Magnitudes*: The average displacement was computed for each of the 27 subregions, defined by dividing each axis into three sections, to quantify the motion in each region. Tables IV and V show these distances. In the table, the different transverse slices presented from inferior to superior. Each transverse slice has nine distance values.

For the preplan to intraoperative displacement, the seeds near the medial line of the prostate (the z axis) moved slightly more on average. Note that no directional information can be drawn from this. For intraoperative to postimplant displacements, there were no significant differences in the amount of motion between the different subregions. In agreement with the average patient data, the intraoperative misplacement was greater than the postimplant movement in all regions.

3) *Displacement Vectors*: It was noted that different magnitudes of displacement occurred in different regions of the prostate. We computed the average displacement vectors for each of the 27 subregions. Tables VI and VII summarize the general displacement directions seen. The displacement vectors are visually illustrated in Figs. 13 and 14. The standard deviation ellipsoids are drawn in separate plots where each ellipsoid is centered in its respective region. Note that the scale is doubled for the postimplant vectors and standard deviations so that they can be seen.

TABLE VI
PREPLAN TO INTRAOPERATIVE MISPLACEMENT DIRECTION RESULTS.
VALUES WITH A MEAN VALUE TO STANDARD DEVIATION RATIO
GREATER THAN 0.95 ARE IN BOLDFACE

Average misplacement direction vectors (x,y,z) (mm)				
		left	mid y	right
inf	ant	(0.33,0.54,- 3.87) $\pm(2.36,2.85,1.79)$	(-0.01,-1.47,- 4.14) $\pm(2.59,2.55,4.20)$	(-0.51,-1.59,-2.88) $\pm(2.05,2.06,3.15)$
	mid x	(-0.24,0.02,0.31) $\pm(1.55,2.01,3.92)$	(0.94,0.31,2.03) $\pm(1.48,2.16,5.56)$	(-0.70,-0.73,0.31) $\pm(1.96,2.14,3.56)$
	post	(0.41,1.01,1.87) $\pm(2.43,1.85,2.67)$	(0.21,-0.05, 3.47) $\pm(3.33,1.14,2.55)$	(1.40,0.07,0.55) $\pm(2.61,1.78,3.22)$
mid z	ant	(1.63 ,0.15,- 3.83) $\pm(1.53,2.47,1.85)$	(1.90,-0.69,-3.71) $\pm(2.31,2.73,4.82)$	(0.42,-0.04,- 4.06) $\pm(2.48,1.82,3.46)$
	mid x	(0.10,-0.97,0.70) $\pm(2.09,1.87,4.15)$	(-0.13,-0.28,3.21) $\pm(1.86,2.36,5.75)$	(-0.79,0.96,0.57) $\pm(2.52,2.49,3.92)$
	post	(0.29,-0.07,1.45) $\pm(2.12,2.12,2.57)$	(-0.60,0.54, 3.46) $\pm(2.83,1.41,2.74)$	(0.00,1.15,0.96) $\pm(1.84,2.08,4.01)$
sup	ant	(3.07 ,-1.48,- 3.51) $\pm(2.02,2.47,1.51)$	(2.58 ,-0.60,-3.56) $\pm(2.31,3.16,4.28)$	(1.68,2.34,- 2.74) $\pm(2.64,2.63,2.86)$
	mid x	(0.12,-1.79,0.36) $\pm(2.60,2.12,4.02)$	(0.11,0.62,2.58) $\pm(2.36,2.35,4.72)$	(-0.70,2.07,0.51) $\pm(2.77,2.80,3.53)$
	post	(-0.41,-0.40,1.35) $\pm(1.99,2.45,2.88)$	(-2.07,0.44, 3.76) $\pm(2.25,1.59,2.69)$	(-1.26,1.76,0.87) $\pm(1.99,2.97,4.01)$

TABLE VII
INTRAOPERATIVE TO POSTIMPLANT MOVEMENT DIRECTION RESULTS.
VALUES WITH A MEAN VALUE TO STANDARD DEVIATION RATIO
GREATER THAN 0.95 ARE IN BOLDFACE

Average movement direction vectors (x,y,z) (mm)				
		left	mid y	right
inf	ant	(0.71,0.57,-0.38) $\pm(1.99,1.16,2.37)$	(1.20,-0.00,-0.09) $\pm(1.56,0.85,3.83)$	(0.29,-0.27,-0.41) $\pm(1.91,0.77,3.03)$
	mid x	(0.38,0.48,0.18) $\pm(2.39,1.13,2.19)$	(1.75,-0.05,0.12) $\pm(2.18,0.98,1.35)$	(0.39,-0.40,0.93) $\pm(2.00,1.29,2.81)$
	post	(-0.01, 1.09 ,0.36) $\pm(1.40,1.15,2.31)$	(0.66,0.04,0.86) $\pm(2.05,0.68,1.89)$	(0.08,- 1.67 ,1.04) $\pm(1.73,1.44,2.30)$
mid z	ant	(-0.38,-0.12,-1.13) $\pm(1.31,1.06,2.91)$	(0.70,-0.06,-1.29) $\pm(1.26,0.74,3.59)$	(0.10,0.29,-1.12) $\pm(1.31,0.98,3.27)$
	mid x	(-1.12,0.72,-0.34) $\pm(1.80,1.53,2.42)$	(-0.02,0.15,-0.66) $\pm(0.46,0.74,1.57)$	(-0.72,-0.33,0.68) $\pm(1.01,0.95,2.72)$
	post	(-0.79,0.97,0.98) $\pm(1.12,1.67,2.37)$	(-0.59,0.03,1.36) $\pm(0.99,0.75,1.85)$	(-0.66,- 1.39 ,0.97) $\pm(1.74,1.35,1.82)$
sup	ant	(0.53,-0.35,-1.65) $\pm(1.25,1.24,3.22)$	(1.11 ,0.08,-0.63) $\pm(1.11,0.99,2.78)$	(1.34 ,0.59,-0.50) $\pm(1.33,1.31,3.85)$
	mid x	(-0.69,0.11,-0.98) $\pm(2.07,1.26,2.32)$	(-0.72,0.07,-1.03) $\pm(1.41,0.94,1.26)$	(-0.11,-0.15,0.10) $\pm(1.63,1.14,2.36)$
	post	(-0.08,0.49,0.14) $\pm(2.01,1.40,2.32)$	(-0.34,-0.05,0.23) $\pm(1.42,0.93,1.99)$	(-0.48,-1.00,0.41) $\pm(1.97,1.46,1.75)$

As with the scalar measurements, the directional displacements from intraoperative to postimplant were smaller than in the preplan to intraoperative case. The significant intraoperative misplacement results can be summarized as follows: 1) inferior displacement of lateral anterior seeds, 2) superior displacement of medial posterior seeds, and 3) anterior misplacement of superior anterior seeds. For the postimplant movement there is: 1) inward lateral movement of inferior posterior seeds and 2) anterior movement of superior anterior seeds.

V. SUMMARY AND CONCLUSION

We have combined several techniques to formulate a new method to identify seeds from stranded implants in different datasets and therefore compute their displacements. The complete process involved: implantation axis detection, needle track detection and needle matching using the insertion plane and the

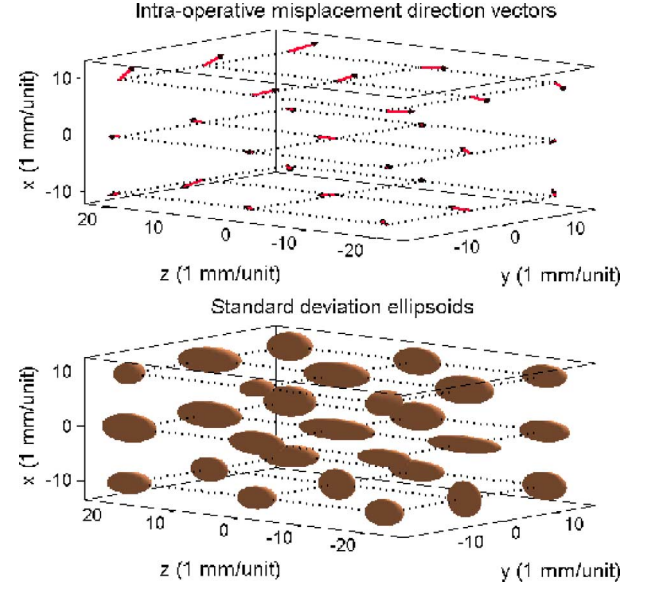


Fig. 13. Intraoperative misplacement vectors (above) and the standard deviation ellipsoids (below).

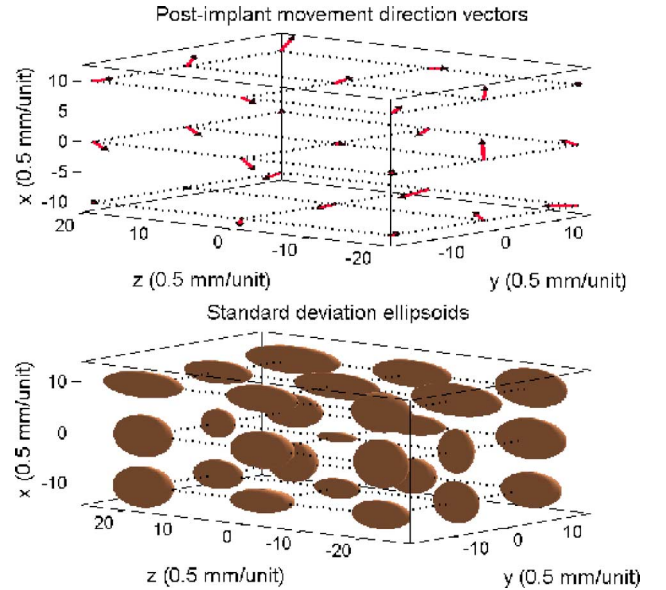


Fig. 14. Postimplant movement vectors (above) and the standard deviation ellipsoids (below). The units in brackets correspond to the vector lengths and not the starting positions. Each unit is 1 mm for these.

number of seeds per needle. Our iterative best line detection has accurately found the implantation axis from rotated data cluster in all the datasets. With the detected implantation axis, seed assignment based on a minimum cost network flow algorithm has an accuracy of 99.3% and 99.4% in the intraoperative and postoperative data.

Given our accurate reconstructions, we were able to measure the magnitude and direction of seed displacements. For the regional displacements, the following conclusions are potential explanations for the results seen.

For the preplan to intraoperative comparison, several regional displacements were noted. The larger amount of misplacement for seeds near the medial line is most likely due to the fact

that this is the longest part of the prostate giving the oncologist more leeway to steer the needles. There is no directional trend to this placement which suggests that it is not due to needle or prostate movement. Similarly, the inferior misplacement of anterior seeds and superior misplacement of posterior seeds is also likely due to oncologist tendencies. There is a lack of implantable tissue in the anterior superior quadrant (close to the bladder) and so seeds are deliberately placed more inferiorly. The greater retraction of lateral anterior seeds is due to the presence of the pubic arch which forces a shallower implant. The divergence of the rectum from the prostate in the superior posterior quadrant leads to a tendency to “over-plan” the medial superior region on the posterior side.

The anterior misplacement of superior anterior seeds can be explained either by prostate rotation or needle deflection. Any transverse displacement of the seeds could be due to needle deflection. We expect that this effect would be most visible with superior seeds. However, this does not explain the anterior direction of the misplacement. Therefore, if we assume that it is due to prostate movement, we can conclude that the base tends to rotate posteriorly away from the pubic arch during insertion. This leads to anterior displacement as the gland rotates back after insertion. We will examine the validity of these explanations in our future studies.

For the intraoperative to postimplant comparison the first directional conclusion can be drawn from the lack of a global outward seed displacement. This suggests that inflammation has little or no effect for immediate postimplant seed movement. The only outward motion is seen with anterior movement of superior anterior seeds. This could be due to pressure from the bladder on the superior side of the gland when the patient pose changes from dorsal lithotomy horizontal recumbent. Inward lateral movement of inferior posterior seeds must also be due to change in patient pose although further analysis of the forces on the gland during the change is needed to verify this.

Our results show that intraoperative seed misplacement is larger than postimplant movement. This confirms results from Chng *et al.* [9], who explain the large impact that both prostate rotation and needle deflection have. This also agrees with work done by Wan *et al.* to evaluate needle deflection [23] and by Lagerburg *et al.* who evaluate prostate rotation during the insertion of needles [24]. Furthermore, our technique could be used to track seed misplacement, therefore providing a measurement-based alternative to studying the sensitivity of delivered dose to seed misplacement errors. Su *et al.* performed a study on the effect of seed misplacement on the delivered dose using random noise to model the misplacement instead of actual measurements [25] and found minimal changes in the D90 measure with misplacements of up to 4 mm. However, the random noise model does not include the trends we found and so the seed identification methods used here could be used to confirm this result in a further study.

We have presented regional, directional displacement measurement techniques for stranded seeds in prostate brachytherapy which can be used both to influence future planned treatment and to provide more post surgery information to patients and oncologists for quality assurance.

The algorithms explained in this paper have been described for preplan to intraoperative fluoroscopic to postimplant CT-data. However, they can also be used to compare seed positions over several days after a surgery to further monitor inflammation. Another application of the developed algorithms is in real-time dosimetry. Complete ultrasound-based brachytherapy seed detection is a notoriously challenging problem. However, Moradi *et al.* have shown that given a complete reconstruction of the fluoroscopic data and identification of the seeds, registration can be performed with an incomplete reconstruction of the seed cloud in ultrasound data [13]. Therefore, the complete seed identification (or labeling) algorithm described here, could make it possible to perform intraoperative dosimetry.

REFERENCES

- [1] W. Morris, M. Keyes, D. Palma, I. Spadinger, M. McKenzie, A. Agranovich, T. Pickles, M. Liu, W. Kwan, and J. Wu, “Population-based study of biochemical and survival outcomes after permanent 125I brachytherapy for low- and intermediate-risk prostate cancer,” *Urology*, vol. 73, no. 4, pp. 860–865, Apr. 2009.
- [2] S. Nag, W. Bice, K. DeWynngaert, B. Prestidge, R. Stock, and Y. Yu, “The american brachytherapy society recommendations for permanent prostate brachytherapy postimplant dosimetric analysis,” *Int. J. Radiat. Oncol. Biol. Phys.*, vol. 46, no. 1, pp. 221–30, Jan. 2000.
- [3] M. Gao, J. Z. Wang, S. Nag, and N. Gupta, “Effects of seed migration on post-implant dosimetry of prostate brachytherapy,” *Med. Phys.*, vol. 34, no. 2, pp. 471–480, 2007.
- [4] P. L. Roberson, N. Vrinda, L. M. Daniel, J. W. Raymond, and P. W. McLaughlin, “Source placement error for permanent implant of the prostate,” *Med. Phys.*, vol. 24b, no. 2, pp. 251–257, Feb. 1997.
- [5] R. Taschereau, J. Roy, and J. Pouliot, “Monte Carlo simulations of prostate implants to improve dosimetry and compare planning methods,” *Med. Phys.*, vol. 26, no. 9, pp. 1952–1959, 1999.
- [6] I. D. Kaplan, P. M. Meskell, M. Lieberfarb, B. Saltzman, S. Berg, and E. J. Holupka, “A comparison of the precision of seeds deposited as loose seeds versus suture embedded seeds: A randomized trial,” *Brachytherapy*, vol. 3, no. 1, pp. 7–9, 2004.
- [7] G. S. Merrick, W. M. Butler, A. T. Dorsey, J. H. Lief, and M. L. Benson, “Seed fixity in the prostate/periprostatic region following brachytherapy,” *Int. J. Radiat. Oncol. Biol. Phys.*, vol. 46, no. 1, pp. 215–220, Jan. 2000.
- [8] L. Archambault, L. Beaulieu, and D. Tubic, “Automatic post-implant needle reconstruction algorithm to characterize and improve implant robustness analyses,” *Med. Phys.*, vol. 30, no. 11, pp. 2897–2903, 2003.
- [9] N. Chng, I. Spadinger, W. Morris, N. Usmani, and S. Salcudean, “Prostate brachytherapy postimplant dosimetry: Automatic plan reconstruction of stranded implants,” *Med. Phys.*, vol. 38, no. 1, pp. 327–342, Jan. 2011.
- [10] M. Pinkawa, B. Gagel, B. Asadpour, M. Piroth, J. Klotz, H. Borchers, G. Jakse, and M. Eble, “Seed displacements after permanent brachytherapy for prostate cancer in dependence on the prostate level,” *Strahlentherapie und Onkologie*, vol. 184, no. 10, pp. 520–525, Oct. 2008.
- [11] M. Pinkawa, B. Asadpour, M. D. Piroth, B. Gagel, J. Klotz, K. Fishedick, H. Borchers, G. Jakse, and M. J. Eble, “Rectal dosimetry following prostate brachytherapy with stranded seeds – Comparison of transrectal ultrasound intra-operative planning (day 0) and computed tomography-postplanning (day 1 vs. day 30) with special focus on sources placed close to the rectal wall,” *Radiotherapy Oncol.*, vol. 91, no. 2, pp. 207–212, May 2009.
- [12] N. Usmani, N. Chng, I. Spadinger, and W. J. Morris, “Lack of significant intraprostatic migration of stranded iodine-125 sources in prostate brachytherapy implants,” *Brachytherapy*, 2010, to be published.
- [13] M. Moradi, S. S. Mahdavi, S. Deshmukh, J. Lobo, E. Dehghan, G. Fichtinger, W. J. Morris, and S. E. Salcudean, “Towards intra-operative prostate brachytherapy dosimetry based on partial seed localization in ultrasound and registration to C-arm fluoroscopy,” in *Proc. Medical Image Computing and Computer Assisted Interventions*, 2011, vol. 6891, LNCS, pp. 291–298.

- [14] P. J. Besl and N. D. McKay, "A method for registration of 3-D shapes," *IEEE Trans. Pattern Anal. Mach. Intell.*, vol. 14, no. 2, pp. 239–256, Feb. 1992.
- [15] H. M. Fagundes, R. J. Keys, M. F. Wojcik, M. A. Radden, C. G. Bertelsman, and W. A. Cavanagh, "Transperineal trus-guided prostate brachytherapy using loose seeds versus rapidstrand: A dosimetric analysis," *Brachytherapy*, vol. 3, no. 3, pp. 136–140, 2004.
- [16] D. R. Reed, K. E. Wallner, G. S. Merrick, S. Arthurs, A. Mueller, W. Cavanagh, W. B. Butler, E. Ford, and S. G. Sutlief, "A prospective randomized comparison of stranded vs. loose 125I seeds for prostate brachytherapy," *Brachytherapy*, vol. 6, no. 2, pp. 129–134, Apr. 2007.
- [17] C. Herbert, W. J. Morris, J. Hamm, V. Lapointe, M. McKenzie, T. Pickles, I. Spadinger, and M. Keyes, "The effect of loose vs. stranded seeds on biochemical no evidence of disease in patients with carcinoma of the prostate treated with iodine-125 brachytherapy," *Brachytherapy*, vol. 10, no. 6, pp. 442–448, Nov. 2011.
- [18] J. R. Lobo, M. Moradi, N. Chng, E. Dehghan, G. Fichtinger, W. J. Morris, G. Fichtinger, and S. E. Salcudean, "Quantifying stranded implant displacement following prostate brachytherapy," in *In Proc. Medical Image Computing and Computer Assisted Interventions*, 2011, vol. 6891, pp. 307–314.
- [19] E. Dehghan, A. Jain, M. Moradi, X. Wen, W. J. Morris, and S. Salcudean, "Brachytherapy seed reconstruction with joint-encoded C-arm single-axis rotation and motion compensation," *Med. Image Anal.*, vol. 15, no. 5, pp. 760–771, Oct. 2011a.
- [20] A. Jain, Y. Zhou, T. Mustufa, E. Burdette, G. Chirikjian, and G. Fichtinger, "Matching and reconstruction of brachytherapy seeds using the hungarian algorithm (MARSHAL)," in *SPIE Med. Imag.*, J. Robert, L. Galloway, and K. Cleary, Eds. Bellingham, WA: SPIE, 2005, vol. 5744, pp. 810–821.
- [21] M. A. Fischler and R. C. Bolles, "Random sample consensus: A paradigm for model fitting with application to image analysis and automated cartography," *Commun. ACM*, vol. 24, no. 6, pp. 381–395, Jun. 1981.
- [22] M. G. Kay and A. N. Parlikad, "Material flow analysis of public logistics networks," *Progress Material Handling Res.*, pp. 205–218, 2002.
- [23] G. Wan, Z. Wei, L. Gardi, D. B. Downey, and A. Fenster, "Brachytherapy needle deflection evaluation and correction," *Med. Phys.*, vol. 32, no. 4, pp. 902–909, 2005.
- [24] V. Lagerburg, M. A. Moerland, J. J. Lagendijk, and J. J. Battermann, "Measurement of prostate rotation during insertion of needles for brachytherapy," *Radiotherapy Oncol.*, vol. 77, no. 3, pp. 318–323, Dec. 2005.
- [25] Y. Su, B. J. Davis, K. M. Furutani, M. G. Herman, and R. A. Robb, "Dosimetry accuracy as a function of seed localization uncertainty in permanent prostate brachytherapy: Increased seed number correlates with less variability in prostate dosimetry," *Phys. Med. Biol.*, vol. 52, no. 11, p. 3105, Jun. 2007.



This article appeared in a journal published by Elsevier. The attached copy is furnished to the author for internal non-commercial research and education use, including for instruction at the authors institution and sharing with colleagues.

Other uses, including reproduction and distribution, or selling or licensing copies, or posting to personal, institutional or third party websites are prohibited.

In most cases authors are permitted to post their version of the article (e.g. in Word or Tex form) to their personal website or institutional repository. Authors requiring further information regarding Elsevier's archiving and manuscript policies are encouraged to visit:

<http://www.elsevier.com/copyright>



Brachytherapy seed reconstruction with joint-encoded C-arm single-axis rotation and motion compensation

Ehsan Dehghan^a, Ameet K. Jain^b, Mehdi Moradi^c, Xu Wen^c, W. James Morris^d, Septimiu E. Salcudean^c, Gabor Fichtinger^{a,*}

^a School of Computing, Queen's University, Kingston, ON, Canada

^b Philips Research North America, Briarcliff, NY, USA

^c Electrical and Computer Engineering Department, The University of British Columbia, Vancouver, BC, Canada

^d Vancouver Cancer Centre, British Columbia Cancer Agency, Vancouver, BC, Canada

ARTICLE INFO

Article history:

Available online 7 June 2011

Keywords:

Brachytherapy
Prostate cancer
Seed reconstruction
C-arm
Motion compensation

ABSTRACT

C-arm fluoroscopy images are frequently used for qualitative assessment of prostate brachytherapy. Three-dimensional seed reconstruction from C-arm images is necessary for intraoperative dosimetry and quantitative assessment. Seed reconstruction requires accurately known C-arm poses. We propose to measure the C-arm rotation angles and computationally compensate for inevitable C-arm motion to compute the pose. We compensate the translational motions of a C-arm, such as oscillation, sagging and wheel motion using a three-level optimization algorithm and obviate the need for full pose tracking using external trackers or fiducials. We validated our approach on simulated and 100 clinical data sets from 10 patients and gained on average, a seed matching rate of 98.5%, projection error of 0.33 mm (STD = 0.21 mm) and computation time of 19.8 s per patient, which must be considered as clinically excellent results. We also show that without motion compensation the reconstruction is likely to fail.

© 2011 Elsevier B.V. All rights reserved.

1. Introduction

Prostate cancer continues to be the leading cancer among men in the United States with an estimated occurrence of 217,730 new cases in 2010 (Jemal et al., 2010). Low dose rate brachytherapy (henceforth, brachytherapy) is an effective treatment for localized prostate cancer that can achieve excellent outcomes (Blasko et al., 2002; Morris et al., 2009a,b). Brachytherapy entails permanent placement of radioactive capsules (seeds) of ¹²⁵I or ¹⁰³Pd inside the prostate and periprostatic tissue to kill the cancer with radiation. Brachytherapy seeds are as small as a grain of rice, approximately 4.5 mm long and 0.8 mm in diameter. The success of the procedure directly depends on the accuracy of seed placement to deliver sufficient dose to eradicate the cancer while sparing the urethra and rectum. The seed positions are preplanned to tailor the dose to the patient's anatomy. Generally 40–130 seeds are implanted depending on the type of the seeds and the volume of the prostate. During the procedure, the physician delivers the seeds

using needles that pass through a guiding template, under real-time visual guidance from transrectal ultrasound (TRUS) (Prestidge et al., 1998). The guiding template confines the needles to move in parallel to the long axis of the probe. C-arm fluoroscopy images are frequently taken during the procedure to qualitatively assess the implant (see Fig. 1).

Accurate execution of the plan is extremely difficult due to prostate displacement and deformation (Lagerburg et al., 2005), needle bending, prostate swelling (Yamada et al., 2003) and, system calibration and human errors. As a result, seed misplacements are still common and may lead to under-dosed regions that necessitate repeated treatment, or over-dosed regions which result in complications, such as rectal ulceration, urinary incontinence and sexual dysfunction. Intraoperative dosimetry and planning methods were introduced to reduce the errors and increase the treatment quality (Nag et al., 2001; Orio et al., 2007; Polo et al., 2010). These methods intermittently calculate the delivered dose during the procedure and modify the insertion plan, in real-time, to compensate for possible errors.

In order to calculate the dose distribution, the position of the implanted seeds, registered to the prostate anatomy, should be known. Ultrasound imaging provides sufficient soft tissue contrast to delineate the prostate; however, despite the efforts (Han et al., 2003; Holmes and Robb, 2004; Feleppa et al., 2002; McAleavey et al., 2003; Mitri et al., 2004; Ding et al., 2006; Wei et al., 2006; Wen et al., 2010), robust seed segmentation in ultrasound is not

* Corresponding author. Address: School of Computing, Queen's University, 557 Goodwin Hall, Kingston, ON, Canada K7L 3N6. Tel.: +1 613 533 3258; fax: +1 613 533 6513.

E-mail addresses: ehsands@cs.queensu.ca (E. Dehghan), ameet.jain@philips.com (A.K. Jain), moradi@ece.ubc.ca (M. Moradi), wenx@ece.ubc.ca (X. Wen), jmorris@bc-cancer.bc.ca (W. James Morris), tims@ece.ubc.ca (S.E. Salcudean), gabor@cs.queensu.ca (G. Fichtinger).

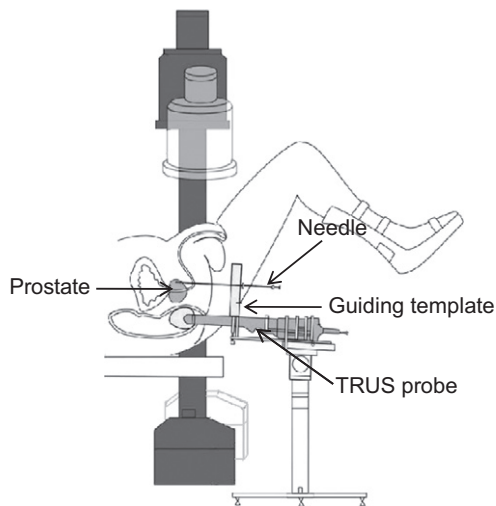


Fig. 1. Brachytherapy procedure. The needle passes through the guiding template in parallel to the long axis of the transrectal probe. The C-arm rotates around the craniocaudal axis of the patient to acquire images. This figure is reproduced from Lee et al. (2009) with permission from the authors.

yet possible (up to 25% of seeds can be hidden even after careful manual segmentation in B-mode images (Han et al., 2003)). X-ray fluoroscopy images provide excellent seed visualization. However, fluoroscopy images do not provide sufficient soft tissue contrast to segment the prostate boundaries. Fluoroscopy-ultrasound fusion can provide a solution for real-time intraoperative dosimetry and has been extensively studied (French et al., 2005; Su et al., 2006; Orio et al., 2007; Tutar et al., 2008; Fallavollita et al., 2010). In this scenario, during and/or immediately after the brachytherapy procedure, several C-arm images are taken from different angles and segmented for seed centroids. Then, the seeds are localized in 3D space using the segmented images. By registration of these seeds to the prostate anatomy localized in ultrasound, the delivered dose to the prostate can be calculated. Upon observation of large seed misplacements or cold spots, the physician can modify the plan and implant new seeds. Reconstruction accuracy and speed are vital for intraoperative dosimetry using fluoroscopy-ultrasound fusion.

Three-dimensional seed reconstruction has been widely investigated in the literature (Amols and Rosen, 1981; Tubic et al., 2001a; Todor et al., 2002; Tutar et al., 2003; Su et al., 2004; Narayanan et al., 2004; Lam et al., 2004; Jain et al., 2005b; Kon et al., 2006; Brunet-Benkhoucha et al., 2009; Lee et al., 2009; Lee et al., 2011). In order to successfully reconstruct the seed positions in 3D, three major problems must be solved.

- (1) *C-arm calibration*: For an accurate reconstruction, C-arm intrinsic parameters, such as image resolution, image center, source to center distance and focal length should be known (Navab et al., 1996; Brack et al., 1996; Jain et al., 2005a).
- (2) *Seed matching*: After segmentation of the 2D coordinates of seed projections in the C-arm images, a seed matching problem should be solved to assign each seed projection in one image to the corresponding seed projections in the other images (see Fig. 2 for an example). Since the seed matching is not known, seed reconstruction using two C-arm images leads to an ambiguity that can be resolved using a third image. Therefore, at least three images are required for seed localization in 3D space. Seed matching has been solved using various methods, such as simulated annealing (Tubic et al., 2001a), heuristic rules (Todor et al., 2002) and the Hungarian algorithm (Jain et al., 2005b). Hidden or overlap-

ping seed projections are common in projection images and result in incomplete data sets that further complicate the seed matching problem (see Fig. 2). The hidden seed problem has been tackled using different approaches, such as pseudo-seed-matching (Narayanan et al., 2004), adaptive grouping (Su et al., 2004), Hough trajectories (Lam et al., 2004), an extension to the Hungarian algorithm using network flow (Kon et al., 2006) and dimensionality reduced linear programming (Lee et al., 2011). It should be noted that tomosynthesis-based reconstruction methods have been proposed that solve the matching problem automatically (Tutar et al., 2003; Brunet-Benkhoucha et al., 2009; Lee et al., 2009). However, these methods generally need a larger number of images.

Jain et al. showed that seed matching is equivalent to a network flow problem which is NP-Hard (Jain et al., 2005b). However, they proposed a pseudo-polynomial yet practical solution for seed matching from three images by mapping the original tripartite problem into three bipartite ones that could be solved using the Hungarian algorithm. Jain's method was abbreviated as MARSHAL (Jain et al., 2005b). The original MARSHAL assumed complete data sets; however, it was later extended to address the hidden seed problem (Kon et al., 2006) (the extended method was abbreviated as XMARSHAL). This algorithm demonstrated clinically acceptable reconstruction rates and time performance on simulated and phantom data, and has been clinically tested (Song et al., 2011; Jain et al., in press). We will discuss XMARSHAL in more details in Section 2.1 as it runs in the core of our algorithm.

- (3) *Pose recovery*: Seed matching and reconstruction are performed using known C-arm poses that provide the relative positions of the C-arm images in 3D space. The C-arm pose is generally recovered using radio-opaque fiducials or beads (Navab et al., 1996; Brack et al., 1996; Zhang et al., 2004; Jain et al., 2005a), or obtained from electromagnetic and optical trackers (Peters and Cleary, 2008). Fiducials may interfere with the image of the anatomy, require segmentation and can limit the working volume. Auxiliary trackers are expensive, need calibration, optical trackers require line of sight, electromagnetic trackers are sensitive to interference and hence, further complicate the intervention. It has been suggested to use the implanted seeds as fiducials to compensate for C-arm pose computation errors (Tubic et al., 2001a; Jain and Fichtinger, 2006; Lee et al., 2009). However, a good initial measurement of the pose is required and is usually obtained by using fiducials and trackers. Pose recovery without a fiducial or tracker can significantly ease the reconstruction process and consequently facilitate the transition of seed reconstruction algorithms from research laboratories to medical practice. In this work, we introduce a method to estimate the pose using sole measurement of rotation angles and computationally compensate for the pose computation errors without fiducials or external trackers.

It is common practice in brachytherapy to acquire several images by rotating the C-arm around the patient. Usually, the rotation axis is approximately aligned with the patient's craniocaudal axis. In ideal cases, joint angle measurements can yield an accurate pose of the C-arm. However, C-arm movements, such as oscillation, sagging and wheel motion are significant and prevent accurate pose recovery based solely on joint angle measurements (see Fig. 3). If uncompensated, these C-arm motions can lead to severe pose computation errors and reconstruction failure.

In this paper, we prove that in the typical case of a C-arm rotated around a single axis within a small angle span, C-arm angle

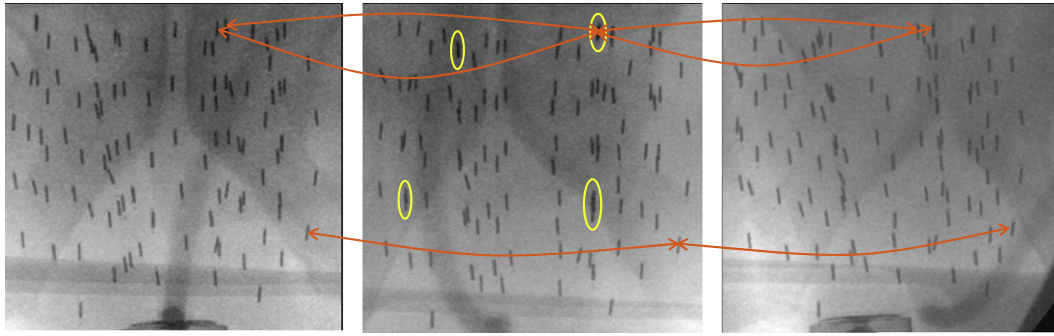


Fig. 2. Three C-arm images taken at different angles. The figure at the middle shows several hidden and overlapping seeds. Three seed matchings are shown using arrows. The seeds move along an almost horizontal line through the images.

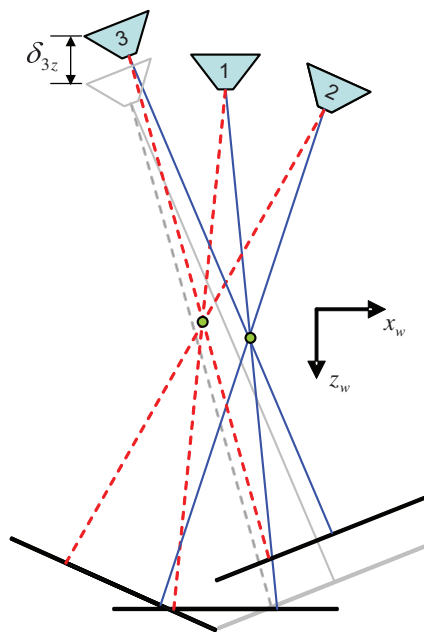


Fig. 3. Initial (gray) and correct C-arm pose (color) for the third C-arm. Translational error along the up-down direction is only added to C-arm 3. The reconstructed seeds are shown after motion compensation. (For interpretation of the references to color in this figure legend, the reader is referred to the web version of this article.)

measurements augmented with a computational method to compensate for C-arm motions suffice for a clinically reliable and accurate seed reconstruction. However, without such a motion compensation algorithm, the reconstruction is prone to failure. We employ joint encoders or digital protractors to measure the rotation angles. The novelty of this work is in the introduction of an effective motion compensation method that obviates the need for full pose tracking using external fiducials or trackers. Considering the simplicity of the implementation, high reconstruction accuracy and favorable computational speed, this algorithm is suitable for clinical translation. The underlying idea and limited preliminary data was presented at a recent conference (Dehghan et al., 2010). This manuscript provides a more detailed description of the methodology and performance analysis on 100 clinical data sets.

This paper is organized as follows. The algorithms for seed matching and motion compensation are explained in Section 2. Numerical simulation, phantom and clinical results are presented in Section 3, followed by discussion in Section 4. The conclusions are drawn and the future work is outlined in Section 5.

2. Methods

We propose an iterative three-level algorithm that takes advantage of the constrained movement of a C-arm during coplanar imaging, compensates for its major translational motions using reconstructed seeds and, in turn, significantly increases the likelihood of finding the correct matching solution in a clinically acceptable time. We compensate for C-arm motions that are mostly translational. That is an approximation of the C-arm motion pattern. However, as our results prove, it is sufficient for successful reconstructions. Our motion compensation algorithm can be used with any seed matching algorithm. For seed matching and reconstruction, we employ XMARSHAL (Kon et al., 2006) that is capable of solving the matching problem in the presence of hidden seeds with low computational cost. For the sake of completeness we briefly outline this method in Section 2.1. As mentioned, tomosynthesis-based reconstruction methods do not require a matching algorithm. However, they suffer from lack of accurate C-arm pose too. Therefore, C-arm motion compensation framework applies to them as well.

2.1. Seed reconstruction using XMARSHAL

Assume that three C-arm images of an implant with N seeds are available and N_i , $i \in \{1, 2, 3\}$ seed projections are segmented in each image. In this case, the seed matching problem in the presence of hidden seeds can be written as the following optimization problem:

$$m_{ijk}^* = \arg \min_{m_{ijk}} \sum_{i=1}^{N_1} \sum_{j=1}^{N_2} \sum_{k=1}^{N_3} c_{ijk} m_{ijk}, \quad (1)$$

$$\text{s.t.} \quad \begin{cases} \sum_{j=1}^{N_2} \sum_{k=1}^{N_3} m_{ijk} \geq 1, & \forall i \\ \sum_{i=1}^{N_1} \sum_{k=1}^{N_3} m_{ijk} \geq 1, & \forall j \\ \sum_{i=1}^{N_1} \sum_{j=1}^{N_2} m_{ijk} \geq 1, & \forall k \\ \sum_{i=1}^{N_1} \sum_{j=1}^{N_2} \sum_{k=1}^{N_3} m_{ijk} = N, \\ m_{ijk} \in \{0, 1\}, \end{cases}$$

where for each $i \in \{1, \dots, N_1\}$, $j \in \{1, \dots, N_2\}$ and $k \in \{1, \dots, N_3\}$, c_{ijk} is the cost of matching seed projections p_i^1 , p_j^2 and p_k^3 from the first, second and third images, respectively, and m_{ijk} is a binary variable showing the correctness of such a match. The constraints in (1) ensure reconstruction of N seeds while taking the hidden seeds into account.

Assume three rays emanating from each of these seed projections p_i^1 , p_j^2 and p_k^3 to its corresponding X-ray source in 3D space. The point with the minimum average distance from these lines is considered as their symbolic intersection. We define the average distance of the symbolic intersection from these lines as their symbolic distance. If we project the symbolic intersection on each image, the summation of the distances between this projection and the corresponding seed projection on each image is considered as the matching cost (c_{ijk}) (Jain et al., 2005b).

Eq. (1) is a weighted-tripartite matching problem that is equivalent to an NP-Hard combinatorial optimization (Jain et al., 2005b) with an exponential complexity. An approximate low computational cost solution to this problem was proposed by Jain et al. by projecting the tripartite matching problem into three bipartite problems (Jain et al., 2005b). In this solution, seed projections p_i^1 and p_j^2 can be matched (with a cost c_{ij}) only if they have a low cost counterpart in the third image. In this method:

$$c_{ij} = \min_k c_{ijk}, \forall k. \quad (2)$$

This is based on the observation that although low c_{ij} , c_{jk} and c_{ki} do not guarantee a low c_{ijk} , a low c_{ijk} guarantees c_{ij} , c_{jk} and c_{ki} to be low.

This solution resembles a network-flow optimization problem in which each seed projection in an image is represented by a node (Jain et al., 2005b; Kon et al., 2006). The matching between two seed projections is represented by a link that flows between them with a cost equal to the matching cost c_{ij} . This network flow problem was extended in Kon et al. (2006) to address the hidden seeds problem. This problem can be solved using a cycle canceling algorithm in practically $O(N^3)$ times (Kon et al., 2006), producing clinically excellent matching.

Given the correct matching and the C-arm poses, the 3D position of the seeds with minimized reconstruction cost is calculated as:

$$s_i = \left[\sum_{j=1}^3 (I - v_{ij}v_{ij}') \right]^{-1} \sum_{j=1}^3 (I - v_{ij}v_{ij}') q_j, \quad (3)$$

$i \in \{1, \dots, N\},$

where s_i is the position of the i th seed, q_j is the position of the X-ray source corresponding to the j th image, v_{ij} is the unit vector along the lines L_{ij} that connect the projection of seed i on image j to q_j and I is a 3×3 identity matrix. The reconstruction cost for seed i is defined as the symbolic distance between lines L_{i1} , L_{i2} and L_{i3} .

2.2. Motion compensation

Let us assume a world coordinate system $Ox_wy_wz_w$ centered at the center of rotation of the C-arm and a source coordinate system Ox_sy_s centered at the X-ray source as shown in Fig. 4. The pose of the C-arm is defined by a transformation matrix sT_w from the world to the source coordinate system as:

$${}^sT_w = \begin{bmatrix} {}^sR_w & -{}^sR_w\delta + \begin{bmatrix} 0 \\ 0 \\ l \end{bmatrix} \\ \mathbf{0}' & 1 \end{bmatrix}, \quad (4)$$

where sR_w is the rotation matrix from the world to the source coordinate frame, l is the distance from the source to the center of rotation and $\delta = [\delta_x \ \delta_y \ \delta_z]'$ is the translational motion of the C-arm caused by oscillation, sagging and wheel motion (see Fig. 3). We can initialize a pose computation by measuring the C-arm rotation angles – which define sR_w – and setting the unknown δ equal to zero. Assuming $\delta = \mathbf{0}$ causes error in the pose computation and sub-

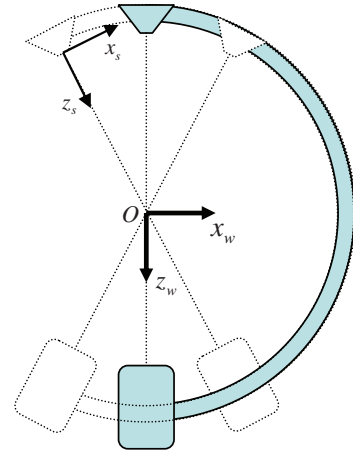


Fig. 4. A C-arm rotating around its primary axis (PA) in a single plane. The angle around the secondary axis (SA) is fixed. The world coordinate system $Ox_wy_wz_w$ is centered at the center of rotation. The source coordinate system Ox_sy_s is centered at the source.

sequent unsuccessful seed reconstruction. Therefore, we should compensate for this error and improve our pose computation.

An iterative scheme can be implemented where the reconstructed seeds with given C-arm poses are used to improve the pose recovery and subsequently enhance the seed reconstruction results. Such iterative schemes were suggested in the literature to compensate for the rotational and translational pose errors (6 DOFs) (Tubic et al., 2001a; Jain and Fichtinger, 2006). It is known that such a problem can be solved up to an unknown scale (Jain and Fichtinger, 2006). This means that the reconstructed seed cloud can arbitrarily shrink or expand. As it is shown in Fig. 5, the X-ray images, C-arm intrinsic parameters, seed matching and relative C-arm rotations are identical between two sets of reconstruction solutions; however, the scaled relative translations result in a scaled seed cloud.

We demonstrate that by making realistic and practical assumptions in accordance with clinical protocols, motion compensation can be reduced to 2 DOFs for mobile C-arms used in brachytherapy. This approach eliminates the scaling problem and results in a clinically adequate implant reconstruction and computational time small enough to be carried out intraoperatively. Pose error com-

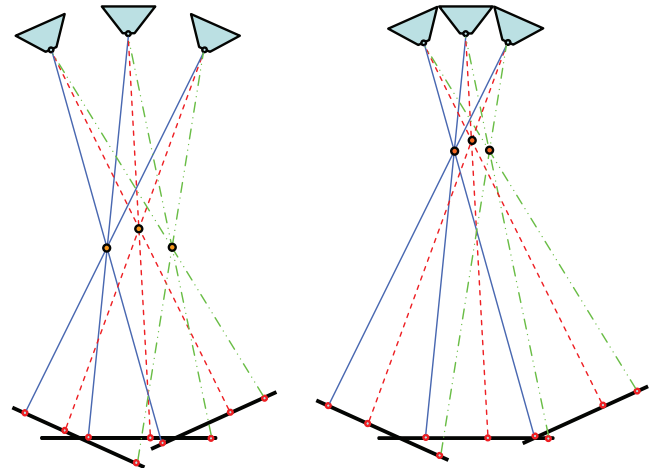


Fig. 5. The scaling effect results from 3 DOF translational motion of the C-arm. The X-ray images, C-arm relative rotations and C-arm intrinsic parameters are identical between the left and right reconstructions. Seed matching solution is independent of the scaling factor.

pensation for 2 DOFs requires less complicated algorithms (compare to 6 DOFs) and thus is computationally faster.

We make the following assumptions:

1. The C-arm images are acquired by rotation of a C-arm around its primary axis (PA) in a small angle span, while the angle around the secondary axis (SA) is fixed (see Fig. 4).
2. C-arm rotation angles are measured.
3. The intrinsic parameters are known and do not change during rotation of the C-arm.
4. 2D coordinates of seed projections are available via manual or automatic segmentation.
5. Most significant C-arm motions are of translational nature, confined to the Oy_wz_w plane – the motion along x_w is negligible ($\delta_{ix} = 0, i \in \{1, 2, 3\}$).

As mentioned before, acquiring images by rotating the C-arm around its PA while the angle around SA is fixed is common practice in brachytherapy. The rotation span around PA is usually limited to approximately $\pm 15^\circ$ due to collision of the C-arm with the operating table, brachytherapy stand or patient's legs. Mobile C-arms are available that employ a fixed axis of rotation and are equipped or can be easily retrofitted with joint encoders (Grzeda and Fichtinger, 2010).

Limited rotation span in a clinical setting results in an insignificant change in the calibration parameters, such as focal length, image center and source to center distance. Image resolution is considered as constant over the lifetime of the device. It has been shown that in such situations recalibration for each C-arm pose is not necessary, because small changes in the calibration parameters do not significantly alter the relative positions of the reconstructed seeds (Jain et al., 2007). It should be noted that we are interested in the relative position of the seeds as the seed cloud as a whole should later be registered to the prostate anatomy.

In this work we relied on manual segmentation to identify the seed centroids. Since XMARSHAL is capable of addressing the hidden seeds problem, it is not required to identify all the implanted but hidden seeds in every image. The effects of hidden seed percentage and seed segmentation error on the performance of XMARSHAL are discussed in Kon et al. (2006).

The last assumption is the cornerstone of our motion compensation algorithm. The most likely source of pose computation error is the oscillation of the C-arm, which is mostly up-down (along the z_w axis) since the C-arm is connected to the base as a cantilever. Our observations confirm this assumption that the C-arm primary motion is in the up-down direction due to oscillation and C-arm weight. The motion in the other two directions are much smaller; however, are not always insignificant. As a result, C-arm pose computation error along z_w is more significant compared to the inaccuracies in the other two directions.

The proposed motion compensation algorithm initializes the C-arm pose using measured joint angles as shown in Fig. 3 and compensates for the inevitable translational motions by finding the optimal translational adjustments (offsets) δ for each source position, by solving the following problem:

$$(m_{ijk}^*, \delta_n^*) = \arg \min_{x_{ijk}, \delta_n} \sum_{i=1}^{N_1} \sum_{j=1}^{N_2} \sum_{k=1}^{N_3} c_{ijk}(\delta_n) m_{ijk}, \quad (5)$$

$$n \in \{1, 2, 3\},$$

subject to the constraints of (1). In order to minimize the scaling effects, we restrict the offsets to be in the Oy_wz_w plane – based on our assumption – and introduce a three-level optimization method to identify them.

2.2.1. First-level optimization

At the first level, the algorithm finds a few matching seed projections in the images to calculate an initial offset estimate with very low computational cost. Since the fluoroscopy images are taken with the rotation of the C-arm around its PA, the seed projections follow almost horizontal lines in the images. Therefore, a seed at the top or bottom of one image is more likely located at the top or bottom of the other images (for example see Fig. 2). Based on this observation, the algorithm automatically selects n seed projections from the top (seeds with maximum ordinate values in the 2D image coordinate system) and n seed projections from the bottom of each image (seeds with minimum ordinate values in the 2D image coordinate system) and solves the matching problem for them, using the initial estimates of the C-arm poses from joint angle readings. Since the selected $2n$ seed projections from one image do not necessarily correspond to the selected $2n$ seed projections in the other images (these $6n$ seed projections may belong to more than $2n$ seeds in 3D), some of the reconstructed seeds have a high reconstruction cost, are erroneously matched, and cannot be used to improve the pose recovery. Therefore, the algorithm selects a subset of $p < n$ reconstructed seeds from the top and p reconstructed seeds from the bottom of the $2n$ reconstructed seeds with the best reconstruction costs for pose recovery. We use $n = 5$ and $p = 2$. In order to estimate the C-arm motion, we assume that the position of the C-arm source corresponding to the first image (henceforth, the first source position) in 3D space is fixed ($\delta_1 = \mathbf{0}$) and optimize the position of the C-arm sources corresponding to the second and third images (henceforth, the second and third source positions) in the Oy_wz_w plane to minimize the reconstruction cost for the selected $2p$ seeds. The seed matching and motion estimation are iteratively performed until there is no change in the seed matching solution.

Since a small number of seed projections are used at this level, the matching problem can be solved extremely quickly using XMARSHAL. With a given matching, 2D offsets for the second and third C-arm source positions can be found by solving a set of linear equations. These equations are derived in (A.6)–(A.15).

2.2.2. Second-level optimization

In this step, the C-arm source positions are initialized in 3D space using the optimal offset values from the first level. Then, the matching problem is solved for all seed projections and the seeds are reconstructed. The C-arm source positions are optimized in 3D space to minimize the average reconstruction cost while the seeds are fixed in space. The matching and source position optimizations are iteratively solved until the reconstruction cost or its change between two iterations is smaller than a predefined threshold. The thresholds were empirically assigned as < 0.1 mm for the former and $< 0.1\%$ for the latter.

The new position of the j th X-ray source at iteration $k + 1$ is calculated as:

$$q_j^{k+1} = \left[\sum_{i=1}^N (I - v_{ij} v_{ij}') \right]^{-1} \sum_{i=1}^N (I - v_{ij} v_{ij}') s_i^k, \quad (6)$$

where s_i^k is the position of the i th seed at iteration k .

Since we employ a 3D optimization at this level, the reconstructed seed cloud may significantly shrink or expand (see Fig. 5). However, optimization in 3D increases the likelihood of finding the correct matching which is independent of the scaling factor. Therefore, we take advantage of 3D optimization at this level, find the correct matching and remove the scaling effects at the next level.

2.2.3. Third-level optimization

At this step, we assume that the correct matching solution is available from the second-level optimization. However, the seed cloud may be scaled due to 3D motion compensation. Therefore, once more, we assume that the C-arm motion along x_w is negligible and optimize for 2D C-arm motion. The C-arm source positions are initialized using the joint angle readings. The first source is fixed in space. Next, 2D offsets of the second and third source positions are optimized to minimize the reconstruction cost with the given matching. Similar to the first level, the 3D seed positions and 2D offsets for the sources have a closed form solution, the equations for which are derived in (A.6)–(A.15). The three steps of the algorithm are shown in Fig. 6.

3. Results

3.1. Simulations

First, the motion compensation algorithm was tested on simulated data. We synthesized four seed clouds based on realistic dosimetry plans of four patients with 100, 102, 108 and 130 seeds. Seed images were synthesized by rotation of the C-arm around the PA at 0° , $\pm 5^\circ$ and $\pm 10^\circ$, while the SA angles were kept constant at 180° . The intrinsic parameters of a GE OEC® 9800 device were used as the intrinsic parameters of the C-arm in the simulations. The seeds were reconstructed using every possible combination of three images out of five. In order to investigate the performance of our motion compensation algorithm, translational and rotational pose errors were added to one of the C-arm source-image pairs. The added errors were 0–10 mm along x_w and y_w , 0–20 mm along z_w with steps of 1 mm and 0 – 3° around SA and PA with steps of 0.5° . The effects of these errors were simulated independently, as only one error was introduced at each simulation. During image synthesis, hidden seed projections were created by merging the seed projections that were close to each other. There were on average 1.6 hidden seeds per image, with a maximum of 14.

The reconstructed seeds were compared against the ground truth after a rigid registration of reconstructed seed cloud to the known seed cloud. The average and standard deviation (STD) of localization error, defined as the distance between the true and reconstructed seeds, are shown in Fig. 7 for all the introduced pose errors. The average and STD of the matching rate are also shown in Fig. 7. The algorithm has an average matching rate of 99.2% when the pose error is zero.

As it can be seen in Fig. 7c–f, the algorithm shows consistently high matching rates and small localization errors over a wide range of errors along y_w and z_w as the C-arm motions in these two directions are compensated. Fig. 7a shows consistently high matching rates for errors of up to approximately 5 mm along x_w . However, the localization error increases monotonically with the error in this direction as shown in Fig. 7b. This is due to the fact that the matching problem is solved at the second level, using a 3D motion compensation; while we reconstruct the seeds using a 2D motion compensation at the third level. Therefore, the correct matching is found at the second level even in the presence of errors along x_w ; however, the seed cloud is deformed at the third level, which leads to a monotonically increasing localization error. The matching and localization errors increase with the rotational pose errors, since the motion compensation algorithm does not compensate for rotational errors. However, the average matching rate is above 95% when rotational pose errors are less than 1.5° . We assume that in a clinical setting, the angles are measured with errors of less than $\pm 1^\circ$.

3.2. Phantom study

We conducted a phantom study on a CIRS Model 053 tissue-equivalent prostate brachytherapy training phantom. An experienced brachytherapist inserted 26 needles to implant 136 dummy stranded seeds inside the phantom.

We took five images from the phantom using a GE OEC® 9800 mobile C-arm by rotation of the device around its PA in a 20° rotation span in approximately 5° intervals. A digital protractor was

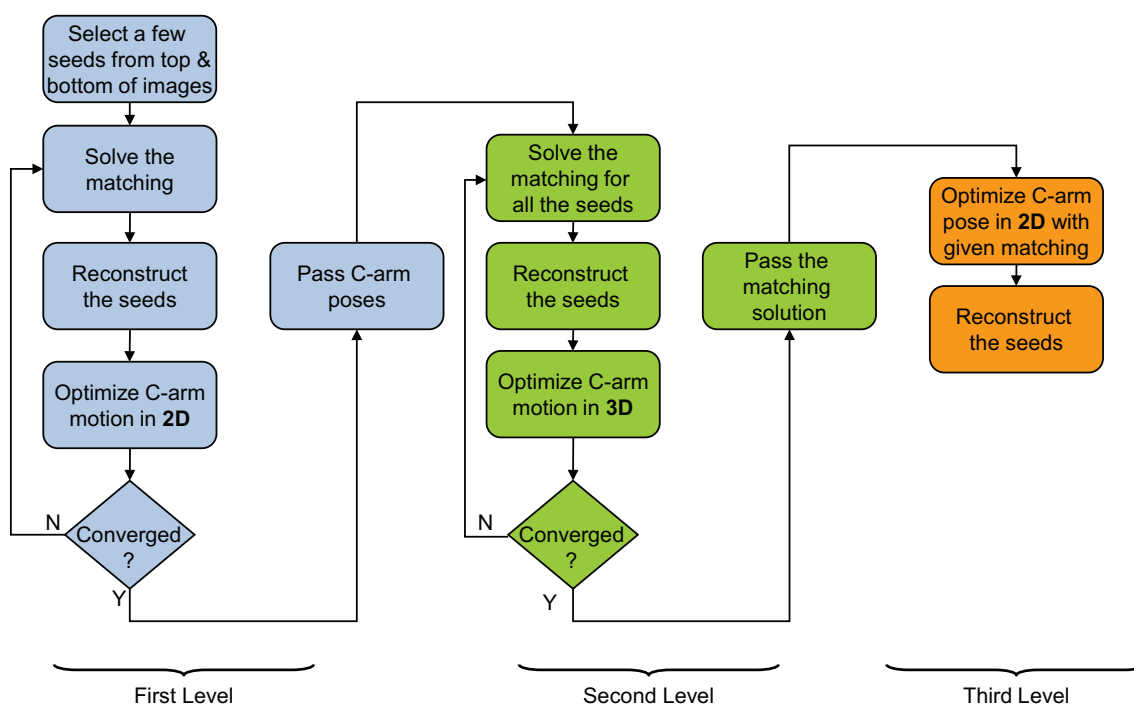


Fig. 6. The proposed three-level motion compensation algorithm.

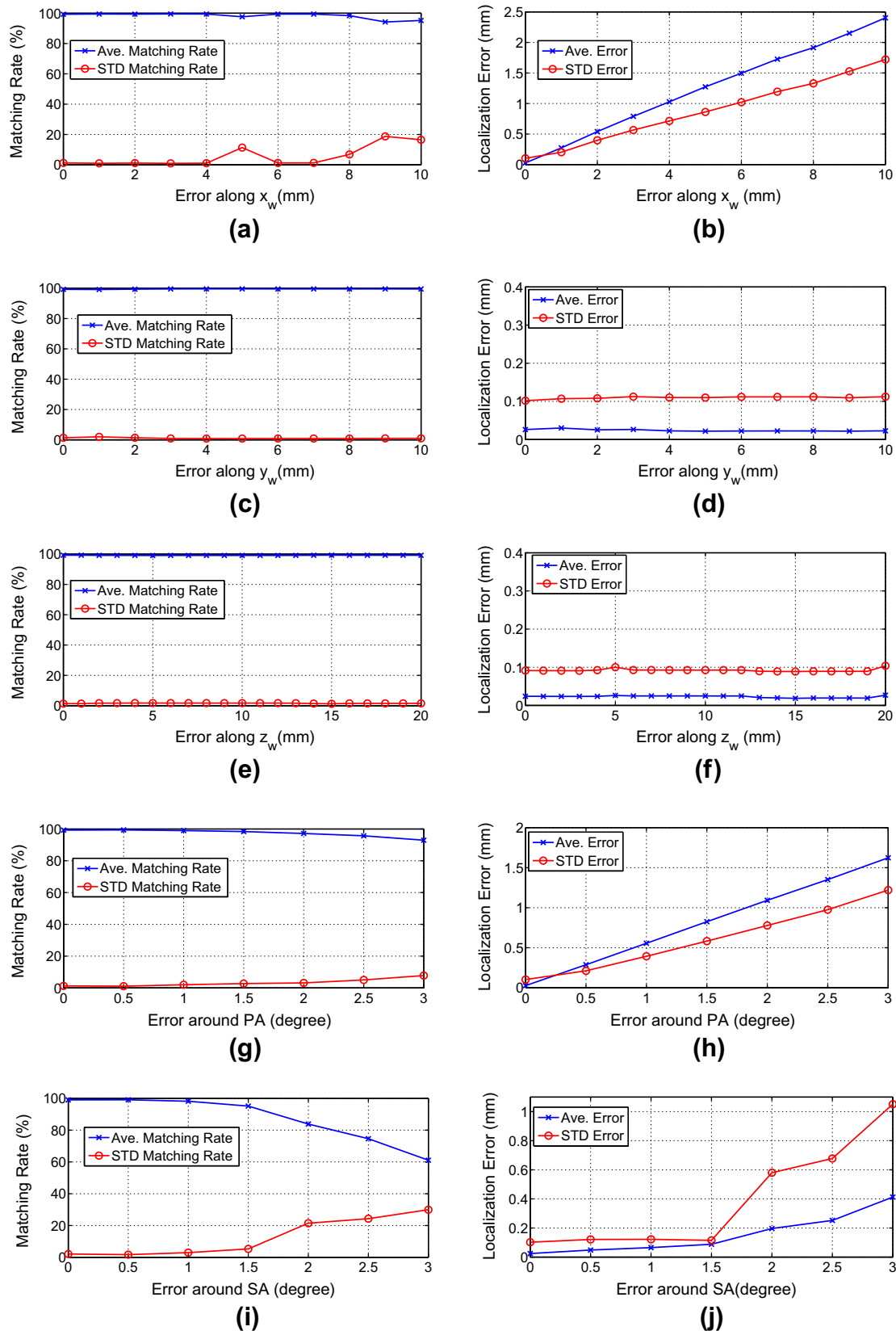


Fig. 7. Simulation results, showing the average and standard deviation of matching rate and localization error for variable pose errors. The average and STD of matching rate for errors along x_w , y_w , z_w , PA and SA are shown in (a), (c), (e), (g) and (i), respectively. The average and STD of localization error for errors along x_w , y_w , z_w , PA and SA are shown in (b), (d), (f), (h) and (j), respectively.

connected to the source casing of the device to accurately measure the rotation angles. The seed projections were manually segmented in the images and the seeds were reconstructed in 3D using every combination of 3 out of 5 images (10 reconstructions) using motion compensation.

The phantom was also scanned using a Picker PQ5000 CT scanner. The seeds in the CT volume were segmented by thresholding and assumed as the ground truth. Although the CT and C-arm images were taken at different times, we assumed that the phantom deformation and seed displacements were negligible. We compared the seeds reconstructed from C-arm images to the seeds from CT after a rigid registration of the two seed clouds and reported the difference as localization error in Table 1.

On average, we achieved a matching rate of 99.0% with 0.9 mm localization error. In order to show the importance of motion compensation, we also tried to reconstruct the seeds without motion compensation and achieved an average of 78.3% for matching rate, which is far below the clinically acceptable level. Su et al. suggested that a seed detection rate of above 95% is required in order to achieve clinically sufficient estimation of dose distribution for contemporary ^{125}I prostate implants (Su et al., 2005).

3.3. Performance on clinical data

The performance of the motion compensation algorithm was also tested on clinical data. Ten patients were implanted with 100–135 ^{125}I seeds (average 112) at the British Columbia Cancer Agency. Five C-arm images were taken from each patient by rotation of the C-arm around the patient's craniocaudal axis at angles approximately 0° , $\pm 5^\circ$ and $\pm 10^\circ$, while the SA angle was fixed. A GE OEC[®] 9800 mobile C-arm was used for imaging. This is a digital device with motorized joints. This device has a heavy intensifier that causes significant sagging and oscillation during image acquisition. For patients 1–8 the rotation angle around the PA was measured by a digital protractor which was attached to the source casing. The digital protractor did not interfere with the image of the anatomy or the working space and did not require precalibration. For the other 2 patients the rotation angles were measured using the joint encoders of the device. The digital protractor had a resolution of 0.1° while the device joint encoders had a resolution of 1° . We expect higher accuracy from the measurements of the protractor. The C-arm joint angle encoders showed a variation of 1° around the SA. This deviation was taken into account for initialization of the C-arm poses. The C-arm intrinsic parameters were once identified in a preoperative calibration and were assumed to be constant for all the rotation angles and all the patients. For each patient, we reconstructed the seeds for every combination of three images out of available five, thus obtaining 100 reconstructions in total. The seeds were manually segmented in the images. There were an average of 2 and maximum of 8 hidden seeds in the images.

Table 1
Matching rates and mean and standard deviation of localization error for phantom.

Rec. #	Matching rate (%)	Localization error mean \pm STD (mm)
1	100.0	1.0 ± 0.6
2	100.0	0.9 ± 0.5
3	100.0	0.7 ± 0.4
4	99.2	0.9 ± 0.6
5	98.5	0.8 ± 0.4
6	98.5	0.8 ± 0.5
7	98.5	1.0 ± 0.6
8	98.5	0.8 ± 0.7
9	99.2	0.8 ± 0.4
10	97.8	0.9 ± 0.5

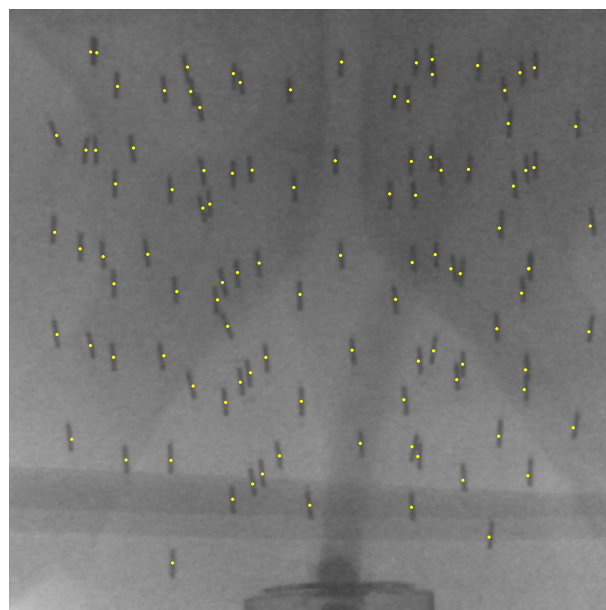


Fig. 8. Reprojected seeds overlaid on a C-arm fluoroscopy image, showing small projection errors.

The reconstructed seeds were reprojected on the images (see Fig. 8) and were meticulously inspected for matching errors. These images were also used to measure the projection error – defined as the distance between the segmented seed centroid and the projected location of the reconstructed seed – to quantify the reconstruction accuracy.

Fig. 9a shows the seed matching rate with motion compensation for each case. Overall, we achieved an average matching rate of 98.5% which is above the clinically accepted level. A perfect reconstruction was accomplished in 54% of the cases, while in 76% and 92% of the cases the matching rate was greater or equal to 98% and 95%, respectively.

In order to demonstrate the necessity of motion compensation, seed reconstruction was performed without motion compensation as well. As it can be seen in Fig. 9b, XMARSHAL without motion compensation achieved an average matching rate of 46.1%, which is a completely inadequate performance. Moreover, calculations show that motions of more than 30 mm in the up-down direction were compensated. This proves our hypothesis that it is necessary to use motion compensation, when only C-arm rotation angles are measured.

Fig. 9b directs us to another important role of the first-level optimization – other than increasing the speed. As it can be seen in Fig. 9b, an initial reconstruction without application of the first-level optimization can result in very unsuccessful matching results in which mismatched seeds are significantly abundant and can even outnumber the correctly matched seeds. In such cases, sole application of the second-level optimization can result in erroneous pose estimations since the large group of mismatched seeds can misguide the optimization algorithm. However, in the first-level optimization, the algorithm selects a handful of seeds from the top and bottom of the images that are very likely to correctly match. These few correctly matched seeds provide a good initial pose computation for the second level. Therefore, the first-level optimization not only shortens the computation time but also increases the robustness of the algorithm.

The mean and the standard deviation of the projection error are shown in Fig. 9c and d for correctly and erroneously matched seeds, respectively. The overall average and standard deviation of the projection error for correctly matched seeds are 0.33 mm and

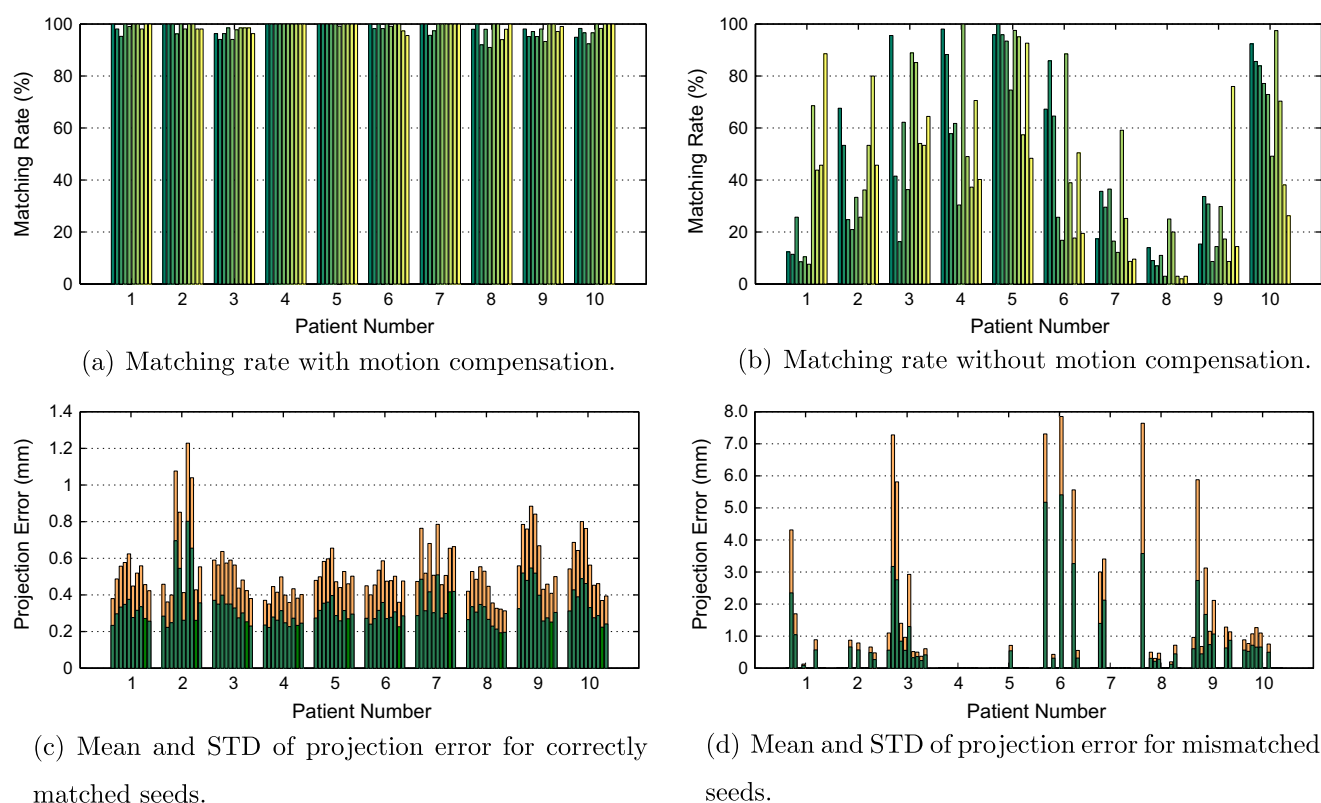


Fig. 9. Clinical results showing the matching rate (a) with and (b) without motion compensation, the mean and STD of the projection error for (c) correctly and (d) erroneously matched seeds. In (c) and (d), the length of the green bars shows the mean, and the length of the orange bars shows the STD.

0.21 mm, respectively, which demonstrates high reconstruction accuracy. The mean and standard deviation of projection errors are 1.12 mm and 1.93 mm, respectively, for mismatched seeds.

It should be noted that the projection error cannot be used to measure the scaling factor. Therefore, we use seed spacing to provide additional confidence in our reconstruction accuracy. The patients in our study were implanted using stranded ^{125}I seeds. In such a case, the seeds that are implanted by a common needle are connected to each other by a bio-degradable strand that keeps them at a fixed center-to-center distance of 10 mm. We measured the center-to-center distances of the seeds that were inserted using a common needle and reported the results for each patient in Table 2. The overall seed spacing was 10.3 mm, which shows that significant scaling did not occur.

4. Discussion

We achieved matching rates comparable to the results reported in Lee et al. (2009), Brunet-Benkhoucha et al. (2009), Lee et al. (2011). In particular, similar matching rates are reported in the original MARSHAL and XMARSHAL papers (Jain et al., 2005b; Kon et al., 2006). However, it should be noted that in all these works the C-arm pose was accurately known by using either a radio-opaque fiducial (Jain et al., 2005b; Kon et al., 2006; Lee et al., 2009; Lee et al., 2011) or a precisely calibrated and accurately tracked radiotherapy simulator in Brunet-Benkhoucha et al. (2009). (It should be noted that therapy simulators are extinct in contemporary radiation oncology). In other words, the C-arm was fully tracked and accurate poses were available. Due to availability of accurate C-arm poses in these works, motion compensation was not necessary. However, in our approach no external tracker was used to estimate the pose. Therefore, the initial pose recovery without motion compensation in our case was not sufficiently accurate for a

Table 2

The average and standard deviation of the distance between two consecutive seeds implanted by one needle.

Patient #	Seed spacing (mm) Mean \pm STD
1	10.4 \pm 0.6
2	10.4 \pm 0.6
3	10.3 \pm 0.4
4	10.3 \pm 0.3
5	10.3 \pm 0.3
6	10.2 \pm 0.4
7	10.3 \pm 0.4
8	10.1 \pm 0.4
9	10.4 \pm 0.5
10	10.3 \pm 0.4
Overall	10.3 \pm 0.5

successful reconstruction (see Fig. 9b). However, with the proposed computational motion compensation method we achieved high matching rates without full pose tracking using any external tracker or fiducial (see Fig. 9a). This, in particular, explains the discrepancy between the successful results reported in Jain et al. (2005b), Kon et al. (2006) and our unsuccessful results with the same matching algorithm when motion compensation was not used.

In current brachytherapy practice, implant geometry is assessed using CT, one or several days after the procedure. However, the fluoroscopy images are taken at the end of the procedure while the patient is still in treatment position and additions to the implant are still possible to patch up cold spots. The prostate swells during and after the procedure which results in a seed displacement over time (Yamada et al., 2003) and even during the procedure (Jain et al., in press). The seeds also tend to migrate after

implantation (Fuller et al., 2004). Moreover, for our patients, the fluoroscopy images were taken while the ultrasound probe was still partially inside the rectum. The probe can deform the prostate and displace the seeds. Therefore, the physical position of the seeds during the CT scan is likely to be different from the position of the seeds when the C-arm images are taken. Hence, CT images of the patient can not be used as a confident ground truth to measure the localization error. Therefore, we relied on the projection error to validate the reconstruction in our clinical study. For the same reason, we had to rely on reprojected images to identify the mismatches. It was shown that seed localization errors of less than 2 mm result in less than 5% deviation in the prostate D90 (the minimum dose delivered to 90% of the prostate volume) (Lindsay et al., 2003; Su et al., 2007). Although it was not possible for us to measure the localization error in our clinical study, the localization errors in our simulations and phantom study were significantly lower than this threshold.

Although the mean and STD of the projection error for mismatched seeds are significantly larger than those of the correctly matched seeds (see Fig. 9c and d), the range of the projection error for correctly and erroneously matched seeds overlap. Therefore, a fixed threshold for the projection error cannot be used as a criterion to reliably detect the mismatches. However, it should be noted that, in some cases, a seed projection is mistakenly matched to a seed projection which is located very close to the correct one. In such cases, the projection error is small. Such mismatches result in small errors in seed localization. This suggests that if the seeds with large projection errors are removed, the rest of the mismatches may result only in an insignificant change in the dosimetry. Statistically, only 17.3% of mismatched seeds had a projection error larger than 2 mm. This is 0.2% of all the reconstructed seeds.

We used three C-arm images for seed reconstruction. While more could have been used, the fewer images used in the OR the better, primarily because it saves time and also reduces radiation exposure to OR staff. The matching rate is likely to improve by using more than three images at the expense of computational complexity (Kon et al., 2006). The motion compensation algorithm and the seed matching method are valid for an arbitrary number of images. Alternatively, seeds can be reconstructed for every combination of three out of all available images for a patient and the best reconstruction can be chosen. The reconstruction algorithm is sufficiently fast to allow for such a scheme in clinical settings. It should be noted that for all the patients, except patient 3, there is at least one reconstruction with perfect matching (see Fig. 9a).

The motion compensation algorithm can be combined with other seed matching algorithms, such as REDMAPS (Lee et al., 2011) as reported in Dehghan et al. (2010). In comparison to XMARSHAL, REDMAPS provides the optimal matching solution. Therefore, slightly better results – in term of matching rate – are expected. However, XMARSHAL is computationally faster than REDMAPS. Since, our matching rates using XMARSHAL are above the clinically acceptable threshold, we prefer XMARSHAL due to its speed.

In our results on clinical data, 8% of reconstructions have a matching rate of less than 95%. Although Su et al. suggested that a detection rate of at least 95% is required for an accurate dose estimation (Su et al., 2005), it should be noted that seed detection and matching rate are not completely equivalent. As mentioned above, many of the mismatches occur when a seed projection is mistakenly matched to a wrong seed projection, which is closely located to the correct seed projection. In this case the reconstructed seed is considered a mismatch but the localization error may be small. Therefore, all of the mismatched seeds cannot be categorized as undetected seeds. As explained, by using more than three images or employing a matching algorithm with optimal outcome such as REDMAPS (Lee et al., 2011), we can increase the matching rate.

We implemented our algorithm using MATLAB on a PC with an Intel 2.33 GHz Core2 Quad CPU and 3.25 GB of RAM. We achieved an average time of 19.4 s per data set, which is more than sufficient for clinical implementation. The first level of the optimization is very fast since only 10 seeds per image are used in the reconstruction and XMARSHAL runs on an $O(N^3)$ runtime. The second level of the algorithm is the most time consuming part, since a full matching problem must be solved at each iteration. However, using the outcomes of the first-level optimization to initialize the second level, significantly decreases the number of iterations necessary for convergence. We used the convergence of the reconstruction error as the stopping condition for the second level, which is a conservative criterion. As an alternative, the convergence of the matching solution can be used – similarly to the first-level optimization. In this case, if the matching solution does not change in two iterations, the optimization will terminate. This stopping condition is satisfied in significantly fewer iterations. However, it was observed during the simulations – although rarely – that a matching solution can change to a better one after three or more iterations. Since, the runtime for the algorithms is already acceptable, we decided to choose the more conservative criterion, in order to increase the seed matching rate. As mentioned before, the third-level optimization and seed reconstruction can be solved using (A.3) and (A.4) with low computational cost.

In our clinical studies, stranded seeds were used. We used the constant center-to-center distance of stranded seeds to show that no significant scaling occurred during motion compensation. It should be noted that our motion compensation and reconstruction algorithms do not rely on any information limited to stranded seeds and can be applied for loose seeds without algorithmic modifications.

In this work the seeds were manually segmented in the images by one observer without extensive efforts to identify all the hidden seeds. Since XMARSHAL is capable of maintaining above 97% matching rate for up to 1mm segmentation error (Kon et al., 2006), our motion compensated reconstruction method can successfully reconstruct the seeds as long as the manual seed segmentation error is below this threshold. Considering the small dimensions of seed projections, this level of accuracy is easily achievable. However, manual seed segmentation is a tedious task due to the large number of implanted seeds. Automatic seed segmentation methods are available that have a high success rate in identification of ^{125}I (Tubic et al., 2001b) or ^{103}Pd seeds (Kuo et al., 2010), even in the presence of overlapping seed projections. These methods can be used to segment the majority of seeds in the images. The missing seeds can be identified and the false positives can be removed with manual intervention. Integration of an automatic segmentation algorithm could facilitate the use of intraoperative dosimetry in a clinical environment.

We assumed that the C-arm rotates around its PA. This assumption – resulting in a horizontal motion of the seed projections in the images – was used in the first-level optimization to justify the selection of seeds from the top and bottom of every image as candidates for matching seeds. If the C-arm rotates around its SA, the seeds move vertically in the images. Therefore, the seeds that appear at the left or right side of one image are more likely to appear at the left or right side of other images. In this case, these seeds can be selected as candidates for matching seeds in the first-level optimization. Similarly to our case, the motion along the up-down direction, and perpendicular to the plane of rotation would be compensated.

Since we did not use radio-opaque fiducials, the C-arm could be positioned to capture the seeds close to the center of the detector. In this situation, the seed segmentation error caused by geometric distortion is below the tolerance level of XMARSHAL (Kon et al.,

2006). Therefore, we did not correct for the geometric distortion. If necessary, the dewarping parameters can be estimated using a single image captured at the center of the rotation span. Jain et al. showed that for small rotation spans, the dewarping parameters obtained from a center image can effectively correct the geometric distortions of all the images (Jain et al., 2007).

5. Conclusions and future work

We demonstrated that the sole measurement of rotation angles of a C-arm with a small angle span in a single plane, combined with a motion compensation algorithm, can result in successful prostate implant reconstruction. For motion compensation, we introduced a three-level optimization method to compensate for C-arm translational motions in the Oy_wz_w plane using a small subset of seeds as fiducials to gain an initial estimate of the C-arm pose. This approach obviates the need full pose tracking with external trackers or fiducials.

In a clinical study of 100 data sets from 10 patients, an off-the-shelf digital protractor or C-arm joint encoders were used to measure the rotation angle around the PA of a C-arm, while the deviations in the angle around the left-right axis were measured using the C-arm joint encoders. Combined seed reconstruction and motion compensation led to on average seed matching rate of 98.5%, projection error of 0.33 mm and 19.8 s computational time. The high matching rate, insignificant scaling effect, low projection error and computation time show the feasibility of our method for intraoperative dosimetry in a clinical setting.

We assumed an insignificant motion of the C-arm along x_w axis. This assumption was validated by high matching rates and small projection errors in our clinical study. However, if on some C-arms this motion is considerably large, a 3D motion compensation is necessary. This, however, may suffer from the scaling problem. An object with a known length can be used to estimate the scale. Investigation on exploiting the length of ^{125}I seeds or seed spacers to recover the scaling factor is part of our future work.

Acknowledgements

Ehsan Dehghan was supported by an Ontario Ministry of Research and Innovation post-doctoral fellowship. Mehdi Moradi was supported by Natural Sciences and Engineering Research Council of Canada, and US Army Medical Research and Material Command under W81XWH-10-1-0201. Gabor Fichtinger was supported as Cancer Care Ontario Research Chair. This work was supported in part by NIH R21CA120232-01 Grant.

Appendix A. Equations for simultaneous reconstruction and motion compensation

In order to find the optimal 2D offsets of M sources (M images) and at the same time, find the 3D position of N implanted seeds, we solve the following optimization problem.

$$(s_i^*, \delta_j^*) = \arg \min_{s, \delta} J \quad (\text{A.1})$$

$$J = \sum_{i=1}^N \sum_{j=1}^M (s_i - q_j - \delta_j)' (I - v_{ij} v_{ij}') (s_i - q_j - \delta_j), \quad (\text{A.2})$$

where J is the total reconstruction cost, q_j is the initial position of j th source calculated from the joint angle readings, and δ_j is its corresponding offset. The minimality necessary conditions imply that:

$$\left[\sum_{j=1}^M V_{ij} \right] s_i - \sum_{j=1}^M V_{ij} \delta_j = \sum_{j=1}^M V_{ij} q_j, \quad (\text{A.3})$$

$$-\sum_{i=1}^N V_{ij} s_i + \left[\sum_{i=1}^N V_{ij} \right] \delta_j = - \left[\sum_{i=1}^N V_{ij} \right] q_j, \quad (\text{A.4})$$

where

$$V_{ij} = (I - v_{ij} v_{ij}'). \quad (\text{A.5})$$

Eqs. (A.3) and (A.4) can be concatenated into a matrix form as below.

$$\mathbf{Ax} = \mathbf{b}, \quad (\text{A.6})$$

$$\mathbf{x} = [s'_1 \ \cdots \ s'_N \ \delta'_1 \ \cdots \ \delta'_M]', \quad (\text{A.7})$$

$$\mathbf{A} = \begin{bmatrix} A^{11}_{(3N \times 3N)} & A^{12}_{(3N \times 3M)} \\ A^{21}_{(3M \times 3N)} & A^{22}_{(3M \times 3M)} \end{bmatrix}, \quad (\text{A.8})$$

$$\mathbf{b} = [b'_1 \ b'_2]', \quad (\text{A.9})$$

where,

$$A^{11} = \sum_{j=1}^M \begin{bmatrix} V_{1j} & 0 & \cdots & 0 \\ 0 & V_{2j} & \cdots & 0 \\ 0 & 0 & \ddots & 0 \\ 0 & 0 & \cdots & V_{Nj} \end{bmatrix}, \quad (\text{A.10})$$

$$A^{22} = \sum_{i=1}^N \begin{bmatrix} V_{i1} & 0 & \cdots & 0 \\ 0 & V_{i2} & \cdots & 0 \\ 0 & 0 & \ddots & 0 \\ 0 & 0 & \cdots & V_{iM} \end{bmatrix}, \quad (\text{A.11})$$

$$A^{12} = - \begin{bmatrix} V_{11} & \cdots & V_{1M} \\ V_{21} & \cdots & V_{2M} \\ \vdots & \ddots & \vdots \\ V_{N1} & \cdots & V_{NM} \end{bmatrix}, \quad (\text{A.12})$$

$$A^{21} = (A^{12})', \quad (\text{A.13})$$

$$b_1 = \sum_{j=1}^M \begin{bmatrix} V_{1j} q_j \\ \vdots \\ V_{Nj} q_j \end{bmatrix}, \quad (\text{A.14})$$

$$b_2 = - \sum_{i=1}^N \begin{bmatrix} V_{i1} q_1 \\ \vdots \\ V_{iM} q_M \end{bmatrix}. \quad (\text{A.15})$$

At this point, the set of linear equations in (A.6) is under-determined and the matrix \mathbf{A} in (A.8) is singular. However, we fixed the first source in space; hence $\delta_1 = 0$. In addition, we assumed that the C-arms move only in Oy_wz_w plane. This places another constraint on the equations in the form of $\delta_{jx} = 0$, $j \in \{1, \dots, M\}$. By removing the rows and columns corresponding to these known variables from \mathbf{A} and removing the corresponding entries in \mathbf{x} and \mathbf{b} , Eq. (A.6) can be solved.

References

- Amols, H.I., Rosen, I.L., 1981. A three-film technique for reconstruction of radioactive seed implants. *Medical Physics* 8, 210–214.

- Blasko, J.C., Mate, T., Sylvester, J.E., Grimm, P.D., Cavanagh, W., 2002. Brachytherapy for carcinoma of the prostate: techniques, patient selection, and clinical outcomes. *Seminars in Radiation Oncology* 12 (1), 81–94. *Advances in Brachytherapy*.
- Brack, C., Götte, H., Gossé, F., Moctezuma, J., Roth, M., Schweikard, A., 1996. Towards accurate X-ray camera calibration in computer-assisted robotic surgery. In: *Proceedings of International Symposium on Computer Assisted Radiology*, pp. 721–728.
- Brunet-Benhoucha, M., Verhaegen, F., Reniers, B., Lassalle, S., Béliveau-Nadeau, D., Donath, D., Taussky, D., Carrier, J.-F., 2009. Clinical implementation of a digital tomosynthesis-based seed reconstruction algorithm for intraoperative postimplant dose evaluation in low dose rate prostate brachytherapy. *Medical Physics* 36 (11), 5235–5244.
- Dehghan, E., Lee, J., Moradi, M., Wen, X., Fichtinger, G., Salcudean, S.E., 2010. Prostate brachytherapy seed reconstruction using C-arm rotation measurement and motion compensation. In: *Proceedings of Medical Image Computing and Computer Assisted Intervention (MICCAI)*, pp. 283–290.
- Ding, M., Wei, Z., Gardi, L., Downey, D.B., Fenster, A., 2006. Needle and seed segmentation in intra-operative 3D ultrasound-guided prostate brachytherapy. *Ultrasonics* 44 (Suppl. 1), e331–e336. *Proceedings of Ultrasonics International (UI'05) and World Congress on Ultrasonics (WCU)*.
- Fallavollita, P., Karim-Aghaloo, Z., Burdette, E., Song, D., Abolmaesumi, P., Fichtinger, G., 2010. Registration between ultrasound and fluoroscopy or CT in prostate brachytherapy. *Medical Physics* 37, 2749–2760.
- Feleppa, E.J., Ramachandran, S., Alam, S.K., Kalisz, A., Ketterling, J.A., Ennis, R.D., Wu, C.-S., 2002. Novel methods of analyzing radio-frequency echo signals for the purpose of imaging brachytherapy seeds used to treat prostate cancer. In: *Proceedings of SPIE*, vol. 4687, pp. 127–138.
- French, D.F., Morris, J., Keyes, M., Goksel, O., Salcudean, S.E., 2005. Intraoperative dosimetry for prostate brachytherapy from fused ultrasound and fluoroscopy images. *Academic Radiology* 12, 1262–1272.
- Fuller, D.B., Koziol, J.A., Feng, A.C., 2004. Prostate brachytherapy seed migration and dosimetry: analysis of stranded sources and other potential predictive factors. *Brachytherapy* 3 (1), 10–19.
- Grzeda, V., Fichtinger, G., 2010. C-arm rotation encoding with accelerometers. *International Journal of Computer Assisted Radiology and Surgery* 5 (4), 385–391.
- Han, B.H., Wallner, K., Merrick, G., Butler, W., Sutlief, S., Sylvester, J., 2003. Prostate brachytherapy seed identification on post-implant TRUS images. *Medical Physics* 30 (5), 898–900.
- Holmes III, D.R., Robb, R.A., 2004. Improved automated brachytherapy seed localization in trans-urethral ultrasound data. In: Galloway, R.L. (Ed.), *Proceedings of SPIE*, vol. 5367, pp. 353–360.
- Jain, A., An, M., Chitphakdithai, N., Chintalapani, G., Fichtinger, G., 2007. C-arm calibration – is it really necessary? In: Cleary, K., Miga, M.I. (Eds.), *Proceedings of SPIE*, vol. 6509.
- Jain, A., Deguet, A., Iordachita, I., Chintalapani, G., Vikal, S., Blevins, J., Le, Y., Armour, E., Burdette, C., Song, D., Fichtinger, G., in press. Intra-operative 3D guidance and edema detection in prostate brachytherapy using a non-isocentric C-arm. *Medical Image Analysis*, doi:10.1016/j.media.2010.07.011.
- Jain, A., Fichtinger, G., 2006. C-arm tracking and reconstruction without an external tracker. In: *Proceedings of Medical Image Computing and Computer Assisted Intervention (MICCAI)*, pp. 494–502.
- Jain, A.K., Mustafa, T., Zhou, Y., Burdette, C., Chirikjian, G.S., Fichtinger, G., 2005a. FTRAC – a robust fluoroscopy tracking fiducial. *Medical Physics* 32 (10), 3185–3198.
- Jain, A.K., Zhou, Y., Mustafa, T., Burdette, E.C., Chirikjian, G.S., Fichtinger, G., 2005b. Matching and reconstruction of brachytherapy seeds using the Hungarian algorithm (MARSHAL). *Medical Physics* 32, 3475–3492.
- Jemal, A., Siegel, R., Xu, J., Ward, E., 2010. Cancer statistics, 2010. *CA: A Cancer Journal for Clinicians* 60, 277–300.
- Kon, R.C., Jain, A.K., Fichtinger, G., 2006. Hidden seed reconstruction from C-arm images in brachytherapy. In: *IEEE International Symposium on Biomedical Imaging: Nano to Macro*.
- Kuo, N., Lee, J., Deguet, A., Song, D., Burdette, E.C., Prince, J., 2010. Automatic segmentation of seeds and fluoroscopy tracking (FTRAC) fiducial in prostate brachytherapy X-ray images. In: Wong, K.H., Miga, M.I. (Eds.), *Proceedings of SPIE*, vol. 7625, pp. 76252T1–76252T9.
- Lagerburg, V., Moerland, M.A., Lagendijk, J.J., Battermann, J.J., 2005. Measurement of prostate rotation during insertion of needles for brachytherapy. *Radiotherapy and Oncology* 77, 318–323.
- Lam, S.T., Cho, P.S., Marks II, R.J., Narayanan, S., 2004. Three-dimensional seed reconstruction for prostate brachytherapy using Hough trajectories. *Physics in Medicine and Biology* 49, 557–569.
- Lee, J., Labat, C., Jain, A.K., Song, D.Y., Burdette, E.C., Fichtinger, G., Prince, J.L., 2011. REDMAPS: reduced-dimensionality matching for prostate brachytherapy seed reconstruction. *IEEE Transactions on Medical Imaging* 30 (1), 38–51.
- Lee, J., Liu, X., Jain, A., Song, D., Burdette, E., Prince, J., Fichtinger, G., 2009. Prostate brachytherapy seed reconstruction with Gaussian blurring and optimal coverage cost. *IEEE Transactions on Medical Imaging* 28 (12), 1955–1968.
- Lindsay, P.E., Van Dyk, J., Battista, J.J., 2003. A systematic study of imaging uncertainties and their impact on ¹²⁵I prostate brachytherapy dose evaluation. *Medical Physics* 30 (7), 1897–1908.
- McAlevey, S., Rubens, D., Parker, K., 2003. Doppler ultrasound imaging of magnetically vibrated brachytherapy seeds. *IEEE Transactions on Biomedical Engineering* 50 (2), 252–254.
- Mitri, F., Trompette, P., Chapelon, J.-Y., 2004. Improving the use of vibro-acoustography for brachytherapy metal seed imaging: a feasibility study. *IEEE Transactions on Medical Imaging* 23 (1), 1–6.
- Morris, W., Keyes, M., Palma, D., Spadinger, I., McKenzie, M., Agranovich, A., Pickles, T., Liu, M., Kwan, W., Wu, J., Berthelet, E., Pai, H., 2009a. Population-based study of biochemical and survival outcomes after permanent ¹²⁵I brachytherapy for low- and intermediate-risk prostate cancer. *Urology* 73 (4), 860–865.
- Morris, W.J., Keyes, M., Palma, D., McKenzie, M., Spadinger, I., Agranovich, A., Pickles, T., Liu, M., Kwan, W., Wu, J., Lapointe, V., Berthelet, E., Pai, H., Harrison, R., Kwa, W., Bucci, J., Rac, V., Woods, R., 2009b. Evaluation of dosimetric parameters and disease response after ¹²⁵Iodine transperineal brachytherapy for low- and intermediate-risk prostate cancer. *International Journal of Radiation Oncology, Biology, Physics* 73 (5), 1432–1438.
- Nag, S., Ciezki, J.P., Cormak, R., Doggett, S., Dewyngaert, K., Edmundson, G.K., Stock, R.G., Stone, N.N., Yan, Y., Zelefsky, M.J., 2001. Intraoperative planning and evaluation of permanent prostate brachytherapy: report of the American brachytherapy society. *International Journal of Radiation Oncology, Biology, Physics* 51, 1422–1430.
- Narayanan, S., Cho, P.S., Marks II, R.J., 2004. Three-dimensional seed reconstruction from an incomplete data set for prostate brachytherapy. *Physics in Medicine and Biology* 49, 3483–3494.
- Navab, N., Bani-Hashemi, A., Mitschke, M., Holdsworth, D.W., Fahrig, R., Fox, A.J., Graumann, R., 1996. Dynamic geometrical calibration for 3D cerebral angiography. *SPIE Medical Imaging* 2708, 361–370.
- Orio III, P.F., Tutar, I.B., Narayanan, S., Arthurs, S., Cho, P.S., Kim, Y., Merrick, G., Wallner, K.E., 2007. Intraoperative ultrasound-fluoroscopy fusion can enhance prostate brachytherapy quality. *International Journal of Radiation Oncology, Biology, Physics* 69 (1), 302–307.
- Peters, T., Cleary, K. (Eds.), 2008. *Image-Guided Interventions: Technology and Applications*. Springer.
- Polo, A., Salembier, C., Venselaar, J., Hoskin, P., 2010. Review of intraoperative imaging and planning techniques in permanent seed prostate brachytherapy. *Radiotherapy and Oncology* 94 (1), 12–23.
- Prestidge, B.R., Prete, J.J., Buchholz, T.A., Friedland, J.L., Stock, R.G., Grimm, P.D., Bice, W.S., 1998. A survey of current clinical practice of permanent prostate brachytherapy in the United States. *International Journal of Radiation Oncology, Biology, Physics* 40 (2), 461–465.
- Song, D.Y., Jain, A.K., Zhang, Z., Deguet, A., Le, Y., Armour, E., Burdette, E.C., Fichtinger, G., 2011. Dynamic intraoperative dosimetry for prostate brachytherapy using a nonisocentric C-arm. *Brachytherapy* 10 (2), 98–106.
- Su, Y., Davis, B.J., Furutani, K.M., Herman, M.G., Robb, R.A., 2007. Dosimetry accuracy as a function of seed localization uncertainty in permanent prostate brachytherapy: increased seed number correlates with less variability in prostate dosimetry. *Physics in Medicine and Biology* 52 (11), 3105–3119.
- Su, Y., Davis, B.J., Herman, M.G., Manduca, A., Robb, R.A., 2005. Examination of dosimetry accuracy as a function of seed detection rate in permanent prostate brachytherapy. *Medical Physics* 32 (9), 3049–3056.
- Su, Y., Davis, B.J., Herman, M.G., Robb, R.A., 2004. Prostate brachytherapy seed localization by analysis of multiple projections: identifying and addressing the seed overlap problem. *Medical Physics* 31 (5), 1277–1287.
- Su, Y., Davis, B.J., Herman, M.G., Robb, R.A., 2006. TRUS-fluoroscopy fusion for intraoperative prostate brachytherapy dosimetry. In: *Medicine Meets Virtual Reality 14: Accelerating Change in Healthcare: Next Medical Toolkit*. Studies in Health Technology and Informatics, vol. 119/2005. IOS Press, pp. 532–537.
- Todor, D.A., Cohen, G.N., Amols, H.I., Zaider, M., 2002. Operator-free, film-based 3D seed reconstruction in brachytherapy. *Physics in Medicine and Biology* 47, 2031–2048.
- Tubic, D., Zaccarin, A., Beaulieu, L., Pouliot, J., 2001a. Automated seed detection and three-dimensional reconstruction. II. Reconstruction of permanent prostate implants using simulated annealing. *Medical Physics* 28 (11), 2272–2279.
- Tubic, D., Zaccarin, A., Pouliot, J., Beaulieu, L., 2001b. Automated seed detection and three-dimensional reconstruction. I. Seed localization from fluoroscopic images or radiographs. *Medical Physics* 28 (11), 2265–2271.
- Tutar, I.B., Gong, L., Narayanan, S., Pathak, S.D., Cho, P.S., Wallner, K., Kim, Y., 2008. Seed-based transrectal ultrasound-fluoroscopy registration method for intraoperative dosimetry analysis of prostate brachytherapy. *Medical Physics* 35, 840–848.
- Tutar, I.B., Managuli, R., Shamdasani, V., Cho, P.S., Pathak, S.D., Kim, Y., 2003. Tomosynthesis-based localization of radioactive seeds in prostate brachytherapy. *Medical Physics* 30, 3135–3142.
- Wei, Z., Gardi, L., Downey, D.B., Fenster, A., 2006. Automated localization of implanted seeds in 3D TRUS images used for prostate brachytherapy. *Medical Physics* 33 (7), 2404–2417.
- Wen, X., Salcudean, S.E., Lawrence, P.D., 2010. Detection of brachytherapy seeds using 3D transrectal ultrasound. *IEEE Transactions on Biomedical Engineering* 57 (10), 2467–2477.
- Yamada, Y., Potters, L., Zaider, M., Cohen, G., Venkatraman, E., Zelefsky, M.J., 2003. Impact of intraoperative edema during transperineal permanent prostate brachytherapy on computer-optimized and preimplant planning techniques. *American Journal of Clinical Oncology* 26, e130–e135.
- Zhang, M., Zaider, M., Worman, M., Cohen, G., 2004. On the question of 3D seed reconstruction in prostate brachytherapy: the determination of X-ray source and film locations. *Physics in Medicine and Biology* 49, 19.

Prostate implant reconstruction from C-arm images with motion-compensated tomosynthesis

Ehsan Dehghan

School of Computing, Queen's University, Kingston, Ontario K7L-3N6, Canada

Mehdi Moradi, Xu Wen, Danny French, and Julio Lobo

Department of Electrical and Computer Engineering, University of British Columbia, Vancouver, British Columbia V6T-1Z4, Canada

W. James Morris

Vancouver Cancer Centre, Vancouver, British Columbia V5Z-1E6, Canada

Septimiu E. Salcudean^{a)}

Department of Electrical and Computer Engineering, University of British Columbia, Vancouver, British Columbia V6T-1Z4, Canada

Gabor Fichtinger

School of Computing, Queen's University, Kingston, Ontario K7L-3N6, Canada

(Received 15 May 2011; revised 12 July 2011; accepted for publication 8 August 2011; published 9 September 2011)

Purpose: Accurate localization of prostate implants from several C-arm images is necessary for ultrasound-fluoroscopy fusion and intraoperative dosimetry. The authors propose a computational motion compensation method for tomosynthesis-based reconstruction that enables 3D localization of prostate implants from C-arm images despite C-arm oscillation and sagging.

Methods: Five C-arm images are captured by rotating the C-arm around its primary axis, while measuring its rotation angle using a protractor or the C-arm joint encoder. The C-arm images are processed to obtain binary seed-only images from which a volume of interest is reconstructed. The motion compensation algorithm, iteratively, compensates for 2D translational motion of the C-arm by maximizing the number of voxels that project on a seed projection in all of the images. This obviates the need for C-arm full pose tracking traditionally implemented using radio-opaque fiducials or external trackers. The proposed reconstruction method is tested in simulations, in a phantom study and on ten patient data sets.

Results: In a phantom implanted with 136 dummy seeds, the seed detection rate was 100% with a localization error of 0.86 ± 0.44 mm (Mean \pm STD) compared to CT. For patient data sets, a detection rate of 99.5% was achieved in approximately 1 min per patient. The reconstruction results for patient data sets were compared against an available matching-based reconstruction method and showed relative localization difference of 0.5 ± 0.4 mm.

Conclusions: The motion compensation method can successfully compensate for large C-arm motion without using radio-opaque fiducial or external trackers. Considering the efficacy of the algorithm, its successful reconstruction rate and low computational burden, the algorithm is feasible for clinical use. © 2011 American Association of Physicists in Medicine. [DOI: 10.1118/1.3633897]

Key words: tomosynthesis, brachytherapy, seed reconstruction, motion compensation, C-arm

I. INTRODUCTION

Since its advent in the early 1980s, ultrasound-guided prostate brachytherapy (hereafter brachytherapy) has become a definitive treatment option for prostate cancer—the leading cancer among men in the United States in 2010 (Ref. 1)—with outcomes comparable to the radical prostatectomy that is considered as the gold standard.^{2–4} The goal of brachytherapy is to kill the cancer in the prostate gland with radiation by permanently implanted radioactive ¹²⁵I or ¹⁰³Pd capsules (seeds). Seed positions are carefully planned to deliver a lethal radioactive dose to the cancerous prostate, while maintaining a tolerable dose to the urethra and rectum. The brachytherapist delivers the seeds using needles under

visual guidance from transrectal ultrasound (TRUS) and qualitative assessment from frequently acquired fluoroscopy images.⁵

The success of brachytherapy depends on accurate placement of the seeds. However, prostate motion and deformation,⁶ needle bending, prostate swelling,⁷ seed migration,⁸ and human and system calibration errors can result in seed misplacement which, in turn, can lead to underdosed regions or over-radiation of the surrounding healthy tissue. In current brachytherapy practice, the implant is quantitatively assessed using CT, postoperatively. In case of major underdosing, external beam radiation is applied as an adjunct. Intraoperative dosimetry can provide the physicians with quantitative

dose assessment in the operating room and enable them to adjust the position and number of the remaining seeds to compensate for the developing cold spots.^{9–11}

Three dimensional localization of the implanted seeds, registered to the prostate anatomy, is required for dose calculation. TRUS provides sufficient soft tissue contrast to delineate the prostate boundaries. However, despite significant efforts in seed localization from ultrasound,^{12–18} robust seed segmentation in ultrasound is not yet possible. It was shown that up to 25% of the seeds can be missed even through manual segmentation of B-mode images.¹²

Mobile C-arms are routinely used in the contemporary prostate brachytherapy for implant visualization. However, the prostate cannot be visualized in the C-arm images. Therefore, TRUS-fluoroscopy fusion offers itself as a practical solution for intraoperative dosimetry.^{10,19–22} In these methods, the seeds reconstructed from C-arm images are spatially registered to the prostate volume visible in TRUS images. The delivered dose to the prostate is evaluated and the plan is modified, accordingly.

The reconstruction of the implanted seeds in 3D space from several x-ray images has been widely studied.^{23–38} These efforts can be categorized into two major groups. In the first group, 2D coordinates of the seed projection centers are identified in the images and a matching problem is solved to identify the corresponding projections of each seed in different images.^{23,25–32} These methods should be preceded with a complicated seed segmentation method to precisely localize the seed projection centroids.^{39–41} It is difficult, or sometimes impossible, to localize the centroid of each individual seed projection in an image due to presence of hidden and overlapping seed projections (see Fig. 1). Therefore, manual intervention is usually necessary in the seed segmentation phase. However, even after manual intervention, some seed projections can remain hidden. Although some seed matching algorithms can address the hidden seed problem,^{27–29,31,32} the performance of these algorithms usually degrades with increasing number of hidden seeds.

The second group of seed reconstruction methods consists of tomosynthesis-based algorithms.^{24,33–37} The tomosynthesis-based reconstruction methods have two advantages over the seed matching methods. First, the matching problem in the presence of hidden or overlapping seed projections is inherently solved by tomosynthesis. Therefore, these methods do not need a seed matching algorithm. Second, the tomosynthesis-based reconstruction methods require a much simpler seed segmentation algorithm, as they do not rely on localization of seed projection centroids in every image. A binary image that only separates the seed projections from the background—without localization of their centers—suffices for a tomosynthesis-based seed reconstruction.

Tomosynthesis-based seed reconstruction is especially attractive for reconstruction of ¹²⁵I seeds, which have a larger projection compared to ¹⁰³Pd seeds. Due to their relatively larger seed projections, overlapping and hidden seed projections are more abundant in the C-arm images of ¹²⁵I implants. Therefore, seed segmentation for matching-based reconstruction is considerably more difficult for ¹²⁵I seeds.

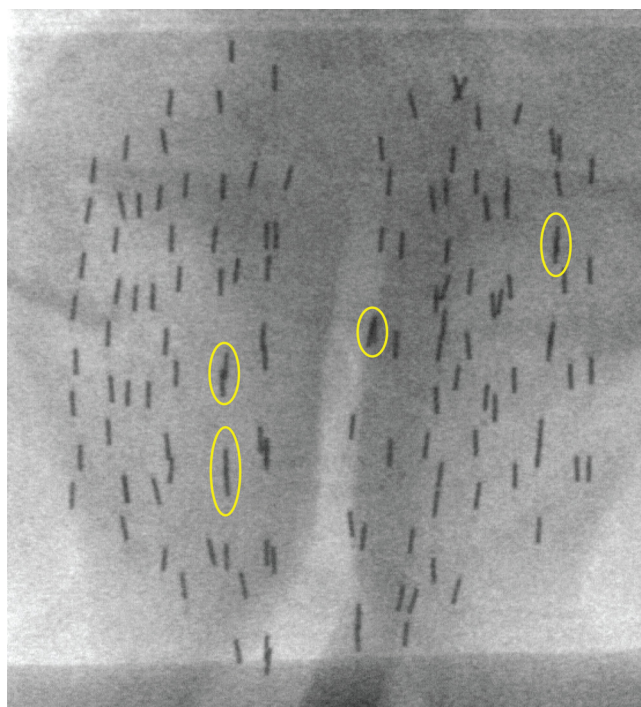


Fig. 1. A typical C-arm image of an implant showing some of the overlapping and hidden seeds. Localization of the seed projection centroids for hidden or overlapping seeds is difficult or sometimes impossible for seed segmentation methods.

This makes tomosynthesis, the preferred method for ¹²⁵I seed reconstruction. However, it should be noted that tomosynthesis-based reconstructions can be used to reconstruct ¹⁰³Pd seeds without any restrictions.

Pokhrel *et al.*³⁸ introduced a seed reconstruction method based on forward projection using cone-beam CT (CBCT). Similarly to tomosynthesis-based methods, their algorithm does not rely on identification of seed projection centroids. However, their method is computationally more extensive compared to tomosynthesis-based algorithms. Also, importantly, CBCT requires a high-end digitally encoded C-arm that is typically not available in brachytherapy. In addition, CBCT demands many C-arm images, exposing the patient and OR crew to more toxic radiation.

C-arm pose—the relative positions of images in 3D space—must be known prior to seed reconstruction. Although, external electromagnetic or optical trackers can yield the C-arm pose,⁴² they are not practically viable due to their cost and added complexity. The C-arm pose can be also computed using radio-opaque fiducials.^{24,43–47} However, fiducials require segmentation,⁴¹ may overlap with the anatomy of interest, occupy precious real estate in the image, and are not part of the standard operating room.

C-arm images are generally acquired by rotating the C-arm around the patient. In ideal cases, C-arm rotation angles can yield accurate pose. However, in real cases, unmeasured C-arm translational motions caused by oscillation and sagging lead to errors in the pose computation and in turn, failure of seed reconstruction.

Researchers have developed approaches to reconstruct the seeds and use them to improve the pose computation, iteratively.^{25,48,49} In these methods, the seeds are reconstructed in 3D using an initial estimate of the pose. Then, a motion compensation method uses the reconstructed seeds to compensate for the errors in pose computation. In Ref. 49, we compensated for 2D translational motion of the C-arm using the reconstructed seeds, in a matching-based reconstruction scheme. The initial pose was obtained from measurements of C-arm rotation angles without external trackers or fiducials.

The aforementioned motion compensation methods, including our own work,⁴⁹ were all developed for matching-based seed reconstruction and hence, cannot be applied to a tomosynthesis-based reconstruction method. Lee *et al.*³⁷ were the first to use a motion compensation method within a tomosynthesis-based reconstruction. They used a radio-opaque tracking fiducial [called FTRAC Ref. (46)] to initially estimate the pose of a C-arm. At the beginning, three images with the best corresponding pose computation quality—based on the residual error of the pose recovery using FTRAC—were used to reconstruct some candidate seeds. Then, the reconstructed candidate seeds were used to improve on the pose and calibration parameters for the remaining images in a process they called “autofocus.” Finally, the seeds were reconstructed using all the images. If FTRAC is not used, the quality of the initial pose computation is not known. Therefore, the three images with the best pose cannot be selected to initialize the reconstruction. In addition, without FTRAC, a tomosynthesis-based seed reconstruction may fail to reconstruct an adequate number of candidate seeds for pose correction, since initial pose computation may not be sufficiently accurate.

In this paper, we introduce a new computational motion compensation algorithm for tomosynthesis-based seed reconstruction. This method compensates for the C-arm motion by maximizing the number of seed voxels in a volume of interest. In contrast to the previous work, this method does not rely on reconstructed seeds to compensate for C-arm motion. Therefore, it can be used to compensate for large motions that prohibit initial reconstruction of a sufficient number of seeds for seed-based motion compensation. The proposed motion compensation method is especially targeted for tomosynthesis-based reconstruction. Therefore, our method inherits the advantages of a tomosynthesis-based reconstruction—such as requiring a simple segmentation and inherently solving the hidden seeds problem—which make it the preferred choice for reconstruction of ¹²⁵I seeds. However, this method is not limited to reconstruction of ¹²⁵I seeds and can be used to reconstruct ¹⁰³Pd seeds as well.

Similarly to Ref. 49, we initialize the pose by sole measurement of C-arm rotation angles. On the one hand, this obviates the need for full pose tracking using radio-opaque fiducials or external trackers. But, on the other hand, this initial pose estimation can fail to provide us with an adequate number of seeds for seed-based pose correction through tomosynthesis. As we will show in Sec. III, maximizing the number of seed voxels in a volume of interest, without

explicit reconstruction of any seeds, surmounts this obstacle and yields accurate C-arm pose computations for successful seed reconstruction.

In Ref. 49, we demonstrated that by making realistic and practical assumptions in defining the imaging protocol in accordance with clinical limitations, a 2D motion compensation scheme will result in a clinically acceptable seed reconstruction. In this paper, we build our motion compensation on the same assumptions.

We assume that:

1. The images are taken by rotating the C-arm around its primary axis PA (y_w axis in Fig. 2) in a limited angle span, while the angle around the secondary axis (SA) is fixed (see Fig. 2).
2. C-arm rotation angles are measured.
3. The intrinsic parameters of the C-arm, such as source to image distance, source to center of rotation distance, image center and image resolution are known and do not change during the C-arm rotation.
4. Significant C-arm motions are translational motions in the Oy_wz_w plane and motion along x_w is negligible.

Single-axis rotation of the C-arm around its PA is common practice in contemporary brachytherapy. Usually, the PA is approximately aligned with the patient's craniocaudal axis. C-arm rotation angles can be measured using the device joint encoders (if available), digital protractors or accelerometers.⁵⁰ Our results in Sec. III C suggest that an accuracy of $\pm 1^\circ$, which is provided by C-arm joint encoders, is sufficient for successful reconstructions. The intrinsic parameters of the C-arm can be measured preoperatively. Since the span of C-arm rotation in a clinical setting is generally restricted to $\pm 10^\circ$ due to space limitations, the intrinsic parameters do not significantly change. Jain *et al.*⁵¹ showed that recalibration is unnecessary since small changes in the calibration

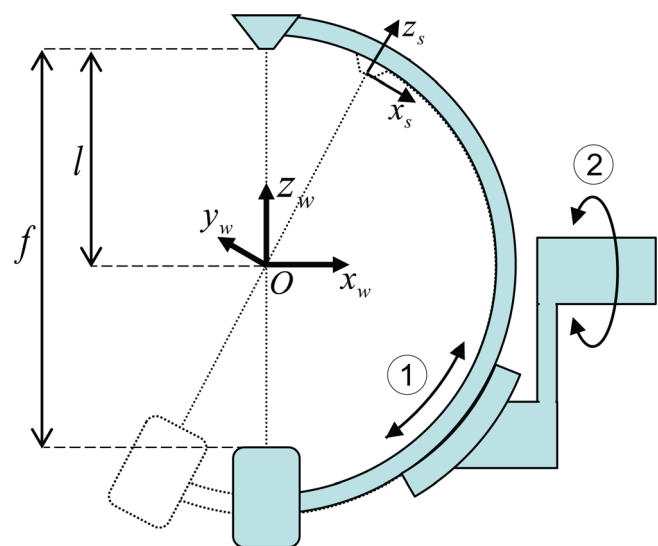


Fig. 2. Schematic of a C-arm rotating around its PA (rotation ①). Rotation ② shows rotation of the C-arm around its SA. The homogeneous world coordinate system $Ox_wy_wz_w$ is centered at the center of rotation. The homogeneous source coordinate system $Ox_sy_sz_s$ is centered at the source position corresponding to each image.

parameters do not have a significant effect on the relative position of the reconstructed seeds. Note that we are interested in the relative position of the seeds, since the reconstructed seeds will be registered to the prostate anatomy for dosimetry.²²

The C-arm forms a cantilever at its connection to the body of the device. The intensifier is heavy and its weight creates a significant torque around the connection point that can lead to significant sagging along the z axis. In addition, due to the length of the C-arm, forces along the y and z axes can create significant torques around this joint (connection to the body) and can cause oscillation in the C-arm. However, the forces along the x axis cannot produce significant torque around this joint. Therefore, the motion caused by the forces along the x axis can only result in translation of the whole C-arm and its body along the x axis. Due to the heavy weight of the C-arm, small forces along this axis cannot cause significant motion when the C-arm wheels are locked.

Assume that images $I_i, i \in \{1, \dots, M\}$ were acquired from a set of seeds located at $s_j = [s_{jx}, s_{jy}, s_{jz}]^T, j \in \{1, \dots, N\}$, while the C-arm source positions were located at $q_i = [q_{ix}, q_{iy}, q_{iz}]^T, i \in \{1, \dots, M\}$, where $(\cdot)^T$ denotes the transpose of a vector or a matrix. It can be shown that, using the same set of images I_i with the same rotation angles, any C-arm source position configuration $q'_i = [q'_{ix}, q'_{iy}, q'_{iz}]^T, i \in \{1, \dots, M\}$ that satisfies $(q'_i - q_1) = \lambda(q_i - q_1)$ will result in a set of reconstructed seeds (s'_i) in which, $(s'_i - q_1) = \lambda(s_i - q_1)$. In other words, a 3D translational motion compensation can result in a reconstruction with an arbitrary scale (λ). If a fiducial is used, a known length on the fiducial can be used to recover the scale.⁴⁸ In order to avoid the scaling problem without a fiducial, we take advantage of the confined motion of the C-arm and assume that the C-arm motion along x_w is negligible. Therefore, we assume that our initial C-arm pose estimations are accurate along the x_w axis (q_{ix}) and we add the constraint $(q'_{ix} - q_{1x}) = (q_{ix} - q_{1x})$ to our equations.

Our assumption about 2D motion of a C-arm is an approximation to the C-arm motion pattern. However, we show in Sec. III, that this approximation is sufficiently accurate for successful reconstruction of brachytherapy implants and results in a negligible error in the estimation of the scale (Table II).

In Sec. II, the methods for tomosynthesis-based seed reconstruction and motion compensation are outlined. Section III shows our numerical simulation, phantom, and clinical results. We discuss our results in Sec. IV, followed by conclusions and future work in Sec. V.

II. MATERIAL AND METHODS

II.A. Image processing and labeling

We use seed-only C-arm images to reconstruct the seeds. A seed-only image is a binary image in which each pixel has a value of 1, if it belongs to a seed projection and zero otherwise. An example of such an image is shown in the left side of Fig. 3. Note that in contrast to seed segmentation for matching-based reconstruction methods, we do not require

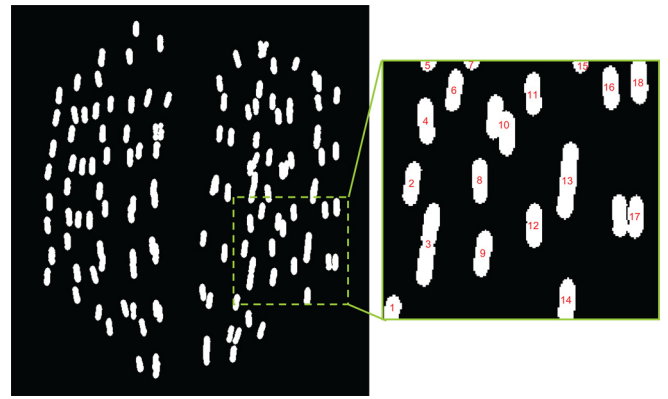


FIG. 3. Left: a dilated seed-only image, right: labeled seed-only image.

the seed projection centroids to be localized. We relied on local thresholding and morphological filtering to produce the seed-only images as explained in Refs. 19 and 52. There are several other methods that can be used to produce the seed-only images.^{18,34,36,39–41} Therefore, we do not discuss image processing in more details in this paper. It should be noted that a false positive projection does not result in a false positive seed, unless there are corresponding false positives in all the other images, and this is very unlikely to occur. However, a missing seed projection in one image, results in a missing seed in the reconstructed seed cloud. Therefore, manual identification of missing seed projections is necessary; however, removal of false positives is precautionary.

In order to increase the likelihood of seed detection and compensate for small pose computation errors, the seed-only images are dilated with a disk structural element of radius r (2–3 pixels in this work).

The dilated seed-only images are then labeled using the connected component labeling algorithm.⁵³ These labeled images are later used to detect and remove false positives.^{35,37} More details are discussed in Sec. II D. A portion of a labeled image is shown in Fig. 3. Note that one or more seed projections can be associated with one label.

II.B. Volume of interest reconstruction

Figure 2 shows the geometry of a C-arm rotated around its primary axis (PA). Every point s in the world homogeneous coordinate system—centered at $Ox_wy_wz_w$ —can be projected on a point p on the i th segmented image homogeneous coordinate system using the following equation:

$$\underline{p} = \begin{bmatrix} -f/\rho_x & 0 & c_x & 0 \\ 0 & -f/\rho_y & c_y & 0 \\ 0 & 0 & 1 & 0 \end{bmatrix} {}^s\mathbf{T}_w^i \underline{s} = \mathbf{P}_i \underline{s}, \quad (1)$$

where ${}^s\mathbf{T}_w^i$ is the transformation matrix from the world homogeneous coordinate system to the source homogeneous coordinate system centered at the x-ray source location that corresponds to the i th image, f is the source to image distance, ρ_x and ρ_y are pixel spacings along the horizontal and vertical axes of the image, c_x and c_y are the coordinates of the image center and \underline{s} represents the coordinates of s in the world homogeneous coordinate system. \mathbf{P}_i is a 3×4

projection matrix from the world homogeneous coordinate system to the image i homogeneous coordinate system. The point p has a pixel value $\psi_i(p)$ equal to 1, if p is inside a seed projection and equal to 0, otherwise.

We assume a volume of interest (VOI) in the 3D space. For every voxel v in the VOI with coordinates \underline{v} in the world coordinate system, the voxel value is defined as:

$$\Psi(\underline{v}) = \sum_{i=1}^M \psi_i(\mathbf{P}_i \underline{v}), \quad (2)$$

where M is the number of images. A voxel is assumed to belong to a seed cluster in 3D space, if

$$\Psi(\underline{v}) = M. \quad (3)$$

This means that voxel v belongs to a seed cluster, if it projects on a seed projection in all of the images. We define \mathbf{S} as a set that contains all the seed voxels.

After populating the VOI, the seed clusters are labeled using the connected component labeling algorithm.⁵³ We use these labeled clusters, their relation with the labeled images, and their centers and volumes in Sec. II D to find the seed centroids and remove the false positives.

Since we are only interested in voxels with a value of M , we can significantly increase the computational speed for VOI reconstruction using the following procedure.

At the beginning, all the voxels are initialized with a voxel value equal to zero. In the first iteration, all the voxels in the VOI are projected on the first image using Eq. (1). If a voxel projects on a seed projection in this image, its voxel value is increased by 1, otherwise its voxel value is kept unchanged (see Fig. 4). The voxels that have a value of zero after this iteration do not have the opportunity to acquire a value of M after projection on the subsequent $M-1$ images. Therefore, in the second iteration, only the voxels with a voxel value of 1 are projected on the second image and their voxel values are updated in the same manner. Likewise, in the i th iteration ($i \leq M$), only the voxels with a value of $(i-1)$ are projected. This decreases the number of projected

voxels significantly after each iteration and increases the computational speed that is very important for clinical seed reconstruction. Since every voxel is projected on M images only, the maximum voxel value is equal to M . This forward-projection approach removes the risk of cross-talk between voxels that may occur in back-projection.

II.C. Motion compensation

The pose computation problem is equivalent to finding the transformation matrix ${}^s\mathbf{T}_w$ in Eq. (1). This matrix can be defined using the following equation:

$${}^s\mathbf{T}_w = \begin{bmatrix} {}^s\mathbf{R}_w & -{}^s\mathbf{R}_w\delta - \begin{bmatrix} 0 \\ 0 \\ l \end{bmatrix} \\ \mathbf{0}^T & 1 \end{bmatrix}, \quad (4)$$

where ${}^s\mathbf{R}_w$ is the rotation matrix from the world to the source coordinate frame, l is the distance from the source to the center of rotation, and $\delta = [\delta_x \ \delta_y \ \delta_z]^T$ is the translational motion of the C-arm caused by oscillation and sagging. We can initialize a pose estimation by measuring the C-arm rotation angles that define ${}^s\mathbf{R}_w$, and setting the unknown C-arm translational motion (δ) equal to zero. The error caused by assuming $\delta=0$ can result in significant pose computation errors and consequently in unsuccessful reconstructions. Therefore, we should compensate for translational motions and improve on our pose computation.

As mentioned, Lee's autofocus method³⁷ is not applicable to our problem, due to the absence of the FTRAC. Therefore, we propose a different motion compensation schemes.

We observed that the cardinality of \mathbf{S} —the total number of seed voxels in the VOI—is maximized when the pose is accurately known. Figure 5 shows the cardinality of \mathbf{S} as a function of C-arm translational pose errors in the up-down direction (along z_w) and perpendicular to the plane of rotation (along y_w). This figure shows a simulated case, in which the poses of 4 images are accurately known, and the errors

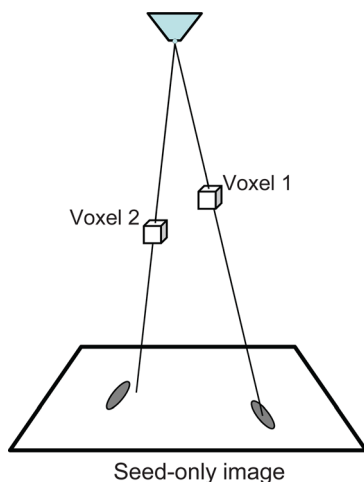


FIG. 4. Projection of two voxels on a seed-only image. In this projection, the voxel value of Voxel 1 is increased by one since Voxel 1 projects on a seed projection in this image. The voxel value of Voxel 2 is unchanged.

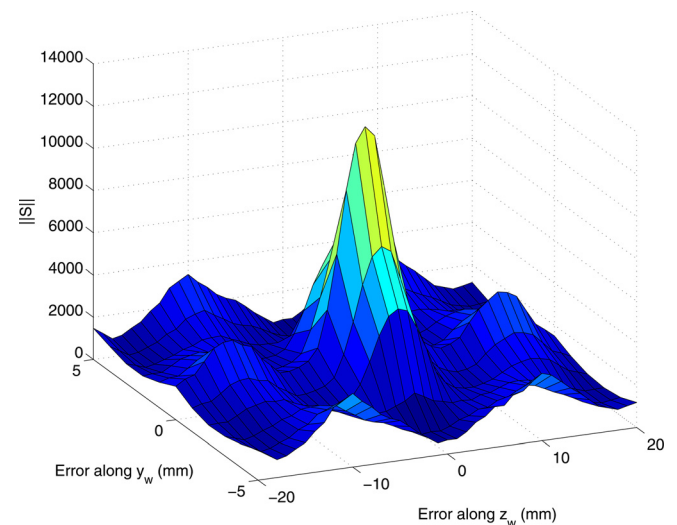


FIG. 5. The total number of seed voxels in a VOI as a function of pose estimation errors. Errors are in the up-down direction (along z_w) and perpendicular to the plane of rotation (along y_w).

are added to the 5th pose. Note that the cardinality of S is an integer-valued function.

In the motion compensation algorithm, we assume that the position of the C-arm corresponding to the first image (henceforth the first C-arm) is fixed in the 3D space and compensate for 2D motion of the rest of the C-arm positions by solving the following problem:

$$\begin{aligned} \delta_i^* &= \arg \max_{\delta_i} \|S\|, \\ \text{s.t. } \delta_{xi} &= 0, \\ i &\in \{2, \dots, M\}, \end{aligned} \quad (5)$$

where $\|\cdot\|$ denotes the cardinality of a set.

Note that unlike motion compensation methods introduced in the previous work,^{25,37,48,49} this method does not require seeds to compensate for pose errors.

The optimization function in Eq. (5) is integer-valued. Furthermore, it has several local maximums, as can be seen in Fig. 5. In order to remedy these problems, we exploit the covariance matrix adaptation evolution strategy (CMA-ES).⁵⁴ This is a stochastic and gradient-free numerical optimization method suitable for nonlinear and nonconvex problems.

Although we benefit from a fast forward-projection method explained in Sec. II B, populating the VOI in every iteration can be time consuming depending on its size and resolution and the number of images. In order to reduce the computational time, the motion compensation is performed on a smaller VOI with a lower resolution. In addition, only a portion of each image is used to populate the smaller VOI.

Rotation of the C-arm around its PA results in horizontal motion of the seeds between images in a way that seed projections located at the top or bottom of one image appear at the top or bottom of the other images. Therefore, we use a narrow band from the top of each seed-only image to populate the smaller VOI during the motion compensation. The size of the VOI during motion compensation is adjusted according to the width of the band. We also observed that extra dilation of the band images increases the capture range of the optimization algorithm and also decreases the number of iterations required to obtain a sufficient motion compensation. Figure 6 shows a sample of a band image used for



FIG. 6. A band image used for motion compensation.

motion compensation. Note that this image is more dilated compared to the image in Fig. 3.

II.D. Seed detection and false positive removal

After motion compensation, the VOI is populated using the improved pose computations. The seed voxels are labeled into different clusters using the so called connected component labeling algorithm.⁵³ Unfortunately, tomosynthesis-based seed reconstruction is prone to producing false positive (FP) seeds, due to the small number of images used (see Fig. 7). These false positive seeds should be removed before dose calculation to avoid overestimating the radiation dose.

The FPs are generated when M cone-shaped back projections from M seed projections intersect or touch in a voxel, which is not a true seed voxel. Therefore, the FP clusters usually have small volumes. However, due to errors in the pose computation (even after motion compensation) and calibration parameters, the clusters in the VOI have a wide range of volumes as shown by a histogram of the cluster volumes after motion compensation for a real patient in Fig. 8. Indeed, some of true seed clusters can have small volumes comparable to volume of a false positive cluster. Thus, an FP removal method purely based on the volume of clusters^{34,36} can also remove some of the true seeds. Lee *et al.*³⁷ used an optimal coverage problem approach and a greedy search to remove the FP seeds. They found the minimum subset of the reconstructed seeds that covers all the seed projections in all the images. Looking at Fig. 7, one can see that if we remove any of the true seeds from the reconstructed seeds, we cannot cover all the seed projections in the seed-only images. Therefore, the three true seeds are the only subset of the reconstructed seeds that cover all the seed projections. However, it should be noted that due to seed projection overlap in the images, the smallest subset of the reconstructed seeds that cover all the projections has significantly fewer members than the number of implanted seeds. Therefore, we use information about the cluster volumes to add a necessary number of seeds to the covering subset to reconstruct all the implanted seeds.

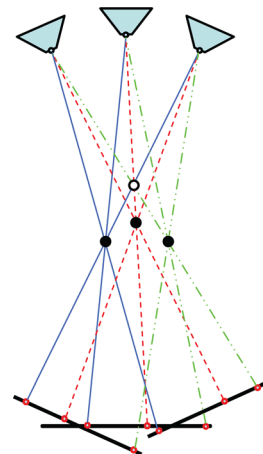


FIG. 7. A false positive seed (white circle) and three true seeds (black circles). If any of the true seeds are removed, one cannot cover all the seed projections in the images.

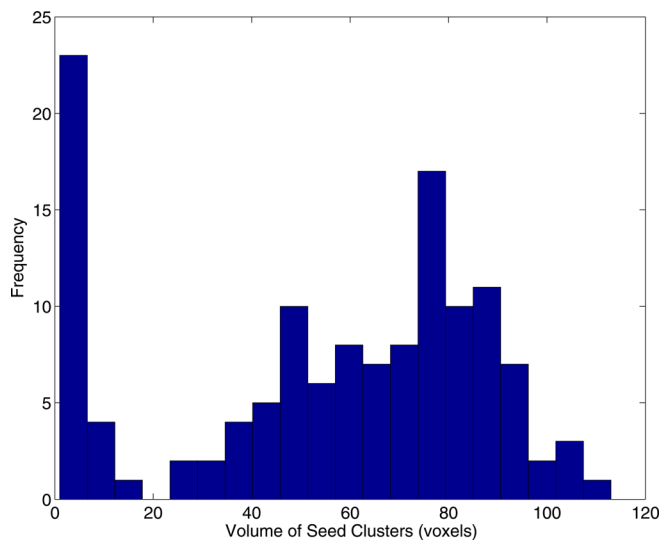


Fig. 8. Histogram of the seed cluster volumes for a real patient. Due to the wide range of cluster volumes, a predefined volume threshold cannot remove the FPs.

We take the following steps to identify and remove the false positives:

1. Clusters with large volumes are separated into multiple clusters. These clusters are generated when two seeds are located very close to each other. Although the seed positions are planned to be at least 5 mm away from each other, due to the seed misplacements, two seeds can be sufficiently close to each other to form a combined cluster. In this paper, we examine all clusters that have a volume greater than the median volume with a 6-neighbor connected component labeling (the initial labeling is performed using 26-neighbor connection). Usually, clusters that are barely touching can be separated into their constituent clusters. In addition, we divide the clusters that have a volume larger than αv_m ($\alpha = 2$ in this work), where v_m is the median volume.
2. The centroids of the seed clusters are calculated as seed candidates and reprojected on the labeled seed-only images.
3. At this point, we generate a $N_t \times M$ assignment table, where N_t is the total number of reconstructed seed centroids (N is the number of implanted seeds). Entry (i, j) of the assignment table shows the label of the seed projection in image j where the i th seed centroid is projected.
4. If two or more seed centroids project on similar seed projections in all the images (have identical rows in the assignment table), the one with the largest cluster volume is saved and the rest are removed, unless the seeds are from a separated large cluster. The seeds that are separated from a large cluster in step 1 are marked and will not be removed.
5. The seed centroids that project on at least one unique seed projection in one image are marked as unique seed centroids and are preserved regardless of their cluster volume. If we remove any of these seeds, we cannot cover all the seed projections.

6. Seed centroids that have a cluster volume smaller than a threshold (20% of the median volume in this work) and are not one of the unique seeds are removed.
7. The list of unique seeds is updated after removal of small clusters. Assume N_u unique seeds are available at this stage. The rest of the seeds share all of their seed projections with other seed centroids. Due to the seed projection overlap (see Figs. 1 or 3), the number of unique seeds is less than the number of implanted seeds.
8. Finally, we add $N - N_u$ seeds with maximum cluster volumes from the remaining seeds to the unique seeds to reconstruct N seeds in total.

II.E. Numerical simulations

Four seed clouds were simulated based on four realistic implant plans with 100, 108, 110, and 130 seeds. Seeds were simulated as capsules with diameter of 1 mm and length of 4.5 mm, approximately equal to the radio-opaque size of ^{125}I seeds. The relative positions of the seed centroids were imported from the plan. We assumed that the long axis of the capsules is parallel to the y_w axis. Seed-only images were synthesized by rotating the C-arm around its PA by angles of 0° , $\pm 5^\circ$, and $\pm 10^\circ$, while the SA angle was kept constantly at 180° . Translational errors of 0–5 mm along the y_w axis with steps of 1 mm and 0–20 mm along the z_w with steps of 2 mm were independently applied to one of the C-arm poses. All of the five images were used to reconstruct the seeds, with and without motion compensation. Intrinsic parameters of a GE OEC[®] 9800 mobile C-arm were used in the simulations.

II.F. Phantom validation

A CIRS Model-053 prostate brachytherapy training phantom (CIRS Inc., Norfolk, VA) was used in our phantom study. An experienced brachytherapist implanted 136 dummy stranded seeds using 26 needles, based on a realistic implant plan prepared by a board-certified medical physicist. A motorized GE OEC 9800 mobile C-arm was used to acquire five images by rotating the device around its PA in a 20° rotation span in approximately 5° intervals. Rotation angles were measured using a digital protractor attached to the C-arm source casing. In order to establish a ground truth, the phantom was also scanned with a Picker PQ5000 CT scanner. We segmented the seeds in the CT volume by thresholding.

II.G. Patient study

Ten patients were implanted with 100–135 (average 112) stranded ^{125}I seeds at the British Columbia Cancer Agency (Vancouver, BC, Canada). The patients had a prescribed dose of 144.0 Gy and an average prostate target volume (PTV) of 54.5 cc. For each patient, five images were taken using a motorized GE OEC 9800. This device has a heavy intensifier that causes significant sagging and necessitates motion compensation for seed reconstruction. The C-arm was rotated around its PA, which was aligned with the craniocaudal axis of the patient. The images were taken at angles of

approximately $0^\circ, \pm 5^\circ$, and $\pm 10^\circ$. Rotation angles were measured using a digital protractor or the device joint encoders. The digital protractor had a resolution of 0.1° and the joint encoders had a resolution of 1° . The rotation angle around SA was fixed at 180° . However, deviations of 1° were observed according to the C-arm joint encoders. These deviations were taken into account during the seed reconstruction.

The C-arm was calibrated preoperatively. We assumed that the C-arm intrinsic parameters were constant for all the rotation angles and patients. The seeds were reconstructed in a $65 \times 80 \times 70 \text{ mm}^3$ VOI with a voxel size of $0.25 \times 0.5 \times 0.5 \text{ mm}^3$ and image dilation radius of 2 or 3 pixels. During the motion compensation, band images with band width of 150 pixels and dilation radius of 6 pixels were used for all the patients. A $65 \times 10 \times 70 \text{ mm}^3$ VOI with a voxel size of $1 \times 1 \times 1 \text{ mm}^3$ was used to achieve higher speeds.

III. RESULTS

III.A. Numerical simulations

For numerical simulations, the localization error was measured as the distance between the reconstructed and synthesized seeds after a rigid registration. Figure 9 shows the seed detection rate and localization error of the reconstructed seeds versus the introduced pose error. As it can be seen, motion-compensated seed reconstruction is able to maintain high seed detection rates and low localization errors, despite the presence of translational pose errors, while the reconstruction without motion compensation fails.

III.B. Phantom study

The seeds reconstructed using the motion-compensated tomosynthesis were compared with the seeds segmented in CT after a rigid registration. Although the CT and fluoroscopy images were taken at different times, we assumed that the phantom deformation and seed displacements were negligible. We achieved a 100% seed detection rate with $0.86 \pm 0.44 \text{ mm}$ (Mean \pm STD) localization difference between CT and C-arm-based reconstructions.

III.C. Clinical results

For our clinical data sets, we reprojected the reconstructed seeds on the C-arm images as shown in Fig. 10. As it can be seen, hidden and overlapping seeds were successfully reconstructed. The images were meticulously inspected for missing seeds. The seed detection rate for each patient is reported in Table I.

Since the real positions of the seeds were unknown, we compared our results with the results of an available motion-compensated matching-based seed reconstruction method⁴⁹ after a rigid registration and reported the registration error in Table I.

We achieved an average seed detection rate of 99.5%, which is a clinically excellent result. Su *et al.*⁵⁵ showed that in ^{125}I prostate implants a seed detection rate of above 95% is sufficient to achieve clinically accurate dose calculations. Our seed detection rates are above this threshold for all the patients. The seed detection rate without motion compensation

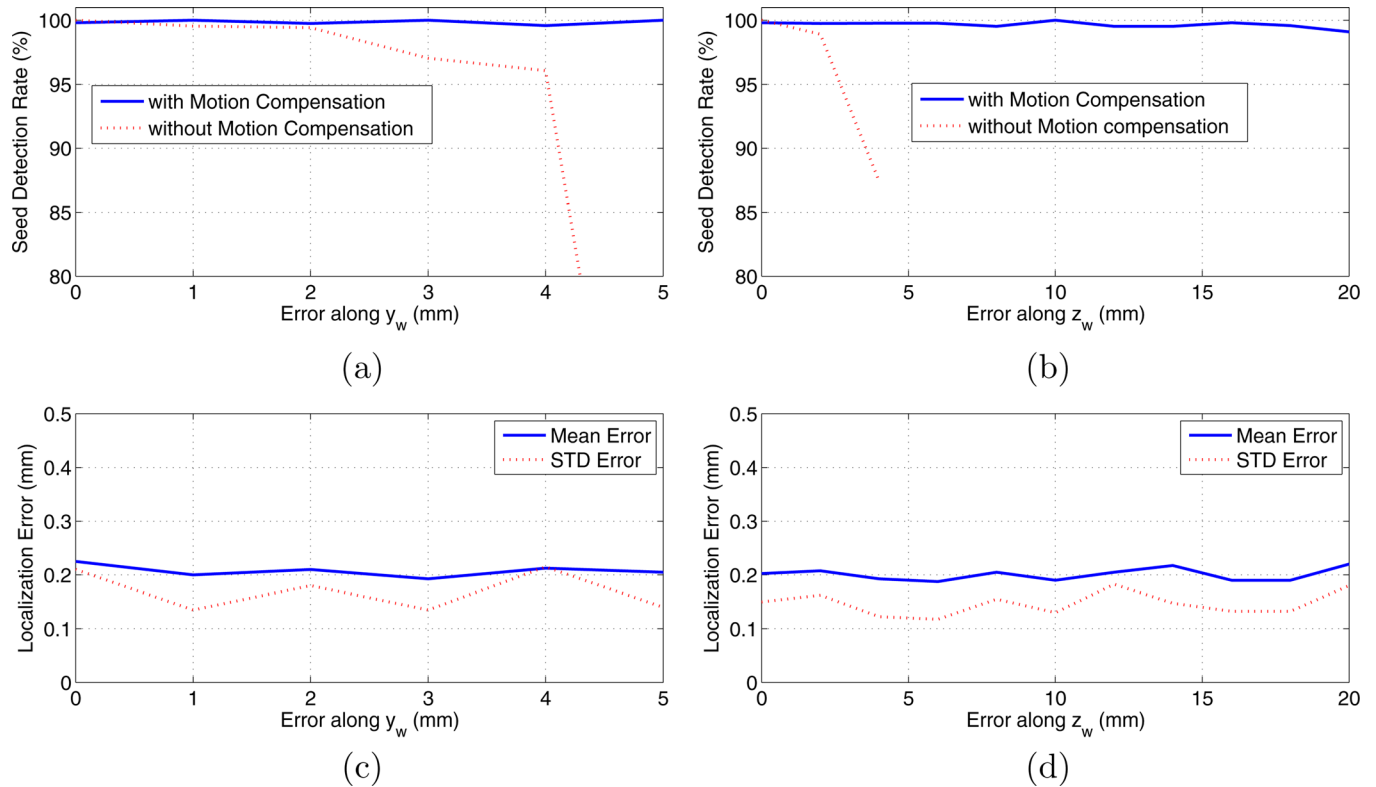


FIG. 9. Simulation results, showing the average seed detection rate and localization error for variable pose errors. The average of seed detection rate for errors along y_w and z_w are shown in (a) and (b), respectively, for reconstructions with and without motion compensation. The mean and STD of localization error for errors along y_w and z_w are shown in (c) and (d), respectively, for reconstruction with motion compensation.

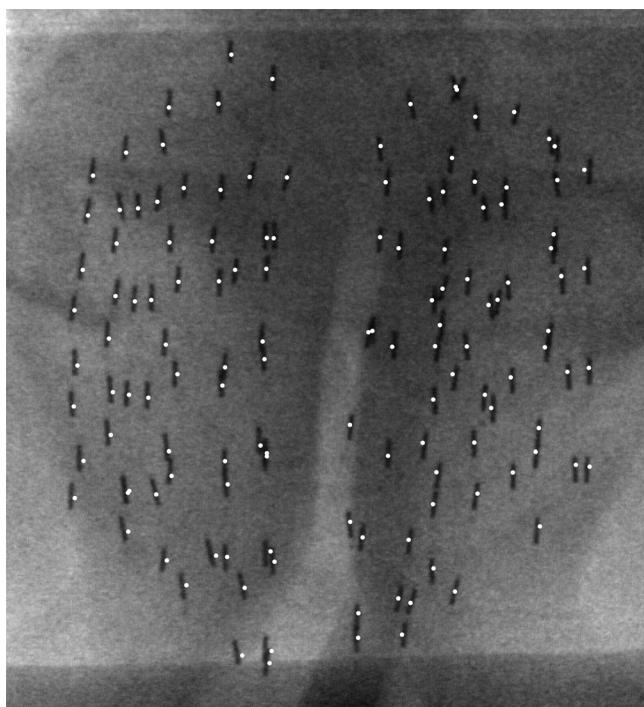


FIG. 10. Reconstructed seed centroids projected on the C-arm image.

was on average below 50%. This shows the necessity of motion compensation, when only C-arm rotation angles are measured.

We used five images for eight of the patients. For patients 9 and 10, seed detection using four images was more successful. This was due to inaccurate rotation angle measurement for one of the images, most likely caused by inaccurate reading of the encoder or protractor while the C-arm was still oscillating. Grzeda and Fichtinger⁵⁰ used accelerometers to measure the C-arm rotation angles with high accuracy. In addition, the accelerometer can sense the C-arm oscillation and send a signal to the operator when the oscillation is sufficiently decayed. Therefore, using accelerometers results in more accurate rotation angle measurement and sharper images.

In the case of the stranded ¹²⁵I seeds used in our clinical study, the seeds in a strand are kept at a fixed center-to-center

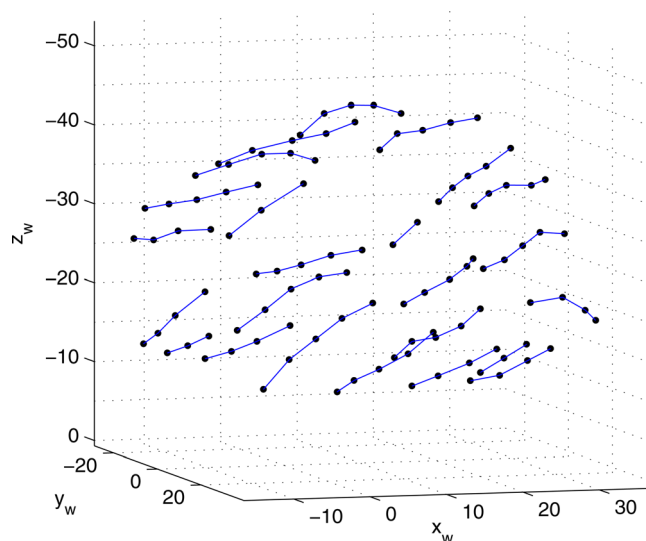


FIG. 11. Reconstructed seed centroids. Seeds on the same strand are connected to each other.

distance of 10 mm. In order to gain more confidence in the reconstruction results and confirm that no significant scaling occurred, we calculated the center-to-center distance of the reconstructed seeds in the different strands.⁵⁶ Figure 11 shows a reconstruction, in which seeds are grouped based on their strand. Table II shows the mean and STD of interseed spacing for all the patients. The interseed spacing has an overall average of 10.3 mm, demonstrating an insignificant scaling effect.

IV. DISCUSSION

IV.A. Large cluster separation

In a brachytherapy plan, seeds are located at least 5 mm apart from each other. Due to a seed misplacement or migration, two seeds may be located sufficiently close to each other to create a combined seed cluster in the VOI. In the case of stranded seeds, two consecutive seeds cannot move toward each other to create a combined cluster. Nevertheless, two adjacent seeds that are not on the same strand may be located sufficiently close to each other to create a combined cluster.

TABLE I. The clinical results. The reconstruction rate is assessed visually based on the projection of the reconstructed seeds on the images. The difference reports the registration error between seed locations computed using the proposed method and an available seed reconstruction method.

Patient #	Number of seeds	Detection rate (%)	Difference (mm) mean \pm STD	Dilation radius (pixel)
1	105	100.0	0.4 \pm 0.3	2
2	105	100.0	0.3 \pm 0.4	2
3	135	100.0	0.4 \pm 0.3	3
4	102	99.0	0.4 \pm 0.3	2
5	122	100.0	0.6 \pm 0.4	2
6	113	100.0	0.5 \pm 0.3	2
7	100	98.0	0.5 \pm 0.5	2
8	120	99.2	0.9 \pm 0.5	3
9 ^a	104	98.1	0.5 \pm 0.3	2
10 ^a	115	99.2	0.6 \pm 0.4	2

^aFor patients 9 and 10, only four images were used.

TABLE II. The mean and STD of the distance between two consecutive seeds on a strand.

Patient #	Seed spacing (mm) mean \pm STD
1	10.3 \pm 0.4
2	10.3 \pm 0.3
3	10.3 \pm 0.3
4	10.3 \pm 0.3
5	10.3 \pm 0.5
6	10.2 \pm 0.4
7	10.4 \pm 0.6
8	10.0 \pm 0.5
9	10.4 \pm 0.3
10	10.2 \pm 0.4
Overall	10.3 \pm 0.4

Due to C-arm calibration and pose computation errors (even after motion compensation), the seed clusters have a wide range of volumes (see Fig. 8). In addition, if two seeds are very close to each other, the volume of the merged cluster will not be significantly larger than a single-seed cluster. Therefore, detection of multiple-seed clusters is not possible by using a uniform threshold on the volume.

As mentioned, ^{125}I seeds have larger seed projections compared to ^{103}Pd seeds, which lead to more overlapping seed projections in the images, which in turn increase the likelihood of having combined clusters in the VOI. In addition, the seed density can affect the likelihood of formation of combined clusters. Our patients had a seed density of approximately 2 seeds per milliliter (total number of seeds divided by PTV), with more concentration at the posterior-peripheral region.³ In treatment plans with a lower seed density, the seeds are more separated and merged clusters are less likely to form.

IV.B. Determination of seed dilation radius

Even after motion compensation, the reconstruction may suffer from minor errors in the rotation angle measurement, calibration parameters, and geometric distortion as well as from motion along the x_w axis. Since seed clusters are formed at the intersection of rays that emanate from a seed projection toward the x-ray source, seed-only image dilation can decrease the effects of the aforementioned errors as it can increase the likelihood of seed detection by increasing the size of the seed projections. However, if the dilation radius is too large, the seed clusters will grow in size and ultimately merge. Therefore, the best dilation radius should be chosen specifically based on the pose and parameter estimation errors. We used a dilation radius of 2 pixels in the numerical simulations and phantom study and a radius of 2 or 3 pixels for the patient data sets (see Table I). However, it should be noted that a fixed dilation radius of 6 pixels was used during the motion compensation phase in simulation, phantom, and clinical studies. Since motion compensation is the most time consuming part of the seed reconstruction algorithm, it is possible to use a fixed dilation radius for motion compensation, then adjust the dilation radius during

final VOI reconstruction and seed detection. The final VOI reconstruction and seed detection take approximately 5 s of runtime.

A variable dilation radius can be helpful in increasing the detection rate without increasing the large clusters. In such a method, the dilation radius will be larger for images or part of images that are affected more by the aforementioned errors, while a small dilation radius can be applied where the errors are small. Investigation on variable dilation radius is part of the future work.

IV.C. Localization error

In contemporary brachytherapy, implants are assessed using CT, one or several days after the procedure. C-arm images are, however, taken during or at the end of the procedure, while the patient is still in treatment position. In addition, in our case, the TRUS probe was still partially inside the rectum during C-arm imaging, while the CT scan was performed without the TRUS. Due to prostate swelling during and after brachytherapy,⁷ postimplant seed migration,⁸ and probe pressure, seed positions during CT scan were different from the position of the seeds when the C-arm images were taken. Therefore, CT images of the patient could not be used to establish a confident ground truth for the position of the seeds in 3D. For this reason, we relied on the projection of the reconstructed seeds on the images and on the comparison with the results of another reconstruction method to assess our reconstructions.

It was shown that a localization uncertainty of less than 2 mm results in less than 5% deviation in the prostate D90 (the minimum dose delivered to 90% of the prostate).^{57,58} Although we could not measure the seed localization error for our clinical data sets, the localization errors in our numerical simulations and phantom studies were significantly lower than this threshold.

IV.D. Computation time

We implemented our algorithm using MATLAB on a PC with an Intel 2.33 GHz Core2 Quad CPU and 3.25 GB of RAM. MATLAB implementation of CMA-ES algorithm was provided by N. Hansen.⁵⁹ The CMA-ES algorithm shows faster convergence if the parameter search region is limited. Thus, we limited the search region to ± 30 mm along the z_w axis and ± 3 mm along y_w . We used the center of mass of the seed-only images to initialize the displacement along y_w . Therefore, displacements of larger than 3 mm in this direction could be recovered in the simulation studies. This search region was sufficiently large for all clinical data sets.

The criterion to terminate the optimization was set to 2000 function evaluations. This resulted in a constant reconstruction time of approximately 1 min per patient (excluding the production of seed-only images). Our code was not optimized for computational speed. We expect to gain faster performance using an optimized C++ implementation. Band images and a smaller VOI with lower resolution were used during the motion compensation phase to decrease the

computation time. Investigation on the optimal image band width and the size and resolution of the VOI for the least computational cost are part of our future work.

On our patient data sets, we achieved an average seed detection rate of 99.5% with computational time of approximately 1 min per patient. Similar detection rates were reported using previously published tomosynthesis-based reconstruction methods. In particular, Lee *et al.*³⁷ reported an average detection rate of 98.8% in approximately 100 s per patient and Brunet-Benkhoucha *et al.*³⁶ reported an average detection rate of 96.7% with 36.5 s average computational time. Brunet-Benkhoucha *et al.* used a radiotherapy simulator, which is a precisely calibrated and accurately tracked device. Hence, they did not require motion compensation.³⁶ As discussed before, Lee *et al.*³⁷ used the FTRAC (Ref. 46) to initialize a pose estimation and also choose the best images to reconstruct some seeds for seed-based motion compensation. The same radio-opaque fiducial was also used by Jain *et al.*,³⁰ Kon *et al.*,³¹ and Lee *et al.*³² to reconstruct the seeds using a matching-based approach. In these works, the pose computation accuracy provided by the FTRAC was sufficient for high detection rates without motion compensation. As mentioned, employing such a fiducial requires an additional segmentation task. Furthermore, image acquisition in presence of this fiducial is more complicated in order to avoid an overlap between the fiducial image and the seed projections.

In our previous work,⁴⁹ we achieved an average seed reconstruction rate of 98.5% with average computational time of 19.8 s per patient using three images in a motion-compensated matching-based reconstruction. Although the detection rate in the current paper is only slightly better than our previous work, the true advantage of the current work is in enabling motion compensation with tomosynthesis-based reconstruction. As discussed earlier, matching-based seed reconstruction methods require a more complicated seed segmentation algorithm as they require the seed projection centroids, which are difficult to localize in the presence of hidden and overlapping projections. Especially for ¹²⁵I seeds that have relatively longer seed projections, overlapping seeds are more common in the projection images. For this reason, in our previous work, we relied on manual seed segmentation which is a time consuming task. Compared to matching-based reconstructions, tomosynthesis-based reconstruction methods require a simple image processing step to separate the seed projection regions from the background. Therefore, our current work introduces an alternative solution for seed reconstruction, which is especially attractive for reconstruction of ¹²⁵I seeds. We should emphasize that the motion compensation method proposed in our previous work is not applicable to tomosynthesis.

As mentioned in Sec. II C, rotation of the C-arm around its PA results in horizontal movement of the seed projections between images. If the C-arm rotates around its SA, the seed projections move along vertical lines in the images. Therefore, vertical bands from the sides of the images can be used for motion compensation. Similarly to our case, the motion in the up-down direction and perpendicular to the plane of rotation should be compensated.

We used the constant center-to-center distance of the stranded seeds to show that no significant scaling occurred. However, the motion compensation and reconstruction methods do not rely on any information limited to stranded seeds. Therefore, we expect similar performance for non-stranded seeds.

The motion compensation method can be extended to use more images at the expense of computational time. Increasing the number of images can reduce the number of false positives and increase the seed detection rate. It can also decrease the likelihood of formation of merged clusters by decreasing the volume of seed clusters. The same effect can be achieved by using a wider rotation span.

In our case, we assumed that the image geometric distortion was negligible as we positioned the C-arm to capture the seed projections close to the center of the image. However, correction of the geometric image distortion can increase the seed detection rate and improve the localization accuracy. Although image distortion is pose dependent, Jain *et al.*⁵¹ showed that in small rotation spans, the correction parameters obtained from an image acquired in the center of the rotation span can considerably correct for the distortion of all the images with insignificant relative deviation in reconstructed seed positions.

V. CONCLUSIONS AND FUTURE WORK

We introduced a computational 2D motion compensation algorithm for tomosynthesis-based seed reconstruction from C-arm images. We initialized the C-arm pose using sole measurements of rotation angles, and we compensated for C-arm motions in the up-down direction and perpendicular to the plane of rotation by maximizing the number of seed voxels in the volume of interest. Our method does not require reconstructed seeds for motion compensation. Therefore, it can be used to recover from severe pose errors that inhibit reconstruction of a sufficient number of initial seeds.

In a clinical study on ten patients, we measured the C-arm rotation angle around its PA using a digital protractor and C-arm joint encoders. Seed reconstruction with motion compensation achieved an average seed detection rate of 99.5%, which is a clinically excellent result, with a 1 min per patient reconstruction time. We also achieved 100% seed detection rate with 0.86 ± 0.44 mm localization error in a phantom study.

Our motion compensation algorithm obviates the need for full pose tracking with radio-opaque fiducials or other external trackers. Considering the simplicity of implementation and high seed detection rates, our algorithm appears to be feasible for clinical application.

Two dimensional motion of the C-arm was an essential assumption in this work. Extension of our motion compensation to 3D and removing the scaling effect using the inter-seed spacing are part of the future work.

ACKNOWLEDGMENTS

The authors would like to thank Lauren Gordon, B.Sc. for preparing the code for seed grouping. Ehsan Dehghan was

supported by an Ontario Ministry of Research and Innovation postdoctoral fellowship. Mehdi Moradi was supported by Natural Sciences and Engineering Research Council of Canada, and US Army Medical Research and Material Command under W81XWH-10-1-0201. W. James Morris is the principal investigator on two randomized control trials that are sponsored, in part, by unrestricted educational grants from Oncura corporation, which makes the ^{125}I sources used in the study. Gabor Fichtinger was supported as Cancer Care Ontario Research Chair. This work was supported in part by NIH Grant No. R21CA120232-01.

^{a)} Author to whom correspondence should be addressed. Electronic mail: tims@ece.ubc.ca

- ¹A. Jemal, R. Siegel, J. Xu, and E. Ward, "Cancer statistics, 2010," *Ca-A Cancer J. Clin.* **60**, 277–300 (2010).
- ²J. C. Blasko, T. Mate, J. E. Sylvester, P. D. Grimm, and W. Cavanagh, "Brachytherapy for carcinoma of the prostate: Techniques, patient selection, and clinical outcomes," *Semin. Radiat. Oncol.* **12**, 81–94 (2002).
- ³W. Morris, M. Keyes, D. Palma, I. Spadinger, M. McKenzie, A. Agronovich, T. Pickles, M. Liu, W. Kwan, J. Wu, E. Berthelet, and H. Pai, "Population-based study of biochemical and survival outcomes after permanent ^{125}I brachytherapy for low- and intermediate-risk prostate cancer," *Urology* **73**, 860–865 (2009).
- ⁴W. J. Morris, M. Keyes, D. Palma, M. McKenzie, I. Spadinger, A. Agronovich, T. Pickles, M. Liu, W. Kwan, J. Wu, V. Lapointe, E. Berthelet, H. Pai, R. Harrison, W. Kwa, J. Bucci, V. Racz, and R. Woods, "Evaluation of dosimetric parameters and disease response after ^{125}I iodine transperineal brachytherapy for low- and intermediate-risk prostate cancer," *Int. J. Radiat. Oncol., Biol., Phys.* **73**, 1432–1438 (2009).
- ⁵B. R. Prestidge, J. J. Prete, T. A. Buchholz, J. L. Friedland, R. G. Stock, P. D. Grimm, and W. S. Bice, "A survey of current clinical practice of permanent prostate brachytherapy in the United States," *Int. J. Radiat. Oncol., Biol., Phys.* **40**, 461–465 (1998).
- ⁶V. Lagerburg, M. A. Moerland, J. J. Lagendijk, and J. J. Battermann, "Measurement of prostate rotation during insertion of needles for brachytherapy," *Radiother. Oncol.* **77**, 318–323 (2005).
- ⁷Y. Yamada, L. Potters, M. Zaider, G. Cohen, E. Venkatraman, and M. J. Zelefsky, "Impact of intraoperative edema during transperineal permanent prostate brachytherapy on computer-optimized and preimplant planning techniques," *Am. J. Clin. Oncol.* **26**, e130–e135 (2003).
- ⁸D. B. Fuller, J. A. Koziol, and A. C. Feng, "Prostate brachytherapy seed migration and dosimetry: Analysis of stranded sources and other potential predictive factors," *Brachytherapy* **3**, 10–19 (2004).
- ⁹S. Nag, J. P. Ciezki, R. Cormak, S. Doggett, K. Dewyngaert, G. K. Edmundson, R. G. Stock, N. N. Stone, Y. Yan, and M. J. Zelefsky, "Intraoperative planning and evaluation of permanent prostate brachytherapy: Report of the American brachytherapy society," *Int. J. Radiat. Oncol., Biol., Phys.* **51**, 1422–1430 (2001).
- ¹⁰P. F. Orto III, I. B. Tutar, S. Narayanan, S. Arthurs, P. S. Cho, Y. Kim, G. Merrick, and K. E. Wallner, "Intraoperative ultrasound-fluoroscopy fusion can enhance prostate brachytherapy quality," *Int. J. Radiat. Oncol., Biol., Phys.* **69**, 302–307 (2007).
- ¹¹A. Polo, C. Salembier, J. Venselaar, and P. Hoskin, "Review of intraoperative imaging and planning techniques in permanent seed prostate brachytherapy," *Radiother. Oncol.* **94**, 12–23 (2010).
- ¹²B. H. Han, K. Wallner, G. Merrick, W. Butler, S. Sutlief, and J. Sylvester, "Prostate brachytherapy seed identification on post-implant TRUS images," *Med. Phys.* **30**, 898–900 (2003).
- ¹³E. J. Feleppa, S. Ramachandran, S. K. Alam, A. Kalisz, J. A. Ketterling, R. D. Ennis, and C.-S. Wu, "Novel methods of analyzing radio-frequency echo signals for the purpose of imaging brachytherapy seeds used to treat prostate cancer," *Proc SPIE*, **4687**, 127–138 (2002).
- ¹⁴S. McAleavey, D. Rubens, and K. Parker, "Doppler ultrasound imaging of magnetically vibrated brachytherapy seeds," *IEEE Trans. Biomed. Eng.* **50**, 252–254 (2003).
- ¹⁵F. Mitri, P. Trompette, and J.-Y. Chapelon, "Improving the use of vibroacoustography for brachytherapy metal seed imaging: A feasibility study," *IEEE Trans. Med. Imaging* **23**, 1–6 (2004).
- ¹⁶M. Ding, Z. Wei, L. Gardi, D. B. Downey, and A. Fenster, "Needle and seed segmentation in intra-operative 3D ultrasound-guided prostate brachytherapy," *Ultrasonics* **44**, e331–e336 (2006), Proceedings of Ultrasonics International (UI'05) and World Congress on Ultrasonics (WCU).
- ¹⁷Z. Wei, L. Gardi, D. B. Downey, and A. Fenster, "Automated localization of implanted seeds in 3D TRUS images used for prostate brachytherapy," *Med. Phys.* **33**, 2404–2417 (2006).
- ¹⁸X. Wen, S. E. Salcudean, and P. D. Lawrence, "Detection of brachytherapy seeds using 3D transrectal ultrasound," *IEEE Trans. Biomed. Eng.* **57**, 2467–2477 (2010).
- ¹⁹D. F. French, J. Morris, M. Keyes, O. Goksel, and S. E. Salcudean, "Intraoperative dosimetry for prostate brachytherapy from fused ultrasound and fluoroscopy images," *Acad. Radiol.* **12**, 1262–1272 (2005).
- ²⁰Y. Su, B. J. Davis, M. G. Herman, and R. A. Robb, "TRUS-fluoroscopy fusion for intraoperative prostate brachytherapy dosimetry," *Studies in Health Technology and Informatics*, **119**, 532–537 (2006).
- ²¹I. B. Tutar, L. Gong, S. Narayanan, S. D. Pathak, P. S. Cho, K. Wallner, and Y. Kim, "Seed-based transrectal ultrasound-fluoroscopy registration method for intraoperative dosimetry analysis of prostate brachytherapy," *Med. Phys.* **35**, 840–848 (2008).
- ²²P. Fallavollita, Z. Karim-Aghaloo, E. Burdette, D. Song, P. Abolmaesumi, and G. Fichtinger, "Registration between ultrasound and fluoroscopy or CT in prostate brachytherapy," *Med. Phys.* **37**, 2749–2760 (2010).
- ²³H. I. Amols and I. I. Rosen, "A three-film technique for reconstruction of radioactive seed implants," *Med. Phys.* **8**, 210–214 (1981).
- ²⁴T. M. Persons, R. L. Webber, P. F. Hemler, W. Bettermann, and J. D. Bourland, "Brachytherapy volume visualization," *Proc. SPIE*, **3976**, 45–56 (2000).
- ²⁵D. Tubic, A. Zaccarin, L. Beaulieu, and J. Pouliot, "Automated seed detection and three-dimensional reconstruction. II. Reconstruction of permanent prostate implants using simulated annealing," *Med. Phys.* **28**, 2272–2279 (2001).
- ²⁶D. A. Todor, G. N. Cohen, H. I. Amols, and M. Zaider, "Operator-free, film-based 3D seed reconstruction in brachytherapy," *Phys. Med. Biol.* **47**, 2031–2048 (2002).
- ²⁷Y. Su, B. J. Davis, M. G. Herman, and R. A. Robb, "Prostate brachytherapy seed localization by analysis of multiple projections: Identifying and addressing the seed overlap problem," *Med. Phys.* **31**, 1277–1287 (2004).
- ²⁸S. Narayanan, P. S. Cho, and R. J. Marks II, "Three-dimensional seed reconstruction from an incomplete data set for prostate brachytherapy," *Phys. Med. Biol.* **49**, 3483–3494 (2004).
- ²⁹S. T. Lam, P. S. Cho, R. J. Marks II, and S. Narayanan, "Three-dimensional seed reconstruction for prostate brachytherapy using Hough trajectories," *Phys. Med. Biol.* **49**, 557–569 (2004).
- ³⁰A. K. Jain, Y. Zhou, T. Mustufa, E. C. Burdette, G. S. Chirikjian, and G. Fichtinger, "Matching and reconstruction of brachytherapy seeds using the Hungarian algorithm (MARSHAL)," *Med. Phys.* **32**, 3475–3492 (2005).
- ³¹R. C. Kon, A. K. Jain, and G. Fichtinger, "Hidden seed reconstruction from C-arm images in brachytherapy," *IEEE International Symposium on Biomedical Imaging: Nano to Macro* (Arlington, Virginia, 2006).
- ³²J. Lee, C. Labat, A. K. Jain, D. Y. Song, E. C. Burdette, G. Fichtinger, and J. L. Prince, "REDMAPS: Reduced-dimensionality matching for prostate brachytherapy seed reconstruction," *IEEE Trans. Med. Imaging* **30**, 38–51 (2011).
- ³³G. Messaris, Z. Kolitsi, C. Badea, and N. Pallikarakis, "Three-dimensional localisation based on projectional and tomographic image correlation: an application for digital tomosynthesis," *Med. Eng. Phys.* **21**, 101–109 (1999).
- ³⁴I. B. Tutar, R. Managuli, V. Shamdasani, P. S. Cho, S. D. Pathak, and Y. Kim, "Tomosynthesis-based localization of radioactive seeds in prostate brachytherapy," *Med. Phys.* **30**, 3135–3142 (2003).
- ³⁵X. Liu, A. K. Jain, and G. Fichtinger, "Prostate implant reconstruction with discrete tomography," *MICCAI 2007, Lecture Notes in Computer Science* 4791, Springer Berlin/Heidelberg, pp. 734–742.
- ³⁶M. Brunet-Benkhoucha, F. Verhaegen, B. Reniers, S. Lassalle, D. Bélieu-Nadeau, D. Donath, D. Taussky, and J.-F. Carrier, "Clinical implementation of a digital tomosynthesis-based seed reconstruction algorithm for intraoperative postimplant dose evaluation in low dose rate prostate brachytherapy," *Med. Phys.* **36**, 5235–5244 (2009).
- ³⁷J. Lee, X. Liu, A. Jain, D. Song, E. Burdette, J. Prince, and G. Fichtinger, "Prostate brachytherapy seed reconstruction with Gaussian blurring and optimal coverage cost," *IEEE Trans. Med. Imaging* **28**, 1955–1968 (2009).

- ³⁸D. Pokhrel, M. J. Murphy, D. A. Todor, E. Weiss, and J. F. Williamson, "Reconstruction of brachytherapy seed positions and orientations from cone-beam CT x-ray projections via a novel iterative forward projection matching method," *Med. Phys.* **38**, 474–486 (2011).
- ³⁹S. T. Lam, R. J. Marks II, and P. S. Cho, "Prostate brachytherapy seed segmentation using spoke transform," *Proc. SPIE*, **4322**, 1490–1500 (2001).
- ⁴⁰D. Tubic, A. Zaccarin, J. Pouliot, and L. Beaulieu, "Automated seed detection and three-dimensional reconstruction. I. seed localization from fluoroscopic images or radiographs," *Med. Phys.* **28**, 2265–2271 (2001).
- ⁴¹N. Kuo, J. Lee, A. Deguet, D. Song, E. C. Burdette, and J. Prince, "Automatic segmentation of seeds and fluoroscope tracking (FTRAC) fiducial in prostate brachytherapy x-ray images," *Proc. SPIE*, **7625**, 76252T1 (2010).
- ⁴²T. Peters and K. Cleary, eds., *Image-Guided Interventions: Technology and Applications* (Springer Science+Business Media, New York, 2008).
- ⁴³N. Navab, A. Bani-Hashemi, M. Mitschke, D. W. Holdsworth, R. Fahrig, A. J. Fox, and R. Graumann, "Dynamic geometrical calibration for 3D cerebral angiography," *Proc. SPIE* **2708**, 361–370 (1996).
- ⁴⁴C. Brack, H. Götte, F. Gossé, J. Moctezuma, M. Roth, and A. Schweikard, "Towards accurate X-ray camera calibration in computer-assisted robotic surgery," *Proceedings of the International Symposium on Computer Assisted Radiology* (Paris, France, 1996), pp. 721–728.
- ⁴⁵M. Zhang, M. Zaider, M. Worman, and G. Cohen, "On the question of 3D seed reconstruction in prostate brachytherapy: The determination of x-ray source and film locations," *Phys. Med. Biol.* **49**, N335–N345 (2004).
- ⁴⁶A. K. Jain, T. Mustufa, Y. Zhou, C. Burdette, G. S. Chirikjian, and G. Fichtinger, "FTRAC—A robust fluoroscope tracking fiducial," *Med. Phys.* **32**, 3185–3198 (2005).
- ⁴⁷P. Fallavollita, E. C. Burdette, D. Y. Song, P. Abolmaesumi and G. Fichtinger, "Technical Note: Unsupervised C-arm pose tracking with radiographic fiducial," *Med. Phys.* **38**, 2241–2245 (2011).
- ⁴⁸A. Jain and G. Fichtinger, "C-arm tracking and reconstruction without an external tracker," MICCAI 2006, Lecture Notes on Computer Science 4190, Springer Berlin/Heidelberg, pp. 494–502.
- ⁴⁹E. Dehghan, A. K. Jain, M. Moradi, X. Wen, W. J. Morris, S. E. Salcudean, and G. Fichtinger, "Brachytherapy seed reconstruction with joint-encoded C-arm single-axis rotation and motion compensation," *Med. Image Anal.* **15**, 760–771 (2011).
- ⁵⁰V. Grzeda and G. Fichtinger, "Rotational encoding of C-arm fluoroscope with tilt sensing accelerometer," MICCAI 2010, Lecture Notes in Computer Science 6363, Springer Berlin/Heidelberg, pp. 424–431.
- ⁵¹A. Jain, M. An, N. Chitphakdithai, G. Chintalapani, and G. Fichtinger, "C-arm calibration—Is it really necessary?," *Proceedings of SPIE*, edited by K. Cleary and M. I. Miga (2007), Vol. 6509, 65092U-1–65092U-16.
- ⁵²D. G. French, "Real-time dosimetry for prostate brachytherapy using TRUS and fluoroscopy," Master's thesis, University of British Columbia, Vancouver, BC, Canada, December 2004.
- ⁵³R. M. Haralick and L. G. Shapiro, *Computer and Robot Vision*, (Addison-Wesley, Boston, 1992), Vol. 1, pp. 28–48.
- ⁵⁴N. Hansen, "The CMA evolution strategy: A comparing review," *Towards a New Evolutionary Computation. Advances on Estimation of Distribution Algorithms*, Studies in Fuzziness and Soft Computing, edited by J. A. Lozano, P. Larranaga, I. Inza, and E. Bengoetxea (Springer, Berlin/Heidelberg, 2006), Vol. 192, pp. 75–102.
- ⁵⁵Y. Su, B. J. Davis, M. G. Herman, A. Manduca, and R. A. Robb, "Examination of dosimetry accuracy as a function of seed detection rate in permanent prostate brachytherapy," *Med. Phys.* **32**, 3049–3056 (2005).
- ⁵⁶L. Gordon, E. Dehghan, S. E. Salcudean, and G. Fichtinger, "Reconstruction of needle tracts from fluoroscopy images in prostate brachytherapy," *Proceedings of the 22nd International Conference of the Society for Medical Innovation and Technology (SMIT)* (Trondheim, Norway, 2010).
- ⁵⁷P. E. Lindsay, J. Van Dyk, and J. J. Battista, "A systematic study of imaging uncertainties and their impact on ¹²⁵I prostate brachytherapy dose evaluation," *Med. Phys.* **30**, 1897–1908 (2003).
- ⁵⁸Y. Su, B. J. Davis, K. M. Furutani, M. G. Herman, and R. A. Robb, "Dosimetry accuracy as a function of seed localization uncertainty in permanent prostate brachytherapy: Increased seed number correlates with less variability in prostate dosimetry," *Phys. Med. Biol.* **52**, 3105–3119 (2007).
- ⁵⁹Available online at: http://www.lri.fr/hansen/cmaes_inmatlab.html.



Contents lists available at ScienceDirect

Medical Image Analysis

journal homepage: www.elsevier.com/locate/media

Evaluation of visualization of the prostate gland in vibro-elastography images

S. Sara Mahdavi^a, Mehdi Moradi^a, Xu Wen^a, William J. Morris^b, Septimiu E. Salcudean^{a,*}^a Department of Electrical and Computer Engineering, University of British Columbia, Vancouver, BC, Canada V6T1Z4^b Department of Radiation Oncology, British Columbia Cancer Agency, Vancouver, BC, Canada

ARTICLE INFO

Article history:

Received 19 January 2010

Received in revised form 1 March 2011

Accepted 15 March 2011

Available online 31 March 2011

Keywords:

Elastography

Prostate

Segmentation

Edge evaluation

ABSTRACT

In this paper, vibro-elastography (VE), an ultrasound-based method that creates images of tissue visco-elasticity contrast, is evaluated as an imaging modality to visualize and segment the prostate. We report a clinical study to characterize the visibility of the prostate in VE images and the ability to detect the boundary of the gland. Measures for contrast, edge strength characterized by gradient and statistical intensity change at the edge, and the continuity of the edges are proposed and computed for VE and B-mode ultrasound images. Furthermore, using MRI as the gold standard, we compare the error in the computation of the volume of the gland from VE and B-mode images. The results demonstrate that VE images are superior to B-mode images in terms of contrast, with an approximately six fold improvement in contrast-to-noise ratio, and in terms of edge strength, with an approximately two fold improvement in the gradient in the direction normal to the edge. The computed volumes show that the VE images provide an accurate 3D visualization of the prostate with volume errors that are slightly lower than errors computed based on B-mode images. The total gland volume error is $8.8 \pm 2.5\%$ for VE vs. MRI and $10.3 \pm 4.6\%$ for B-mode vs. MRI, and the total gland volume difference is $-4.6 \pm 11.1\%$ for VE vs. MRI and $-4.1 \pm 17.1\%$ for B-mode vs. MRI, averaged over nine patients and three observers. Our results show that viscoelastic mapping of the prostate region using VE images can play an important role in improving the anatomic visualization of the prostate and has the potential of becoming an integral component of interventional procedures such as brachytherapy.

© 2011 Elsevier B.V. All rights reserved.

1. Introduction

Prostate cancer is the most prevalent type of cancer among men and is projected to affect 24,600 men in Canada (Canadian Cancer Society, 2010) and 217,730 in the United States (National Cancer Institute, 2010) in 2010. It is the most numerous cancer diagnosed in European men (382,000 cases in 2008) (Ferlay et al., 2010). Common treatment options include brachytherapy and radical prostatectomy. Low dose rate (LDR) prostate brachytherapy is generally used for early stage, intra-capsular prostate cancer and has rapidly gained acceptance due to its highly successful clinical results (Morris et al., 2009). In this treatment, 40–150 small radioactive seeds (Iodine-125 or Palladium-103) are inserted through the perineum and permanently implanted into the prostate and periprostatic tissue. In high dose rate (HDR) brachytherapy, temporary catheters are placed inside the prostate which allow the placement of high dose rate sources delivering the radiation treatment over a number

of fractions, typically over a few days. Radical prostatectomy is a surgical option in which the prostate is removed either by laparoscopic or open surgery. The surgical margin within which the prostate is removed depends on the stage of the disease.

Effective treatment of prostate cancer, regardless of the treatment method used, requires accurate visualization of the gland and its surrounding region. Accurate delineation of the prostate and appropriate visualization of the prostatic region has the potential to reduce some of the possible side-effects of the current treatment methods. These complications include urinary incontinence, impotence, and damage to the rectum and urethra (Thompson et al., 2007).

Ultrasound is the most commonly used modality for imaging of the prostate. This is due to its availability, safety and ease of use. However, ultrasound B-mode images do not always delineate the prostate reliably. As a result, prostate boundary extraction becomes a highly subjective process (Smith et al., 2007). This is observed specifically at the base of the gland, where the prostate merges with the bladder neck, and the apex, where it blends into the pelvic floor muscles. It has been shown that user segmentation variability is large in these areas (Choi et al., 2009; Tong et al., 1998).

Many attempts have been made to improve the visibility of the prostate in ultrasound B-mode images. These vary from the processing of the images (Sahba et al., 2005; Pathak et al., 2000),

* Corresponding author. Address: Department of Electrical and Computer Engineering, University of British Columbia, 5500-2332 Main Mall, Vancouver, BC, Canada V6T1Z4. Tel.: +1 604 822 3243; fax: +1 604 822 5949.

E-mail addresses: saram@ece.ubc.ca (S. Sara Mahdavi), moradi@ece.ubc.ca (M. Moradi), wenx@ece.ubc.ca (X. Wen), jmorris@bccancer.bc.ca (W.J. Morris), tims@ece.ubc.ca (S.E. Salcudean).

to the use of additional information from other modalities such as MR (Daanen et al., 2006). Another recently developed option is the use of ultrasound elastography.

Elastography (Ophir et al., 1991, 1996) is a promising technique for imaging soft tissues and relies upon measuring tissue strain in response to a mechanical excitation. Indeed, when compressed by an external mechanical exciter, e.g., by the inward motion of the ultrasound transducer in the image axial direction, softer tissue will compress more than stiffer tissue, and therefore experience larger strain, which can be measured and displayed by processing the ultrasound echo data. Alternatively, tissue vibration induced by the exciter can be measured with Doppler ultrasound (Lerner et al., 1988), with larger vibrations corresponding to softer tissue. In transient elastography, the propagation of a shear wave is imaged with parallel receive ultrasound (Tanter et al., 2002). When the excitation is dynamic, the shear modulus can be estimated as a complex function of frequency, thus providing information on the viscoelastic properties of tissue. In the last few years various clinical applications of elastography have been reported in the literature. These include, but are not limited to, breast lesions (Garra et al., 1997; Sinkus et al., 2000; Kadour and Noble, 2009; Li et al., 2009), liver fibrosis (Castéra et al., 2005; Huwart et al., 2008; Yin et al., 2007), vascular vulnerable plaque (Schaar et al., 2003), elastic properties of skeletal muscle (Dresner et al., 2001), thyroid gland tumors (Lyshchik et al., 2005), and assessment of thermal tissue ablation (Wu et al., 2001) and for the detection of prostate cancer (Cochlin et al., 2002; Souchon et al., 2003; Miyagawa et al., 2009; Zhang et al., 2008; Pallwein et al., 2007; Gravas et al., 2009; Kamoj et al., 2008; Fleming et al., 2009).

Elastography has been shown to be promising in improving the visibility of the prostate gland and the cancer within it. In Egorov et al. (2006) the stress pattern on the rectal wall is directly measured with the use of a transrectal probe equipped with a pressure sensor array. Temporal and spatial changes in the stress pattern provide information for calculating prostate features such as size, shape and hardness. Phantom and in vivo results show that such a method has the potential to replace digital rectal examination (DRE). The usefulness of elastography was evaluated on 311 patients in Miyagawa et al. (2009). They showed that the sensitivity of elastography and elastography + TRUS imaging in detecting cancer (confirmed by biopsy) is higher than that of DRE or TRUS only. A higher prostate-specific antigen (PSA) level and smaller prostate

volume are reported to increase the sensitivity of elastography and elastography + TRUS. However, the high frequency of false-positive elastography results and difficulty in the detection of cancer in the peripheral zone are two main problems reported in their work.

Vibro-elastography is a dynamic ultrasound elastography method (Turgay et al., 2006) which models viscoelastic properties of tissue. The approach is illustrated in Fig. 1. The technique relies on the continuous real time acquisition of unprocessed ultrasound echo data as a time series of 'radio-frequency' (RF) data images, while, simultaneously, tissue is externally vibrated with a broad-band mechanical excitation. A time series of tissue displacements or strain images are computed from consecutive RF data images. The tissue displacement as a function of time at a given spatial location can be viewed as the output of a linear system whose input is the motion of the exciter as a function of time. Therefore a frequency response or Transfer Function (TF) that relates the tissue motion at any spatial location with the exciter motion as a reference can be computed in the frequency domain. Alternatively, if the exciter motion is not measured, a tissue region, typically in the focal area of the ultrasound beam, can be selected as the reference. For display, the change in the transfer functions from one spatial location to another can be computed, for example as the L_2 -norm of the difference between the transfer functions over the vibration frequency range.

In Salcudean et al. (2006) we introduced prostate ultrasound vibro-elastography. The signal processing used to obtain the transfer function images used in this paper are presented in detail in Salcudean et al. (2006), together with phantom images and initial in vivo prostate imaging data from three patients. We showed qualitatively that this method has the potential to improve the visibility of the prostate. In this article, our goal is to evaluate quantitatively the ability of vibro-elastography to visualize the prostate in comparison to the commonly used B-mode imaging.

Toward this goal, two groups of evaluation measures are proposed: image-based and volume-based measures. We first evaluate the quality of the images, by computing the standard measure of 'contrast-to-noise ratio' (CNR) in VE and B-mode images. Since the CNR measure does not effectively assess edge quality, we also analyze the quality of edges based on edge strength and edge continuity. For edge strength, we use a gradient-based edge filter and a statistical edge detector. For edge continuity, we compute the similarity of adjacent edge points using a

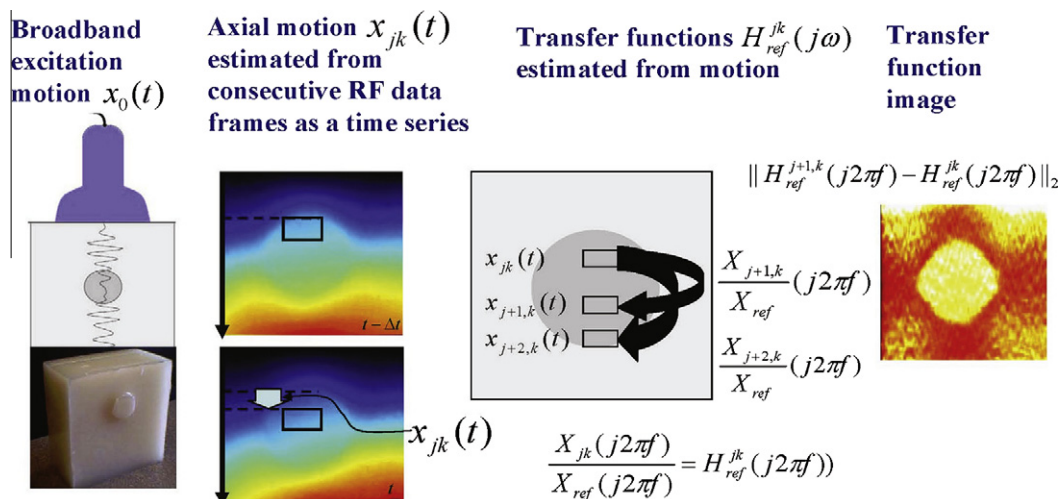


Fig. 1. Schematic representation of vibro-elastography imaging. From left to right, a broad-band external mechanical excitation $x_0(t)$ is applied to the sample; the axial motion $x_{jk}(t)$ of a tissue block indexed axially by j and laterally by k within the ultrasound image is obtained from RF images at time t and $t - \Delta t$; transfer functions from a reference to each of the tissue blocks are estimated, with the illustration showing the reference being the motion $x_{jk}(t)$ of block jk ; images are produced by displaying the L_2 -norm of the difference in transfer functions.

correlation-based measure. We compare the edge evaluation results in VE vs. B-mode images. Then, in order to assess whether the delineated prostate boundary in VE images is indeed the prostate, we use volume-based measures to compare the overall shape and size of the gland as seen in VE and B-mode ultrasound images, with MR images as the gold standard.

The quality assessment criteria used in this paper are based on both standard measures (percentage volume difference, percentage volume error, CNR, gradient filter results) and on new measures, such as changes in image statistics at edges and edge continuity. These new measures had to be developed to deal with the particular situation of prostate segmentation, which requires the identification of a thin capsule within a background of relatively uniform echogenicity.

A preliminary version of the results presented in this paper, however with limited details and analyses, and fewer patients, has appeared in Salcudean et al. (2009) and Mahdavi et al. (2009).

The paper is organized as follows: In Section 2 we summarize the patient data acquisition and the vibro-elastography imaging method used in this study. In Section 2.1, our data acquisition and the resulting images are described. The proposed evaluation measures of this paper are presented in Section 2.2. The results of applying these measures to the collected MRI, B-mode ultrasound and VE data are described in Section 3. Finally, conclusions and a discussion of our results are found in Section 4, which also provides avenues for future research.

2. Materials and methods

2.1. Data acquisition

The B-mode ultrasound, VE, and MR images used in this paper were acquired from patients going through the standard LDR prostate brachytherapy procedure at Vancouver Cancer Center, BC Cancer Agency, or radical prostatectomy at the Vancouver General Hospital. The institutional ethics approval and informed patient consent were obtained prior to data collection.

The MR images were collected between one and two weeks prior to treatment. T2-weighted transverse MR images (slice spacing 4 mm, pixel size $0.27 \text{ mm} \times 0.27 \text{ mm}$) were collected at the UBC MRI research centre, Vancouver, with a Philips Medical Systems Achieva 3.0 Tesla MRI scanner. To minimize the deformation of the gland and for patient comfort, imaging was carried out in a supine position and a cardiac coil was used.

The ultrasound data were collected intra-operatively, just prior to the actual brachytherapy or prostatectomy intervention, using the hardware described in Section 2.1.1 and the signal processing described in Section 2.1.2.

2.1.1. VE system hardware

Fig. 2 shows the transrectal ultrasound (TRUS) VE actuation system developed in our research group for VE imaging of the prostate. An LDR brachytherapy stepper (EXII, CIVCO Medical Solutions) was modified to enable acquisition of RF data volumes. The rotation of the cradle was motorized to enable smooth rotation of the TRUS transducer and a shaker was mounted on the transducer cradle in order to radially vibrate the TRUS probe. Fig. 3 displays a close-up view of the motorized cradle. A PC-based control interface allows the user to control the rotation motion range (-45° to 50° , 0° being the mid-sagittal plane), the amplitude, and frequency range of the transducer vibration. Synchronized with the motion of the probe, frames of RF data are collected from a SonixRP ultrasound machine with the sagittal array of a dual-plane linear/microconvex broad-band 5–9 MHz endorectal transducer (Ultrasonix Medical Corp.). The RF sampling frequency is 20 MHz.

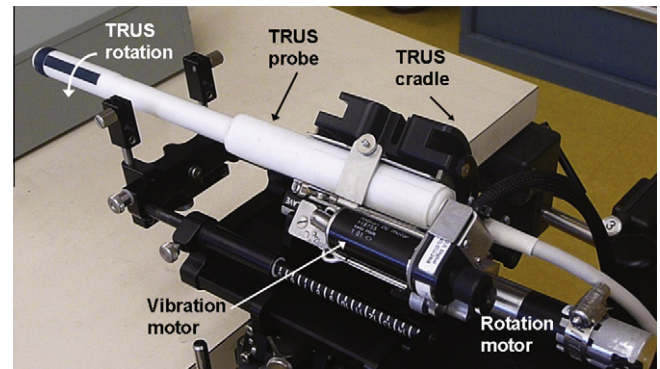


Fig. 2. System setup for vibro-elastography data acquisition.

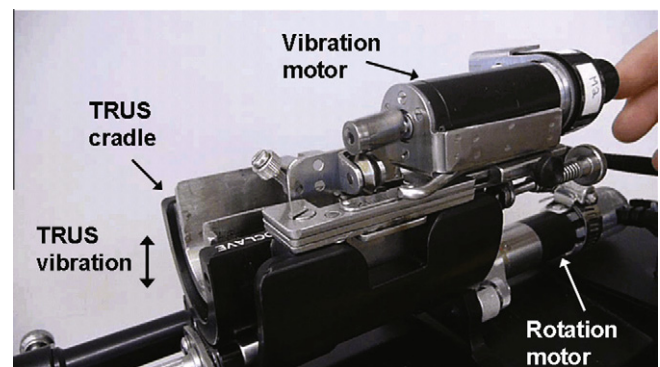


Fig. 3. Details of the motorized cradle.

The vibrating TRUS probe, with a vibration range of 2–10 Hz (for the first 14 cases) and 2–5 Hz (for the last six cases) and vibration amplitude of approximately 1 mm, was swept from -45° to 50° covering a fan of longitudinal planes passing through the transducer axis with a predefined angular separation of 2° . At each angle, one B-mode image and frames of RF data were collected continuously for 2 s at an approximate frame rate of 40 fps. Imaging depth was set to 5 cm (or 6 cm for large prostates). Fig. 4 displays the orientation of the fan of longitudinal planes at which data is collected, with respect to the prostate and the TRUS probe. These planes, which we will simply refer to as 'longitudinal', pass through the transducer axis and include the mid-sagittal plane at angle 0° .

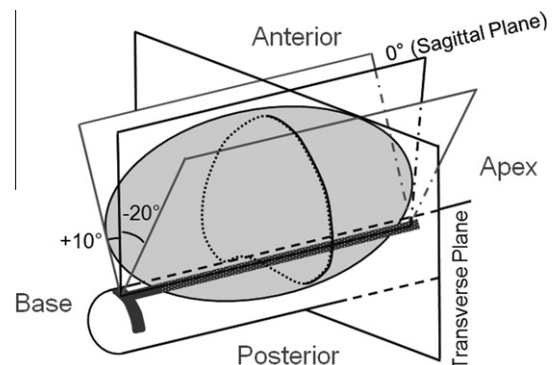


Fig. 4. An illustration of the longitudinal planes at which data is collected, with respect to the prostate and TRUS probe. Here, the mid-sagittal plane, at 0° , and two other planes at angles of -20° and $+10^\circ$ are shown. The orientation of a transverse plane in the mid-gland is also displayed.

2.1.2. VE system signal processing

The RF data were processed to obtain longitudinal VE transfer function images. Single DOF axial motion estimation was used in processing the RF data. Each RF data frame has 128 lines of RF data, each having 1296 samples (1424 for larger prostates). The collected RF data lines are split into blocks of 26 samples, or equivalently 1 mm, with 50% block overlap. The axial displacement $x_{jk}(t)$ of each block at axial location k and lateral location (line) j , and subsequently the axial strain, were computed from one RF data frame to the next by using a correlation-based method, as described in Zahiri-Azar and Salcudean (2006), resulting in axial displacement images of 128 lines by 100 blocks.

An image-based reference was used to compute the transfer function images. It was computed as the average strain, at half the tissue imaging depth, of all the 128 lines. This specific depth was chosen due to two reasons. First, the ultrasound imaging focal point is usually set at this depth, resulting in a more accurate motion estimation. Second, in our images, the half depth line is more likely to be enclosed entirely within the prostate, resulting in more uniform mechanical properties along the line.

The transfer functions $(H_{ref}^{jk}(j2\pi f))$ from this reference to each of the blocks in the strain images were computed using standard signal processing methods described in Salcudean et al. (2006). Transfer function images were generated by computing:

$$TF_{jk} = \frac{1}{f_2 - f_1} \sqrt{\int_{f_1}^{f_2} (H_{ref}^{jk}(j2\pi f) - H_{ref}^{j-1,k}(j2\pi f))^2 df} \quad (1)$$

where $[f_1, f_2]$ describes the frequency range of interest, which in this paper coincides with the range of the broad-band vibration applied to tissue.

If we assume that the Fourier transform of the reference described above is unity, then the contrast in the transfer function image from one spatial location (e.g. a reference) to another corresponds to the strain energy difference between these locations in the frequency range f_1 to f_2 . By computing the ‘difference’ between transfer functions of consecutive blocks j and $j - 1$ on line k , with respect to reference ref (Eq. (1)), changes in stiffness, including the prostate boundary, are highlighted. Throughout this paper, we will refer to these vibro-elastography transfer function images as VE images. An approach to obtain both elasticity contrast and relaxation-time/viscosity contrast using a Voigt tissue model to represent the transfer functions is presented in Eskandari et al. (2008).

From these sets of longitudinal images, 3D VE volumes were generated by interpolation (slice spacing in transverse direction, 0.43 mm, pixel size 0.5 mm \times 0.5 mm). Similarly, the 3D B-mode volume (slice spacing in transverse direction 0.43 mm, pixel size 0.37 mm \times 0.37 mm) was created from the collected longitudinal B-mode images. Various approaches to creating 3D volumes are described in detail in Fenster et al. (2001). Our method of constructing a 3D volume by interpolating longitudinal images suffers from a decrease in image resolution as the depth increases. However, the resolution can be increased by using finer angle increments at the expense of scan time. Another alternative is to use the transverse (convex) array of the TRUS probe to generate a 3D sector view by changing the depth of the transducer with respect to the prostate. This approach also has the issue of decreasing resolution at increased depth because the scan is acquired with a convex array. Furthermore, such a transverse plane sweep changes the TRUS position in the rectum causing the prostate to move as a function of probe depth, which is clearly undesirable. The analysis performed in this paper uses the transverse plane of the constructed 3D volumes for evaluation. This choice was made because of the preference of the transverse view by the clinicians, and also for agreement with the transverse MRI images.

Fig. 5 shows transverse VE, B-mode and MRI images of the prostate mid-gland of two patients. Half of the prostate boundary is delineated in one of the image sets. In Fig. 6 mid-sagittal VE (top row) and B-mode (bottom row) prostate images of three different patients can be seen. The prostate is the stiffer region as outlined in the VE image.

Table 1 describes the image types and number of cases used in this paper. VE and B-mode images were obtained from 20 patients. Among these 20 cases, which consist of 178 co-registered VE and B-mode image pairs, 107 images are in the transverse plane and are used for edge evaluation. The remaining 71 images are in the longitudinal plane at multiples of 5° intervals with the mid-sagittal plane and are used along with the 107 transverse images, for CNR analysis. MRI data was also available for nine of the patients. These nine data sets are used for volume evaluation. The initial study started by recruiting patients for VE imaging at the time of the volume examination. However, we found that the patients were nervous and very uncomfortable with the additional time required to take the images with a different ultrasound machine. In some cases we were able to collect US data, but the same patients were not available for MRI, due to illness, ineligibility for MRI, and difficulty traveling for the additional medical exam. For the data acquired

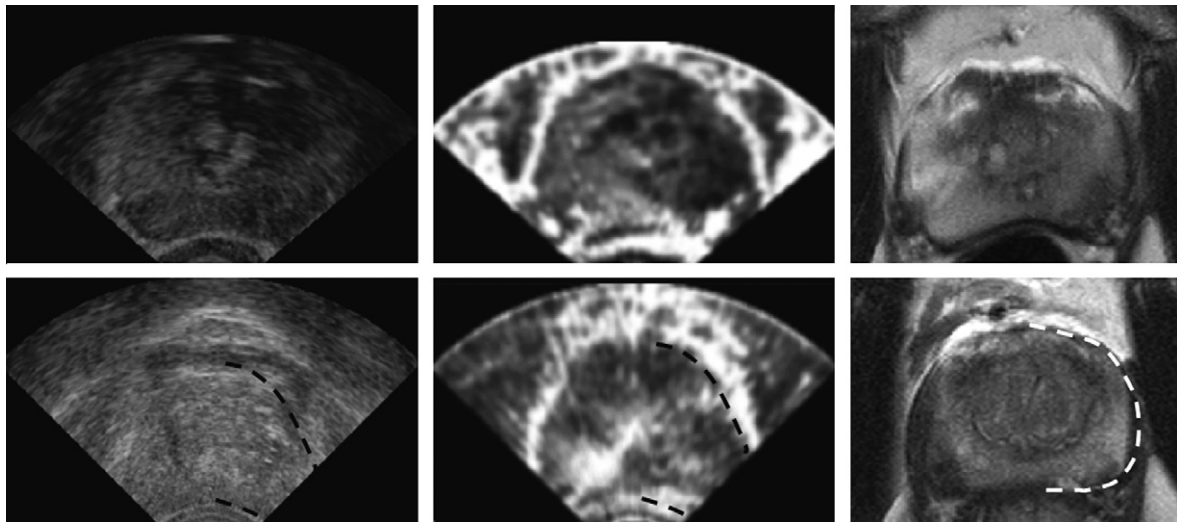


Fig. 5. Transverse B-mode (left), VE (middle) and MRI (right) prostate images of two patients. The boundary of the prostate is partially segmented in the second set of images.

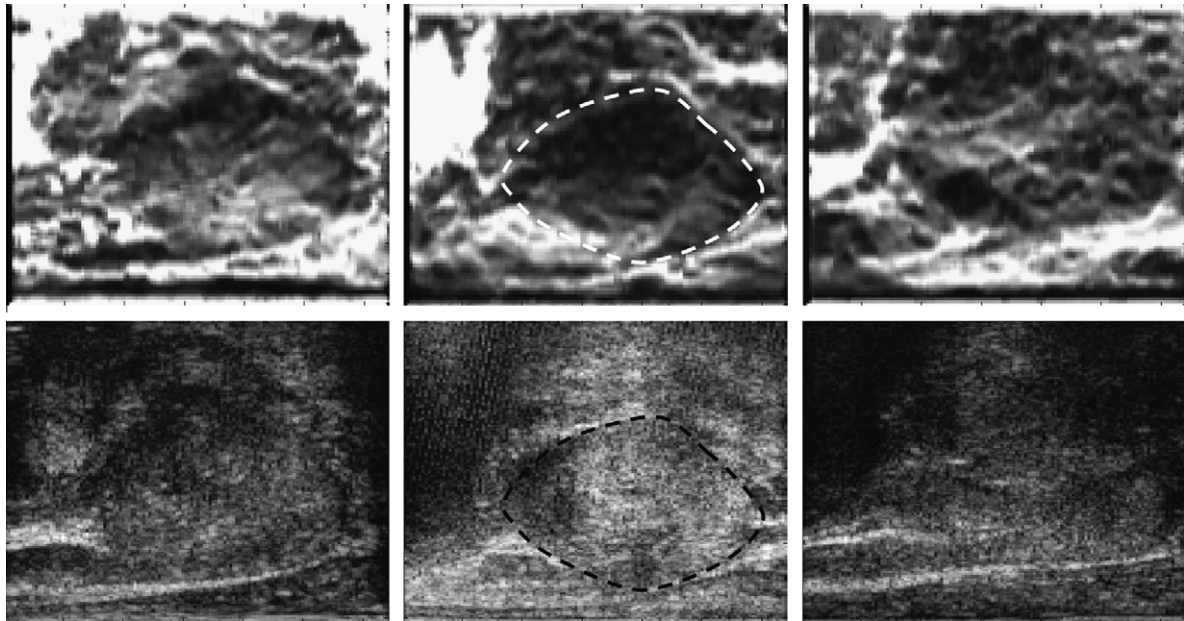


Fig. 6. VE (top) and B-mode (bottom) sagittal images of the prostate of three different patients. The boundary of the prostate is outlined in one of the patients.

Table 1

Description of the data used in this paper.

	Data set size	Image type	Image plane
Volume analysis	9 cases	MRI, VE, B-mode	transverse
CNR analysis	178 images (20 cases)	VE, B-mode	107 transverse, 71 longitudinal
Edge analysis	107 images (11 cases)	VE, B-mode	transverse

during the volume study, the acquisition time had to be minimized. Therefore the number of MRI scans that we have used in our study is limited. Nevertheless, this number is similar to that used in Smith et al. (2007) that compares B-mode based prostate segmentation to MRI. Furthermore, in Smith et al. (2007) and most of the studies cited therein, *post-operative* MRI is compared with TRUS. However, tissue will change as a result of treatment. We believe that comparison based on *pre-operative* images is necessary for general assessment of the gland's visibility and treatment planning.

2.2. Evaluation methods

In order to assess the visibility of the prostate in VE images, we utilize several evaluation measures. These include image-based measures, which consist of contrast-to-noise ratio, edge continuity and edge strength, and volume-based measures, which consist of volume error and volume difference. For more accurate region-based evaluation, the results of these measures will be reported for nine sectors of the gland. To do so, as shown in Fig. 7, the prostate is divided into the base, mid, and apex regions. Then, each region is further divided into posterior, anterior and lateral parts. Quadrant-based division of the prostate is a common approach in the literature (Sidhu et al., 2002; Thomas et al., 2007). However, for our application, this subdivision scheme provides more detailed reporting of results for different regions of the gland. This is motivated by the difference in the importance of the prostatic and periprostatic tissue in various regions. For example, various clinical studies have shown that in LDR brachytherapy, overdosing the

posterior region of the prostate results in rectal complications (Snyder et al., 2001).

2.2.1. Image-based measures

Accurate delineation of the prostate is affected by how the prostate is visualized. A “good” image of the prostate is one in which the prostate has high contrast relative to the background and has well-defined edges. A good edge should be both “continuous” and “strong”. In this analysis, VE images of the prostate are compared to B-mode ultrasound images using the measures of contrast, edge strength, and edge continuity as described below.

2.2.2. The contrast-to-noise ratio

To compare the contrast of VE and B-mode images, the contrast-to-noise ratio (CNR) was calculated using the following equation (Bilgen and Insana, 1997):

$$\text{CNR} = \frac{2(m_t - m_b)^2}{\sigma_t^2 + \sigma_b^2} \quad (2)$$

in which m and σ^2 are the mean and variance of pixel intensities of the target, t , and background, b , in a region of interest (ROI). The ROI of the target and background were manually selected in four regions of the prostate (lateral left, lateral right, anterior and posterior). The target is an area inside the prostate while the background is an area outside the prostate close to the target ROI (respectively yellow¹ and blue boxes in Fig. 8). The physical size and position of the ROI in VE and B-mode images were similar. Additionally, to ensure similarity between the intensity range in both set of images, histogram stretching [0–255] was initially applied to the images.

The contrast between the prostate and its background is typically low in B-mode ultrasound images (see Fig. 5). However, due to the presence of a visible edge, delineation of the prostate is still possible. Therefore, CNR alone can not evaluate the visibility of an object in an image and edge evaluation is also required.

2.2.3. Edge strength

An edge can be defined as the boundary between two regions in an image that are different from each other with respect to some

¹ For interpretation of color in Figs. 1–3, 8, 9 and 13–15, the reader is referred to the web version of this article.

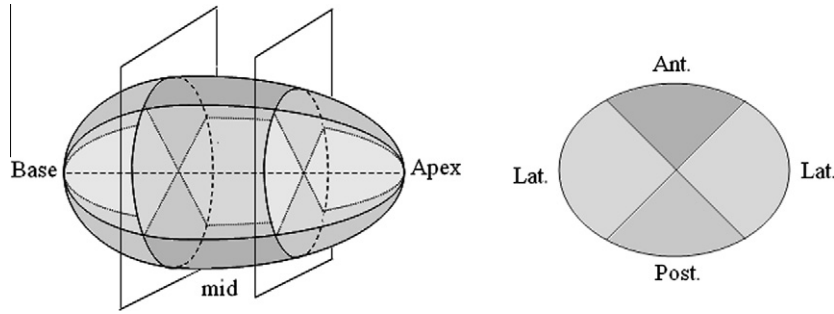


Fig. 7. Division of the prostate into nine sectors.

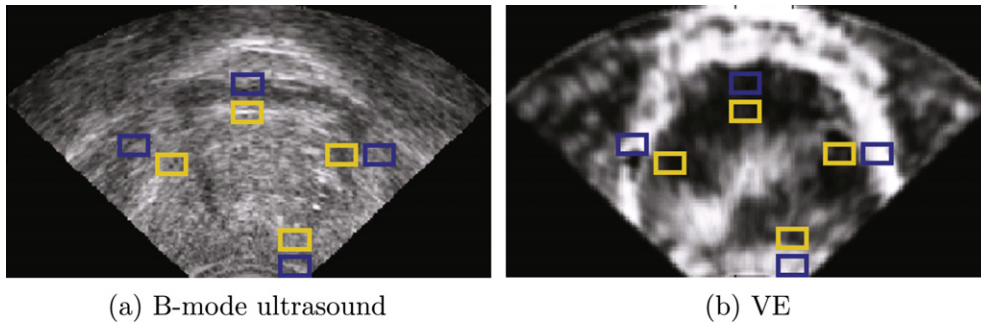


Fig. 8. Selection of inside (yellow boxes) and outside (blue boxes) regions of the prostate for CNR computation in (a) B-mode and (b) VE images. (For interpretation of the references to colour in this figure legend, the reader is referred to the web version of this article.)

local property (Kitchen and Rosenfeld, 1981). While conceptually clear, this definition is difficult to quantify. However, for the purpose of this study we need quantitative measures. Two different measures of edge strength are presented here. One is a conventional gradient-based edge filter and the second one is a test that identifies the statistical changes in image intensity. The edge strength measures are computed for radial edge profiles formed as follows: On each transverse image, we extended radii at $\theta_i = i \times 30^\circ, i = 1, \dots, 12$ in polar coordinates originating from a manually selected center point, C, inside the prostate. The intersections $r_{\theta_i}, i = 1, \dots, 12$, of these radii with the prostate boundary were manually identified for each angle θ_i . For each edge point, a radial edge intensity profile $I_{\theta_i}(r)$ was extracted. The measures of edge strength were calculated for the window of $r \in [r_{\theta_i} - \Delta d, r_{\theta_i} + \Delta d]$, where Δd is half the length of the edge intensity profile (see Fig. 9).

where Δd is half the length of the edge intensity profile (see Fig. 9).

Gradient-based measure of edge strength: The following gradient formulation, also used in Abolmaesumi and Sirouspour (2004), was used as the edge filter acting on a radial edge intensity $I(r)$, where we remove, for convenience, the θ_i index of I :

$$f_{\text{edge}}(r) = 1/3 \times [I(r + 2\Delta r) + I(r + \Delta r) + I(r) - I(r - \Delta r) - I(r - 2\Delta r) + I(r - 3\Delta r)]^2 \quad (3)$$

where Δr is the physical size of the image pixel.

M , our measure of edge strength, is the sum of the filter outputs on windows of size n pixels (n an odd integer) normalized to the sum of edge filter values on the entire edge profile:

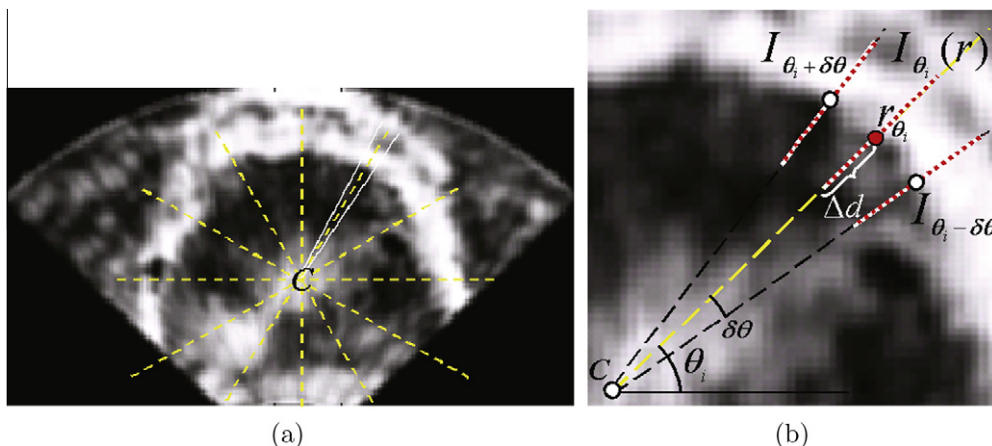


Fig. 9. (a) The radii used for edge profile extraction in a VE image, originating from C and with angles $\theta_i = i \times 30^\circ, i = 1, \dots, 12$. For one of the radii, the two neighboring radii are also illustrated. (b) A close-up view of one of the rays used for extracting the edge profile $I_{\theta_i}(r)$. The measures of edge strength are calculated for the window of $r \in [r_{\theta_i} - \Delta d, r_{\theta_i} + \Delta d]$, where r_{θ_i} is a manually selected edge point along the ray. The neighboring edge profiles $I_{\theta_i \pm \delta\theta}$ are extracted similarly and used along with I_{θ_i} in the edge continuity measure.

$$M(r) = \frac{\sum_{j=r-(n-1)\Delta r/2}^{j=r+(n-1)\Delta r/2} f_{\text{edge}}(j)}{\sum_{j=r_{\theta_i}-\Delta d}^{j=r_{\theta_i}+\Delta d} f_{\text{edge}}(j)} \quad (4)$$

The normalization is performed so that we can compare results for different areas. M is computed along $r \in [r_{\theta_i} - \Delta d, r_{\theta_i} + \Delta d]$, and is expected to have a strong peak at the edge. In our implementation, parameter values were set to $\Delta d = 0.5$ cm and $n = 5$ pixels.

DF statistical test: The performance of the gradient-based edge detector can be plagued by local minima in US images. Therefore, we present a new approach that models the difference of the radial edge intensity profile as an autoregressive process. The edge strength is characterized based on the degree of stationarity of this process. The stationarity of the edge profile is tested using the statistical test proposed by Dickey and Fuller (1979). Each radial intensity profile, was considered as a time series $I_{\theta_i}(k) := I_{\theta_i}(k\Delta r)$, where the discretized radial distance k , such that $k\Delta r \in [r_{\theta_i} - \Delta d, r_{\theta_i} + \Delta d]$, replaces the usual time index.

The edge profiles, $I_{\theta_i}(k)$, can be modeled as a first order autoregressive AR(1) processes as follows:

$$I_{\theta_i}(k) = \rho I_{\theta_i}(k-1) + e_r \quad (5)$$

where ρ is a real number and e_r is a sequence of independent normal variables with mean 0 and variance σ^2 . In order to show that an AR(1) model is sufficient for modeling the edge profiles, we computed the partial autocorrelation function (PACF) of $I_{\theta_i}(k)$. The PACF of an AR(1) process has significant values only at lag = 1. In 78% of the edge profiles extracted from both B-mode and VE images, at the significance level of 0.05, the PACF function only has significant values at lag = 1.

$I_{\theta_i}(k)$ is stationary if $|\rho| < 1$. If a unit root exists ($|\rho| = 1$), then the variance of $I_{\theta_i}(k)$ is $\rho\sigma^2$, and therefore $I_{\theta_i}(k)$ is non-stationary. In many economics applications, the existence of the unit root, which is an indication of a “trend” or a “shock”, is important for modeling and forecasting the future observations of a time series. Dickey and Fuller (1979) provided a statistical method to test an AR model for the null hypothesis of the existence of a unit root. If we re-write (5) as follows:

$$\begin{aligned} \Delta I_{\theta_i}(k) &= I_{\theta_i}(k) - I_{\theta_i}(k-1) \\ &= (\rho - 1)I_{\theta_i}(k-1) + e_r \\ &= \gamma I_{\theta_i}(k-1) + e_r \end{aligned}$$

then the DF test is formulated as follows:

$$H_0 : \rho = 1 \leftrightarrow H_0 : \gamma = 0 \quad (6)$$

$$H_1 : \rho < 1 \leftrightarrow H_0 : \gamma < 0 \quad (7)$$

Note that the test is performed on the residuals and not the time series samples. Therefore, the standard t-distribution cannot be used. Dickey and Fuller provide a non-standard statistic τ , which depends on the number of observations, and provide tables of critical values for it. In other words, based on the calculated value of τ , they provide the significance level at which the null hypothesis above can be rejected. We used the implementation reported in Kanzler (1998) to perform the DF test.

The statistical properties of the intensity profile are altered at the edge. The existence of a strong edge in the time series is an obvious trend. A signal with a trend cannot be stationary, since its statistical moments depend on time, or in our model, on distance. In other words, if one traces the image in the radial direction, the intensity profile tends to become non-stationary upon passing through an edge. To evaluate the edge quality, we compute and report the percentage of edge profiles for which, according to the DF test, the stationarity hypothesis is strongly rejected ($p < 0.05$) for the edge profile. For an image with strong edges, one expects to see a high percentage of edge profiles for which

the unit root exists and the stationarity hypothesis is strongly rejected.

2.2.4. Edge continuity

Detecting an edge point on a single edge profile can not guarantee the presence of an edge. Continuity of the presence of such a point within a neighborhood is an important factor for the visibility of the edge. We measure this continuity by measuring the similarity of the edge region within a neighborhood.

For a continuous edge, two neighboring edge profiles are expected to be similar, although slight differences may be present due to image noise or in the case of ultrasound, speckle. The normalized cross-correlations $R_{\theta_i, \theta_i \pm \delta\theta}(r)$ of the two neighboring edge intensity profiles $I_{\theta_i}(r)$ and $I_{\theta_i \pm \delta\theta}(r)$, $r \in [r_{\theta_i} - \Delta d, r_{\theta_i} + \Delta d]$ and the average $c(\theta_i)(r) = \frac{1}{2}[R_{\theta_i, \theta_i + \delta\theta} + R_{\theta_i, \theta_i - \delta\theta}]$ were calculated for each point, r_{θ_i} , at which the radius r_{θ_i} intersects the edge (see Fig. 9). The parameters we used for this implementation were $\theta_i = i \times 30^\circ$, $i = 1, \dots, 12$, $\Delta d = 0.2$ cm, and $\delta\theta$ such that the arc length between the two adjacent edge profiles is 0.2 cm.

For a large similarity between adjacent edge profiles, c_{θ_i} should have a shape similar to the shape of a Gaussian function with large peak at the edge point and a small standard deviation. Thus, we propose that the following edge continuity measure, $K(\theta_i)$, be calculated:

$$K_{\theta_i} = \frac{P^2(\theta_i)}{\sigma(\theta_i)} \quad (8)$$

in which $P(\theta_i)$ and $\sigma(\theta_i)$ are the peak and standard deviation of a Gaussian function fitted to c_{θ_i} .

2.2.5. Volume-based measures

The volume of the prostate is an important parameter in planning the dose distribution in LDR brachytherapy. A well-defined 3D shape can also aid prostatectomy. To evaluate the shape and size of the prostate created from VE images, we compare them with the shape and size extracted from the commonly used B-mode ultrasound images. Since MR images of the prostate provide more anatomical details including visualizing the boundaries, the 3D surface extracted from MR images is used as the gold standard. Contouring in all three image types was performed manually and by three observers: one radiation oncologist and two trained by experts. The ‘volume difference’ and ‘volume error’ between surfaces created from MR and VE/B-mode images (i.e. MR vs. VE or MR vs. B-mode) provide shape and size similarity errors that can be used to compare to the gold standard provided by MRI.

The percent volume difference provides a measure of the difference in the size of the total gland and each of the nine sectors in VE/B-mode images compared to the gold standard MRI. It is defined as:

$$V_{\text{diff}}\% = 100 \times (V_{\text{VE/B-mode}} - V_{\text{MRI}})/V_{\text{MRI}} \quad (9)$$

The percent volume error is the volume of the non-overlapping region between the surface of the prostate generated from VE/B-mode images and that of MR, divided by the sum of the two volumes. This is defined as:

$$V_{\text{err}}\% = 100 \times \left((V_{\text{VE/B-mode}} + V_{\text{MRI}} - 2(V_{\text{VE/B-mode} \cap \text{MRI}})) / (V_{\text{VE/B-mode}} + V_{\text{MRI}}) \right) \quad (10)$$

In other words, it provides a measure of the difference in the shape of the gland compared to the gold standard. This definition is equivalent to $1 - \text{DSC}$, in which DSC is the Dice Similarity Coefficient (Dice, 1945).

The 3D shape of the prostate, in each modality, was extracted by manually segmenting the 2D images with the use of the Stradwin (Treece et al., 2000) software. This software was then used to

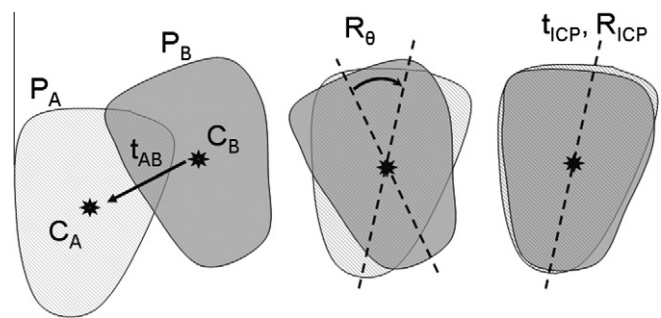


Fig. 10. Registration of B-mode/VE prostate surfaces to MRI.

Table 2
CNR comparison of VE and B-mode images.

	Base	Mid	Apex
CNR VE	10.25 ± 12.83	13.73 ± 5.85	20.51 ± 23.13
CNR B-mode	2.07 ± 1.06	1.43 ± 0.75	1.56 ± 1.16

transform the 2D contours into a 3D surface which could be opened in MATLAB®. MATLAB® is the environment in which we performed all our calculations.

To register the MRI and ultrasound images we opted for a rigid registration approach, as opposed to a deformable registration one. Indeed, these images were not acquired at the same time and the patients were in the dorsal lithotomy position during B-mode and VE acquisition and supine position during MR acquisition. Furthermore, the patients were anaesthetized and relaxed prior to the procedure, while they were awake and possibly tense during the MRI exam. A non-rigid (deformable) registration is not a suitable registration option since the goal is to understand the differences between the manually segmented surfaces. A deformable registration which maps one surface to the other will conceal these differences.

We assume that the main cause of mis-registration of the surfaces is the angle of the prostates' base-apex axis with the TRUS probe. This is mainly a result of the patient's orientation during

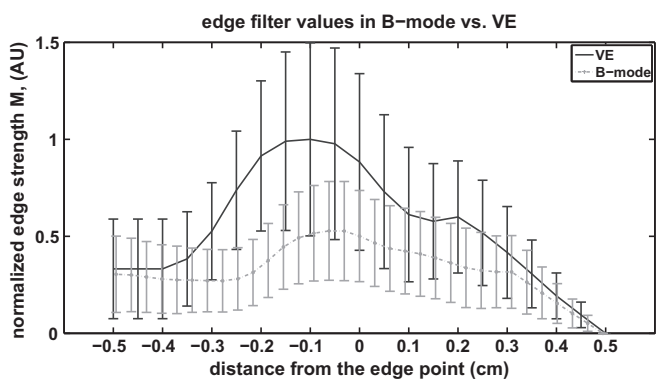


Fig. 12. The values of the gradient-based edge strength measure (M) along the edge profiles for VE and B-mode images. Error bars represent the inter-patient standard deviation of the M values.

Table 3
The percentage of non-stationary prostate edge profiles in different areas of the B-mode and VE images. Standard deviations reported characterize inter-patient variations.

%	VE			B-mode ultrasound		
	Base	Mid	Apex	Base	Mid	Apex
Ant.	67.9 ± 4.6	99.2 ± 1.1	99.9 ± 0.2	71.4 ± 2.8	80.8 ± 4.1	76.6 ± 7.5
Lat.	79.5 ± 3.1	98.8 ± 0.9	98.1 ± 1.7	66.1 ± 3.5	81.3 ± 2.5	88.9 ± 5.1
Post.	78.6 ± 3.5	99.2 ± 1.9	99.8 ± 0.2	67.9 ± 3.2	80.8 ± 4.1	84.1 ± 8.1

imaging. We also assume that the size of the prostate does not change between data collection sessions and the prostate does not rotate around its base-apex axis by a large angle. For each surface, this axis was obtained by fitting a line to the centers of the prostate contours in each image slice.

With these assumptions, to register the prostate surfaces P_B (the VE or B-mode surface) to P_A (the MRI surface), a translation t_{AB} is first applied in order to match their geometric centers C_A and C_B . A rotation R_θ around the matched geometric center is then applied to rotate the base-apex axis of the translated prostate P_B to the

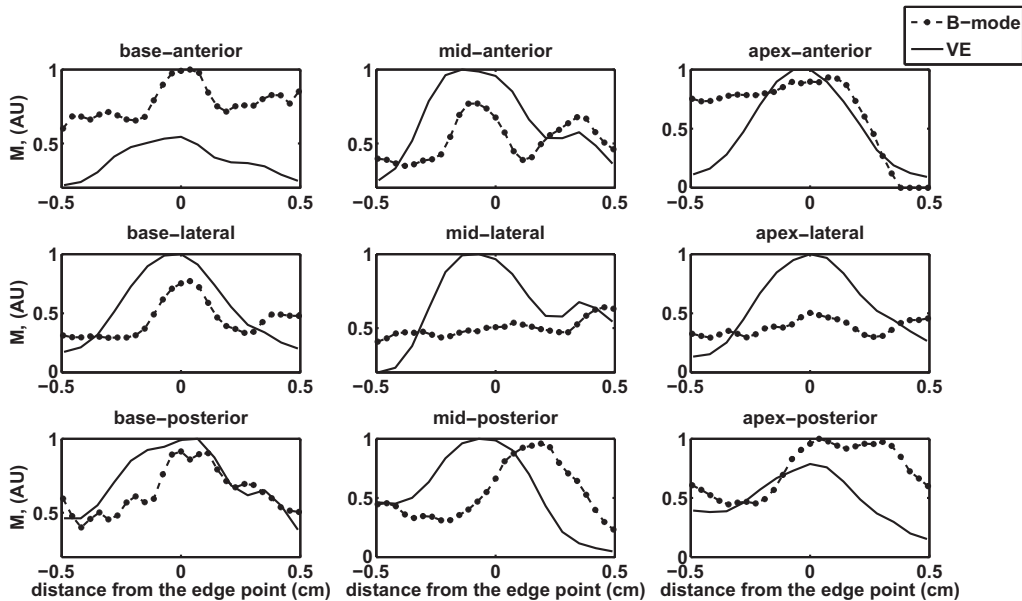


Fig. 11. The values of the normalized gradient-based edge strength measure (M) in arbitrary units vs. the distance from the edge in cm, separated for the nine regions of the prostate gland.

main axis of P_A . θ is the angle between the base-apex axis of the two surfaces, obtained as described above. Finally a six degree-of-freedom Iterative Closest Point (ICP) method (Besl and McKay, 1992) translates (\vec{t}_{ICP}) and rotates (R_{ICP}) the resulting surface to fine-tune the registration, resulting in $P_{B-registered}$ (Fig. 10), is described as:

$$P_{B-registered} = R_{ICP} [R_0(P_B + \vec{t}_{AB}) + \vec{t}_{ICP}] \quad (11)$$

The volume error and volume difference is calculated for the rigidly registered surfaces.

3. Results

3.1. Image comparison

3.1.1. The contrast

The CNR of VE and B-mode images, averaged over the three sections of the prostate, is shown in Table 2. Data from 178 images (from 20 patients) were used in this analysis. In all three regions the CNR of VE is significantly higher than that of B-mode ($p < 0.05$ for base, and $p < 0.001$ for the mid-gland and apex regions).

3.1.2. Edge strength: gradient-based measure

The gradient-based measure of edge strength, M , was computed for edge profiles in the nine regions described in Section 2.2 (Fig. 7). The VE and B-mode images have different resolutions. This is due to the fact that the window size used for displacement estimation in VE images is larger than the B-mode pixel. Therefore, the choice of n (the window size), affects the value computed for M . We examined values of window sizes in the range of $n = 2$ to $n = 10$ and in all cases, the results of edge analysis were consistent. The reported results were acquired for $n = 5$. The result, extracted from 107 images of 11 patient datasets, is illustrated in Fig. 11 for the nine regions and in Fig. 12 for all regions combined. As illustrated in Fig. 11, the VE edges are notably stronger than B-mode edges with the exception of the anterior base and the posterior apex. The other observation of note is that the values of M show an evident peak in all areas of VE images, with the exception of

the anterior base. In the case of B-mode images, in some areas such as the lateral and anterior apex and the lateral mid-gland, the edges are very weak and are not represented by a dominant peak in the gradient values. In the posterior region of the prostate (the last row in Fig. 11) the B-mode edge strength appears to be similar or slightly higher than the VE edge strength.

It is evident from Fig. 12 that, overall, edges in VE images are stronger. At the edge point, the normalized M value is 2.2 times larger in VE images compared to B-mode images.

3.1.3. Edge strength: DF test of stationarity

Table 3 shows the percentage of edge profiles for which the DF test strongly shows a unit root ($p < 0.05$), and therefore, non-stationarity. 107 images from 11 patient datasets and 12 edge profiles within each image, were used in this analysis. This result is reported separately for the nine regions. The edges appear stronger in VE images in all areas, with the exception of the anterior base (matching the result from the gradient-based edge strength). In general, the edges in the base region are relatively weak in both modalities.

3.1.4. Edge continuity

Table 4 shows the edge continuity value, K , computed for VE and B-mode images in nine regions of the gland. 107 images from 11 patients were used in this analysis. The edge continuity of VE in all regions except for the anterior base and posterior apex is shown to be superior to that of B-mode images. This is also in agreement with the results of the gradient-based measure of edge strength (Fig. 11).

3.2. Volume comparison

Fig. 13 shows an example of VE (magenta) and B-mode (green) 3D surfaces compared to that of MRI (blue) for one of the patients. Figs. 14 and 15 compare the percent volume error and volume difference between B-mode and MRI and between VE and MRI prostate surfaces manually created by one radiation oncologist (Figs. 14 and 15b) and two individuals trained by experts (Figs. 14, 15a and Figs. 14, 15c). Images from nine patient data sets were used. From Fig. 14 it can be seen that in most regions of the prostate, the mean

Table 4
Average edge continuity measure, K , for the nine regions of the gland.

	$K(\theta_i)$ VE			$K(\theta_i)$ B-mode ultrasound		
	Base	Mid	Apex	Base	Mid	Apex
Ant.	0.64 ± 0.37	0.87 ± 0.33	0.84 ± 0.37	0.71 ± 0.52	0.69 ± 0.41	0.50 ± 0.32
Lat.	0.84 ± 0.39	1.15 ± 0.36	0.85 ± 0.27	0.63 ± 0.40	0.48 ± 0.23	0.39 ± 0.29
Post.	0.99 ± 0.44	0.82 ± 0.35	0.60 ± 0.55	0.52 ± 0.38	0.51 ± 0.32	0.75 ± 0.55

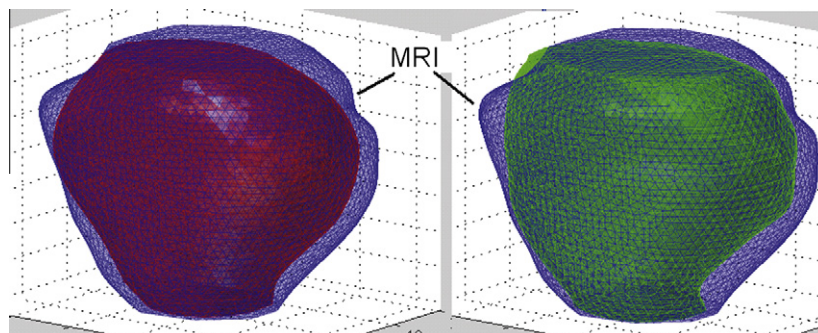
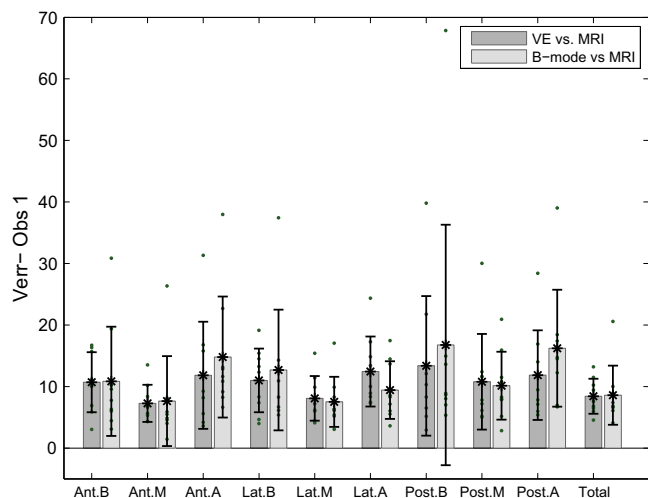
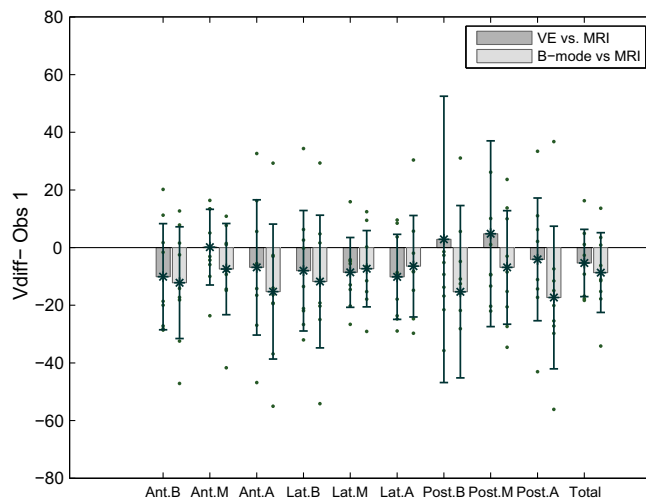


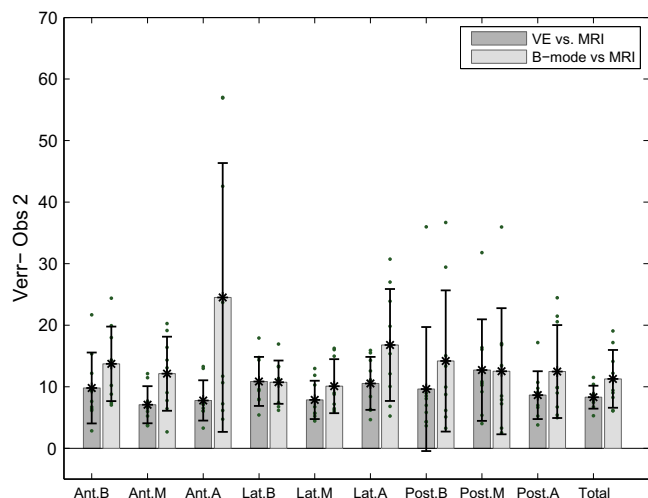
Fig. 13. Comparison of VE (magenta) vs. MRI (blue) 3D surfaces, on the left, and B-mode (green) vs. MRI (blue) 3D surfaces, on the right, from one of the patients. (For interpretation of the references to colour in this figure legend, the reader is referred to the web version of this article.)



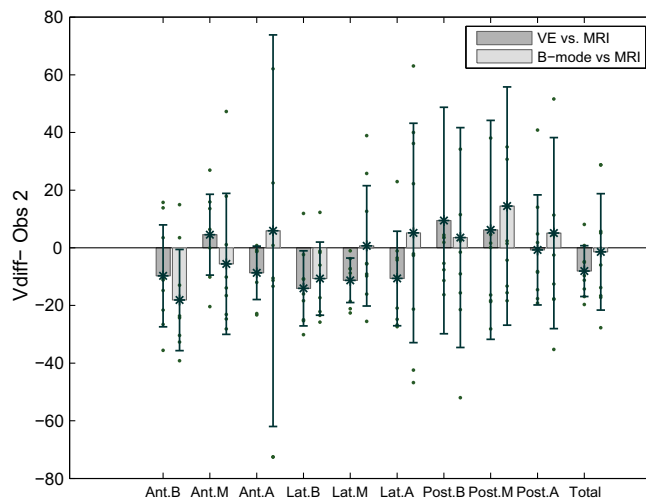
(a) Observer 1: trained by expert



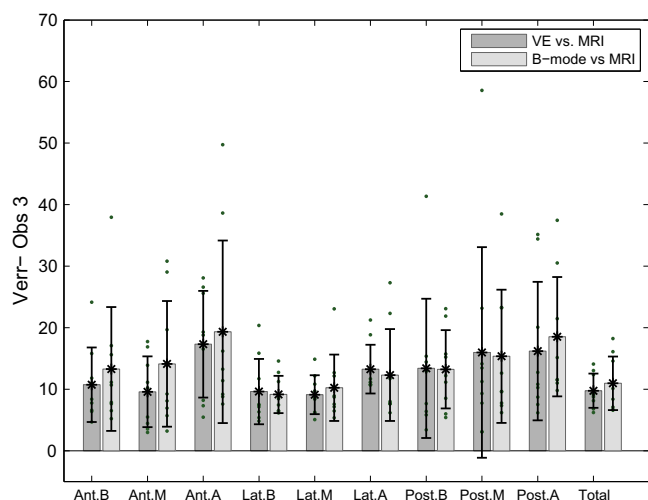
(a) Observer 1: trained by expert



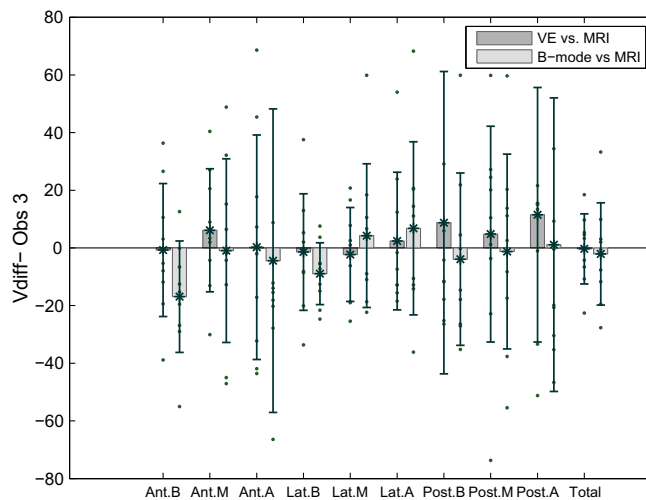
(b) Observer 2: Radiation Oncologist



(b) Observer 2: Radiation Oncologist



(c) Observer 3: trained by expert



(c) Observer 3: trained by expert

Fig. 14. A comparison between VE vs. MRI volume error and B-mode vs. MRI volume error, showing the mean and inter-patient standard deviation of $V_{err}\%$ for three observers. Sample data points are also shown as gray dots.

volume error between VE and MRI is less than that between B-mode and MRI.

Fig. 15. A comparison between VE vs. MRI volume difference and B-mode vs. MRI volume difference, showing the mean and inter-patient standard deviation of $V_{diff}\%$ for three observers. Sample data points are also shown as gray dots.

Over the total gland, a volume error of $8.8 \pm 2.5\%$ for VE vs. MRI and $10.3 \pm 4.6\%$ for B-mode vs. MRI, and a volume difference of

$-4.6 \pm 11.1\%$ for VE vs. MRI and $-4.1 \pm 17.1\%$ for B-mode vs. MRI, averaged over nine patients and three observers, were obtained. However, a one-sided analysis of variance does not show any statistically significant difference, which may also be due to the limited number of patients. In general because the prostate is not discernible at the base and apex, a larger error in shape (volume error) and size (volume difference) between VE or B-mode surface and the gold standard in these two regions compared to the mid-gland is expected. However, in general, and over the three observers, VE errors are smaller than those from B-mode.

4. Discussion and conclusions

In this paper ultrasound vibro-elastography was evaluated as an imaging modality for the visualization of the prostate. VE transfer function (TF) images were qualitatively and quantitatively compared with the commonly used B-mode ultrasound. The evaluation measures used were both image-based (CNR, edge continuity and edge strength) and volume-based (volume error and volume difference). A nine sector analysis was used for more detailed characterization. The results on 178 images suggest that the VE images are significantly superior to B-mode images in terms of contrast of the gland. The gradient-based and the DF-based measures of edge strength and the edge continuity measure, on 107 images, all show that on average VE images provide stronger edges as well. It is important to emphasize that the statistically significant outcomes of our analysis of edge continuity and gradient-based edge strength are consistent: the edges in base-lateral, mid-lateral, mid-anterior, and lateral apex are significantly stronger and more continuous ($p < 0.05$ for the one-sided analysis of variance) in VE images compared to B-mode images. The K and M values, in addition to the visual inspection of the images, show that on average the anterior base and posterior apex of the prostate has weak edges on VE images.

The B-mode data used in this paper was collected simultaneously with the RF data used for creating the VE images. In other words, B-mode and VE images were acquired under exactly similar conditions and are co-registered.

The comparison of volumes calculated from VE and B-mode prostate images show that VE volumes are closer to the MRI gold standard in most regions of the prostate, both in terms of shape and size. This confirms that the outlined region used in the image-based evaluation of VE, is indeed the prostate. In this comparison, prostate images from 9 patients were manually delineated by three observers (one expert and two trained by experts). The total gland volume error for VE vs. MRI was $8.4 \pm 2.9\%$, $8.3 \pm 1.8\%$, and $9.8 \pm 2.8\%$ for the three observers. For B-mode vs. MRI, these values were $8.6 \pm 4.8\%$, $11.3 \pm 4.7\%$, and $11.0 \pm 4.4\%$. The total gland volume difference for VE vs. MRI was $-5.3 \pm 11.7\%$, $-8.1 \pm 8.8\%$, and $-0.3 \pm 12.1\%$ for the three observers. For B-mode vs. MRI, these values were $-8.7 \pm 13.8\%$, $-1.4 \pm 20.2\%$, and $-2.1 \pm 17.7\%$.

It is also worth noting that V_{diff} (see Eq. (9)) measures the prostate volume ratios for B-mode/MRI and VE/MRI ($V_{\text{diff}} = V_{\text{B-mode}}/V_{\text{MRI}} - 1$). Smith et al. (2007) report a MR/US prostate volume ratio of 1.11 ± 0.10 averaged over prostate surfaces from 10 patients outlined by seven observers, repeated twice. Similar results from other work have been listed in a table therein. The MR/US prostate volume ratios for the nine patients in our database are 1.12 ± 0.18 , 1.05 ± 0.21 , and 1.05 ± 0.19 , for the three observers, which support previous work. For MR/VE, these values are 1.07 ± 0.13 , 1.10 ± 0.10 , and 1.02 ± 0.13 . However, the volume ratio or V_{diff} only report differences in the size of the prostate, whereas two prostate surfaces can be greatly different in shape but have equal volumes. V_{err} , which we have included in this paper, can provide useful characterization of the shape difference.

Currently, one dimensional axial motion estimation is used for creating the VE images. Any out of plane motion, including the lateral motions caused by the slippage between the protective sheath on the probe and the surface of the rectum during VE data collection, can affect the VE images. This can be improved upon by using 2D motion estimation techniques to account for lateral tissue motion. We have not used 2D motion tracking because most of the displacement estimates between consecutive frames of RF data are sub-sample. We have shown that the gain based from 2D motion estimation in such cases is not significant enough to warrant its use (Zahiri-Azar et al., 2010) unless beam-steering is employed, such that the lateral motion is estimated from two axial measurements at different beam angles, e.g. $\pm 10^\circ$. The increase in the number of axial measurements lowers the sampling rate and we opted not to do that in this set of experiments.

One should also keep in mind that the presence of the TRUS probe results in deformation of the posterior region of the gland in both VE and B-mode surfaces. For more accurate registration of these surfaces with those from MRI, this deformation could be accounted for. However, since the B-mode and VE images that we use in this paper are exactly registered to each other, this deformation will only result in a bias in the volume error and volume difference, especially in the posterior region, with MRI surfaces. The result of such a bias can be seen to be a generally larger mean and standard deviation in the volume error and volume difference of the posterior region in all three observers, compared to that of the lateral and anterior regions.

It is important to note that several papers have reported in vivo and in vitro studies on healthy vs. cancerous human prostate tissue showing that prostate tumors are stiffer than normal tissue (Parker et al., 2011; Zhang et al., 2008; Kamoi et al., 2008; Salomon et al., 2008). In a study by Kallel et al. (1999) elastography images showed contrast between anatomical structures of freshly excised canine prostates. The central gland was consistently softer than the peripheral gland. In the current work we addressed in vivo validation of ultrasound elastography as a tool for delineation of the human prostate gland itself.

As a final note, the best validation of the prostate gland segmentation could be a comparison to pathology, the undisputed gold standard. Such a study requires access to the whole mount pathology, and viable solutions to the open problem of how to register the shrunk, misaligned pathology slices to pre-operative images.

We have quantitatively shown that VE is a promising imaging modality for delineation of the prostatic region and the use of such data along with B-mode ultrasound can improve the visualization of the gland. Determination of the clinical value of VE in cancer detection is the subject of our future research.

Acknowledgments

We would like to thank Dr Tom Pickles, Dr Michael McKenzie, Dr Larry Goldenberg, Dr Chris Nguan, Dr Anthony Koupparis, Dr Nicholas Buchan and the staff at Vancouver Cancer Center and Vancouver General Hospital for their help during the data collection process. Also we acknowledge the collaborations of Dr Reza Zahiri-Azar and Dr Orcun Goksel. This project was partially funded by NIH Grant R21 CA120232, the Natural Sciences and Engineering Research Council of Canada, the Canadian Institutes of Health Research, and the US Army Medical Research and Materiel Command under W81XWH-10-1-0201.

References

- Abolmaesumi, P., Sirouspour, M.R., 2004. An interacting multiple model probabilistic data association filter for cavity boundary extraction from ultrasound images. *IEEE Trans. Med. Imaging* 23 (6), 772–784.

- Besl, P., McKay, H., 1992. A method for registration of 3D shapes. *IEEE Trans. Pattern Anal. Mach. Intell.* 14 (2), 239–256.
- Bilgen, M., Insana, M.F., 1997. Predicting target detectability on acoustic elastography. In: *IEEE Ultrasonics Symposium*, pp. 1427–1430.
- Canadian Cancer Society, 2010. Canadian Cancer Statistics. Tech. Rep. <<http://www.cancer.ca/>>.
- Castéra, L., Vergnol, J., Foucher, J., Le Bail, B., Chanteloup, E., Haaser, M., Darriet, M., Couzigou, P., de Lédinghen, V., 2005. Prospective comparison of transient elastography, fibrotest, APRI, and liver biopsy for the assessment of fibrosis in chronic hepatitis C. *Gastroenterology* 128 (2), 343–350.
- Choi, Y.J., Kim, J.K., Kim, H.J., Cho, K.-S., 2009. Interobserver variability of transrectal ultrasound for prostate volume measurement according to volume and observer experience. *Am. J. Roentgenol.* 192 (2), 444–449.
- Cochlin, D.L., Ganatra, R.H., Griffiths, D.F.R., 2002. Elastography in the detection of prostatic cancer. *Clin. Radiol.* 57 (11), 1014–1020.
- Daanen, V., Gastaldo, J., Giraud, J.Y., Fournier, P., Descotes, J.L., Bolla, M., Collomb, D., Troccaz, J., 2006. MRI/TRUS data fusion for brachytherapy. *Int. J. Med. Robot.* 2 (3), 256–261.
- Dice, L.R., 1945. Measures of the amount of ecologic association between species. *Ecology* 26 (3), 297–302.
- Dickey, D.A., Fuller, W.A., 1979. Distribution of the estimators for autoregressive time series with a unit root. *J. Am. Stat. Assoc.* 74 (366), 427–431.
- Dresner, M.A., Rose, G.H., Rossman, P.J., Muthupillai, R., Manduca, A., Ehman, R.L., 2001. Magnetic resonance elastography of skeletal muscle. *J. Magn. Reson. Imaging* 13 (2), 269–276.
- Egorov, V., Arapetyan, S., Sarvazyan, A.P., 2006. Prostate mechanical imaging: 3-D image composition and feature calculations. *IEEE Trans. Med. Imaging* 25 (10), 1329–1340.
- Eskandari, H., Salcudean, S.E., Rohling, R., 2008. Viscoelastic parameter estimation based on spectral analysis. *IEEE Trans. Ultrason. Ferroelectr. Freq. Control* 55 (7), 1611–1625.
- Fenster, A., Downey, D.B., Cardinal, H.N., 2001. Three-dimensional ultrasound imaging. *Phys. Med. Biol.* 46 (5), R67–R99.
- Ferlay, J., Parkin, D.M., Steliarova-Foucher, E., 2010. Estimates of cancer incidence and mortality in Europe in 2008. *Eur. J. Cancer* 46 (4), 765–781.
- Fleming, I.N., Rivaz, H., Macura, K., Su, L.M., Hamper, U., Lagoda II, G.A., A.L.B., Lotan, T., Taylor, R.H., Hager, G.D., Bector, E.M., 2009. Ultrasound elastography – enabling technology for image guided laparoscopic prostatectomy. In: *Medical Imaging 2009: Visualization, Image-Guided Procedures, and Modeling*. Proc. SPIE, vol. 7261, pp. 726121.
- Garra, B.S., Cespedes, E.I., Ophir, J., Spratt, S.R., Zuurbier, R.A., Magnant, C.M., Pennanen, M.F., 1997. Elastography of breast lesions: initial clinical results. *Radiology* 202 (1), 79–86.
- Gravas, S., Mamoulakis, C., Rioja, J., Tzortzis, V., de Reijke, T., Wijkstra, H., de la Rosette, J., 2009. Advances in ultrasound technology in oncologic urology. *Urol. Clin. North Am.* 36 (2), 133–145, vi.
- Huwart, L., Sempoux, C., Vicaud, E., Salameh, N., Annet, L., Danse, E., Peeters, F., ter Beek, L.C., Rahier, J., Sinkus, R., Horsmans, Y., Beers, B.E.V., 2008. Magnetic resonance elastography for the noninvasive staging of liver fibrosis. *Gastroenterology* 135 (1), 32–40.
- Kadour, M.J., Noble, J.A., 2009. Assisted-freehand ultrasound elasticity imaging. *IEEE Trans. Ultrason. Ferroelectr. Freq. Control* 56 (1), 36–43.
- Kallel, F., Price, R.E., Konofagou, E., Ophir, J., 1999. Elastographic imaging of the normal canine prostate in vitro. *Ultrason. Imaging* 21 (3), 201–215.
- Kamoi, K., Okihara, K., Ochiai, A., Ukimura, O., Mizutani, Y., Kawauchi, A., Miki, T., 2008. The utility of transrectal real-time elastography in the diagnosis of prostate cancer. *Ultrasound. Med. Biol.* 34 (7), 1025–1032.
- Kanzler, L., 1998. A Study of the Efficiency of the Foreign Exchange Market through Analysis of Ultra-high Frequency Data. Ph.D. thesis. Oxford University, Oxford, UK.
- Kitchen, L., Rosenfeld, A., 1981. Edge evaluation using local edge coherence. *IEEE Trans. Syst. Man Cybern.* 11 (9), 597–605.
- Lerner, R., Parker, K., Hohen, J., Gramiak, R., Waag, R., 1988. Sono-elasticity: medical elasticity images derived from ultrasound signals in mechanically vibrated targets. *Acoust. Imaging* 16, 317–327.
- Li, J., Cui, Y., English, R.E., Noble, J.A., 2009. Ultrasound estimation of breast tissue biomechanical properties using a similarity-based non-linear optimization approach. *J. Strain Anal.* 44 (5), 363–374.
- Lyshchik, A., Higashi, T., Asato, R., Tanaka, S., Ito, J., Mai, J.J., Pellot-Barakat, C., Insana, M.F., Brill, A.B., Saga, T., Hiraoka, M., Togashi, K., 2005. Thyroid gland tumor diagnosis at us elastography. *Radiology* 237 (1), 202–211.
- Mahdavi, S.S., Moradi, M., Wen, X., Morris, W.J., Salcudean, S.E., 2009. Vibro-elastography for visualization of the prostate region. In: *Medical Image Computing and Computer Assisted Intervention, Part II, LNCS*, vol. 5762, Springer-Verlag, Berlin Heidelberg, pp. 339–347.
- Miyagawa, T., Tsutsumi, M., Matsumura, T., Kawazoe, N., Ishikawa, S., Shimokama, T., Miyayama, N., Akaza, H., 2009. Real-time elastography for the diagnosis of prostate cancer: evaluation of elastographic moving images. *Jpn. J. Clin. Oncol.* 39 (6), 394–398.
- Morris, W.J., Keyes, M., Palma, D., Spadinger, I., McKenzie, M.R., Agranovich, A., Pickles, T., Liu, M., Kwan, W., Wu, J., Berthelet, E., Pai, H., 2009. Population-based study of biochemical and survival outcomes after permanent 125I brachytherapy for low- and intermediate-risk prostate cancer. *Urology* 73 (4), 860–865, discussion 865–867.
- National Cancer Institute, 2010. <<http://www.cancer.gov/cancertopics/types/prostate/>>.
- Ophir, J., Céspedes, I., Ponnekanti, H., Yazdi, Y., Li, X., 1991. Elastography: a quantitative method for imaging the elasticity of biological tissues. *Ultrason. Imaging* 13 (2), 111–134.
- Ophir, J., Céspedes, I., Garra, B., Ponnekanti, H., Huang, Y., Maklad, N., 1996. Elastography: ultrasonic imaging of tissue strain and elastic modulus in vivo. *Eur. J. Ultrasound* 3 (1), 49–70.
- Pallwein, L., Mitterberger, M., Struve, P., Pinggera, G., Horninger, W., Bartsch, G., Aigner, F., Lorenz, A., Pedross, F., Frauscher, F., 2007. Real-time elastography for detecting prostate cancer: preliminary experience. *BJU Int.* 100 (1), 42–46.
- Parker, K.J., Doyley, M.M., Rubens, D.J., 2011. Imaging the elastic properties of tissue: the 20 year perspective. *Phys. Med. Biol.* 56 (1), R1–R29.
- Pathak, S.D., Chalana, V., Haynor, D.R., Kim, Y., 2000. Edge-guided boundary delineation in prostate ultrasound images. *IEEE Trans. Med. Imaging* 19 (12), 1211–1219.
- Sahba, F., Tizhoosh, H.R., Salama, M.M., 2005. A coarse-to-fine approach to prostate boundary segmentation in ultrasound images. *Biomed. Eng. Online* 4, 58.
- Salcudean, S.E., French, D., Bachmann, S., Zahiri-Azar, R., Wen, X., Morris, W.J., 2006. Viscoelasticity modeling of the prostate region using vibro-elastography. *Med. Image Comput. Assist. Intervent.* 9 (Pt 1), 389–396.
- Salcudean, S.E., Wen, X., Mahdavi, S., Moradi, M., Morris, J., Spadinger, I., 2009. Ultrasound elastography an image guidance tool for prostate brachytherapy. *Brachytherapy* 8 (2), 125–126.
- Salomon, G., Kllerman, J., Thederan, I., Chun, F.K.H., BudSus, L., Schlomm, T., Isbarn, H., Heinzer, H., Huland, H., Graefen, M., 2008. Evaluation of prostate cancer detection with ultrasound real-time elastography: a comparison with step section pathological analysis after radical prostatectomy. *Eur. Urol.* 54 (6), 1354–1362.
- Schaar, J.A., Korte, C.L.D., Mastik, F., Strijder, C., Pasterkamp, G., Boersma, E., Serruys, P.W., Steen, A.F.W.V.D., 2003. Characterizing vulnerable plaque features with intravascular elastography. *Circulation* 108 (21), 2636–2641.
- Sidhu, S., Morris, W.J., Spadinger, I., Keyes, M., Hilt, M., Harrison, R., Otto, K., McKenzie, M., Agranovich, A., 2002. Prostate brachytherapy postimplant dosimetry: a comparison of prostate quadrants. *Int. J. Radiat. Oncol. Biol. Phys.* 52 (2), 544–552.
- Sinkus, R., Lorenzen, J., Schrader, D., Lorenzen, M., Dargatz, M., Holz, D., 2000. High-resolution tensor MR elastography for breast tumour detection. *Phys. Med. Biol.* 45 (6), 1649–1664.
- Smith, W.L., Lewis, C., Bauman, G., Rodrigues, G., D'Souza, D., Ash, R., Ho, D., Venkatesan, V., Downey, D., Fenster, A., 2007. Prostate volume contouring: a 3D analysis of segmentation using 3DTRUS, CT, and MR. *Int. J. Radiat. Oncol. Biol. Phys.* 67 (4), 1238–1247.
- Snyder, K.M., Stock, R.G., Hong, S.M., Lo, Y.C., Stone, N.N., 2001. Defining the risk of developing grade 2 proctitis following 125I prostate brachytherapy using a rectal dose-volume histogram analysis. *Int. J. Radiat. Oncol. Biol. Phys.* 50 (2), 335–341.
- Southern, R., Hervieu, V., Gelet, A., Ophir, J., Chapelon, J.Y., 2003. Human prostate elastography: in vitro study. In: *IEEE Symposium on Ultrasonics*, vol. 2, pp. 1251–1253.
- Tanter, M., Bercoff, J., Sandrin, L., Fink, M., 2002. Ultrafast compound imaging for 2-D motion vector estimation: application to transient elastography. *IEEE Trans. Ultrason. Ferroelectr. Freq. Control* 49 (10), 1363–1374.
- Thomas, C.W., Kruk, A., McGahan, C.E., Spadinger, I., Morris, W.J., 2007. Prostate brachytherapy post-implant dosimetry: a comparison between higher and lower source density. *Radiother. Oncol.* 83 (1), 18–24.
- Thompson, I., Thrasher, J.B., Aus, G., Burnett, A.L., Canby-Hagino, E.D., Cookson, M.S., D'Amico, A.V., Dmochowski, R.R., Eton, D.T., Forman, J.D., Goldenberg, S.L., Hernandez, J., Higano, C.S., Kraus, S.R., Moul, J.W., Tangen, C.M., A.U.A. Prostate Cancer Clinical Guideline Update Panel, 2007. Guideline for the management of clinically localized prostate cancer: 2007 update. *J. Urol.* 177 (6), 2106–2131.
- Tong, S., Cardinal, H.N., McLoughlin, R.F., Downey, D.B., Fenster, A., 1998. Intra- and inter-observer variability and reliability of prostate volume measurement via two-dimensional and three-dimensional ultrasound imaging. *Ultrasound Med. Biol.* 24 (5), 673–681.
- Treecce, G.M., Prager, R.W., Gee, A.H., Berman, L., 2000. Surface interpolation from sparse cross sections using region correspondence. *IEEE Trans. Med. Imaging* 19 (11), 1106–1114.
- Turgay, E., Salcudean, S.E., Rohling, R., 2006. Identifying the mechanical properties of tissue by ultrasound strain imaging. *Ultrasound Med. Biol.* 32 (2), 221–235.
- Wu, T., Felmlee, J.P., Greenleaf, J.F., Riederer, S.J., Ehman, R.L., 2001. Assessment of thermal tissue ablation with MR elastography. *Magn. Reson. Med.* 45 (1), 80–87.
- Yin, M., Talwalkar, J.A., Glaser, K.J., Manduca, A., Grimm, R.C., Rossman, P.J., Fidler, J.L., Ehman, R.L., 2007. Assessment of hepatic fibrosis with magnetic resonance elastography. *Clin. Gastroenterol. Hepatol.* 5 (10), 1207–1213.e2.
- Zahiri-Azar, R., Salcudean, S.E., 2006. Motion estimation in ultrasound images using time domain cross correlation with prior estimates. *IEEE Trans. Biomed. Eng.* 53 (10), 1990–2000.
- Zahiri-Azar, R., Goksel, O., Salcudean, S.E., 2010. Sub-sample displacement estimation from digitized ultrasound RF signals using multi-dimensional polynomial fitting of the cross-correlation function. *IEEE Trans. Ultrason. Ferroelectr. Freq. Control* 57 (11), 2403–2420.
- Zhang, M., Nigwekar, P., Castaneda, B., Hoyt, K., Joseph, J.V., di Sant'Agnes, A., Messing, E.M., Strang, J.G., Rubens, D.J., Parker, K.J., 2008. Quantitative characterization of viscoelastic properties of human prostate correlated with histology. *Ultrasound Med. Biol.* 34 (7), 1033–1042.

Machine learning for target selection in MR-guided prostate biopsy: A preliminary study

Mehdi Moradi¹, Andriy Fedorov¹, William M Wells¹, Kemal Tuncali¹, Sandeep N Gupta², Fiona M Fennessy¹, and Clare M Tempny¹

¹Radiology, Brigham and Women's Hospital - A Teaching Affiliate of Harvard Medical School, Boston, MA, United States, ²GE Global Research Center, Niskayuna, NY

Introduction – With an estimated 240,890 cases to be diagnosed in 2011, prostate cancer (PCa) remains among the most common male malignancies with an annual death toll of 33,270 men. Prostate tumors are not visible in the transrectal ultrasound (TRUS) B-mode images used for the guidance of routine biopsies. Therefore, TRUS biopsy is not targeted. There is strong evidence that multiparametric MRI (mpMRI) including Diffusion Weighted (DW) and Dynamic Contrast-Enhanced imaging (DCE) in addition to the T2-weighted MRI can improve the accuracy of PCa localization and staging [1]. We have reported transperineal MR-guided prostate biopsy with highly accurate targeting as a solution to improve the accuracy of the biopsy process in detection of prostate cancer [2, 3]. The targets are selected by a team of three radiologists, based on pre-operative mpMRI (Fig. 1). The objective of the work presented here is to assess the feasibility of quantitative analysis of mpMRI aided by a machine learning approach to assist the target selection process. The idea is to train a classifier on the mpMRI data from radical prostatectomy patients with histologically confirmed PCa. The resulting classifier is used retrospectively on the data from patients that have undergone MR-guided prostate biopsy, in the areas selected as targets by the radiologists, to compute a measure of the probability of cancer and compare with the histological analysis of the core biopsy samples.

Materials and Methods – *Data*: All patients were enrolled in a prospective clinical study approved by the institutional review board. All patients underwent mpMRI exams in a GE 3T MR scanner using an endorectal coil and included T1w, T2w, DWI and DCE sequences. The training group (N=13) comprised of the patients that had confirmed PCa and underwent radical prostatectomy. In this group, an expert radiologist contoured areas of the prostate peripheral zone (PZ) that were cancerous as reported in the histopathology report and suspicious on T2W (low SI), raw DCE (rapid enhancement and wash out after gadolinium agent administration) and Average Diffusion Coefficient ADC maps (low SI) sequences. The opposite characteristics were considered true of normal prostate PZ. This yielded 16 cancerous and 5 normal regions with a total voxel count of 1499. The second group of patients included all of the cases that have undergone 3T MR-guided biopsy with our current protocol in place as of January 2011, and have at least one biopsy target in the PZ. This amounted to five cases with a total of ten PZ biopsies.

Classification approach: The values of ADC from DWI b0-500, and K^{trans} , v_e , time to peak (TTP) and area under the curve (AUC) from perfusion imaging were available for each pixel. It was observed that only the values of ADC formed distinctly different distributions in the cancer vs. normal regions in the training dataset (Figure 2). We employed two machine learning approaches. First we used our previously reported multi-feature support vector machine (SVM) for mpMRI classification [4] with all possible combinations of the five available parameters. Training and cross-validation was performed on the prostatectomy dataset with a leave-one-patient-out validation scheme. The best outcome was achieved when only ADC was used as the sole feature. Guided by this outcome, we then used a single-feature Bayesian framework using only ADC to build a machine learning solution to predict the outcome of the biopsies. In the Bayesian approach, based on the bell-shaped distributions of the ADC values in the two classes, we assumed Gaussian distributions for the likelihood of ADC values in cancer $P(ADC=a | C)$ and normal areas $P(ADC=a | N)$. The mean and standard deviations for these distributions were derived from a Gaussian fit to the ADC in each class. The priors for cancer and normal were set to $P(C) = P(N) = 0.5$. Using the Bayes rule, we computed the posterior probability of cancer $P_c = P(C|a) = P(a|C)P(C) / [P(a|C)P(C) + P(a|N)P(N)]$.

Results – The leave-one-patient-out cross validation in the prostatectomy dataset yielded an area under the ROC curve of 0.966 using SVM with ADC as the only feature. It was noted that adding the other features to ADC did not improve this results. In a similar cross-validation, the Bayesian classifier resulted in an area under ROC curve of 0.964. Then, using the Bayesian classifier, with the likelihoods estimated on all the 13 training cases, we created maps of P_c values for the patients in the second group. The results are listed in Table 1 and show that in eight of the ten PZ targets, the classification outcome was confirmed by the biopsy finding (P_c close to 1 for cancer and $P_c < 0.5$ for benign findings). All three cancer outcomes are correctly classified. Five of the seven benign outcomes are also correctly identified. This outcome suggests that the classification method, if validated on a larger sample size, has the potential to be used to improve the biopsy yield by testing the regions of the proposed targets, maintaining a high sensitivity and removing some of the false suggested targets.

Conclusions and limitations – In this retrospective feasibility study, we conducted a preliminary evaluation of a classifier in identifying cancer areas in the prostate peripheral zone. Our results show that classification results in the majority of cases agree with the histopathology analysis of the collected sample. The process of ROI selection for training in this work was guided by approximate histology location, the ADC maps and raw DCE data. Among the five parameters we considered, only ADC was used directly for visual differentiation in the training stage which likely explains the strong separation in distributions we observed. Our results confirm the value of ADC in PCa characterization and suggest that the supervised classification approach may have assistive value in target selection for biopsy planning. In the future, we will move towards using wholemount histopathology as the gold standard for ROI selection in the training stage. This might also enable us to extend the methodology beyond the peripheral zone. The number of patients in both training and testing stages will increase as we continue our 3T MR guided biopsy program.

Acknowledgments – NIH: R01 CA111288 (BRP), P41 RR019703 (NCIGT), P01 CA067165, U01 CA151261; and US Army Medical Research and Materiel Command under W81XWH-10-1-0201. **References** – [1] Padhani AR, *et al.*, Clin Radiol 2000; 55:99–109. [2] Tuncali, K. *et al.*, ISMRM 2011, p. 53. [3] Tokuda J., *et al.*, ISMRM 2011, p. 3761. [4] Moradi, M, *et al.*, ISMRM 2011, P 2638.

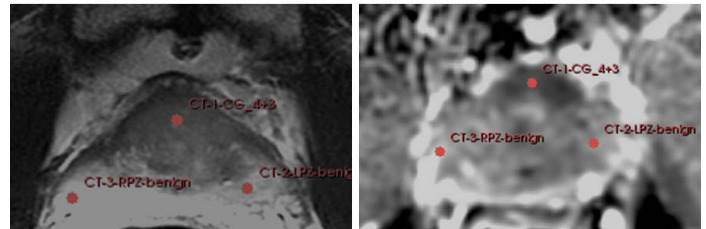


Fig 1. Sample T2 (left) and ADC (right) images for target selection.

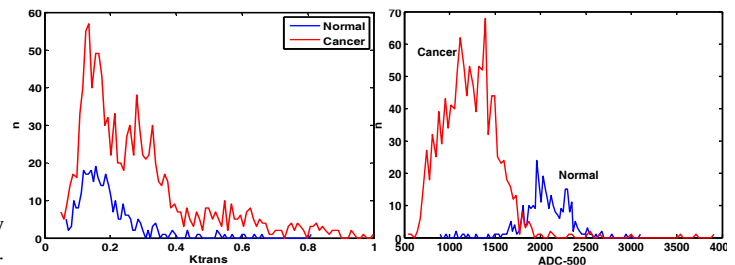


Fig 2. The distribution of K^{trans} and ADC in cancer and normal ROIs.

Samples	Finding	P_c
P1 – RPZ	Benign	0.0
P1 – LPZ	Benign	0.4
P1 – LPZ	Benign	0.9
P2 – LPZ	Benign	0.4
P2 – LPZ	Benign	0.0
P3 – Mid RPZ	3 + 4	1.0
P4 – Mid LPZ	Benign	0.9
P5- RPZ (Apex)	3+3	0.9
P5- RPZ (Base)	3+3	0.8
P5 – LPZ	Benign	0.1

Table 1. The biopsy findings and the computed value of P_c .

Towards Intra-operative Prostate Brachytherapy Dosimetry Based on Partial Seed Localization in Ultrasound and Registration to C-arm Fluoroscopy

Mehdi Moradi^{1,*}, S. Sara Mahdavi¹, Sanchit Deshmukh², Julio Lobo¹,
Ehsan Dehghan³, Gabor Fichtinger³,
William J. Morris⁴, and Septimiu E. Salcudean^{1,*}

¹ Department of Electrical and Computer Engineering,
University of British Columbia, Vancouver, Canada
{moradi,saram,juliol,tims}@ece.ubc.ca

² Indian Institute of Technology, Bombay, India

³ School of Computing, Queen's University, Kingston, ON, Canada

⁴ British Columbia Cancer Agency

Abstract. Intraoperative dosimetry during prostate brachytherapy is a long standing clinical problem. We propose a novel framework to address this problem by reliable detection of a subset of seeds from 3D transrectal ultrasound and registration to fluoroscopy. Seed detection in ultrasound is achieved through template matching in the RF ultrasound domain followed by thresholding and spatial filtering based on the fixed distance between stranded seeds. This subset of seeds is registered to the complete reconstruction of the implant in C-arm fluoroscopy. We report results, validated with a leave-one-needle-out approach, both in a phantom (average post-registration seed distance of 2.5 mm) and in three clinical patient datasets (average error: 3.9 mm over 113 seeds).

1 Introduction

Low dose rate brachytherapy is a minimally invasive therapeutic procedure for prostate cancer that has rapidly gained acceptance due to highly successful clinical results. In this procedure, a number of small radioactive sources or seeds (^{125}I or ^{103}Pd) are permanently implanted into the prostate using brachytherapy needles. The aim is to deliver a sufficient radiation dose to kill cancerous tissue while limiting the dose in radio-sensitive regions such as the bladder, urethra and rectum. Transrectal ultrasound (TRUS) is used to intraoperatively guide the transperineal insertion of needles. As a result of prostate edema, motion of the gland due to needle forces, and possible intra-operative changes to the plan due to various factors such as interference with the pubic arch, the locations of the implanted seeds do not necessarily match with the initial treatment plan. Hence, for quality assurance, intra-operative dosimetry is highly beneficial.

* Corresponding authors.

Researchers have approached ultrasound-based seed detection [1]. However, accurate seed localization based on ultrasound has proven to be a very difficult task due to clutter from other highly reflecting objects such as calcifications resulting in false positive appearances, seed specularities and shadowing, and limited field of view. Even when hand-segmented, up to 25% of the seeds remain hidden in ultrasound images [2]. Therefore, C-arm fluoroscopy is commonly used for visual assessment of the implanted seeds. However, the prostate gland is not discernible in fluoroscopy images. Fusion of the fluoroscopy images and ultrasound is therefore considered as a possible solution [3–6]. If complete seed localization and implant reconstruction from fluoroscopy images is available, the registration of the result to ultrasound will enable dosimetry. In recent years, the fluoroscopy reconstruction problem has been extensively addressed. Given 3–5 fluoroscopy images, and the relative pose of the C-arm in each acquisition, the back-projection technique can be used to reconstruct the 3D implant [7]. For registration, attaching fiducial markers to the ultrasound probe [8], using the ultrasound probe itself as a fiducial [4], or using the seeds as fiducials [9] have been mentioned. Due to patient and equipment motion between the acquisition of ultrasound and fluoroscopy, registration based on static markers is not reliable. Furthermore, the use of fiducial markers is an unwelcome addition to the ordinary setup in the operating room due to time and space limitations.

In this work we propose using a subset of seeds extracted from ultrasound images to perform point-based registration between the seed clouds from fluoroscopy and 3D ultrasound. We present several technical innovations. Instead of conventional B-mode ultrasound, we use RF signals processed to enhance seed contrast. Template matching with a variety of *in vivo* and *ex vivo* seed templates is reported. To enable dosimetry, we have devised a two stage strategy consisting of first 2D registration of needle projections from the ultrasound and fluoroscopy, followed by the 3D registration of only the seeds in the matched needles. We provide the results of this approach on both clinical and phantom data. This novel methodology targets a complicated and long standing problem, with no addition to the routine therapeutic procedure. We show that our method has good promise to address this clinical challenge.

2 Methods

The outline of our methodology is presented in Figure 1. For reconstruction of the implant in fluoroscopy, we implemented and used the method described in [7]. The steps for acquiring the fluoroscopy reconstruction included C-arm pose estimation from rotation angle and compensation for sagging, followed by back-projection of the seeds, and finally seed to needle assignment using a minimum cost flow (MCF) algorithm. The outcome was validated in terms of number of seeds, needles, and seed to needle assignments based on the brachytherapy plans, both in patient and phantom datasets. In this article we focus on ultrasound-based partial seed detection, needle matching and registration from ultrasound to fluoroscopy.

2.1 Seed Detection

3D Ultrasound Setup and Data: We developed a 3D ultrasound system based on a brachytherapy stepper (EXII, CIVCO Medical Solutions) modified by motorizing the cradle rotation. The sagittal array of a dual plane linear/microconvex broadband 5 – 9 MHz endorectal transducer (Ultrasonix) was used. RF data was recorded at a frame rate of 42 fps, during the probe rotation from -45° to 50° (0° corresponded to the probe aligned with the central sagittal cross section of the prostate gland). 2D frame size was 5×5.5 cm. We present the results of our work on data collected immediately after seed implantation in the OR, from three brachytherapy patients in Vancouver Cancer Center. We also present data from a CIRS Model 053 tissue-equivalent ultrasound prostate phantom (CIRS, Inc., Norfolk, VA). For this phantom, a plan consisting of 135 seeds and 26 needles was created which was carried out by a radiation oncologist.

RF Signal Processing: In order to improve the seed to background contrast, we averaged the signal power over windowed blocks of the RF signals. In other words, we replaced a segment of length n at depth d of an RF line with the reflected power P_d computed as:

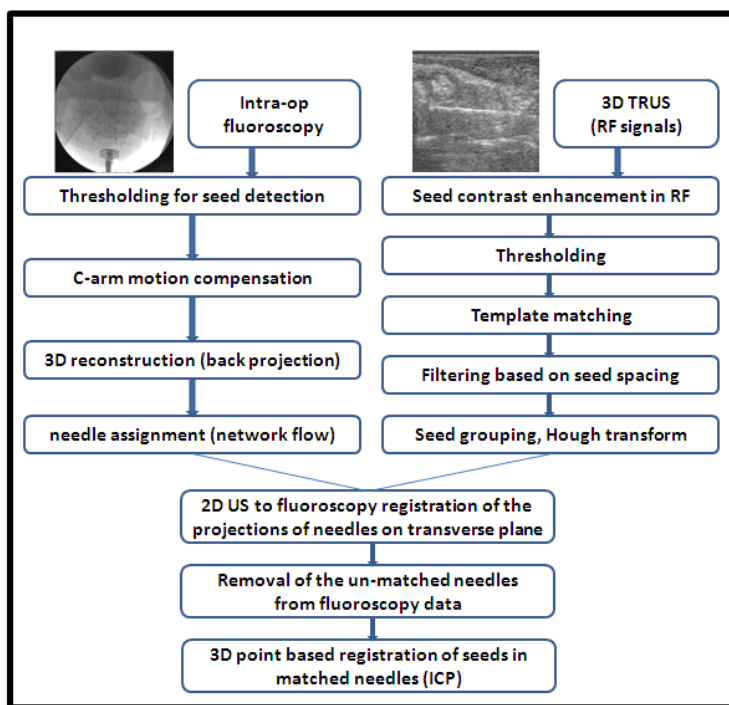


Fig. 1. Workflow of the seed detection method

$$P_d = \frac{\sum_{k=1}^n w(k)x(k)^2}{n} \quad (1)$$

where $x(k)$ ($k = 1, \dots, n$) are the samples in the RF segment, and $w(k)$ are Hamming window weights. This step was applied with $n=10$ and a 50% overlap between consecutive blocks. We have previously reported that this process doubles the contrast to noise ratio (CNR) between the seed regions and the background [10]. Furthermore, the resulting five fold reduction in the size of the RF signals improved the speed of the template matching step.

Seed Templates: Simple thresholding of the contrast enhanced RF data results in a large number of seed candidates and seed-like clutter. In order to reduce false positive detections, we computed the normalized cross correlation of the seed regions with seed templates. We experimented with three groups of templates and will provide a comparison.

Ex vivo templates: We created a 3D template acquired by imaging a seed in water, placed parallel to the probe at the center of the ultrasound probe. The 3D template was formed by rotating the probe and acquiring 21 sagittal images.

In vivo templates: In the clinical situation, the existence of background tissue, blood and edema significantly alters the appearance of seeds on ultrasound images compared to the described *ex vivo* templates, resulting in low normalized cross correlation values. Therefore, we created a second set of templates extracted from *in vivo* data. These were extracted from different cases to ensure that the template extracted from a specific patient dataset, was not used for seed detection in that dataset. They were acquired by manually clicking the center of a visually distinct seed in *in vivo* 3D data.

In vivo and *ex vivo* two-seed templates: We also created templates, both *in vivo* and *ex vivo*, in which the template area contained two seeds. The two-seed templates were examined as a potential solution to reduce the number of false positives, given the fact that in stranded brachytherapy performed in our institution, the distance between seeds is fixed at 1 cm with very few exceptions. Therefore, the existence of two strong seed candidates, 1 cm apart, is an indication of a true detection.

NCC-Based 3D Template Matching: The normalized cross correlation of the 3D template g and a cropped area of the image f equal in size with g and centered at location (i, j, k) can be computed as:

$$f \star g(i, j, k) = \frac{(\sum_{x,y,z} f_{i,j,k}(x, y, z) - \overline{f_{i,j,k}}) \cdot (g(x, y, z) - \overline{g})}{\sqrt{[\sum_{x,y,z} (f_{i,j,k}(x, y, z) - \overline{f_{i,j,k}})^2 \sum_{x,y,z} (g(x, y, x) - \overline{g})^2]}} \quad (2)$$

where x , y and z represent the directions in the image coordinate system. Computation of $f \star g$ results in a new image of the same size as f , with values in range of $[0,1]$ with largest values representing the centers of areas most similar to the template. The frequency domain implementation of NCC was completed in under six minutes on a regular PC with MATLAB for template size of $30 \times 60 \times 21$, and

image size of $128 \times 258 \times 391$. Note that NCC is not invariant to scale. However, in our case, the images and the templates were acquired with similar imaging parameters, therefore the scales matched.

Thresholding, Spatial Filtering, and Grouping in the NCC Image: The NCC image was thresholded. Starting from the point with the highest NCC, a neighborhood of the size of the seed was cleared around each non-zero voxel. This was necessary because each seed consists of several bright voxels, while we need a single voxel to represent the seed. The remaining voxels were grouped into needles using the Hough transform [11] followed by eliminating single seeds that could not be grouped into lines. Using the knowledge of the fixed 1 cm distance between the seeds in our data, we applied an additional trimming step. On each needle, starting from the seed with the highest NCC value, any other seed candidate that was within 0.8 cm was removed.

2.2 Matching and Registration

After applying a transformation that matched the centers of mass of the two datasets, we applied a 2D needle matching process. This provided an initial alignment and reduced the risk of local minima due to the unbalanced number of seeds in ultrasound and fluoroscopy. Matching was performed by applying a 2D rigid registration between the needle projections on the transverse plane passing through the prostate mid-gland in the fluoroscopy implant. Assuming that X is the set of n projection points from ultrasound, and Y is the set of m projection points from fluoroscopy, the rotation and translation parameters of the transformation T were found to minimize $\sum_{i=1:n} d_c[T(X_i), Y]$ where $d_c[T(X_i), Y]$ is the Euclidean distance of the ultrasound projection point X_i from its closest match in the point set Y . After the matching step, the fluoroscopy needles without a match in ultrasound were removed and the standard 3D point-based Iterative Closest Point (ICP) registration algorithm [12] was applied.

3 Results and Conclusions

We quantified the outcome of our ICP seed registration method based on 1) the post-registration distances between ultrasound seeds and their closest fluoroscopy counterparts, 2) the stability of needle matches and the recorded registration errors subject to the removal of any of the detected needles.

Registration Errors: Table 1 presents the results of ultrasound seed detection and registration for the CIRS phantom. The best outcome was achieved when the two-seed *ex vivo* template set was used. The post-registration seed distances from ultrasound to the closest matching fluoroscopy seed was 2.48 mm. Note that the best registration result was obtained when the lowest number of seeds (73 out of 135, 17 needles out of 26) were detected. The result of the 2D matching and 3D registration of the seed clouds for the phantom data, using the two-seed *ex vivo* template, is depicted in Figure 2.

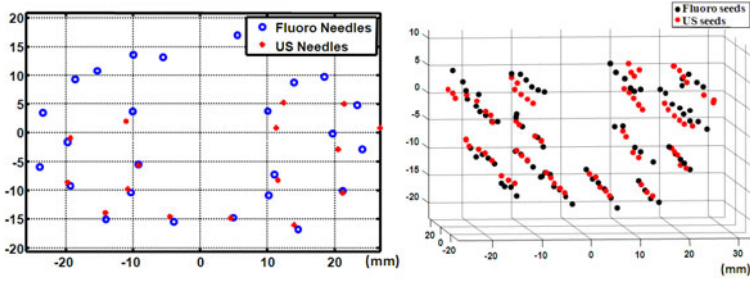


Fig. 2. Phantom results: 2D matching of needle projections in transverse plane (left), 3D seed cloud registration using the matched needles from fluoroscopy and ultrasound

Table 1. Phantom result: # of detected seeds, registration errors with all detected needles, and average registration error for the leave-one-needle-out validation test

Phantom	dist. er.(mm)	dist. er.	# fl	# fl seeds,	# of detected
	all needles	(mm)	seeds	in matching	seeds in
		L.O.O	Total	needles	ultrasound
1-seed, <i>ex vivo</i> templ.	2.69 ± 2.03	2.71 ± 1.98	135	95	86
1-seed, <i>in vivo</i> templ.	4.33 ± 2.21	4.40 ± 2.24	135	101	95
2-seed, <i>ex vivo</i> templ.	2.48 ± 1.52	2.48 ± 1.41	135	82	73

Table 2 presents the results for the three patient datasets. The one-seed and the two-seed templates did not result in significantly different error values. We obtained errors of 3.36 mm, 3.73 mm, and 4.76 mm for the three cases on *in vivo* templates. With *ex vivo* templates, we witnessed a decrease in the number of detected seeds for all cases and an error increase in two patients with a slight improvement in case 3 in terms of registration error (to 4.38, 4.08 and 4.22 mm). For case 2, Figure 3 illustrates the results of 2D matching and 3D registration. In both Figures 2 and 3 one can see that the unmatched needles tend to be from the anterior side (top of the images), while the posterior seeds that are closest to the probe are accurately detected. This is likely due to signal attenuation and the depth dependent reduction in the resolution of our 3D ultrasound system.

Leave-one-needle-out Validation of the Registration Process: In order to study the stability of our matching and registration procedure, we also ran a leave-one-needle-out experiment. For each patient and the phantom case, assuming that n ultrasound needles were identified, we repeated the matching and registration procedure n times, each time with $n - 1$ needles. This amounted to the removal of three to seven (10% to 20%) of the seeds in each round for patient cases. The idea is that if the registration is valid, and not just a local minimum, the removal of any specific needle should not drastically change the outcome.

The average of the errors in the leave one out experiments (column 3 in Tables 1 and 2) were close to the errors when all detected seeds were used in the registration step (column 2). We also examined the stability of the needle

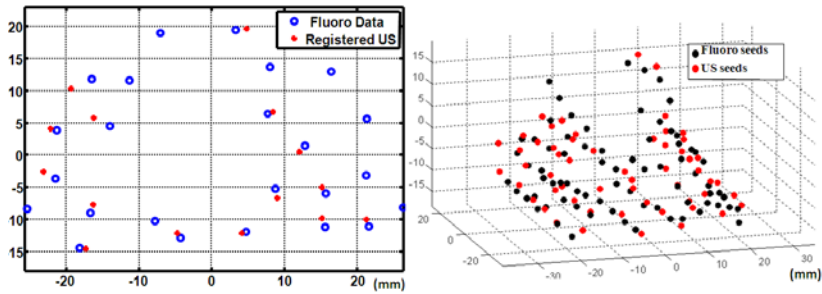


Fig. 3. A patient case: 2D matching (left), registered seeds in matched needles (right)

Table 2. Number of the detected seeds, registration errors and leave-one-needle-out errors for the 3 patient datasets

Case	dist. er.(mm) all needles	dist. er. (mm) L.O.O	# fl seeds Total	# fl seeds, in matching needles	# of detected seeds in ultrasound
P1 1-seed <i>in vivo</i> templ.	3.72 ± 1.86	3.85 ± 1.96	102	51	35
P1 2-seed <i>in vivo</i> templ.	3.36 ± 1.78	3.44 ± 1.95	102	57	37
P1 <i>ex vivo</i> templ.	4.07 ± 2.10	4.38 ± 1.87	102	30	16
P2 1-seed <i>in vivo</i> templ.	3.98 ± 2.50	3.77 ± 2.27	115	74	56
P2 2-seed <i>in vivo</i> templ.	3.73 ± 1.86	3.79 ± 1.94	115	71	49
P2 <i>ex vivo</i> templ.	3.74 ± 2.8	4.08 ± 2.58	115	55	37
P3 1-seed <i>in vivo</i> templ.	4.76 ± 1.87	4.90 ± 2.12	100	35	27
P3 2-seed <i>in vivo</i> templ.	4.88 ± 1.95	4.79 ± 2.25	100	33	23
P3 <i>ex vivo</i> templ.	4.52 ± 1.65	4.22 ± 1.49	100	26	16

matching step subject to removal of needles. In the case of the phantom data, and case 1 among the patient datasets, it was noted that regardless of which needle was removed in the leave one out experiment, the matched fluoroscopy needle for the rest of ultrasound needles remained the same (number of detected needles: $n=17$). In patient cases 2 and 3, on average, the match for one needle changed due to the removal of a needle ($n=14$ and $n=12$).

4 Conclusions

We showed that it is feasible to use contrast enhanced RF ultrasound data, template matching, and spatial filtering to detect a reliable subset of brachytherapy seeds from ultrasound to enable registration to fluoroscopy. Real-time implementation requires the matching process to be computationally improved though parallelization to enhance the current computation time of around six minutes. More robustness analysis and additional registration approaches will be implemented in future work. The 3D ultrasound system used in this work acquired sagittal images while rotating radially. This results in a significant decrease in

spatial resolution at increasing distances from the probe. The use of a comprehensive depth dependent set of templates can improve our results. It is also possible to perform the ultrasound seed detection after only a part of the implant, for example the top row of needles, is completed. This will reduce the shadowing effects. Clinical data is being acquired to test these possibilities.

Acknowledgments. Dr T. Pickles and Mr N. Chng (data acquisition); Dr X. Wen (RP imaging codes). M. Moradi held an NSERC PDF and the US DoD PCRP Award W81XWH-10-1-0201, S. Mahdavi was supported by the Prostate Cancer Foundation of BC, G. Fichtinger was supported as Cancer Care Ontario Research Chair, S. E. Salcudean was supported by NSERC and CIHR.

References

1. Mamou, J., Ramachandran, S., Feleppa, E.J.: Angle-dependent ultrasonic detection and imaging of brachytherapy seeds using singular spectrum analysis. *Journal of the Acoustical Society of America* 123(4), 2148–2159 (2008)
2. Jain, A.K., Zhou, Y., Mustufa, T., Burdette, E.C., Chirikjian, G.S., Fichtinger, G.: Matching and reconstruction of brachytherapy seeds using the hungarian algorithm (MARSHAL). In: *SPIE Medical Imaging*. SPIE, vol. 5744, pp. 810–821 (2005)
3. Fallavollita, P., Karim-Aghaloo, Z., Burdette, C.E., Song, D.Y., Abolmaesumi, P., Fichtinger, G.: Registration between ultrasound and fluoroscopy or CT in prostate brachytherapy. *Med. Phys.* 37(6), 2749–2760 (2010)
4. French, D., Morris, J., Keyes, M., Salcudean, S.E.: Real-time dosimetry for prostate brachytherapy using TRUS and fluoroscopy. In: Barillot, C., Haynor, D.R., Hellier, P. (eds.) *MICCAI 2004*. LNCS, vol. 3217, pp. 983–991. Springer, Heidelberg (2004)
5. Su, Y., Davis, B.J., Furutani, K.M., Herman, M.G., Robb, R.A.: Seed localization and trus-fluoroscopy fusion for intraoperative prostate brachytherapy dosimetry. *Comput. Aided Surg.* 12(1), 25–34 (2007)
6. Todor, D.A., Zaider, M., Cohen, G.N., Worman, M.F., Zelefsky, M.J.: Intraoperative dynamic dosimetry for prostate implants. *Physics in Medicine and Biology* 48, 1153–1171 (2003)
7. Dehghan, E., Lee, J., Moradi, M., Wen, X., Fichtinger, G., Salcudean, S.E.: Prostate brachytherapy seed reconstruction using C-arm rotation measurement and motion compensation. In: Jiang, T., Navab, N., Pluim, J.P.W., Viergever, M.A. (eds.) *MICCAI 2010*. LNCS, vol. 6361, pp. 283–290. Springer, Heidelberg (2010)
8. Zhang, M., Zaider, M., Worman, M., Cohen, G.: On the question of 3D seed reconstruction in prostate brachytherapy: the determination of x-ray source and film locations. *Phys. Med. Biol.* 49(19), N335–N345 (2004)
9. Tutar, I.B., Gong, L., Narayanan, S., Pathak, S.D., Cho, P.S., Wallner, K., Kim, Y.: Seed-based transrectal ultrasound-fluoroscopy registration method for intraoperative dosimetry analysis of prostate brachytherapy. *Med. Phys.* 35(3), 840–848 (2008)
10. Wen, X., Salcudean, S.E., Lawrence, P.D.: Detection of brachytherapy seeds using 3-D transrectal ultrasound. *IEEE Trans. Biomed. Eng.* 57(10), 2467–2477 (2010)
11. Duda, R.O., Hart, P.E.: Use of the Hough transformation to detect lines and curves in pictures. *Communications of the ACM* 15, 11–15 (1972)
12. Besl, P.J., McKay, N.D.: A method for registration of 3-D shapes. *IEEE Transactions on Pattern Analysis and Machine Intelligence* 14(2), 239–256 (1992)

Prostate Cancer Probability Estimation Based on DCE-DTI Features and Support Vector Machine Classification

M. Moradi¹, S. E. Salcudean¹, S. D. Chang², E. C. Jones³, S. L. Goldenberg^{4,5}, and P. Kozlowski^{2,6}

¹Electrical and Computer Engineering, University of British Columbia, Vancouver, BC, Canada, ²Radiology, University of British Columbia, ³Pathology and Laboratory Medicine, University of British Columbia, ⁴Urologic Sciences, University of British Columbia, ⁵Vancouver Prostate Centre, University of British Columbia, ⁶MRI Research Centre, University of British Columbia, Vancouver, Canada

Introduction: Prostate cancer is the most common noncutaneous malignancy among men. The clinical routine for diagnosis is biopsy under ultrasound guidance. However, as a result of the multi-focal nature of the disease, clinically significant cases of cancer can be missed, resulting in repeated biopsies. We have previously shown that Diffusion Tensor Imaging (DTI) and Dynamic Contrast Enhanced (DCE) MRI provide a high degree of sensitivity in detecting prostate cancer [1,2]. In this study we present a framework of classification using multi-parametric MRI feature vectors and Support Vector Machines (SVMs) to detect prostate cancer and to create cancer probability maps that highlight areas of tissue with high risk of cancer. The correlation of this probability with Gleason Grade is also studied.

Data: Twenty nine men with a high clinical suspicion for prostate adenocarcinoma were included in this study. All MRI exams were carried out on a 3T Philips Achieva MRI scanner. Twelve axial slices (4 mm, no gap) across the prostate gland were acquired for both DTI and DCE MRI data with FOV of 24 cm. The DTI data were processed off-line to generate maps of Apparent Diffusion Coefficient (ADC) and Fractional Anisotropy (FA) [2]. Three DCE-based pharmacokinetic parameters, namely volume transfer constant K^{trans} , fractional volume of the extra-vascular extra-cellular space v_e , and fractional plasma volume v_p , were calculated by fitting the Gd concentration vs. time curves to the extended Kety model [3]. After imaging, from 8 to 12 needle biopsies were collected from each subject depending on the size of the prostate. The dataset included a total of 240 negative biopsy cores and 29 positive biopsy cores. The histology was interpreted with assignment of the Gleason score by a number of different anatomic pathologists who practice general and subspecialty uropathology

Classification and mapping method: Each biopsy core in the dataset was represented by a feature vector consisting of the average values of the five DCE-DTI features ($X = [K^{trans}, v_e, v_p, ADC, FA]$) in its corresponding area in the MRI data. Following [2], for negative biopsies, this corresponding area was set to be the entire biopsy target volume (e.g. mid-left-lateral), while for positive cores, this area was determined from a combination of manual segmentation and thresholding based on biopsy (see [2] for details). SVM classification with radial basis kernel function [4] was used to separate the data into “normal” and “cancer” classes based on these feature vectors. The parameters of the SVM kernel function were chosen in a grid-based search [5,6]. The training-testing validation was performed in leave-one-patient-out manner. For each patient, we trained the SVM based on biopsy cores from all other patients and tested it on the cores from the patient in question. To acquire post-classification cancer probabilities ($P_c = P(cancer|X)$), the extension of the SVM training proposed by Platt [7] was used. The P_c value acquired for each biopsy core was used as a decision threshold for cancer detection. The Receiver Operating Characteristic (ROC) curve was obtained by setting this detection threshold to values in the range of [0,1]. Given X for all pixels in one MRI slice, cancer probability maps were created by calculating and plotting the values of P_c - using the SVM trained on data from all other subjects - for the entire prostate region in the slice.

Results and discussion: The ROC curves were obtained separately for DCE features $X_{DCE} = [K^{trans}, v_e, v_p]$, for DTI features $X_{DTI} = [ADC, FA]$, and for the combined feature vector $X = [K^{trans}, v_e, v_p, ADC, FA]$ resulting in area under ROC curve (AUC) values of 0.867, 0.919 and 0.956 respectively (Fig.1). The combined feature vector resulted in higher AUC than DCE ($p=0.002$) and DTI ($p=0.01$). With the combined feature vector, at the decision threshold of $P_c = 0.5$, three of the 29 tumors were misclassified while a specificity of 91% was obtained. At the decision threshold of $P_c = 0.7$, only one tumor was misclassified, while a high specificity of 87% was maintained. We also noted a correlation between the P_c value and the Gleason grade of the tumors. The average P_c value was 0.555 for tumors of grade 3+3 (number of tumors=7), 0.778 for tumors of grade 3+4 and 4+3 ($n=19$), and 0.963 for grade 4+5 ($n=3$). The increase in P_c values was significant from Grade 6 to 7 ($p=0.01$). The small number of tumors in grade 4+5 did not warrant an analysis of statistical significance. None of the 4+5 tumors were misclassified in any of the experiments. The T2W image and the cancer probability map obtained for the mid slice MRI data of a patient with positive biopsy cores in the mid-left-lateral and mid-left-medial regions of the prostate are illustrated in Fig. 2.

Conclusions: Our result is in agreement with the previous work that shows the diagnostic power of combined DTI and DCE MRI [2]. The developed SVM-based probabilistic approach to cancer detection provides a high level of sensitivity while maintaining high specificity. The observed increase in cancer probability with increasing Gleason grade is promising. This suggests that multi-class SVM-based classification is a potential tool for non-invasive grading, given a sufficiently large dataset to enable training on tumors of different grades.

Acknowledgments: This work was supported by a research grant from the Canadian Institutes for Health Research and a Prostate Cancer Training Award from the Congressionally Directed Medical Research Program, United States Department of Defense.

References: [1] Kozlowski P, et al. *ISMRM*, 2009, p. 2245; [2] Kozlowski P, et al. *Magn Reson Imaging*, 2010, **28**, 621; [3] Tofts PS, et al. *J Magn Reson Imaging*, 1999, **10**, 223; [4] Vapnik VN, *The Nature of Statistical Learning Theory*, Springer-Verlag, 1995. [5] Fan RE, et al. *Machine Learning Research*, 2005, **6**,1889; [6] Moradi et al., *IEEE Trans. Biomed. Eng.*, 2009, **56**, 2214; [7] Platt J, *Advances in Large Margin Classifier*, MIT Press, 1999.

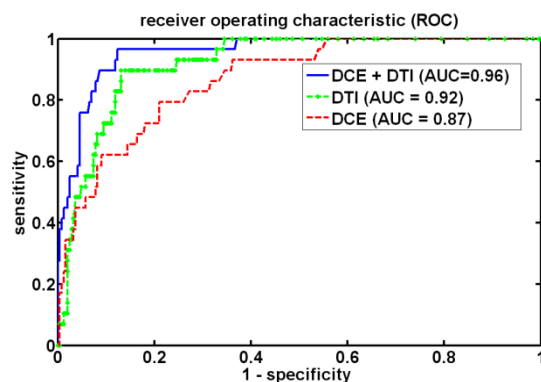


Figure 1- ROC curves, for different groups of features acquired by changing the decision threshold, P_c , from 0 to 1.

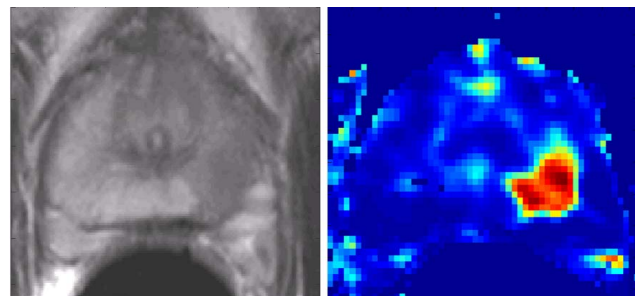


Figure 2 – Left: T2W image of mid region of a patient with biopsy confirmed cancer in mid-left region. Right: The SVM-based cancer probability map, with hot colors corresponding to higher P_c . The tumor is distinguished.

Automatic Prostate Segmentation Using Fused Ultrasound B-Mode and Elastography Images

S. Sara Mahdavi¹, Mehdi Moradi¹, William J. Morris²,
and Septimiu E. Salcudean¹

¹ Department of Electrical and Computer Engineering,
University of British Columbia, Vancouver, Canada
{saram,moradi,tims}@ece.ubc.ca

² Vancouver Cancer Center, British Columbia Cancer Agency, Vancouver, Canada
jmorris@bccancer.bc.ca

Abstract. In this paper we propose a fully automatic 2D prostate segmentation algorithm using fused ultrasound (US) and elastography images. We show that the addition of information from mechanical tissue properties acquired from elastography to acoustic information from B-mode ultrasound, can improve segmentation results. Gray level edge similarity and edge continuity in both US and elastography images deform an Active Shape Model. Comparison of automatic and manual contours on 107 transverse images of the prostate show a mean absolute error of 2.6 ± 0.9 mm and a running time of 17.9 ± 12.2 s. These results show that the combination of the high contrast elastography images with the more detailed but low contrast US images can lead to very promising results for developing an automatic 3D segmentation algorithm.

1 Introduction

Low dose rate (LDR) prostate brachytherapy is a common method for treating patients with low risk prostate cancer. In this treatment, 40-100 small radioactive seeds are permanently inserted in the prostate and its periphery. Treatment planning and delivery relies on transrectal ultrasound (TRUS) imaging. In order to create the treatment plan, a pre-operative volume study is carried out in which a set of transverse ultrasound images are collected. These images are then manually segmented to extract the prostate boundaries. A plan is devised to deliver sufficiently high radiation dose to the cancerous tissue while maintaining a tolerable dose to healthy tissue. Reliable segmentation and visualization of the prostate is a vital step in dose planning. Manual segmentation is time consuming and, due to the low signal to noise ratio of ultrasound images, inter and intra-observer variabilities are high. Even though various 2D prostate segmentation methods and some 3D methods have been proposed in the literature [1,2,3,4,5], the effective automatic segmentation of ultrasound images of the prostate has remaining challenges such as user initialization and limited accuracy.

In this paper, we propose a prostate segmentation method based on intra-modality fusion of ultrasound B-mode and elastography. Elastography [6], in

which mechanical properties of tissue are characterized, has shown to be promising in improving the visibility of the prostate gland [7,8]. In a recent study, we have shown that ultrasound dynamic elastography images of the prostate have superior object-background contrast compared to B-mode ultrasound, especially at the base and apex [9]. This is due to the fact that prostate tissue is generally stiffer than the surrounding tissue. We utilize this advantage and combine elastography and US image data for 2D segmentation of the prostate. The elastography images are acquired using a system described in [9] which enables the simultaneous registered acquisition of B-mode and elastography images, thereby eliminating the concerns about image registration and cost.

We use an Active Shape Model (ASM) [10] approach which starts with an initial shape extracted from a large number of elastography and B-mode prostate images. The deformation of this initial shape is restricted to conform to the statistical model and is guided by edge detection from both elastography and B-mode images based on edge gradient similarity and continuity. The use of a statistically created model ensures the compliance of the resulting contours with the overall shape of the organ. Additionally, the restricted deformation results in robustness to poor image quality. The use of a measure of edge continuity [9] in addition to gradient similarity, reduces the effects of strong speckle-induced local edges on the algorithm which improves the rate of convergence. We provide a statistical analysis of the accuracy of our 2D image segmentation method and show that the combined use of elastography and B-mode images improves the accuracy and the convergence rate. Further, we describe a preliminary framework for extending the proposed method to an automatic 3D segmentation algorithm and present an example.

2 Methods

The US and elastography images used in this paper were acquired from patients going through the standard LDR prostate brachytherapy procedure at Vancouver Cancer Center, BC Cancer Agency. Intra-operatively, prior to the procedure, RF data and US images were simultaneously collected using the system described in [9]. In this system RF data is collected at approximately 40 fps from the sagittal array of a vibrating (amplitude 0.5-2 mm, frequency range 2-10 Hz) and rotating (-45° to 50°) TRUS probe (dual-plane linear/microconvex broadband 5 - 9 MHz endorectal transducer, Ultrasonix Medical Corp.). The RF data were processed [11] to obtain sagittal elastography strain images from which conventional transverse images of the prostate were achieved.

Our 2D segmentation approach combines the information from elastography and US images within an Active Shape Model (ASM) which deforms based on gray level similarity and edge continuity. We follow the approach from [10]. First, we construct a training set by manually selecting 30 specific points on the prostate boundary in $N = 25$ mid-gland images from 7 patients. The set of images used for creating the training set does not include the images to be segmented. The manually segmented contours are aligned by using least-squares-based iterative scaling, rotation and translation and the average of the resulting

contours, \bar{x} , is used as the initial contour. Then, in order to capture the statistics of the training set, we calculate the covariance matrix, $S = \sum_{i=1}^N dx_i dx_i^T$, where dx_i in the training phase is the distance between each point on the manual contour and the corresponding point on the mean shape. The modes of variation of the shape are described by the eigenvalues, λ_i , and eigenvectors, p_i , of S , from which the t largest eigenvalues are selected as the most significant modes of variation. We selected t such that for $i = 1, \dots, t$, $\lambda_i / \sum \lambda > 5\%$. A shape instance consistent with the training set can thus be created using Eq.(1):

$$x = \bar{x} + Pb \quad (1)$$

where $P = (p_1 \dots p_t)$ is the matrix of the first t eigenvectors and $b = (b_1 \dots b_t)^T$ is a vector of weights. Hence, in the shape fitting phase, given a shape deformation, dx , the shape parameter adjustments, db , can be calculated using Eq.(2).

$$db = P^T dx \quad (2)$$

To calculate the movement, dx_i , for each model point i , a measure of edge gray level similarity was used in [10]. For each point i of each image j of the training set, a normalized edge derivative profile, g_{ij} normal to the boundary, centered at the model point and of length n_p is extracted. g_{ij} is averaged over all images from which the covariance matrix S_{g_i} is calculated to obtain a statistical description of the gray level appearance for every point. During the shape fitting, at each iteration and for every point, sample edge derivative profiles $h_i(d)$ of distance d ($d = -l, \dots, l$) from the boundary point and length n_p are extracted in a similar manner. The square of the Mahalanobis distance of these profiles from the model profile, g_i , give a measure of edge gray level similarity. For each point, the d resulting in the least Mahalanobis distance suggests the required point movement along a line normal to the boundary. The physical values of l and n_p are set to 8 and 5 mm, respectively.

In our data set, we observed that the gray level edge similarity measure alone, gives many false positives due to ultrasound speckle or sharp edge-like structures since only 1D information (normal to the edge) is being analyzed. Therefore, in our approach, we incorporate our edge continuity measure [9] which measures the continuity of the edge in a direction orthogonal to the edge profile. At a distance d from each point, we compute the average normalized cross-correlation, $c_i(d)$, between the edge intensity profile $e_i(d)$ (obtained similar to g_{ij}), of length n_p , with its two neighboring left and right edge intensity profiles. For a continuous edge (i.e. large similarity between $e_i(d)$ and its left and right neighboring profiles), $c_i(d)$ should have a shape similar to a Gaussian function with a large peak and a small standard deviation. We define the edge continuity measure, $K_i(d) = P_{c_i}^2 / \sigma_i(d)$ in which P_{c_i} characterizes the peak and σ_i is the standard deviation of a Gaussian function fitted to $c_i(d)$. For each point, the d resulting in the maximum continuity measure suggests the required point movement along a line normal to the boundary.

We define u_n to be the vector normal to the boundary at the boundary point, d_{gE} , to be the distance from the boundary point suggested by the gray level

similarity, and d_{KUS} , and d_{KE} to be the distances from the boundary point computed from the edge continuity measures in US and elastography images, respectively. Based on the above equations, at each iteration, k , the following steps are performed to deform the current shape points, $x_{current}$ into the next shape, x_{next} .

1. Find the required shape deformation:

$$dx = x_{next} - x_{current} = d_f u_n$$

$$d_f = \alpha_1 d_{gE} + \alpha_2 d_{KUS} + \alpha_3 d_{KE}$$

2. Calculate the optimum pose parameters: scaling, translation and rotation, corresponding to dx , apply this transformation to obtain $T(x_{current})$. Adjusting the pose is required to align $x_{current}$ to be as close as possible to x_{next} before adjusting the shape [10].
3. Calculate $db = P^T(x_{next} - T(x_{current}))$

$\alpha = [\alpha_1 \ \alpha_2 \ \alpha_3]$ are corresponding weights. Due to the large amount of noise in US images, gray level similarity matching in these images does not improve results but degrades convergence, and therefore, it is not included. Our criteria for convergence is when 94% of the contour points have a dx of less than $n_p/2$. Fig. 1 illustrates how d_{gE} and d_{KE} are obtained in an elastography image.

We will provide a comparison of segmentation results using gray level similarity from elastography images, combined edge continuity and gray level similarity from elastography images and finally edge continuity and gray level similarity from both elastography and US images.

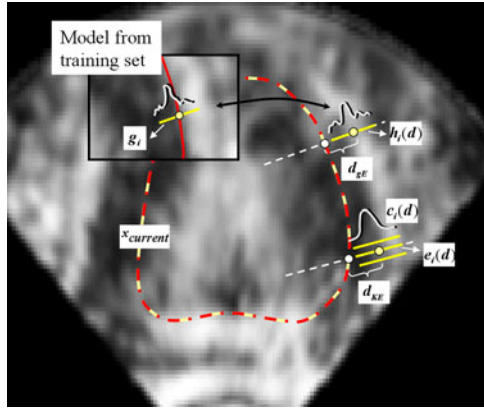


Fig. 1. An illustration of how d_{gE} (top point) and d_{KE} (bottom point) are obtained in an elastography image. The gray level similarity measure is compared to that of the model for each corresponding point. The edge continuity measure is maximized over the line normal to the boundary. For clarity, these measures are shown on two different points, whereas they are calculated for single points.

3 Results

To evaluate our 2D segmentation results we measure the mean absolute distance (MAD) and maximum distance (MaxD) between 2D automatic and manual contours. Table 1 provides the mean and standard deviations of MAD and MaxD between 107 manual and automatic contours selected from 7 patients. The results are presented separately for elastography gray level similarity only ($\alpha_a=[1 \ 0 \ 0]$), elastography gray level similarity and edge continuity ($\alpha_b=[0.5 \ 0 \ 0.5]$), and elastography gray level similarity and edge continuity plus US edge continuity ($\alpha_c=[0.5 \ 0.25 \ 0.25]$). Fig. 2 shows an example of segmentation results for the three sets of weight parameters.

The most accurate segmentation results were acquired when $\alpha_c=[0.5 \ 0.25 \ 0.25]$. By using this selection of weight parameters, deformation is mainly guided by the coarser elastography images but also refined by the finer US images. It is specifically seen in the posterior region of the prostate, where elastography image quality is low, that the addition of edge continuity in US images improves segmentation results. This can be observed in Fig. 2. The choice of α_c also results in the convergence of the algorithm in an average of 22 iterations vs. 37 and 98 iterations for α_b and α_a . The maximum number of iterations was set to 50 for α_b and α_c and 100 for α_a . In the case of α_a , 95% of the cases did not converge within 100 iterations.

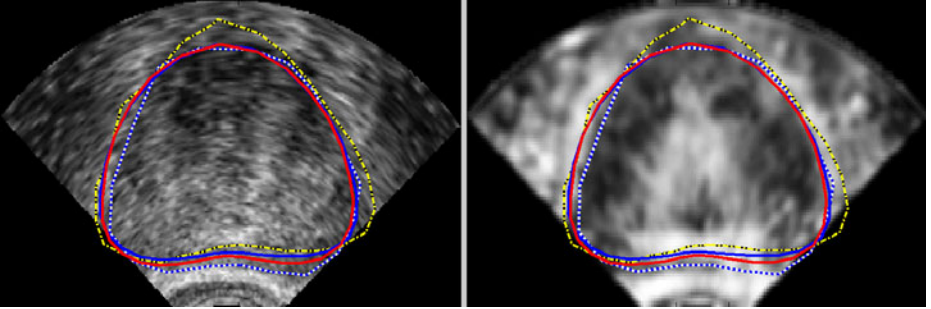


Fig. 2. 2D automatic segmentation results using elastography gray level similarity (yellow dashed line), elastography edge continuity and gray level similarity (blue line), and elastography gray level similarity and edge continuity plus US edge continuity (red line) on US (left) and elastography (right) images. The manual contour is shown as a blue/white dotted line.

4 Discussion

By visual inspection of the automatic segmentation results, we observed that most of the 2D segmentation error of the mid-gland slice was in the anterior and posterior regions. In elastography images, the blood vessels which lie on the anterior of the prostate appear as stiff tissue and are not always distinguishable

Table 1. Comparison of 2D manual and automatic segmentation showing the Mean Absolute distance (MAD) and Maximum Distance (MaxD - positive sign meaning larger automatic contour) between manual and automatic prostate contours, the number of iterations and duration of the algorithm. K : edge continuity measure, d_g : gray level similarity measure.

	d_g in elast.	d_g and K in elast.	d_g and K in elast. and K in US
MAD (mm)	3.4 ± 1.8	3.4 ± 1.7	2.6 ± 0.9
MaxD (mm)	1.0 ± 9.8	-6.5 ± 7.0	-4.9 ± 4.7
no. of iter.	98 ± 13	37 ± 17	22 ± 15
duration (s)	10.7 ± 1.4	17.3 ± 0.8	17.9 ± 12.2

from the prostate itself. In such cases, the automatic contour extends beyond the actual boundary. In the posterior, due to the relatively low contrast in this region, the automatic contour converges to the darker tissue inside the prostate. By including edge continuity data from US images this problem has been partially resolved. We attribute this low contrast to mainly the slippage between the protective sheath on the probe and the surface of the rectum during elastography data collection. By replacing the 1D axial strain computation with 2D axial/lateral and by increasing the resolution of elastography imaging such problems can be subsided.

Our current elastography data acquisition system has the benefit of collecting inherently registered elastography and US data. Currently the TRUS rotation range is within $\pm 50^\circ$ which may result in missing data in the mid-lateral regions of large prostates. Also, the quality of the B-mode US images acquired along with the elastography data is affected by the computational limitations of the real-time data acquisition system and the ultrasound machine. We are currently working on resolving these problems to improve segmentation results.

The proposed 2D prostate segmentation method using fused elastography and US image information can be extended into 3D by modifying the method that we proposed in [12] which was based on fitting an *a priori* shape to a set of parallel transverse ultrasound images. The algorithm was initialized by the user manually selecting some initial boundary points on the mid-slice. These points were used to un-warp and un-taper all images resulting in a set of elliptical prostate shapes. With the aid of the Interacting Multiple Model Probabilistic Data Association (IMMPDA) [13] edge detector and ellipse fitting, a tapered ellipsoid was fitted to all contours which was then sliced at image depths. The resulting 2D contours were reversely tapered and warped to match the initial images. We showed [12] that the method is fast, and produces smooth contours that are in agreement with the brachytherapy requirements. However, the need for manual initialization limits its use for real-time applications and makes it user dependent. Also, the poor visibility of the boundary at the base and apex complicates segmentation of these regions.

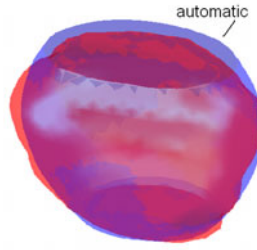


Fig. 3. An example of 3D surface of the prostate created manually (red) and by the automatic algorithm (blue)

To resolve these issues we replace the manual initialization of the 3D semi-automatic segmentation with the described 2D segmentation. Additionally, we employ elastography along with US images for propagating the mid-gland segmentation to the rest of the images. This is done by including an additional IMMPDA edge detection on the coarser elastography images to guide the edge detection on the finer US images. The described framework for automatic 3D prostate segmentation was applied to one patient data set. Fig. 3 shows 3D surfaces created from automatic (blue) and manual (red) segmentation of the prostate for this patient. 11 images were used to construct this surface model. The volume of the manually created surface is 33.9 ml, the volume of the automatically created surface is 34.4 ml, and the volume of the non-overlapping region between the two surfaces is 4.9 ml. A thorough clinical study is required to evaluate this 3D segmentation framework.

5 Conclusions

In this paper we outlined a novel 2D method of prostate segmentation that combines ultrasound elastography imaging with B-mode data. This is the first instance of using such a combination for prostate segmentation and reinforces efforts to improve US segmentation outcomes using elastography data [14]. With the fusion of information from elastic properties of tissue provided by elastography with the acoustic properties of tissue provided by B-mode we developed an automatic and accurate segmentation of the prostate which gives good results in 2D. The automatically generated 2D contours can be used to initialize the mid-slice for 3D segmentation and remove user variability. Additionally, the method can be utilized to register pre and intra-operative prostate images and has the potential of improving intra-operative dosimetry.

Acknowledgments. This project was funded by NSERC Canada (Discovery Grant and Postdoctoral Fellowship). Data collection was funded by NIH grant R21 CA120232-01.

References

1. Penna, M.A., Dines, K.A., Seip, R., Carlson, R.F., Sanghvi, N.T.: Modeling prostate anatomy from multiple view TRUS images for image-guided HIFU therapy. *IEEE Trans. Ultrason. Ferroelectr. Freq. Control* 54(1), 52–69 (2007)
2. Tutar, I.B., Pathak, S.D., Gong, L., Cho, P.S., Wallner, K., Kim, Y.: Semiautomatic 3-D prostate segmentation from TRUS images using spherical harmonics. *IEEE Trans. Med. Imaging* 25(12), 1645–1654 (2006)
3. Zhan, Y., Shen, D.: Deformable segmentation of 3-D ultrasound prostate images using statistical texture matching method. *IEEE Trans. Med. Imaging* 25(3), 256–272 (2006)
4. Hodge, A.C., Fenster, A., Downey, D.B., Ladak, H.M.: Prostate boundary segmentation from ultrasound images using 2D active shape models: optimization and extension to 3D. *Comput. Methods Programs Biomed.* 84(2-3), 99–113 (2006)
5. Shen, D., Zhan, Y., Davatzikos, C.: Segmentation of prostate boundaries from ultrasound images using statistical shape model. *IEEE Trans. Med. Imaging* 22(4), 539–551 (2003)
6. Ophir, J., C  pedes, I., Ponnekanti, H., Yazdi, Y., Li, X.: Elastography: a quantitative method for imaging the elasticity of biological tissues. *Ultrason. Imaging* 13(2), 111–134 (1991)
7. Cochlin, D.L., Ganatra, R.H., Griffiths, D.F.R.: Elastography in the detection of prostatic cancer. *Clin. Radiol.* 57(11), 1014–1020 (2002)
8. Souchon, R., Hervieu, V., Gelet, A., Ophir, J., Chapelon, J.: Human prostate elastography: in vitro study. In: *IEEE Symposium on Ultrasonics*, vol. 2, pp. 1251–1253 (2003)
9. Mahdavi, S.S., Moradi, M., Wen, X., Morris, W.J., Salcudean, S.E.: Vibro-elastography for visualization of the prostate region: method evaluation. In: Yang, G.-Z., Hawkes, D., Rueckert, D., Noble, A., Taylor, C. (eds.) *MICCAI 2009*. LNCS, vol. 5762, pp. 339–347. Springer, Heidelberg (2009)
10. Cootes, T., Taylor, C., Cooper, D., Graham, J.: Active shape models-their training and application. *Comput. Vis. Image Underst.* 61, 38–59 (1995)
11. Zahiri-Azar, R., Salcudean, S.E.: Motion estimation in ultrasound images using time domain cross correlation with prior estimates. *IEEE Trans. Biomed. Eng.* 53(10), 1990–2000 (2006)
12. Mahdavi, S.S., Morris, W.J., Spadinger, I., Chng, N., Goksel, O., Salcudean, S.E.: 3D prostate segmentation in ultrasound images based on tapered and deformed ellipsoids. In: Yang, G.-Z., Hawkes, D., Rueckert, D., Noble, A., Taylor, C. (eds.) *MICCAI 2009*. LNCS, vol. 5762, pp. 960–967. Springer, Heidelberg (2009)
13. Abolmaesumi, P., Sirouspour, M.R.: An interacting multiple model probabilistic data association filter for cavity boundary extraction from ultrasound images. *IEEE Trans. Med. Imaging* 23(6), 772–784 (2004)
14. von Lavante, E., Noble, J.A.: Segmentation of breast cancer masses in ultrasound using radio-frequency signal derived parameters and strain estimates. In: *IEEE ISBI*, pp. 536–539 (2008)

Poster P3-17

ULTRASOUND-BASED TECHNIQUES FOR ENHANCING DIAGNOSTIC AND THERAPEUTIC PROSTATE INTERVENTIONS

Mehdi Moradi, Septimiu E. Salcudean, Purang Abolmaesumi, Sara Mahdavi, Alexander Yuen, Ramin Sahebjavaheer, Anthony Koupparis, Silvia D. Chang, Edward C. Jones, Robert Rohling, Piotr Kozlowski, Christopher Ngan, and S. Larry Goldenberg

University of British Columbia

Background and Objectives: In virtually all diagnostic and treatment interventions related to the prostate, new imaging tools that can combine accurate visualization of the prostate region and the cancerous tumors could reduce the rate of complications and have an enormous impact. We have developed ultrasound-based imaging techniques that have potential in improving the visualization of prostate gland and detection of cancer. These are ultrasound vibro-elastography (VE) for visco-elastic imaging of the prostate and RF time series analysis for tissue typing. Within our 2009 proposal to Department of Defense Prostate Cancer Research Program, we have proposed to use these methods for real-time visualization and detection of the boundaries of the prostate gland and to enhance the prostatectomy and brachytherapy procedures by detecting cancer and the extent of extra-capsular extension of prostate cancer.

Brief Description of Methodologies: An LDR brachytherapy stepper was modified to enable the collection of radio frequency (RF) data volumes for VE and time series imaging. After acquisition of the institutional ethics approval and informed consent, patients undergoing radical prostatectomy at the Vancouver General Hospital are registered into this study and go through pre-operative magnetic resonance imaging (MRI) and intra-operative ultrasound imaging. The ultrasound RF data are analyzed offline to acquire VE images and RF time series feature maps. The extracted prostate specimens are subjected to whole mount histopathology analysis to acquire gold standard cancer maps. Both VE and pathology images are registered to MRI images, which act as a link between VE and pathology data sets. The registration approach is intensity-based with mutual information as the similarity measure.

Results to Date: Based on data acquired from 12 patients, VE images improve the visualization of the prostate gland. VE images are superior to B-mode images in terms of contrast (with an approximately sixfold improvement in contrast-to-noise ratio) and edge strength (with an approximately twofold improvement in gradient in the direction normal to the edge). In terms of cancer detection, we have received three sets of histopathology data, which show that prostate tumors appear as dark areas on VE images due to their increased stiffness.

Conclusions: VE imaging significantly enhances the visualization of the prostate gland. In terms of cancer detection, our results are preliminary, and we expect to increase the specificity of cancer detection by the addition of the RF time series analysis based on supervised training, and combining it with visco-elastic features of tissue provided by VE.

Impact Statement: If successful, the combination of VE and RF time series analysis will drastically improve image-based treatment guidance. In particular, surgical resection planes could be defined to avoid damaging critical anatomical structures.

This work was supported by the U.S. Army Medical Research and Materiel Command under W81XWH-10-1-0201 and the Natural Sciences and Engineering Research Council of Canada.

Towards joint MRI-US based tissue typing and guidance for prostate interventions in AMIGO

Mehdi Moradi, PhD; Tina Kapur, PhD; William M. Wells, PhD; Firdaus Janoos, PhD; Andriy Fedorov, PhD;
Kemal Tuncali, MD; Paul L Nguyen, MD; Clare M. C. Tempany, MD

Department of Radiology, Brigham and Women's Hospital, Harvard Medical School, Boston, MA

Purpose: With an estimated 240,890 cases to be diagnosed in 2011, prostate cancer remains the most common malignancy (other than skin) among the men and is projected to cause 33,270 deaths. A non-invasive imaging technique that can reliably characterize and grade prostate cancer has the potential to improve the delivery of prostate interventions such as biopsy, prostatectomy and brachytherapy by providing the local extent of the disease and facilitating focal therapy. This can result in targeted biopsies, more accurate positive margins in prostatectomy, and enhanced dynamic dosimetry in brachytherapy. We have previously developed cancer detection and characterization techniques based on both multiparametric MRI [1] and ultrasound-based methods [2]. The goal of this work is to leverage our previous efforts and experience in the two areas and create the translational technology to perform MR-guided interventions assisted by tissue typing information from registered MRI and ultrasound.

Methods: The recent launch of the Advanced Multimodality Image Guided Operating (AMIGO) suite at BWH provides us with a unique opportunity to develop and validate the enabling technology to combine the state of the art methods in ultrasound and MRI based tissue typing techniques. The AMIGO suite features a 3T MRI wide bore (70 cm) Siemens Verio scanner streaming data through an OpenIGT link to 3D Slicer, and a Pro Focus ultrasound system (BK Medical Systems) with the capability of streaming both the B-mode images and raw RF ultrasound signals to an external PC through a camera link and custom software under development.

The access to ultrasound RF data gives us the ability to extract tissue typing features from the spectral analysis of the RF data [2,3], and work towards developing ultrasound elastography to compute tissue elasticity. MRI and ultrasound will be registered in 3D slicer environment and tissue typing features from ultrasound (texture features, RF spectral features, elasticity) and MRI (DCE and DTI features) will be combined for tissue classification. An MR compatible and US transparent adjustable sleeve template assembly is being developed to house the transrectal ultrasound probe and the MRI coil, interchangeably, during the procedures. This will ensure similar configurations of the prostate and the rectal wall during MRI scan and the ultrasound scan performed using a non-MR compatible transducer after the MRI magnet is moved out of the central part of the AMIGO suite.

Previous experience: Currently in BWH, brachytherapy procedures are performed with dynamic intraoperative dosimetry and robotic delivery. MRI is acquired pre-operatively in the assessment stage. However, images are not available during the implant procedure. The addition of MR-ultrasound fusion to the procedure will be the first step in the new initiative. Transition to AMIGO will follow and will take advantage of the MRI-compatible robotic technology developed in our group [4]. In the past we have reported on the BWH clinical experience with 3T MRI-guided transperineal prostate biopsy [5], and have now completed the first case of that type in AMIGO.

Conclusions: The AMIGO suite affords us the opportunity to develop and quantitatively validate the effects of registered MRI and ultrasound tissue typing. The final product will be translated to the conventional TRUS-guided interventional environment by using 3D ultrasound as the intraoperative modality and registration to pre-operative MRI. This will enable wider accessibility of the developed technology.

Acknowledgment: This work is partially supported by NIH grants R01CA111288 and P41RR019703, and DoD W81XWH-10-1-0201.

References:

- [1] Chan I, et al., "Detection of prostate cancer by integration of line-scan diffusion, T2-mapping and T2-weighted magnetic resonance imaging; a multichannel statistical classifier," *Medical Physics*, 2003: 2390-2398.
- [2] M. Moradi, et al., "Augmenting Detection of Prostate Cancer in Transrectal Ultrasound Images Using SVM and RF Time Series," *IEEE TBME*, 2009: 2214-2224.
- [3] Feleppa EJ, et al., "Recent developments in tissue-type imaging (TTI) for planning and monitoring treatment of prostate cancer." *Ultrasonic Imaging*, 2004: 163-712.
- [4] Fischer GS, et al., "Development of a Robotic Assistant for Needle-Based Transperineal Prostate Interventions in MRI," *Proc. MICCAI 2007*: pp 425-433.
- [5] K. Tuncali, et al., "3T MRI-guided Transperineal Targeted Prostate Biopsy: Clinical Feasibility, Safety, and Early Results, *Proc. ISMRM 2011*: 53.